UNIVERSITY OF
BIRMINGHAM

THE ELECTROCHEMISTRY OF METAL NANOPARTICLES FOR OXYGEN REDUCTION AND NITRATE/NITRITE REDUCTION

by

WILAI SIRIWATCHARAPIBOON

A thesis submitted to
The University of Birmingham
for the degree of
DOCTOR OF PHILOSOPHY

School of Chemistry
College of Engineering and Physical Sciences
The University of Birmingham

ABSTRACT

Heterogeneous catalysts have been widely applied for reactions at solid/liquid interfaces in electrochemistry. This research has scientific aims focused on two important electrochemical reactions: oxygen reduction and nitrate/nitrite reduction. A series of rhodium (Rh) deposited on gold nanorods (Au NRs) and gold nanoparticles (Au NPs) were synthesised by wet chemical reduction. The growth of Rh on Au was initially investigated on Au NRs. The scanning transmission electron microscopy (STEM) showed that Rh has a preferential deposition and epitaxial growth at the end of Au NRs. Cyclic voltammetry and rotating disc electrode (RDE) measurements were performed to study the oxygen reduction at these Au:Rh/C catalysts. The composition of the Rh on Au surface enables control of the selectivity of the reaction. Diluted Rh atoms on a Au surface give rise to a high H_2O_2 selectivity, similar to that of pure Au, while a Rh-rich phase on a Au surface give rise to a high H_2O selectivity.

Pyrolysed cobalt triethylenetetraamine on a carbon substrate (Co/TETA/C) was employed to produce H_2O_2 from the ORR. The results from the rotating ring disc electrode (RRDE) reveal that the heat treatment influences the H_2O_2 selectivity. The Co/TETA/C heated at 1000 °C yields the highest H_2O_2 selectivity while the Co/TETA/C heated at 700 °C yields the lowest H_2O_2 selectivity.

Rh/C, Au:Rh/C nanoparticles and Sn modified Rh/C nanoparticles were employed for nitrate/nitrite reduction in acidic media. The catalytic activity of Rh/C and the selectivity towards N_2 can be enhanced by Sn modification. Results from on-line electrochemical mass spectrometry (OLEMS) reveal that the modified electrode generates N_2 from further reduction of the nitrous oxide (N_2O) intermediate. Ion chromatography (IC) shows that ammonium is the main product at Rh/C. Hydroxylamine can also be detected after Sn modification on Rh/C.

To my dearest family

ACKNOWLEDGEMENTS

First and foremost I would like to acknowledge my supervisor, Dr Sarah L. Horswell for giving me the opportunity to collaborate in her research group and for all her support, guidance and patience throughout this PhD. This thesis would have never been possible without her input.

I would like to thank Dr Horswell's research group, especially my friend Elena for the help and company since the beginning of my PhD and John for his tips and good discussions.

I would like to thank Prof. Marc T.M. Koper for his advice and for allowing me to spend time in his group to learn OLEMS and ion chromatography, Yang Jian for his kind help on nitrate reduction experiments, Youngkook Kwan for his support on ion chromatography experiments and all members of Catalysis and Surface Chemistry, University of Leiden.

I would also like to thank Johnson Matthey Technology Centre, Dr Robert Potter for his advice, encouragement and the opportunity to work at Johnson Matthey, Maria Campos for the collaboration and friendship, Dr Sarennah Longworth and Dr Hoy Dobson for providing TEM images and XRD data.

I would like to thank Dr Ziyou Li for suggestions and Ruth Chantry for STEM images, Prof. Roy Johnston and Andy Logsdail for discussion on optical properties.

I would like to thank Dr Zoe Schnepp for TEM images, Marzena Allan for her help with XPS, Stuart Arkless, Steve Williams, Steve West, Wayne Yates and Cheryl Powell for their generous technical support.

I am grateful for the financial support from the European Union FP7 Initial Training Network "ELCAT" (Grant Agreement No. 214936-2). I would like to thank the ELCAT network for providing the opportunity for learning more about electrochemistry and all the knowledgeable discussions.

A massive thanks must be expressed to my friends, Anchalee for her encouragement and support, Jane for her support and invaluable tips and discussion in electrochemistry, Ying, Evin, Chao, Yang, Jing and Hongjiao for their help and being supportive friends, all those who I have shared time with over the past few years and friends who are from far away.

Most of all I would like to express my sincere thanks to my parents and my beloved family for their unconditional support, care throughout and encouragement. Without them I would never been able to gain this incredible experience of studying abroad and having the chance to make them proud of me.

TABLE OF CONTENTS

CHAPTER 1
INTRODUCTION

1.1 Preface

This thesis focuses on the preparations and the electrochemical analysis of catalysts for oxygen reduction and nitrate reduction. Gold nanoparticles (Au NPs) have been used for much research. The properties of Au NPs are significantly size- and shape- dependent. Au nanorods (Au NRs) are used in many applications, such as medical imaging[1] and sensors[2] owing to their tunable optical properties. Au NPs present a catalytic activity towards the oxygen reduction reaction (ORR) in acidic or alkaline media *via* 2-electron or 4-electron pathways. Rhodium (Rh), which is in the Pt group, can also be used as a catalyst for the ORR. The catalytic activity of Rh nanoparticles is size- and shape- sensitive. The first objective of this work was to study the feasibility of Rh coated on Au NRs and Au NPs as an electrocatalyst for the ORR and to study the electrocatalytic activity of Rh-coated Au NPs from different methods of Rh deposition: co-reduction and sequential reduction.

As a result of the high cost of precious metals, non-precious metals, such as Fe[3] and Co[4], have been studied for over decades as catalysts for the ORR. Co alone is a relatively ineffective catalyst for the ORR. Its activity is enhanced after forming a metal complex with N−ligands. Its stability during the ORR is obtained after a heat treatment is introduced during catalyst preparation. Although most examples have contained aromatic N-ligands, triethylenetetraamine (TETA), an aliphatic source of nitrogen, can also be used to form a Co-N complex.[5] The electrocatalytic activity of Co/TETA/C towards the ORR depends on the heat treatment during catalyst preparation. The second objective of this work was to investigate the formation of active sites of Co/TETA/C catalysts during heat treatment and the selectivity and the kinetics of the ORR for each catalyst.

Nitrate reduction is part of the nitrogen cycle. Nitrate conversion is usually catalysed by enzymes in the environment. Nitrate becomes an environmental issue as a result of its reduction into harmful species, which threaten human life. Rh also presents promising catalytic activity for nitrate reduction. One of the main objectives of this work was to investigate the electrocatalytic activities of Rh/C, Au:Rh/C and Sn-modified Rh/C for nitrate reduction and nitrite reduction by using electrochemical techniques combined with more direct analytical techniques: mass spectrometry and ion chromatography.

In this chapter, an overview of electrocatalysis will introduce some important aspects of electrocatalytic reactions. Secondly, an introduction to the synthesis of Au NRs and Au NPs in surfactants containing aqueous solution is given. The description and the mechanism of the ORR both precious metals and non-precious metals will be described. At the end of this chapter, a description of nitrate reduction will be given.

1.2 Catalysis

Catalysis is a chemical reaction in which the chemical reaction rate is increased by the participation of a substrate called a catalyst. A catalysed reaction has a lower activation energy than an uncatalysed reaction, resulting in a higher reaction rate compared at the same temperature.[6] The catalyst is involved in multiple steps of chemical reactions. The activity of the catalyst is influenced by several factors, such as temperature, concentration, inhibitor, promoter, electronic effect, support effect etc. In terms of kinetics, the rate of chemical reaction is related to the frequency of collision of reactants. The catalyst is generally involved in the slowest step. Catalysts can be classified into 2 main types: heterogeneous catalysts and homogeneous catalysts.

A heterogeneous catalyst functions in a different phase from the reactant. Most heterogeneous catalysts are in the solid phase and react with the reactants in either a liquid or a gas phase.[7] Many transition metals, such as Pt, Rh, Pd, Au etc., have been used for several reactions. The reaction takes place when the reactants are adsorbed on the active sites of catalysts. The surface area of the catalyst has an effect on the rate of the reaction. With heterogeneous catalysts, the catalysts are typically deposited in another substrate in order to enhance their efficiency and reduce the cost. A homogeneous catalyst acts in the same phase as the reactant.[8] The reaction and the catalyst are generally in a gas or liquid phase. The catalyst is typically dissolved by the solvent and introduced into the reactant.

1.3 Electrocatalysis

In an electrochemical reaction, many chemical reactions do not take place or take place with slow rate at the metal/electrolyte interface at the potential near their thermodynamically favourable potential.[9] In the absence of catalyst, the electrochemical reaction may occur with a high overpotential and yield a low current density because of poor kinetics. The aim of electrocatalysis is therefore, to seek the alternative: lower activation energy pathways and to catalyse the electrode reaction at the potential near the equilibrium potential with high current density. The activity of the catalyst can be varied by the structure of the electrode surface, such as crystal planes, clusters, alloys and surface defects and also varied by the electrolyte. Electrocatalysis is important for many applications of electrochemistry. The energy efficiency is necessary. This is taken into account by overpotential on both the anode and the cathode. Eq. (1.1) shows that the overpotential depends on both a Tafel slope and an exchange current density.[10]

$$\eta = \frac{2.3\,RT}{\alpha AnF}[\log I - \log I_0] \qquad (1.1)$$

The electrochemical reaction involves a transfer of electric charges between the electrode surface and species dissolved in the electrolyte. The charge carrier can be an ion or an electron.[11] The additive to the electrolyte can either increase or decrease the rate of the reaction. The term "eletrocatalysis" is generally applied to the systems where reduction or oxidation requires bond formation or interaction between reactant, intermediate or product with the electrode surface. The driving force of an electrode reaction is controlled by parameters, such as temperature, concentration and pressure but also the external electric force characterised by the electrode potential, which was altered by the external applied potential. The catalyst can be the electrode material itself or the substrate adsorbed on the electrode surface. There are a number of electrode reactions that involve adsorbed species, such as hydrogen evolution, oxygen reduction and evolution, methanol oxidation, nitrate reduction etc.

In order to understand the electrochemical reaction, the first step is to distinguish between the thermodynamics and kinetics of the electrochemical reaction. Thermodynamics only describe the changes in energy and entropy during the electrochemical reaction at equilibrium or at least very near to the equilibrium.[12,9] The two fundamental states can determine to what extent a reaction will proceed and the equilibrium constant. Nothing can be expressed about a rate constant and a mechanism of the reaction. For kinetics, either a galvanic or electrolytic cell is involved with a charge transfer across the interface of two adjacent phases. The reaction rate is a strong function of potential. The rate of the reaction is determined by the slowest step and the overall rate is related to the unit area of the interface. The electrode reaction involves all processes accompanying by charge transfer step. These are called "Electrode Processes".[13] The electrode processes comprise electrode reaction and mass transport processes. Mass transport processes include diffusion, migration and convection.

These must be considered to determine the kinetics of the reaction and are discussed in more detail in chapter 2.

1.4 The Synthesis of Au Nanoparticles and Au Nanorods

1.4.1 Overview of Au nanoparticles and Au nanorods

Metal nanoparticles have been extensively investigated over decades, especially Au nanoparticles (Au NPs) owing to their properties and activities. Gold has been used since the ancient Roman times. Colloidal gold was used for colouring glass and ceramics. In 1857, Faraday reported the formation of pure Au colloids by chemical reduction of $AuCl_4^-$ reagent with phosphorus in CS_2.[14] He investigated the optical properties. Several methods for the synthesis of Au colloids were reported and revealed in the 20th century.[15-17] Schmid reported that metal colloids can be generated by 2 typical methods: dispersion method and reduction method.[15] The metal particles from the former method are not stable and present a distribution of size and shape compared with the latter method. The most widely used method for preparing Au NPs is wet chemical synthesis, which can yield uniform size and shape of Au NPs.[18] This method requires a reducing agent and a stabiliser. The effective reducing agents are citrate salts,[19] $NaBH_4$[20,21] and polyols[22]. The two-phase reduction introduced by Brust *et al.* also became a popular procedure for preparing Au NPs. The reduction of $AuCl_4^-$ salt was reduced by borohydride in thiol-containing organic compound.[16] Due to their high surface energy, Au NPs are active and tend to aggregate together in the solution. A stabiliser or a protecting agent is used to prevent an aggregation and precipitation of nanoparticles.

1.4.2 Synthesis of Au nanorods

The fundamental aims of many researches are the synthesis and the design of particle size and shape. The properties of Au NPs are significantly size- and shape- dependent. Here we focus

on a rod-like particle, especially Au nanorods (Au NRs). In several procedures for Au NR formation, the seed-mediated method has been the most efficient and useful procedure.[23-25] This method required the soft template formation of cationic surfactant micelles to induce the growth of Au NRs. Likewise, the surfactants provide a colloidal stability.[26] In this work, we used CTAB, a cationic surfactant, for synthesis of Au NRs. The seed-mediated method involves the reduction of $AuCl_4^-$. Initially, Au seeds of 1-5 nm, capped with CTAB, are formed in the first nucleation stage by using $NaBH_4$ as a strong reducing agent. The growth step is typically carried out in an aqueous solution of concentrated CTAB, $AgNO_3$, $HAuCl_4$ and ascorbic acid. Ascorbic acid is a weak reducing agent, which cannot reduce Au salt to Au NRs in the presence of surfactant micelles without seed addition. In this stage, Au^{3+} ions are only reduced to Au^+ ions. The secondary nucleation in the growth step takes place by addition of Au seeds, an electron-rich particle, which reduces Au^+ to Au^0. The interactions between CTAB and $HAuCl_4$ in aqueous solution are represented by the following equations.[25,27]

$$[AuCl_4]^- + 4CTAB \quad \leftrightarrow \quad CTA{-}[AuBr_4] + 4Cl^- + 3CTA^+ \qquad (1.2)$$

First reduction Au^{3+} to Au^+

$$CTA{-}[AuBr_4] + C_6H_8O_6 \leftrightarrow CTA{-}[AuBr_2] + C_6H_6O_6 + 2H^+ + 2Br^- \qquad (1.3)$$

Second reduction Au^+ to Au^0

$$2CTA{-}[AuBr_2] + C_6H_8O_6 \leftrightarrow 2Au + C_6H_6O_6 + 2CTA^+ + 2H^+ + 4Br^- \qquad (1.4)$$

Overall reaction

$$2CTA{-}[AuBr_4] + 3C_6H_8O_6 \leftrightarrow 2Au + 3C_6H_6O_6 + 2CTA^+ + 6H^+ + 8Br^- \qquad (1.5)$$

CTAB coats Au NRs by forming a bilayer; this is based on the mechanism where the head groups of CTAB adsorbs onto the first layer on the surface of Au NRs, as shown in Figure 1.1. The adsorptions of head groups of CTAB are crystallographic facet-sensitive with a preferential adsorption along the sides rather than at the ends of Au NRs.[24,28] The head

groups, counter ions and length of hydrocarbon tails have effects on the formation of Au NRs. Keeping the headgroups and counter ions constant, the longer hydrocarbon chain length yields and leads to the longer Au NRs.[29] Br^- counter ions are necessary for Au NR formation. Comparing the same hydrophilic head with Br^- and Cl^-, such as CTAB and CTAC, CTAB yields short Au NRs, while CTAC only yield spherical Au NPs. This may relate to the electrostatic interaction between the counter ion and the headgroup of surfactant or to adsorption strength of Cl^- or Br^- on Au facets.

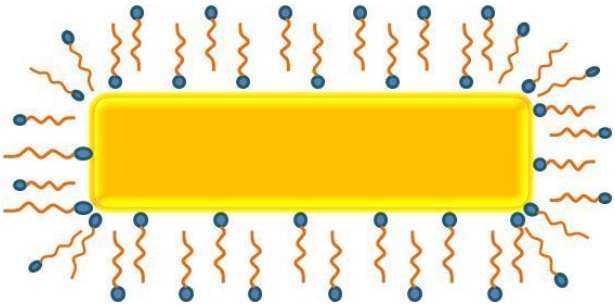

Figure 1.1 The adsorption of CTAB bilayer on Au NRs.

The presence of $AgNO_3$ in the solution is essential in order to obtain high yield of Au NRs; however, there is a critical concentration of Ag^+ ion, where above this concentration the formation of Au NRs is decreased.[24] The high yield of Au NRs may be explained by one mechanism of the soft template, in which it proposed that Ag^+ ions are in between the headgroups of CTAB in the form of AgBr pairs. The AgBr pairs can reduce the charge density of Br^-, resulting in reducing the repulsion between headgroups and so stabilising the template.[24] The effect of Ag^+ on Au NR aspect ratio is still unclear. It may be that Ag^+ ions form AgBr pairs with Br^- ion (counter ion from CTAB) and restrict the growth of the AgBr passivated crystal facet.[30] In the absence of Ag^+ ion, Au NRs with longer aspect ratio are obtained, which indicates that the length of Au NRs increases when Au precursor is still

available. In the presence of Ag^+ ion, the aspect ratio of Au NRs increases until it reaches the critical concentration and then decreases after that concentration, indicating that excess AgBr pairs restrict the preferential growth at the tips.[31]

The structure of Au NRs prepared by the seed-mediated method has been basically investigated a crystal structure by using TEM and STEM combines with a field emission gun. The atomic crystallography was analysed. There were several models which were introduced. One of the most common models suggested that Au NRs composed of the twin defect structures on the {110} crystal face along with [100] direction connected with {111} surfaces.[32,33] Recently, the surface facets of Au NRs were determined by atomic-scale 3D reconstruction technique and HAADF-STEM images.[34] The Au NRs prepared from CTAB mainly comprises (110) and (100) facets on the side, corresponding with previous reports. This revealed that the cross-section of Au NRs is formed by alternating {110} and {100} planes.

1.5 The Structure of Surfactant

A surfactant is a substance that, when dissolved in liquid, can lower the surface tension of liquid or an interfacial tension between two phases. A surfactant is an amphiphilic molecule. It can be classified as a nonionic, cationic, anionic or amphoteric surfactant. Cetyltrimethyl ammonium bromide (CTAB) is one of the cationic surfactants widely used in nanoparticle synthesis. The CTAB structure comprises a hydrophilic head group, which is trimethyl ammonium with bromide counter ion and a hydrophobic tail, which is a hydrocarbon chain of $C_{16}H_{33}$, as shown in Figure 1.2.

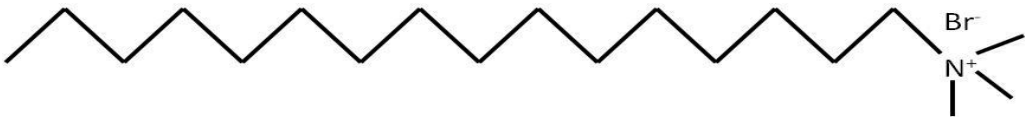

Figure 1.2 Structure of hexadecyl-trimethyl-ammonium bromide (C_{16}TAB).

In bulk solution, the molecules of CTAB at low concentration are present in the aqueous solution as solvated polymers. The surface tension of aqueous solution typically changes with the concentration of CTAB. After reaching a critical micelle concentration (CMC)[35], the surface tension becomes constant and the concentration of the surfactants is sufficient to form a micelle. The additional surfactants added to the aqueous solution go towards the micelles.[35] In typical aqueous solutions, the hydrophobic tails segregate from the aqueous solution and aggregate into colloidal micelles, which have a hydrophobic interior and a hydrophilic surface[36], as shown in Figure 1.3. Thermodynamically, micelle formations are spontaneously formed in order to balance entropy and enthalpy. The assembling of surfactants reduces their entropy.[37]

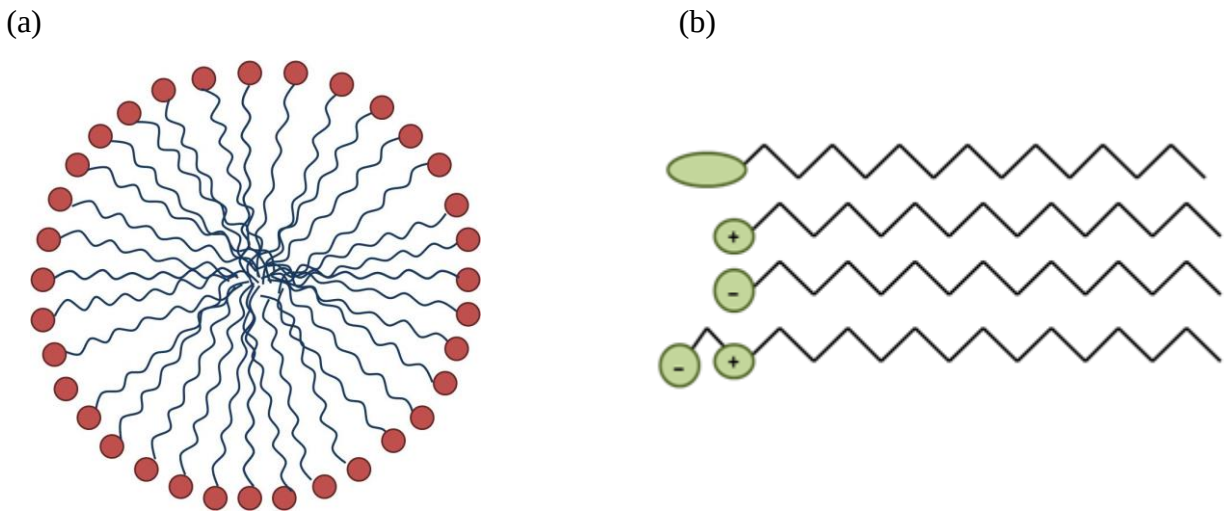

Figure 1.3 (a) micelle structure in aqueous solution and (b) different types of surfactants.

The adsorption of ionic surfactants on the solid surface involves several forces, such as covalent bonding, electrostatic attraction, hydrogen bonding and non-polar interactions between the adsorbed species.[38] At low surfactant concentrations, the electrostatic force between charged species and oppositely charged solid surface induces the surfactant adsorption. On increasing surfactant concentrations, the interactions of hydrocarbon tails

increase and induce hemi-micelles or admicelles. The adsorption sharply increases at this region due to the interactions of hydrocarbon tails and the electrostatic interactions. When the solid surfaces are neutralized by charged species, the increase of adsorption decreases because the electrostatic interactions are no longer operative and only interactions between hydrocarbon tails are present. When the concentration reaches the CMC, the surfactant monoactivity becomes constant and it does not change the adsorption activity. The CTAB concentration increase only contributes to the micellisation.[4]

1.6 Rhodium Nanoparticles

Rhodium is one of the platinum group metals. Despite its expensive nature, Rh is used as a catalyst for several reactions, such as oxygen reduction, nitrate reduction, CO oxidation, hydrogenation,[39] hydroformylation,[40] hydrocarbonylation[41] and combustion reactions[42]. In this work, we utilise Rh for oxygen reduction, nitrate reduction and nitrite reduction. There are fewer reports on Rh nanoparticles than other precious metals. The catalytic activity of Rh particles is size- and shape- sensitive. Somorjai *et al.* reported a number of papers on the size and shape control of Rh, such as multipods, cubes, horns and cuboctahedra, prepared by seed mediation in a polyol system.[43,44] The different shaped Rh particles exhibited different optical properties.

Rh yields high electrocatalytic activity on oxygen reduction. The volcano plot in Figure 1.4 shows the trends of oxygen reduction for each metal according to the oxygen binding energy obtained from the literature.[45] There is some room for improvement of the catalytic activity of each metal by forming an alloy with another metal. Rh is also an important catalyst for nitrate and nitrite reduction. Wasberg and Horanyi showed that Rh has high catalytic activity on nitrate reduction.[46] These agree well with the report from Brylev *et*

al. that the main product of nitrate reduction on Rh electrode is ammonium without gaseous product.[47] The high catalytic activity of Rh is due to its high affinity for anions.

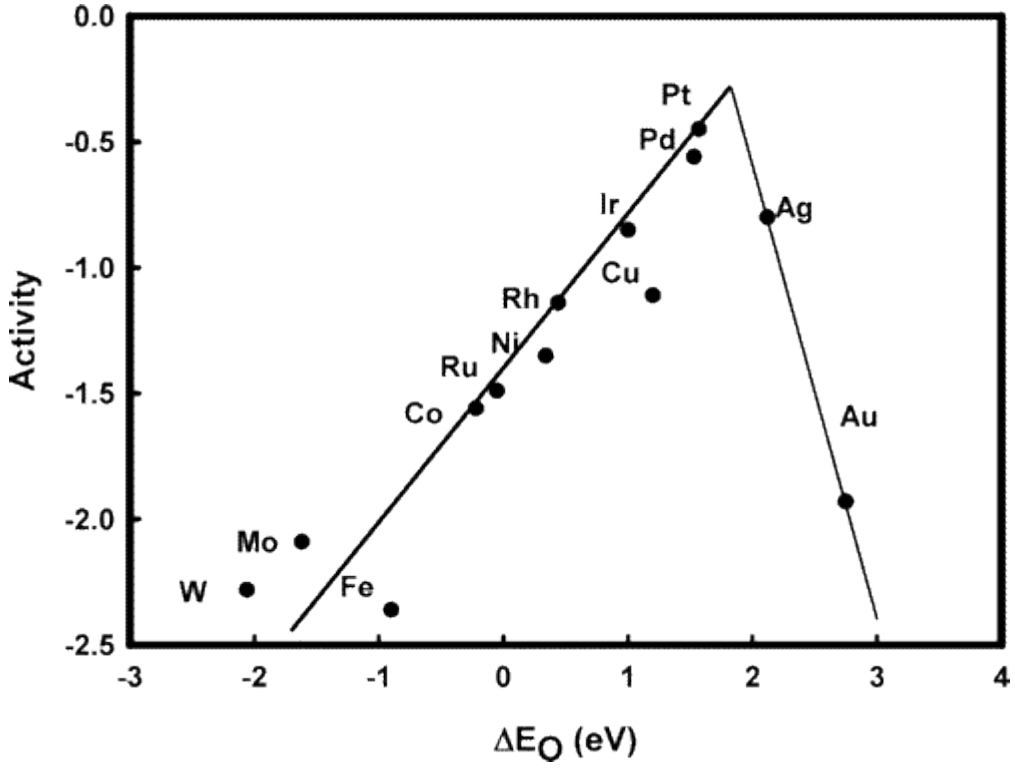

Figure 1.4 Trends in oxygen reduction activity plotted as a function of the oxygen binding energy.[45]

1.7 The Oxygen Reduction Reaction (ORR)

1.7.1 Molecular orbital of oxygen Molecule

The electronic structure of an oxygen molecule can be described by a molecular orbital diagram, as shown in Figure 1.5. In the ground state, a molecule of O_2 forms an O−O bond by a π bond between 2p atomic orbitals. There are 2 unpaired electrons in the anti-bonding orbital. In the oxygen reduction reaction (ORR), the electrons added occupy anti-bonding orbitals, decreasing the bond order for O−O. This increases the O−O bond distance, weakening the O−O bond. The excess of bonding electrons over antibonding electrons causes

the high stability of the O_2 molecule, with low reactivity, resulting in a high overpotential for its reduction.

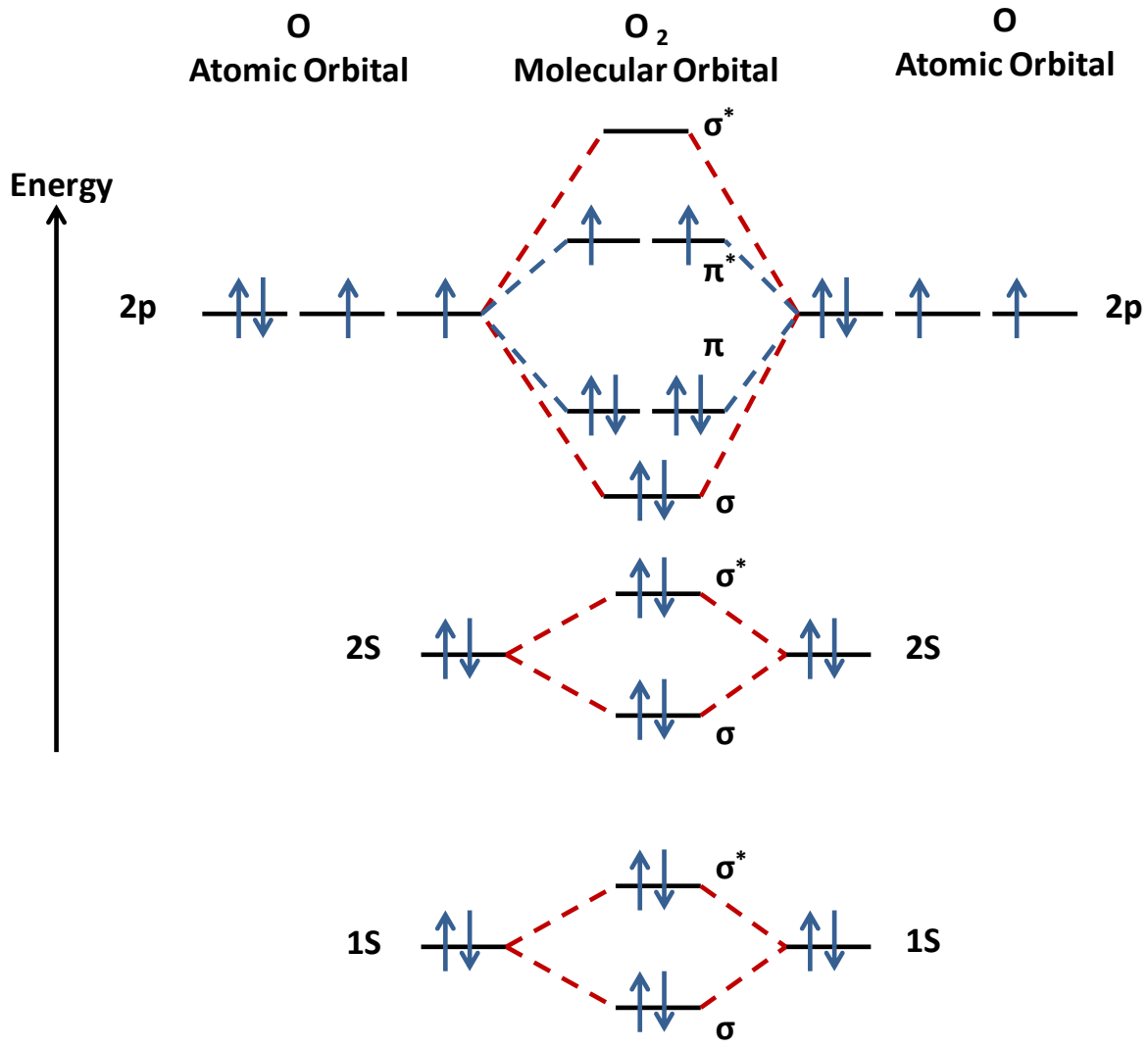

Figure 1.5 Molecular orbital diagram of the oxygen molecule in the ground state.[48]

1.7.2 Mechanism of the oxygen reduction reaction

The oxygen reduction reaction (ORR) is the key reaction at the cathode in a fuel cell. The ORR has been intensively studied because its reaction is slow, with a high overpotential, which impacts on the energy efficiency of fuel cells.[49] This limitation can be overcome by the application of an effective electrocatalyst. The overall scheme, valid for both acid and base and all the electrode materials discussed here, is given in Figure 1.6.[50] The ORR in aqueous

solution takes place mainly *via* two parallel pathways: the direct 4-electron reduction of O_2 pathway to produce H_2O (or to OH^- in base) and the indirect 2-electron reduction of O_2 to produce hydrogen peroxide (H_2O_2) as a product or an intermediate.

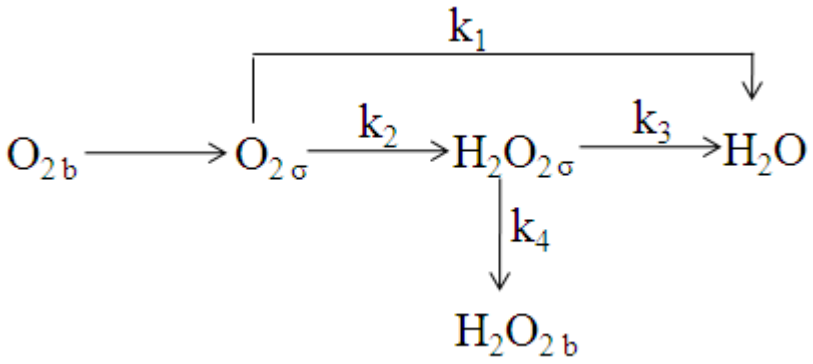

Figure 1.6 Pathways for the oxygen reduction reaction in both acid and in base. The subscripts b and σ refer to species located in the bulk and at the surface, respectively.[50]

The reaction pathways strongly depend on some conditions in an experiment, such as pH and electrode material. The reactions proceed in the following forms.

In acidic media:

Direct reduction

$$O_2 + 4H^+ + 4e^- \rightarrow 2H_2O \qquad E^0 = 1.23\ \text{V}\ vs\ \text{RHE} \qquad (1.6)$$

Indirect reduction

$$O_2 + 2H^+ + 2e^- \rightarrow H_2O_2 \qquad E^0 = 0.682\ \text{V}\ vs\ \text{RHE} \qquad (1.7)$$

$$H_2O_2 + 2H^+ + 2e^- \rightarrow 2H_2O \qquad E^0 = 1.77\ \text{V}\ vs\ \text{RHE} \qquad (1.8)$$

In alkaline media:

Direct reduction

$$O_2 + 2H_2O + 4e^- \rightarrow 4OH^- \qquad E^0 = 0.401\ \text{V}\ vs\ \text{RHE} \qquad (1.9)$$

Indirect reduction

$$O_2 + H_2O + 2e^- \rightarrow HO_2^- + OH^- \qquad E^0 = -0.076\ \text{V}\ vs\ \text{RHE} \qquad (1.10)$$

$$HO_2^- + H_2O + 2e^- \rightarrow 3OH^- \qquad E^0 = 0.88\ \text{V}\ vs\ \text{RHE} \qquad (1.11)$$

H_2O_2 can decompose either homogeneously or heterogeneously (also yielding an overall 4-electron reduction)

$$2H_2O_2 \rightarrow O_2 + 2H_2O \qquad (1.12)$$

The ORR in non-aqueous solution takes place *via* 1-electron reduction to superoxide in the following form.

$$O_2 + e^- \rightarrow O_2^- \qquad (1.13)$$

The ORR is a multiple-electron process, which leads to different products, intermediates and reaction steps. The various possible intermediates and potential of chemical reactions in acidic electrolyte is shown in Figure 1.7. The diagram shows that the oxygen reduction can operate *via* many different routes. It also shows that the intermediates will react with an electrode surface. Therefore, their chemical potential will depend on the nature of the electrode surface at the site of the intermediate's adsorption, as well as the influence of neighbouring adsorbates and the electrolyte; however, the diagram does not show the activation energy from one intermediate to another. The parallel path, involving the dissociation of the oxygen and its subsequent reduction to water in the diagram, shows that a parallel path involving an atomic oxygen type intermediate would require an electrode surface that could significantly reduce the chemical potential of the intermediate.

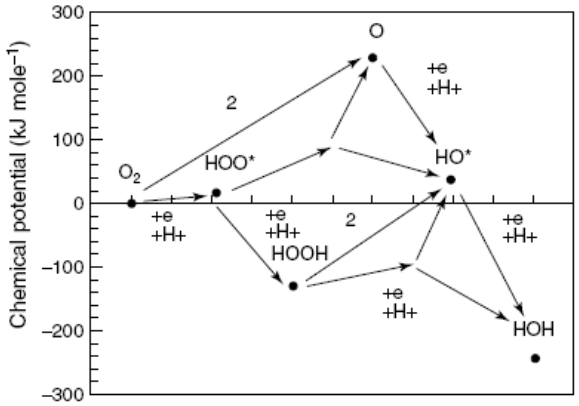

Figure 1.7 The chemical potentials of various oxygen reduction intermediates in acidic water. (Note the pk_a of H_2O_2 is 11.6 and of HO_2 is 7.3.)[51]

Figure 1.8 presents the mechanism for the $4e^-$ reduction of oxygen reduction. The O_2 moves towards the metal surface and forms a π-bond complex between the O_2 molecule and the metal surface, resulting in weakening the O−O bond.[13] The O−O bond is then cleaved *via* a concerted mechanism. The M−OH bond is formed by the protonation and reduction of O_{ads} atom.[13] The M−OH bond is then reduced further to form H_2O. The formation of π-bond complex depends on suitable energy levels to receive the donated electron. The mechanism of the direct $4e^-$ pathway would be:

$$O_2 \rightarrow 2\bullet O_{ads} \quad (1.14)$$

$$2\bullet O_{ads} + 2H^+ + 2e^- \rightarrow 2OH_{ads} \quad (1.15)$$

$$2OH_{ads} + 2H^+ + 2e^- \rightarrow 2H_2O \quad (1.16)$$

The dissociation of O_2 is relatively high (498.3 kJ mol^{-1}).[52] The direct $4e^-$ reduction requires dissociation of the O_2 molecule prior to the first electron transfer. Hence, a metal with high O_2 adsorption is needed to form strong enough M−O bonds. However, metals with very strong M−O bond strengths exhibit poor catalytic activity for the oxygen reduction reaction because the reaction stops at the surface OH formation step.

The reduction of O_2 to H_2O *via* the peroxide intermediate is energetically more favourable because during this mechanism the first electron is transferred to the O_2 molecule before it dissociates. The mechanism for the reduction of O_2 to H_2O *via* an $H_2O_{2,ads}$ intermediate is:[53]

$$O_2 \rightarrow O_{2,ads} \quad (1.17)$$

$$O_{2,ads} + e^- + H^+ \rightarrow HO_{2,ads} \quad (1.18)$$

$$HO_{2,ads} + e^- + H^+ \rightarrow H_2O_{2,ads} \quad (1.19)$$

$$H_2O_{2,ads} + e^- + H^+ \rightarrow H_2O + HO_{ads} \quad (1.20)$$

$$HO_{ads} + e^- + H^+ \rightarrow H_2O \quad (1.21)$$

A rotating disc electrode (RDE) and a rotating ring-disc electrode (RRDE) are employed to detect the intermediates. The RDE was first applied to the ORR by Mueller and Nekrasov[54] and it still can be used. The ring of the electrode can monitor the amount of hydrogen peroxide formed at the disc. The $2e^-$ and $4e^-$ ORR can occur at the disc and the H_2O_2 is re-oxidised to O_2 at the ring.[55]

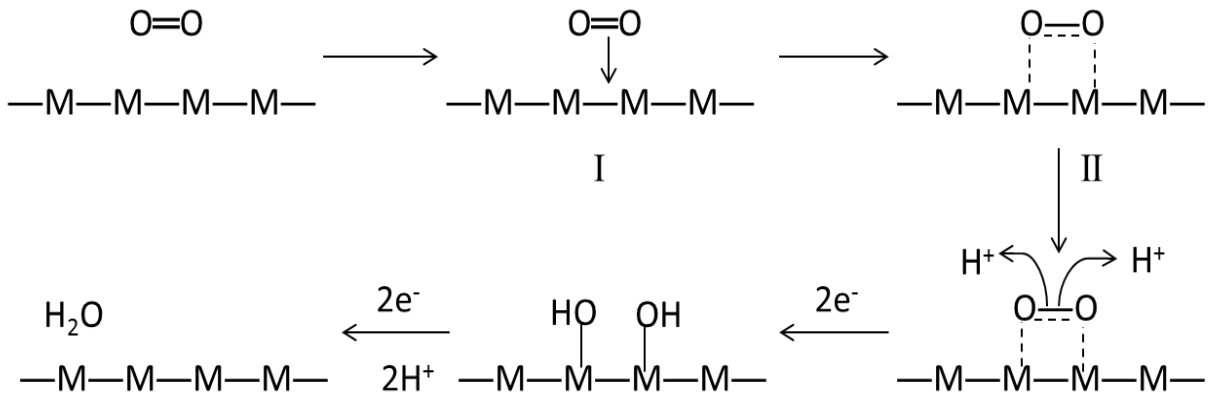

Figure 1.8 One mechanism for the $4e^-$ reaction of oxygen in a sequence involving the formation of a π-complex between O_2 and the surface I, cleavage of the O−O bond with concerted formation of M−O bands (II), and protonation and reduction to form water.[13]

1.7.3 Oxygen reduction on precious metal catalysts

Several transition metals have been used to catalyse the ORR. The predominantly used catalysts for 2-electron reduction are Hg, Au (except Au(100) in alkaline solution)[56], carbon, most metal oxides, oxide-covered metal and non-precious metals[57,58]. The predominantly used catalysts for $4e^-$ reduction are Pt[59], Pt group metals: Rh, Pd, Au, Pt alloys[59], Au (100) in alkaline solution[56], Ag and metallic iron in neutral solution[60]. The catalytic activity towards the ORR of the other precious metals is still lower than that of Pt. The catalytic activity decreases in the order Pt > Pd > Ir > Rh.[4] The catalytic activity of a metal can be enhanced by forming an alloy with a second metal, resulting in a change of catalyst structure, geometry and electronic structure.

The ORR on a Pt electrode is widely studied. In the presence of oxygen, the Pt surface is a mixture of Pt, PtO and its hydroxide compound. The catalytic activity has been influenced by the electronic structure of the Pt catalyst (Pt *d*-band vacancy) and the Pt-Pt interatomic distance (geometric effect).[45] Pt is the metal surface on which the direct $4e^-$ reduction is possible: it forms a bond with the oxygen strong enough for O_2 dissociation to occur, but not too strong, for it allows OH_{ads} to be reduced further to H_2O. Figure 1.9 presents the models that have been proposed for the chemisorptions of O_2 molecules: (a) is on-top end-on adsorption, where a single oxygen atom from the O_2 molecule is adsorbed onto a single Pt atom (Pauling model); (b) is bridge end-on adsorption where one oxygen atom is adsorbed onto two or more Pt atoms; (c) shows on-top side-on adsorption (Griffiths model) and (d) shows hollow adsorption (bridge model).[61]

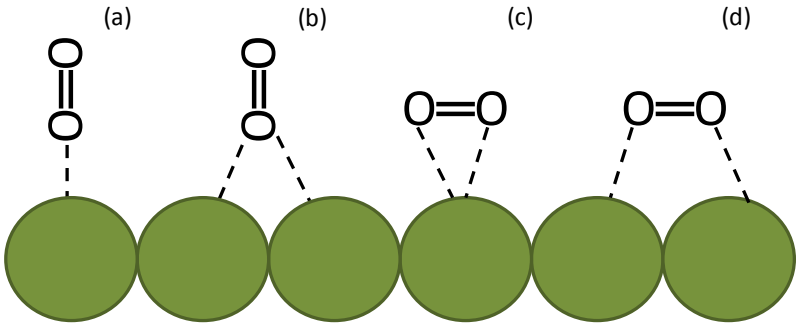

Figure 1.9 Adsorption of O_2 on Pt *via* the following configurations: (a) on-top end-on, (b) bridge end-on, (c) on-top side-on and (d) hollow.

Zinola *et al.* analysed the O_2 adsorption on Pt (100) and Pt (111) by semi-empirical quantum calculations. They suggested that the bridge adsorption of O_2 molecule on two or more Pt atoms, in Figure 1.19b, is the most stable on both Pt (100) and Pt (111) surfaces.[62] The type of bonding on the Pt surface determines the rate of the oxygen reduction reaction. The more stable Pt−O interaction results in H_2O formation. The rate of the oxygen reduction is less when the ad-atoms, such as surface oxide[63] or halides[64], are present because the stable

bridge bonding of O_2 on Pt atoms is less to occur on a partial partially blocked Pt surface. Markovic *et al.* concluded that this observed decrease in the oxygen reduction activity on the Pt surface arises from the ad-atoms' adsorption, which results in the loss of adsorption sites capable of breaking the O−O bond.[65] The bridge end-on bonding could facilitate the $2e^-$ oxygen reduction pathway *via* the H_2O_2 intermediate. The direct four-electron reduction is more feasible if the oxygen is side-on or hollow-adsorbed because the O−O bond can be weakened by electron transfer from the Pt surface to the π antibonding orbitals of O_2.

The oxygen reduction on Pt in acidic electrolyte is structure-sensitive to the adsorption of anions from the electrolyte, such as (bi)sulphate or halide anions.[65] The oxygen reduction on Pt (111), (110) and (100) in H_2SO_4 has lower activity than in $HClO_4$, suggesting that the adsorption of (bi)sulphate ions strongly influences the kinetics of the reaction; this is particular strong on Pt (111). The oxygen reduction was fastest at the (110) plane and slowest at the (111) plane in sulphuric acid.[66] The (bi)sulphate adsorption onto Pt surface inhibits the reduction of O_2 molecules by a site-blocking effect. OH_{ads} formation can also takes place on Pt surface. The OH_{ads} has a different inhibiting effect on each crystal face. OH_{ads} is also present when is used in KOH. In KOH, the variation in kinetics rate with crystal face is significant but much smaller than that in sulphuric acid. In the same study, it was shown that in perchloric acid, there was a small dependence of the oxygen reduction reaction rate on surface morphology and in potassium hydroxide, it was much larger, with the (100) plane the least active and the (111) plane the most active. This was attributed to the effect of a greater degree of OH adsorption on the (100) plane.[67,68] This is because the very open surface adsorbed OH_{ads} more strongly, significantly blocking O_2 adsorption sites and consequently reducing the rate of electron transfer to O_2.

For an Au surface, the difference in activity could qualitatively be attributed to the much weaker interaction of OH_{ad} and O_{ad} on the Au surface. Therefore the transfer of protons and electrons to oxygen from an Au surface would happen less easily than it would to oxygen from a Pt surface. The weak binding of oxygen on an Au surface would indicate that the barrier for oxygen dissociation is large because it has been shown that there is a linear dependence between oxygen binding energy and the barrier for oxygen dissociation.[45] In alkaline electrolyte, the oxygen reduction is sensitive to Au surface structure. Au (100) in alkaline electrolyte is the exception because it shows Pt-like activity at potentials above 0.8 V, where the formation of H_2O_2 does not appear in the solution.[69] In acidic electrolyte, the activity of Au is less sensitive to the surface structure. The onset potential of the oxygen reduction is shifted to more negative potential than that of Pt, due to weaker adsorption of O_2.

1.7.4 Oxygen reduction on non-precious metal catalysts

The replacement of Pt as a catalyst for the ORR in fuel cells by non-precious metals is intensively investigated. Metal−N_4 chelates, such as Fe−N_4 and Co−N_4 chelates, present remarkable catalytic activity toward the ORR.[70] In this work, we focus on Co−N_4 chelates. Their electrocatalytic activity enhancement and stability can be improved by a heat treatment in an inert atmosphere; however, it is more effective for Co−N_4 chelates than on Fe−N_4 chelates. The Co−N chelates yield hydrogen peroxide as the main product of the reaction. Interactions between oxygen molecules and the metal centre in Co−N_4 chelates take place in the redox mechanism where electrons are partially transferred from the orbitals of the metal to the orbitals of the oxygen molecule, resulting in a further reduction to yield an intermediate, such as hydrogen peroxide or water, as follows:[48,71]

$$M\text{-}N_4(III)OH + e^- \rightleftarrows M\text{-}N_4(II) + OH^- \quad (1.22)$$

$$M\text{-}N_4(II) + O_2 \rightleftarrows M\text{-}N_4(III) - O_2^- \quad (1.23)$$

$$M\text{-}N_4(III) - O_2^- + e^- \rightleftarrows M\text{-}N_4(II) + \text{intermediates} \quad (1.24)$$

Hydrogen peroxide can be the product of a reaction or can be an intermediate, where it can be decomposed or reduced further to yield water. The increase of hydrogen peroxide decomposition rate constant increases the ORR in acid solution on metal-N_4 chelates.[11] The metal centre with the lower electron density contributes to the higher catalytic activity of the ORR.[72] Both 2+ and 3+ oxidation states of the metal centre require stability in order to activate the ORR. The mechanism of the ORR on Co−N_4 chelates is similar to the ORR mechanism described above. The interaction of the oxygen molecule with Co−N_4 chelates depends on the orientation of the oxygen molecule and the N_4 metal plane, involving different orbitals.[48] Triethylenetetraamine (TETA), a simple and cheap N-ligand, can be used to prepare the Co/TETA/C for the ORR. The electrocatalytic activity of Co/TETA/C on the ORR is in the range of 2-electron and 4-electron, depending on the heat treatment.

1.8 Nitrate Reduction

Nitrate reduction and nitrite reduction have been attractive in liquid-phase heterogeneous catalyst and electrocatalysis due to concerns over contamination in groundwater. Electrochemical techniques have been applied for the conversion of nitrate and nitrite to harmless species with a view to utilizing them in environmental remediation. There are several N−compounds involved in nitrate reduction, such as nitrite (NO_2^-), nitric oxide (NO), nitrous oxide (N_2O), nitrous acid (HNO_2), ammonia (NH_3) and hydroxylamine (NH_2OH).[73] The complexity of nitrate reduction is due to the wide range of intermediates. The mechanism of nitrate reduction can be considered in 2 different operations: one is the mechanism operating at the moderate nitrate concentration and acidity, which is a practical condition in

laboratory; another one is the mechanism operating in high nitrate concentration (>1 M) and acidity (pH<0).[74,75] The Tafel slope of nitrate reduction at Rh catalyst is close to 120 mV dec^{-1}, suggesting that the rate-determining step is the step of nitrate reduction reduced to nitrite, as follows.[46,76]

$$NO_3^- + 2e^- + 2H^+ \rightarrow NO_2^- + H_2O \qquad (1.25)$$

Nitrate reduction is sensitive to the adsorption of the other species, such as hydrogen and anions. These impact less on Rh than on Pt.[76]

Bimetallic system can accelerate nitrate reduction. The activity of transition metals on nitrate reduction can be enhanced by: (i) metals in Pt group itself, such as PtRh[77], PtPd[78], PdCu (overlayers)[79], PdCu (alloys)[80] or CuZn[81]; (ii) p-block metals, such as Sn (overlayers SnRh, SnPt, SnPd)[82,83], In (bimetallic PdIn, adatoms PtIn)[84,85] or Ge (adatoms GePt, GePd)[86]. The promoting mechanisms of these modifiers appear to be varied. Cu is a good catalyst for nitrate reduction[13] so it is applied to the pure metal as a modifier.[79] Cu adatoms on Pt(111) accelerate nitrate reduction in sulfuric and perchloric acid, where NO and ammonia were found to be the main products.[87] PdCu alloys is also the promising heterogeneous for nitrate reduction. Sn has been introduced as an effective promoter on Pt, Pd, Rh for nitrate reduction.[88,89] The selectivity towards dinitrogen is enhanced. It seems like Sn modification enhances nitrate adsorption on catalyst surface; however, the product is dependent of the electrode itself. The gaseous products during electrochemical nitrate reduction can be detected by on-line Differential Electrochemical Mass Spectrometry (DEMS)[90] or On-line Electrochemical Mass Spectrometry (OLEMS)[76]. In this work Rh and Au:Rh nanoparticles were used for nitrate and nitrite reduction due to their promising catalytic activity. In order to enhance the activity and improve the selectivity of Rh, Sn modification was applied by electrodepostion on Rh nanoparticles.

1.9 References

(1) Durr, N. J.; Larson, T.; Smith, D. K.; Korgel, B. A.; Sokolov, K.; Ben-Yakar, A. *Nano Letters* **2007**, *7*, 941.

(2) Lee, K. S.; El-Sayed, M. A. *Journal of Physical Chemistry B* **2006**, *110*, 19220.

(3) Ohms, D.; Herzog, S.; Franke, R.; Neumann, V.; Wiesener, K.; Gamburcev, S.; Kaisheva, A.; Iliev, I. *Journal of Power Sources* **1992**, *38*, 327.

(4) Song, C.; Zhang, J. In *PEM Fuel Cell Electrocatalysts and Catalyst Layers*; Springer: London, 2008, p 89.

(5) Zhang, H. J.; Jiang, Q. Z.; Sun, L. L.; Yuan, X. X.; Ma, Z. F. *Electrochimica Acta* **2010**, *55*, 1107.

(6) Cornils B. , H. W. A., Schlögl R. , Wong C.-H. *Catalysis from A to Z*; Wiley-VCH: Weinheim/New York, 2000.

(7) Ertl G., K. H. *Heterogeneous Catalysis*; Wiley VCH: Weinheim/New York, 1997; Vol. 1-4.

(8) Cornils B. , H. W. A. *Applied Homogeneous Catalysis with Organometallic Compounds*; Wiley-VCH: Weinheim/New York, 1996; Vol. 1

(9) Bard A.J. , F. L. R. *Electrochemical Methods, Fundamentals and Applications*; Second Edition ed.; John Wiley and Sons: New York, 2001.

(10) Greef R., P. R., Peter L. M., Pletcher D., Robinson J *Instrumental Methods in Electrochemistry*; Ellis Horwood: Great Britain, 1990.

(11) Vielstich, W., Lamm, A., Gasteiger, H.A. *Handbook of Fuel Cells*; John Wiley & Sons: Chichester, 2003; Vol. Vol. 2.

(12) Bond A..M. , C. R. G., Fiedler D.A.,Inzelt G, Kahlert H , Komorsky-Lovric S., Lohse H. , Lovric M., Marken F., Nudeck A , Retter U., Scholz F. and Stojek Z. *Electroanalytical Methods: Guide to Experiments and Applications*; 2nd, revised and extended edition ed.; Springer: New York, 2010.

(13) Pletcher, D. *A First Course in Electrode Processes*; Second Edition ed.; RSC Publishing, 2009.

(14) Daniel, M. C.; Astruc, D. *Chemical Reviews* **2004**, *104*, 293.

(15) Schmid, G. *Chemical Reviews* **1992**, *92*, 1709.

(16) Bethell, D.; Brust, M.; Schiffrin, D. J.; Kiely, C. *Journal of Electroanalytical Chemistry* **1996**, *409*, 137.

(17) Shan, J.; Tenhu, H. *Chemical Communications* **2007**, 4580.

(18) Liz-Marzán, L. M. In *Matetial today* 2004; Vol. 7, p 26.

(19) Xu, Y. Q.; Xie, X. F.; Guo, J. W.; Wang, S. B.; Wang, Y. W.; Mathur, V. K. *Journal of Power Sources* **2006**, *162*, 132.

(20) Bai, J.; Li, Y. X.; Yang, S. T.; Du, J. S.; Wang, S. G.; Zheng, J. F.; Wang, Y. Z.; Yang, Q. B.; Chen, X. S.; Jing, X. B. *Solid State Communications* **2007**, *141*, 292.

(21) Anumol, E. A.; Halder, A.; Nethravathi, C.; Viswanath, B.; Ravishankar, N. *Journal of Materials Chemistry* **2011**, *21*, 8721.

(22) Wang, H.; Jusys, Z.; Behm, R. J. *Journal of Physical Chemistry B* **2004**, *108*, 19413.

(23) Jana, N. R.; Gearheart, L.; Murphy, C. J. *Journal of Physical Chemistry B* **2001**, *105*, 4065.

(24) Nikoobakht, B.; El-Sayed, M. A. *Chemistry of Materials* **2003**, *15*, 1957.

(25) Perez-Juste, J.; Liz-Marzan, L. M.; Carnie, S.; Chan, D. Y. C.; Mulvaney, P. *Advanced Functional Materials* **2004**, *14*, 571.

(26) Grzelczak, M.; Perez-Juste, J.; Mulvaney, P.; Liz-Marzan, L. M. *Chemical Society Reviews* **2008**, *37*, 1783.

(27) Perez-Juste, J.; Pastoriza-Santos, I.; Liz-Marzan, L. M.; Mulvaney, P. *Coord. Chem. Rev.* **2005**, *249*, 1870.

(28) Johnson, C. J.; Dujardin, E.; Davis, S. A.; Murphy, C. J.; Mann, S. *Journal of Materials Chemistry* **2002**, *12*, 1765.

(29) Gao, J. X.; Bender, C. M.; Murphy, C. J. *Langmuir* **2003**, *19*, 9065.

(30) Jana, N. R.; Gearheart, L.; Murphy, C. J. *Chemistry of Materials* **2001**, *13*, 2313.

(31) Mulvaney, P.; Giersig, M.; Henglein, A. *Journal of Physical Chemistry* **1993**, *97*, 7061.

(32) Boyes, E. D.; Gai, P. L. *Ultramicroscopy* **1997**, *67*, 219.

(33) Gai, P. L. *Microscopy and Microanalysis* **2002**, *8*, 21.

(34) Goris, B.; Bals, S.; Van den Broek, W.; Carbo-Argibay, E.; Gomez-Grana, S.; Liz-Marzan, L. M.; Van Tendeloo, G. *Nature Materials* **2012**, *11*, 930.

(35) Wilkinson, A. D. M. a. A. *IUPAC: Compendium of Chemical Terminology*; 2nd ed.; Blackwell Scientific Publications: Oxford.

(36) Romsted, L. S. *Adsorption and Aggregation of Surfactants in Solution*; Marcel Dekker: New York, 2005.

(37) Butt H. J., G. K., Kappl M *Physics and Chemistry of Interfaces*; Wiley-VCH: Weinheim 2006.

(38) Zhang, R.; Somasundaran, P. *Advances in Colloid and Interface Science* **2006**, *123*, 213.

(39) Pellegatta, J. L.; Blandy, C.; Colliere, V.; Choukroun, R.; Chaudret, B.; Cheng, P.; Philippot, K. *Journal of Molecular Catalysis a-Chemical* **2002**, *178*, 55.

(40) Yoon, T. J.; Kim, J. I.; Lee, J. K. *Inorganica Chimica Acta* **2003**, *345*, 228.

(41) Halttunen, M. E.; Niemela, M. K.; Krause, A. O. I.; Vaara, T.; Vuori, A. I. *Applied Catalysis a-General* **2001**, *205*, 37.

(42) Gayen, A.; Baidya, T.; Biswas, K.; Roy, S.; Hegde, M. S. *Applied Catalysis a-General* **2006**, *315*, 135.

(43) Humphrey, S. M.; Grass, M. E.; Habas, S. E.; Niesz, K.; Somorjai, G. A.; Tilley, T. D. *Nano Letters* **2007**, *7*, 785.

(44) Hoefelmeyer, J. D.; Niesz, K.; Somorjai, G. A.; Tilley, T. D. *Nano Letters* **2005**, *5*, 435.

(45) Norskov, J. K.; Rossmeisl, J.; Logadottir, A.; Lindqvist, L.; Kitchin, J. R.; Bligaard, T.; Jonsson, H. *Journal of Physical Chemistry B* **2004**, *108*, 17886.

(46) Wasberg, M.; Horanyi, G. *Electrochimica Acta* **1995**, *40*, 615.

(47) Brylev, O.; Sarrazin, M.; Roue, L.; Belanger, D. *Electrochimica Acta* **2007**, *52*, 6237.

(48) Zagal, J. H. *Coord. Chem. Rev.* **1992**, *119*, 89.

(49) Quaino, P.; Luque, N. B.; Nazmutdinov, R.; Santos, E.; Schmickler, W. *Angew. Chem.-Int. Edit.* **2012**, *51*, 12997.

(50) Damjanov.A; Genshaw, M. A.; Bockris, J. O. *Journal of Chemical Physics* **1966**, *45*, 4057.

(51) Pourbaix, M. *Atlas of Electrochemical Equilibria in Aqueous Solutions*; 2nd Edition ed.; NACE: Houston, 1974.

(52) Yeager E., R. M., Gervasio D., Razaq A. and Tryk D. *Structural Effects in Electrocatalysis and Oxygen Electrochemistry*; Pennington: NJ, 1992; Vol. 92-11.

(53) Zagal, J. H. *Coord Chem Rev* **1992**, *119*.

(54) Nekrasov, L. M. a. L. *Electrochim. Acta* **1964**, *9*, 1015.

(55) Antoine, O.; Durand, R. *Journal of Applied Electrochemistry* **2000**, *30*, 839.

(56) Adzic R. R. , S. S., Anastasijevic N. *Mater. Chem Phys.* **1989**, *22*, 349.

(57) Chen, Z. W.; Higgins, D.; Yu, A. P.; Zhang, L.; Zhang, J. J. *Energy & Environmental Science* **2011**, *4*, 3167.

(58) Jaouen, F.; Proietti, E.; Lefevre, M.; Chenitz, R.; Dodelet, J. P.; Wu, G.; Chung, H. T.; Johnston, C. M.; Zelenay, P. *Energy & Environmental Science* **2011**, *4*, 114.

(59) Markovic, N. M.; Schmidt, T. J.; Stamenkovic, V.; Ross, P. N. *Fuel Cells* **2001**, *1*, 105.

(60) Adzic, R. *Recent Advances in the Kinetics of Oxygen Reduction in "Electrocatalysis"*; Wiley-VCH: New York, 1998.

(61) Tarasevich M.R., S. A. a. Y. E. *Oxygen Electrochemistry*; Plenum Press: N.Y., 1983; Vol. 7.

(62) Zinola C.F., A. A. J., Estia G.L. and Castro E.A. *J Phys Chem* **1994**, *98*, 7576.

(63) Maillard F., M. M., Gloaguen F. and Leger J.M. *Electrochimica Acta* **2002**, *47*, 3440.

(64) Gasteiger H.A., M. N. M. a. R. P. N. *Langmuir* **1996**, *12*, 1414.

(65) Markovic N.M., G. H. A. a. R. J. P. N. *J Phys Chem* **1995**, *99*, 11.

(66) Markovic N.M., A. R. R., Cahan B.D. and Yeager E.B. *J. Electroanal. Chem* **1994**, *377*, 249.

(67) Markovic N.M., G. H. a. R. P. N. *J. Phys. Chem.* **1996**, *100(16)*, 6715.

(68) Markovic N.M., G. H. a. R. P. N. *J. Electrochem. Soc.* **1997**, *144(5)*, 1591.

(69) Taylor E. J., V. N. R. K. a. G. A. *J. Electrochem. Soc.*, *136*, 1939(1989).

(70) Bezerra, C. W. B.; Zhang, L.; Lee, K. C.; Liu, H. S.; Marques, A. L. B.; Marques, E. P.; Wang, H. J.; Zhang, J. J. *Electrochimica Acta* **2008**, *53*, 4937.

(71) Beck, F. *Journal of Applied Electrochemistry* **1977**, *7*, 239.

(72) Zagal, J. H.; Gulppi, M.; Isaacs, M.; Cardenas-Jiron, G.; Aguirre, M. J. *Electrochimica Acta* **1998**, *44*, 1349.

(73) Rosca, V.; Duca, M.; de Groot, M. T.; Koper, M. T. M. *Chemical Reviews* **2009**, *109*, 2209.

(74) da Cunha, M.; De Souza, J. P. I.; Nart, F. C. *Langmuir* **2000**, *16*, 771.

(75) de Groot, M. T.; Merkx, M.; Koper, M. T. M. *Comptes Rendus Chimie* **2007**, *10*, 414.

(76) Dima, G. E.; de Vooys, A. C. A.; Koper, M. T. M. *Journal of Electroanalytical Chemistry* **2003**, *554*, 15.

(77) Hasnat M. A., I. M. A., Borhanuddin S. M., Chowdhury M. R. U.,; ., M. M. *J. Mol. Catal. A: Chem* **2010**, *317*, 61.

(78) Souza Garcia J., T. E. A., Climent V., Feliu J. M.,; *Electrochim. Acta* **2009**, *54*, 2094.

(79) de Vooys, A. C. A.; van Santen, R. A.; van Veen, J. A. R. *Journal of Molecular Catalysis a-Chemical* **2000**, *154*, 203.

(80) Anastasopoulos A., H. L., Hayden B. E. *Journal of Catalysis* **2013**, *305*, 27.

(81) Macova Z., B. K. *J. Appl. Electrochemistry Communications* **2005**, *35* 1203.

(82) Piao, S.; Kayama, Y.; Nakano, Y.; Nakata, K.; Yoshinaga, Y.; Shimazu, K. *J. Electroanal. Chem.* **2009**, *629*, 110.

(83) Shimazu, K.; Goto, R.; Piao, S. Y.; Kayama, R.; Nakata, K.; Yoshinaga, Y. *J. Electroanal. Chem.* **2007**, *601*, 161.

(84) Witonska, I.; Karski, S.; Rogowski, J.; Krawczyk, N. *Journal of Molecular Catalysis a-Chemical* **2008**, *287*, 87.

(85) Marchesini, F. A.; Irusta, S.; Querini, C.; Miro, E. *Applied Catalysis a-General* **2008**, *348*, 60.

(86) Safonova, T. Y.; Petrii, O. A. *J. Electroanal. Chem.* **1998**, *448*, 211.

(87) Molodkina, E. B.; Ehrenburg, M. R.; Polukarov, Y. M.; Danilov, A. I.; Souza-Garcia, J.; Feliu, J. M. *Electrochimica Acta* **2010**, *56*, 154.

(88) Safonova, T. Y.; Petrii, O. A. *Russian Journal of Electrochemistry* **1998**, *34*, 1137.

(89) Shimazu, K.; Goto, R.; Piao, S.; Kayama, R.; Nakata, K.; Yoshinaga, Y. *Journal of Electroanalytical Chemistry* **2007**, *601*, 161.

(90) de Groot, M. T.; Koper, M. T. M. *Journal of Electroanalytical Chemistry* **2004**, *562*, 81.

CHAPTER 2

THEORY AND TECHNIQUES

The aim of this chapter is to introduce the fundamental concepts of electrochemistry and the methodology of the techniques used in this study. The electrochemical techniques were used for electrochemical analysis in association with other techniques, such as mass spectrometry (MS) and ion chromatography (IC), in order to study the electrochemical reactions and to detect the intermediates and the products of the reactions. Transmission electron microscopy (TEM) and scanning transmission electron microscopy (STEM) were used to examine the morphology and the distribution of the metal nanoparticles. The existence of metallic nanoparticles was confirmed by X-ray photoelectron spectroscopy (XPS) and energy dispersive spectroscopy (EDS). Thermal analysis (TA), such as thermo gravimetric analysis (TGA) and differential thermal analysis (DTA), were used to analyse thermal properties of some samples.

2.1 Electrical Double Layer

In order to understand the electron transfer process in heterogeneous electrocatalysis, the electrode/electrolyte interface needs to be explained. When an electrode is immersed into an electrolyte, a specific interface is formed. This region is called the Electrical Double Layer (EDL).[1] An applied potential causes characteristic charges on an electrode surface. The excess charge on the electrode surface must be balanced by the opposite charge in the electrolyte. The applied potential from the external source generates a charge on the metal electrode (σ_m) and a charge in the solution (σ_s). The potential where the surface charge is zero is called the potential of zero charge (E_{pzc}).[1] An ideal polarised electrode is commonly analysed by a

measurement of interfacial capacity or capacitance (*C)*, following a change of charge on the electrode (σ_{m}) and a change in potential, as shown in Eq. (2.1).[2]

$$C = \frac{d\sigma_m}{dE} \tag{2.1}$$

The double layer model was first proposed in 1879 by Helmholtz[1,3], as shown in Figure 2.1(a). The theoretical model assumes that all charges on the metal electrode are neutralised by a compact monolayer of opposite charges in the solution, resulting in potential difference between the metal surface and the solution, ($\Phi_{\mathrm{M}} - \Phi_{\mathrm{s}}$), which changes steeply and linearly with the thickness of this layer (x_{H}).[1,4] Outside this layer, cations and anions randomly move in the solution. This model does not consider a structural dependence on the applied potential or concentration of electrolyte. The second model was introduced by Gouy and Chapman,[1,2,4-7] as seen in Figure 2.1(b). Known as a diffuse double layer, the model takes into account the assumption that the charges in the solution are free to move, and thus, retains the concept of electrostatic theory. The double layer is not compact as it is in Helmholtz's model. The potential smoothly decreases until it reaches the bulk solution. The model was further developed by Stern,[4,8,9] who suggested a model that combined the compact monolayer of ions and the diffuse double layer, as shown in Figure 2.1(c). The potential difference gradually changes with the distance in the bulk solution and steeply changes with the distance in the compact layer. The expression of the capacitance in this model is presented in Eq. (2.2).[1]

$$\frac{1}{C_{\mathrm{d}}} = \frac{1}{C_{\mathrm{compact}}} + \frac{1}{C_{\mathrm{diffuse}}} \tag{2.2}$$

where $C_{\mathrm{d}}, C_{\mathrm{compact}}$ and C_{diffuse} are the measured capacitance, the capacitance of the compact layer and of the diffuse double layer, respectively.

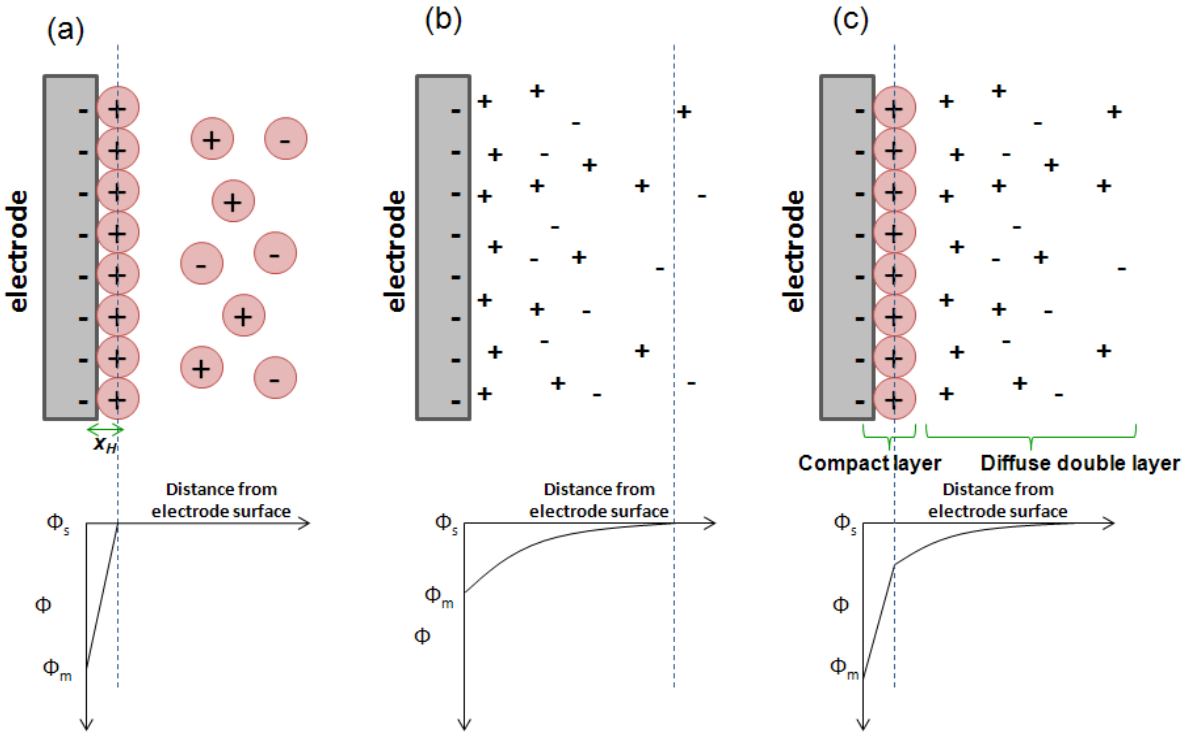

Figure 2.1 The schematic of the electrical double layer of (a) the Helmholz model, (b) the Gouy-Chapman model and (c) the Stern model with the potential drop across the interface.[1]

The more recent models take into account several facts, particularly the specific adsorption of ions on the metal surface that was pointed out by Grahame.[10,11] The model was consequently developed by Bockris.[12] The solvent solvation has been taken into account. The ions are hydrated and can freely move in the diffuse layer. Contact made between hydrated ions and the surface of the metal electrode results in the Outer Helmholtz Plane (OHP). When the hydration shells are partially or fully stripped from the ion, a bond between the ion and metal surface is formed closer to the metal surface, resulting in an Inner Helmholtz Plane (IHP). This model proposed is a triple layer model, as shown in Figure 2.2.

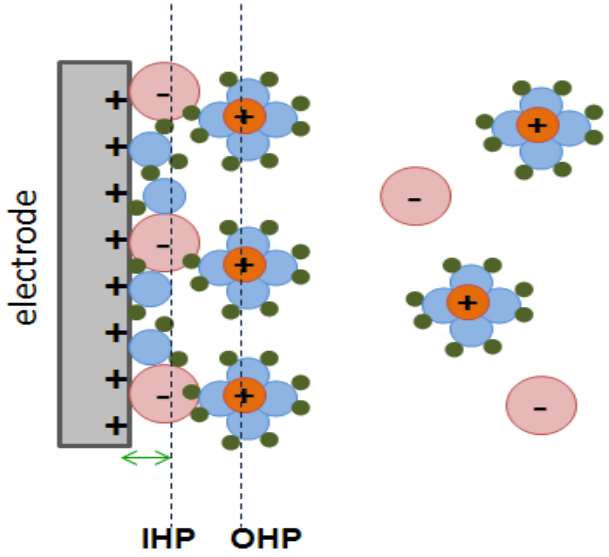

Figure 2.2 The schematic of Bockris model for electrical double layer.[4]

2.2 Kinetics of Electron Transfer

An electrode reaction is a heterogeneous process that involves a charge transfer step across the electrical double layer. The rate of reaction is determined by the rate-determining step. The reaction rate can be determined by measuring the current in the electrical circuit, following Eq. (2.3). [2]

$$j = nFv \tag{2.3}$$

where j is current density, n is the number of electrons and v is the reaction rate normalised to surface area.

The potential applied to a working electrode is a driving force for an electrode reaction, controlling the energy of electrons within the working electrode. The electron energy of both the electrode and the molecule in the solution are influential the electron transfer. Metals contain a lattice closely packed atoms which have strong overlapping between each atomic orbital. This behaviour makes the electrons in the metals can move freely. The electrons occupy an effective continuum of energy states in the metal. The behaviour of electron in metal can be explained by the Fermi Level which it corresponds to the energy of

the highest occupied molecular orbital (HOMO). The applied potential influences the Fermi level of metal. The reduction and oxidation processes are presented in Figure 2.3. Driving the electrode to more negative potential raises the highest occupied energy level of an electron in the metal, which, once it reaches a certain level, allows an electron to be transferred to the lowest unoccupied molecular orbital (LUMO) of a species in the solution. Likewise, driving the electrode to more positive potential decreases the highest occupied energy level of electrons in the metal until it is lowered enough to transfer an electron from the molecule in the solution to the electrode.

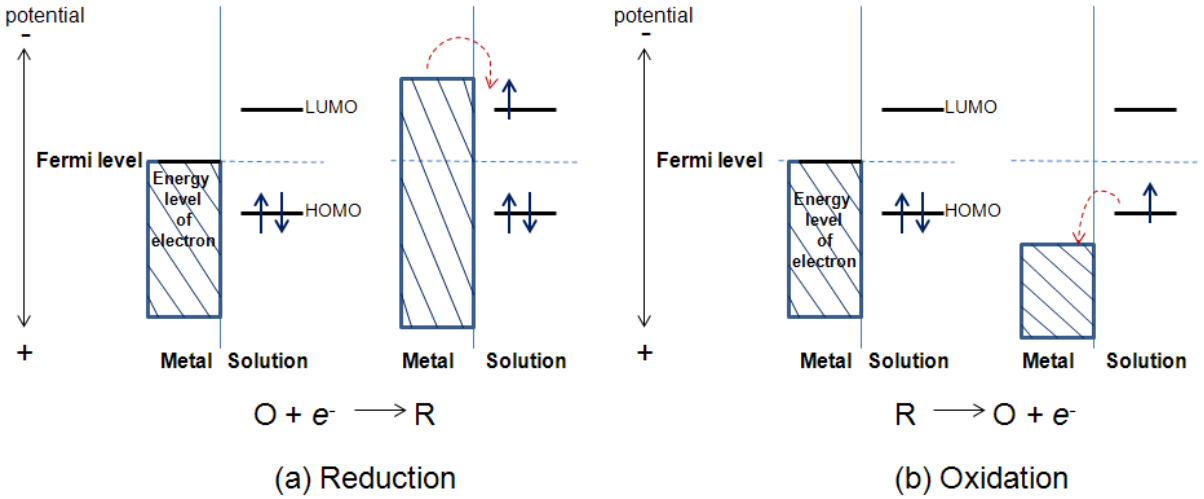

Figure 2.3 Representation of (a) the reduction and (b) the oxidation processes, where O and R are the oxidized and reduced forms.[13]

The charge transfer relates to a potential difference, which can be evaluated by the Nernst equation, Eq. (2.4).[13]

$$E_{\mathrm{e}} = E_{\mathrm{e}}^{0} + \frac{2.303RT}{nF}\log\frac{\mathrm{C_O}}{\mathrm{C_R}} \qquad (2.4)$$

The simple thermodynamics and kinetics of the electrode reaction are considered.

$$\mathrm{O} + n\mathrm{e}^{-} \underset{k_{\mathrm{ox}}}{\overset{k_{\mathrm{red}}}{\rightleftarrows}} \mathrm{R} \qquad (2.5)$$

where O and R are the oxidised and reduced forms, respectively. k_{red} and k_{ox} are the rate constants of reduction and oxidation reactions, respectively. The net conversion rate of O to R in the non-equilibrium system is:[1]

$$\nu = \nu_{red} - \nu_{ox} = k_{red}c_O(0,t) - k_{ox}c_R(0,t) = \frac{j}{nF} \quad (2.6)$$

From Eq. (2.3) and (2.6), the overall current is:[1]

$$j = j_c - j_a = nF[k_{red}c_O - k_{ox}c_R] \quad (2.7)$$

where j is the net current. j_c and j_a are the current densities during the reduction and oxidation reactions. c_O and c_R are the concentrations of oxidised and reduced forms.

Arrhenius recognised that the rate constant varies with temperature, as expressed in Eq. (2.8).[13] Further consideration based on Arrhenius' equation took into account the energy unit E_A, which corresponds to the standard free energy of activation ΔG, expressed in the Eq. (2.9).[1,4,13]

$$k = Ae^{-\frac{E_A}{RT}} \quad (2.8)$$

$$k_{red} = Ae^{\left(-\Delta G^{\ddagger}_{red}/RT\right)} \text{ and } k_{ox} = Ae^{\left(-\Delta G^{\ddagger}_{ox}/RT\right)} \quad (2.9)$$

Figure 2.4 presents the effect of the potential changes on the standard free energy. If the potential is changed by ΔE to a new value, E, the relative value of the electron resident on the electrode becomes: $-F\Delta E = -F(E - E^0)$. A transfer coefficient α is introduced as the fraction of applied potential which drives the reaction. The value of α is in between 0 and 1. This value depends on the shape of the energy barrier. Thus:[13]

$$\Delta G^{\ddagger}_{red} = \Delta G^{\ddagger}_{0\,red} + \alpha nF(E_e - E^0_e) \quad (2.10)$$

$$\Delta G^{\ddagger}_{ox} = \Delta G^{\ddagger}_{0\,ox} - (1-\alpha)nF(E_e - E^0_e) \quad (2.11)$$

From Eq. (2.9)

$$k_{red} = Ae^{\left(\frac{-\Delta G^{\ddagger}_{0,red}}{RT}\right)}e^{\left(\frac{-\alpha nF(E_e - E^0_e)}{RT}\right)} \quad (2.12)$$

$$k_{\mathrm{ox}} = Ae^{\left(\frac{-\Delta G^{\ddagger}_{0,\mathrm{ox}}}{RT}\right)} e^{\left(\frac{(1-\alpha)F(E_{\mathrm{e}}-E^{0}_{\mathrm{e}})}{RT}\right)} \tag{2.13}$$

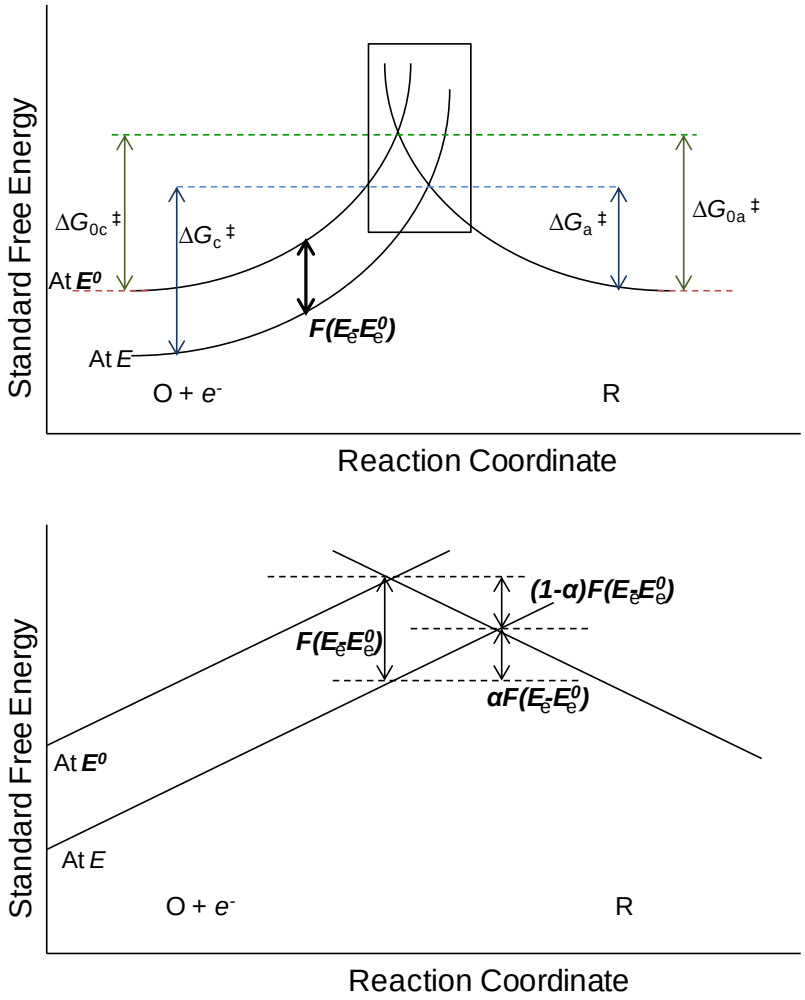

Figure 2.4 The effect of potential change on the standard free energies if activation for reduction and oxidation. The lower figure is a magnification of the boxed area in the upper figure.[13]

The first two terms in Eq. (2.12) and (2.13) are independent of the potential. When $E = E^0$, the rate constants for the forward and reverse reactions are equal, resulting in the standard rate constant k_0.

$$k_{\mathrm{red}} = k_0 e^{\left(\frac{-\alpha nF(E_{\mathrm{e}}-E^{0}_{\mathrm{e}})}{RT}\right)} \tag{2.14}$$

$$k_{\mathrm{ox}} = k_0 e^{\left(\frac{(1-\alpha)nF(E_{\mathrm{e}}-E^{0}_{\mathrm{e}})}{RT}\right)} \tag{2.15}$$

The term E-E^0 is referred to the overpoential (η). The Butler-Volmer formulation Eq. (2.16),[13] which widely used in electrode kinetics, was derived from Eq. (2.7) – (2.15).

$$j = nFk_0 \left[e^{\left(\frac{-\alpha nF\eta}{RT}\right)} - e^{\left(\frac{(1-\alpha)nF\eta}{RT}\right)} \right] \quad (2.16)$$

At equilibrium potential, the anodic and cathodic current densities are equal to the exchange current density j_o, which leads to the Butler-Volmer equation in the form of Eq. (2.17).

$$j = j_o \left[e^{\left(\frac{-\alpha nF\eta}{RT}\right)} - e^{\left(\frac{(1-\alpha)nF\eta}{RT}\right)} \right] \quad (2.17)$$

A general plot of j_o *vs* η respected to Eq. (2.17) is presented in Figure 2.5. The overpotential increases when decreasing the exchange current density.

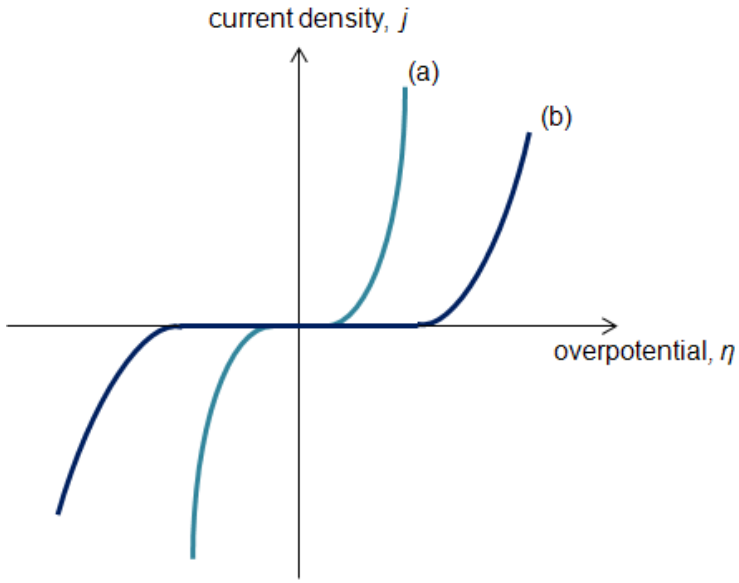

Figure 2.5 The variation of current density as a function of overpotential, corresponding to the Butler-Volmer equation for an exchange current density of (a) a high exchange current density and (b) a low exchange current density.[13]

Eq. (2.17) representing the oxidation and reaction reactions can also be written in the form of Eq. (2.18) and (2.19), respectively. They are known as Tafel equations.

$$\log j = \log j_o + \frac{\alpha_a nF}{2.3RT}\eta \quad (2.18)$$

$$\log -j = \log j_o - \frac{\alpha_c nF}{2.3RT}\eta \quad (2.19)$$

Figure 2.6 shows a Tafel plot of current density *vs* overpotential for both oxidation and reduction reactions. The transfer coefficient can be obtained from the slope of the plot, whereas the exchange current density is obtained from the intercept of the plot.

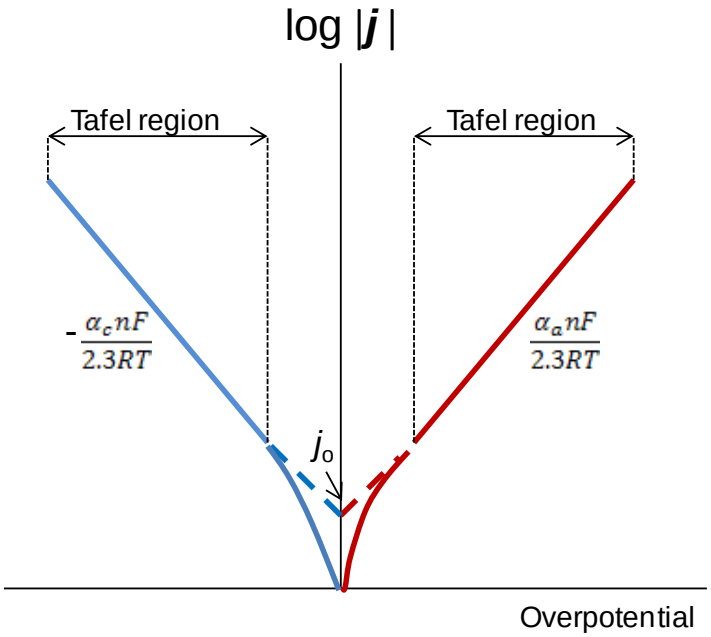

Figure 2.6 Tafel plot for anodic and cathodic current densities.[13]

2.3 Cyclic Voltammetry

Cyclic voltammetry is a frequently used technique, which provides both the thermodynamic and kinetic details of many chemical systems. The current flowing is measured as a function of applied potential. The experiment is conducted using a three-electrode cell, which is connected to a potentiostat. The potential of a working electrode is held with respect to a stable reference electrode. The current only flows between the working electrode and a counter electrode to avoid potential changing of the reference electrode and to minimise ohmic (IR) drop. Figure 2.7 presents a simplified potentiostatic circuit. Figure 2.8(a) shows the variation of the applied potential *vs* time in the cyclic voltammertry experiment. The potential starts from E_1 and reaches E_2 for the forward scan and the electrode potential is

scanned reversely back to the potential of E_1. The response of the cell to the applied potential is normally presented in a current *vs* potential plot, as shown and detailed in Figure 2.8(b).

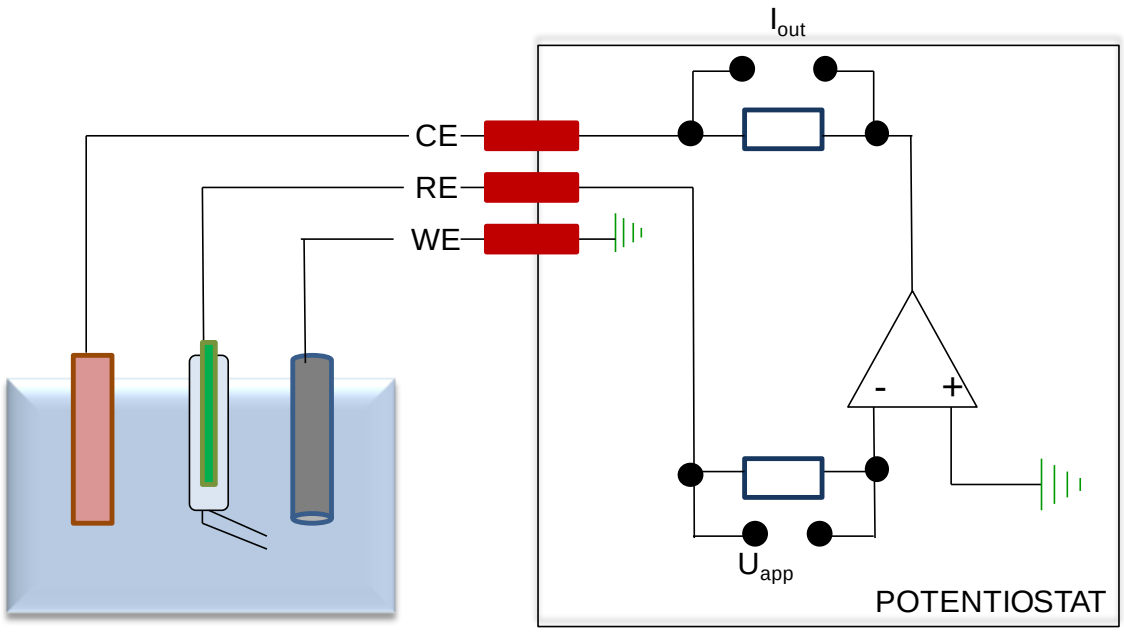

Figure 2.7 Illustration of a simplified circuit diagram for the three-electrode system.

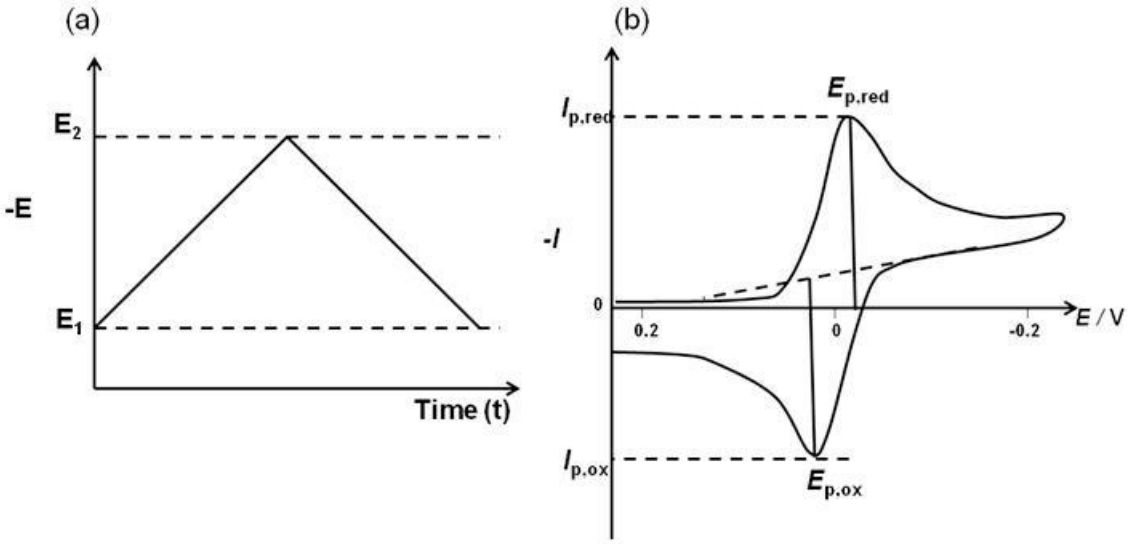

Figure 2.8 (a) Variation of the applied potential as a function of time in a cyclic voltammetry, (b) cyclic voltammogram for reversible electron transfer reaction with defined peak potentials and peak currents for reduction and oxidation.[8]

2.3.1 Reversible Electron Transfer

This system is also called the Nernstian system. Considering the reaction $O + ne^- \rightleftarrows R$, the electron transfer reaction of this system is rapid. The Nernst equation written with the concentration of oxidised and reduced forms is shown in Eq. (2.20). For the reversible system, the formal potential is in the form of Eq. (2.21).[13]

$$\frac{C_O(0,t)}{C_R(0,t)} = exp\frac{nF(E_i + \nu t - E_e^o)}{RT} \quad (2.20)$$

$$E_e^o = \frac{E_p^a + E_p^c}{2} \quad (2.21)$$

At 25 °C, the diffusion coefficient is included and the Randlles-Sevǒik equation is formed to evaluate the peak current density j_p:[13]

$$j_p = 2.69 \times 10^5 n^{3/2} D_0^{1/2} C_0 \nu^{1/2} \quad (2.22)$$

When the peak is somewhat broad, the peak potential E_p is difficult to determine. The half-peak potential $E_{p/2}$ is more convenient to determine the number of electrons transferred in the reaction *n*, using Eq. (2.23).[13]

$$\left|E_p - E_{p/2}\right| = 2.20\frac{RT}{nF} = \frac{56.5}{n} \text{ mV at 25 °C} \quad (2.23)$$

The scan rate influences the current density of voltammogram, as seen from Eq. (2.22), which shows that the current density is proportionate to $\nu^{1/2}$. An increase in the scan rate reduces the time to change the surface concentration, resulting in a thinner diffusion layer.

2.3.2 Irreversible Electron Transfer

When the electron transfer is insufficiently fast to maintain the equilibrium, the reaction becomes irreversible. Thus, the surface kinetics needs to be considered. The voltammogram peak of the irreversible system is slightly lower and less steep than that of the reversible

system because it takes longer time for the surface concentration to reach zero. The expression for the peak current density of the irreversible process is presented in Eq. (2.24).[13]

$$j_{\mathrm{p}} = (3 \times 10^5)(n_{\mathrm{a}}\alpha)^{1/2} D_0^{1/2} C_0 \nu^{1/2} \quad \text{at } 25\ ^{\circ}\mathrm{C} \qquad (2.24)$$

The current density is proportional to $\nu^{1/2}$; however, the slope of a plot of the irreversible process is different from that of the reversible process. The peak potential of the irreversible system varies with the scan rate according to Eq. (2.25).[13]

$$E_{\mathrm{p}} = E^{\mathrm{o}\prime} - \frac{RT}{\alpha n_{\mathrm{a}} F}\left[0.780 + \ln\left(\frac{D_{\mathrm{O}}^{1/2}}{k^0}\right) + \ln\left(\frac{\alpha n_{\mathrm{a}} F \nu}{RT}\right)^{1/2}\right] \qquad (2.25)$$

Where

$$\left|E_{\mathrm{p}} - E_{\mathrm{p}/2}\right| = 1.857\frac{RT}{\alpha n_{\mathrm{a}} F} = \frac{47.7}{\alpha n_{\mathrm{a}}}\ \mathrm{mV\ at\ 25\ ^{\circ}C} \qquad (2.26)$$

The transfer coefficient may be obtained from the peak shape. The kinetics of the electron-transfer reaction can thus be evaluated from the voltammogram.

2.3.3 Surface processes

For solution processes, we assumed that all the reactants and products are freely to move in the solution. The balance between kinetics and mass transport produced the voltammetric profiles of reversible and irreversible reaction given in the previous sections. When surface processes, such as reactant or product adsorption, phase formation and removal, are taken into account, the voltammetric profiles have different shapes from those discussed so far and the shape depends on potential scan rates. These changes indicate that the surface processes involve in the reaction. Cyclic voltammetry is suitable for providing the information of surface processes involving adsorption processes.

2.3.3.1 Cyclic voltammetry: Only adsorbed O and R electroactive (Nernstian Reaction)

The simplest case for an adsorption process is that where only the adsorbed forms of O and R, not dissolved O, are electroactive in the potential range under investigation.[4] This can be found in the case that the scan rate is so large that the dissolved O does not have time to diffuse to electrode surface. The peak of adsorbed O is at a more positive potential than that of dissolved O. If the electron transfer is reversible and the diffuse layer is thin, the mass transport effect can be neglected in both cases. The *i-E* curve is similar to that shown in Figure 2.9. The peak current is given by:[13]

$$i_p = \frac{n^2F^2}{4RT} \nu A \Gamma_{\mathrm{O}}^* \tag{2.27}$$

where Γ_{O}^* is the surface excess of O before the start of the sweep. The peak potential by:[13]

$$E_p = E^{0\prime} - \left(\frac{RT}{nF}\right) \ln\left(\frac{b_{\mathrm{O}}}{b_{\mathrm{R}}}\right) = E_{\mathrm{a}}^{\mathrm{o}\prime} \tag{2.28}$$

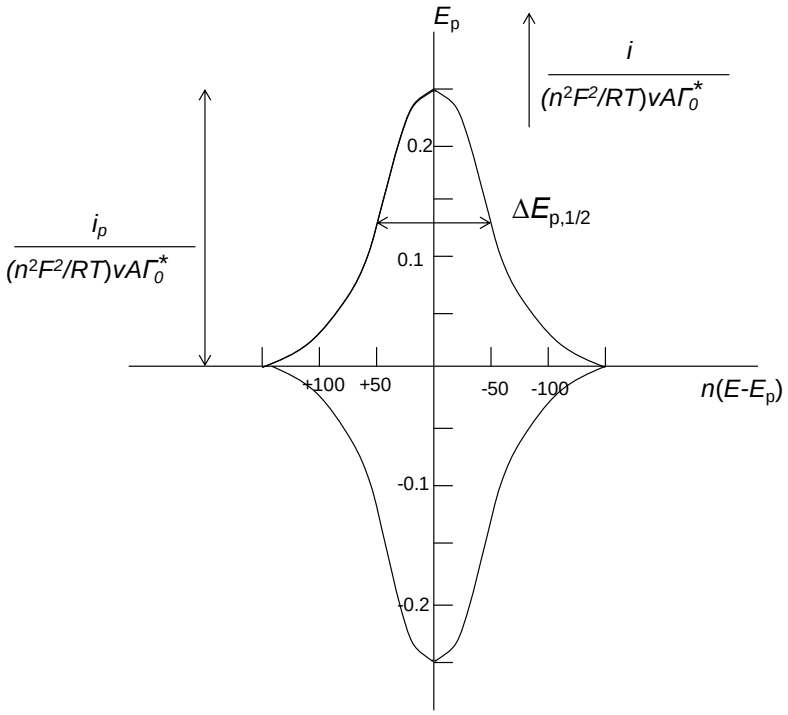

Figure 2.9 Cyclic voltammetric curve for reduction and subsequent reoxidation of adsorbed O. Current is given in normalized form and the potential axis is shown for the case at 25 °C.[13]

If the reaction is ideal Nerstian reaction under Langmuir isotherm conditions, $E_{pa} = E_{pc}$ and the total width at half-height of either the cathodic or anodic wave is given by.[13]

$$\Delta E_{p,1/2} = 3.53 \frac{RT}{nF} = \frac{90.6}{n} \text{ mV} \quad (25\ ^\circ\text{C}) \tag{2.29}$$

2.3.3.2 Cyclic voltammetry: Only adsorbed O electroactive (Irreversible reaction)

The irreversible reaction is the case where adsorbed O is reduced in a totally irreversible one-step reaction. The shape of the cyclic voltammogram changes by the forward ceases to be symmetric and there is no reverse peak. The Langmuirian-Nerstian boundary condition is replaced by a kinetic one, similar to that used for dissolved reactants. It is assumed that the sweep rate starts at sufficiently positive potential. The potential dependence of the current obtained is shown in Figure 2.10. The shape does not depend on ν and rate constant. The peak values are given by:

$$i_p = \frac{\alpha F^2 \nu A \Gamma_O^*}{2.718RT} \tag{2.30}$$

$$E_p = E^{0\prime} + \left(\frac{RT}{\alpha F}\right) \ln\left(\frac{RT}{\alpha F}\frac{k^0}{\nu}\right) = E_a^{o\prime} \tag{2.31}$$

$$\Delta E_{p,1/2} = 2.44 \frac{RT}{\alpha F} = \frac{62.5}{\alpha} \text{ mV} \quad (25\ ^\circ\text{C}) \tag{2.32}$$

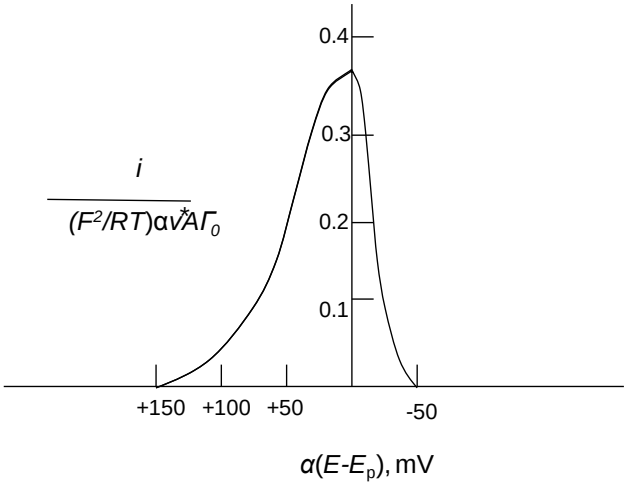

Figure 2.10 Theoretical linear sweep voltammograms for a system where adsorbed O is irreversibly reduced.

2.4 Rotating Disc Electrode (RDE)

A rotating disc electrode (RDE) is a hydrodynamic electrode, in which the mass transport is forced by convection. It is employed to study the kinetics of irreversible processes with high overpotential, such as the oxygen reduction reaction (ORR). The RDE comprises a small metallic disc, which serves as working electrode, embedded in a larger insulating material cylinder. The electrode is connected to a potentiostat and placed into an electrochemical cell. The electrode is rotated at a constant speed. The electrode acts as a pump enabling fresh solution to be drawn vertically up towards the disc of electrode. This technique is designed to allow laminar flow, as seen in Figure 2.11. The limiting current increases with the rotation rate of the disc since the velocity of the solution towards the disc of the electrode is larger at higher rotation rates. Likewise, an increase in the rotation rate enhances the convection, as well as decreasing the diffusion layer thickness.

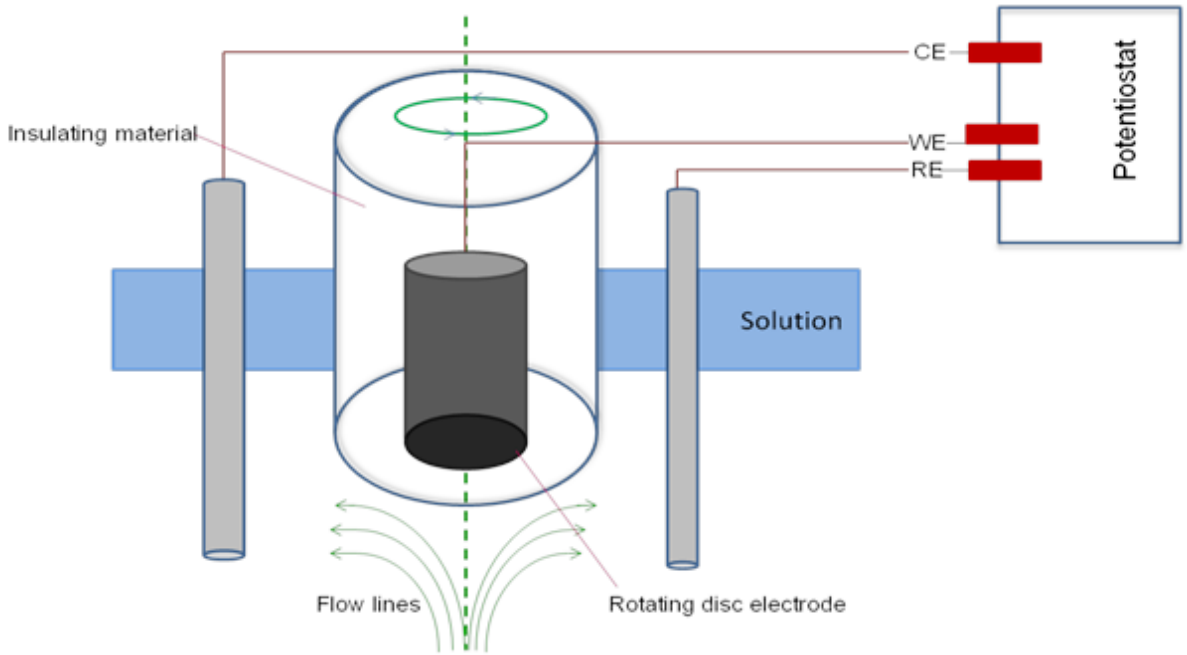

Figure 2.11 Schematic of the rotating disc electrode with the insulating sheet in the electrolyte. The lower green arrows indicate the laminar flow lines at the rotating disc electrode.[14]

At potentials where the reaction is mass transport-controlled, it can be assumed that the concentration of electroactive species on the electrode surface is zero. Thus, the limiting current density is expressed by Eq. (2.33), which is called the Levich equation.

$$j_{\mathrm{L}} = 0.62 \frac{nFD^{2/3}}{\nu^{1/6}} \omega^{1/2} \qquad (2.33)$$

where j_{L} is a limiting current density, F is the Faraday constant (96,485 C mol^{-1}), n is the number of electrons, D is the diffusion coefficient, C is the concentration of species in the bulk, ω is the rotation rate of disc electrode (rad s^{-1}), k is the rate constant of the reaction and ν is the kinematic viscosity of the solution. The mass transport control in a RDE experiment is independent to the potential and a plot of j_{L}^{-1} *vs* $\omega^{-1/2}$ is linear and passes through the origin. On a plot of *j vs E* at potentials close to the equilibrium potential (j = 0), the current density is under kinetics control. At higher overpotentials, the current density is in a mixed control region and progressively depends on the rotation rate at more negative potentials. When the current density reaches the limiting current, the mass transport control region is observed.[13]

2.5 Rotating Ring Disc Electrode (RRDE)

The rotating ring disc electrode (RRDE) is developed from the RDE in order to investigate the species formed during the reaction at the disc electrode. An additional ring is added to surround the disc electrode with a thin insulating layer between them. The disc and the ring are separately controlled by a bipotentiostat. Most experiments for the RRDE are collection experiments. The solution is drawn to the disc of the electrode, where it generates species, and is then thrown out to the ring, where a different potential is maintained. Figure 2.12 presents the view of the RRDE and solution flow profile.

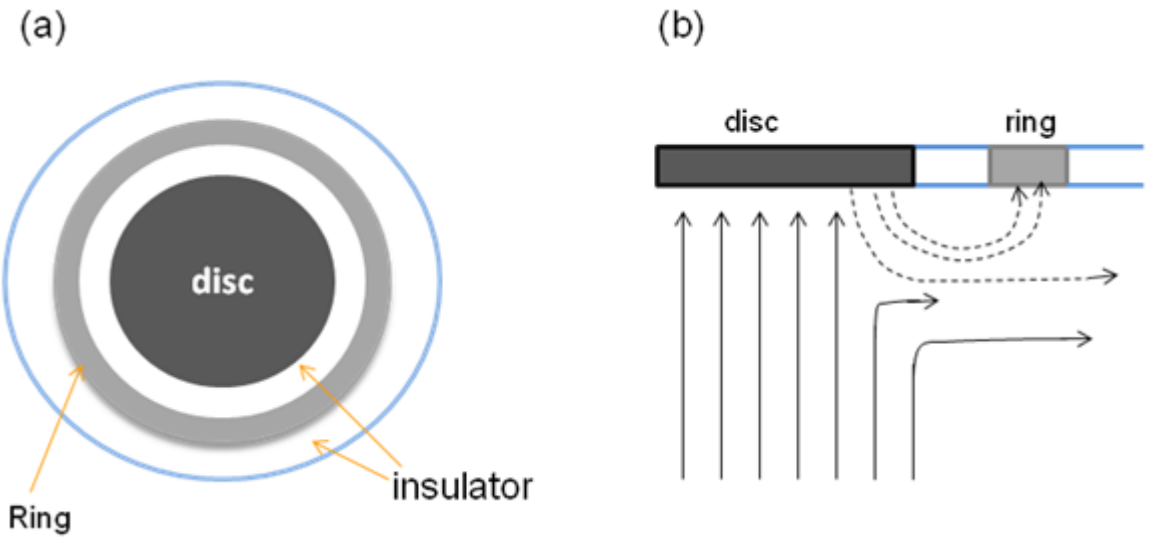

Figure 2.12 (a) view of the rotating ring disc electrode (RRDE) and (b) the pattern of solution flow at the RRDE.

It is noteworthy that not all species produced at the disc will be detected at the ring. In order to know the fraction of species transported to the ring, the collection efficiency N is calculated by the fraction of species formed at the disc that is detected at the ring, as shown in Eq. (2.34). N is normally evaluated from a standard experiment, such as the oxidation of ferrocyanide and the reduction of ferricyanide. ORR is a good candidate for investigation with a RRDE experiment. Oxygen is reduced at the disc and the hydrogen peroxide intermediate is oxidised at the ring.

$$N = \frac{-i_{\mathrm{R}}}{i_{\mathrm{D}}} \qquad (2.34)$$

2.6 Ultraviolet/Visible (UV-Vis) Spectroscopy

2.6.1 The UV-visible spectrophotometer

UV-visible spectroscopy is a technique that applies the method of an absorption or reflectance spectroscopy in an ultraviolet-visible spectra region. The absorption of visible light causes the

colour of an object emission. Figure 2.13 shows a diagram of the electromagnetic spectrum. The visible light lies in a range of 400-700 nm. During absorption, the electrons in the molecules can absorb the energy in the ultraviolet or visible region. The electrons are excited to a different level.

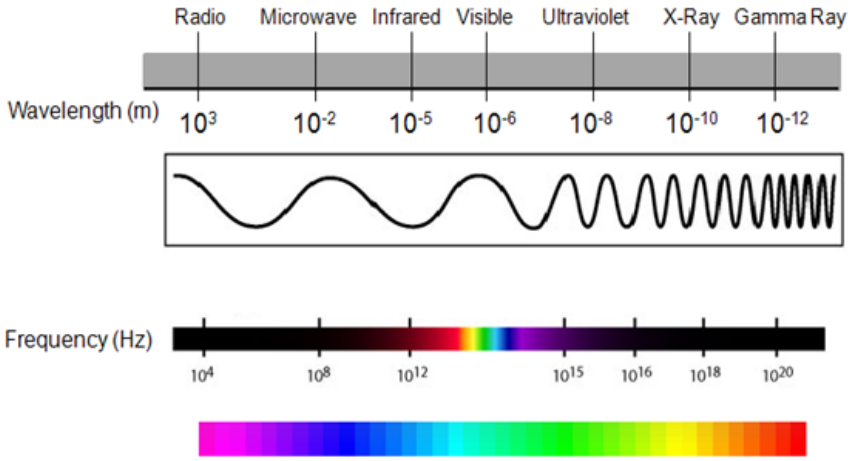

Figure 2.13 Regions of the electromagnetic spectrum.[15]

According to Beer's law[15], the absorption is proportional to the number of absorbing species, which are related to the concentration of species in dilute solution. Lambert's law shows that the fraction of radiation absorbed is independent of the intensity of the radiation. These two laws are combined together and expressed as the Beer-Lambert law,[15] Eq. (2.35), which is the often used to determine quantitatively concentration absorbing species in the solution.

$$A = log_{10}\frac{I}{I_0} = \varepsilon lc \qquad (2.35)$$

where A is the measured absorbance, I_0 and I are the intensity of the incident radiation and the intensity of transmitted radiation, respectively, ε is a constant for each absorbing material, or also called the molar absorption coefficient ($mol^{-1}dm^3cm^{-1}$), l is the length of the absorbing solution (cm) and c is the concentration of the absorbing species in mol dm^{-3}. The other useful

value is the wavelength (λ_{max}), where the maximum absorption takes place. The λ_{max} is a characteristic value and is strongly influenced by surroundings.[15]

Figure 2.14 presents diagrams of a typical spectrometer. A beam of the visible or ultraviolet light source is separated into its components by the prism or diffraction grating. The beam then travels to the narrow slit to ensure that it is a monochromatic wavelength. The rotating segment mirror splits the beam into two equal intensity beams; one beam is reflected to the sample cell (cuvette) and another beam is reflected to the reference cell. The intensity of the beam from the sample cell (I) is measured by the detector and is compared with the intensity of the beam from the reference cell (I_0), which should have no light absorption. The spectrometer measures this for all the component wavelength and reports the values of absorbance *vs* wavelength.

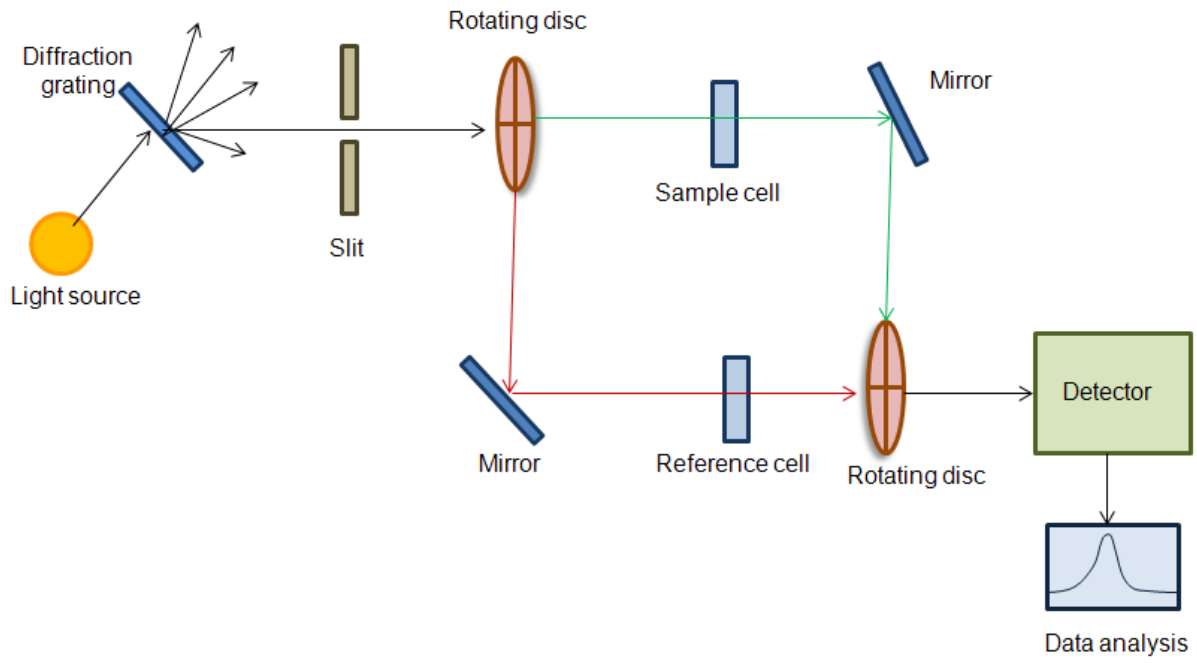

Figure 2.14 Diagram of the ultraviolet/visible spectrometer.[15] (The colours of the light beams are not identical to the beams. The colours are used in order to distinguish the different beams.)

2.6.2 Surface Plasmon Resonance (SPR)

Surface Plasmon Resonance (SPR) is a coherent oscillation of free electrons on a metal surface stimulated by electromagnetic incident light. The resonance condition takes place when the frequency of oscillation of conduction electrons matches with the frequency of incident light.[16] This causes the electrons on metal surface to move away from their equilibrium position to a charge separation region.[17] The intensity and the position of SPR are influenced by shape, size, structure and dielectric properties of metals. The optical property of precious metals begins from the SPR. The study of SPR provides a better understanding of the optical properties of nanostructured materials.[17] The resonances of spherical Au, Ag and Cu nanoparticles occur in the visible region of the spectrum, while the resonances of most of the other metals are in the ultraviolet region.

Au nanoparticles (Au NPs) absorb light to give the peak of SPR. For Au nanorods (Au NRs), the SPR is separated into bands, which are transverse plasmon resonance (TSPR) and longitudinal surface plasmon resonance (LSPR)[18], corresponding to the oscillation of the free electrons perpendicular to and along with the long axis of Au NRs, as shown in Figure 2.15. The LSPR of Au NRs is at a higher wavelength than the TSPR due to a lower frequency of oscillation of free electrons. The increase in aspect ratio has a strong effect on the LSPR since the free electrons have decreased in frequency, suggesting a positive shift in the wavelength.

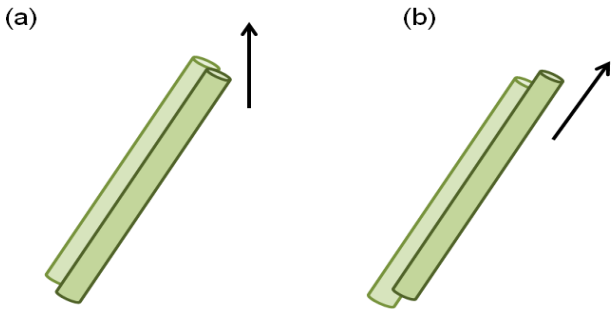

Figure 2.15 Surface plasmon resonance (SRR) of (a) transverse surface plasmon resonance (TSPR) and (b) longitudinal surface plasmon resonance (LSPR).[18]

2.7 X-Ray Photoelectron Spectroscopy (XPS)

XPS is a versatile non-destructive technique that provides surface analysis information. The XPS technique was pioneered by Siegbahn and co-workers in the mid-1960's using Einstein's explanation about the photoelectric effect.[19] Photoelectron spectroscopy is based on the principle of a "single photon in, an electron out" procedure. The photon energy is related to the following equation:[19]

$$E = hv \tag{2.36}$$

where h is the Planck constant (6.62×10^{-34} J s) and v is the frequency of the radiation (Hz). In XPS, a monochromatic X-ray beam is incident on the sample surface, where a photon is absorbed by an atom of the sample. Electrons will be ejected from both the core and valence levels of the surface atom into its surrounding vacuum when the photon energy is higher than the work function in the solid. The kinetic energy of electron is measured in the vacuum level. The kinetic energy of an electron can be measured using an appropriate analyser. Following the principle of energy conservation, the energy of the photon must be conserved and can be separated into three terms:[19]

$$KE = hv - BE + \Phi \tag{2.37}$$

where KE is the kinetic energy of the photo electron, hv is the energy of the photon, BE is the binding energy of the electron in the solid and Φ is the spectrometer work function.

Each electron of every element has a characteristic binding energy, depending on its atomic orbital. The presence of a peak at a specific binding energy is indicative of the specific element. The exact binding energy of an electron depends not only upon the level from which the electrons of the atoms are photoemitted, but also upon the formal oxidation state of the

atom and the local chemical and physical environment. These cause changes in the binding energy of a core electron of an element in the chemical bonding of that element, creating "chemical shift".[19] The specific chemical shift is the difference in BE values of one specific chemical state versus the BE of the pure element. The chemical shift is another fingerprint of the compounds. For instance, the carbon atom of a carboxyl group will behave slightly differently from that of a carbon atom in a methyl group.[19] The chemical shift in XPS is observable because the technique is of high intrinsic resolution.

XPS provides a quantitative analysis of surface composition. The intensity of the peak is related to the concentration of the element, in which the sensitivity factor of that particular element needs to be accounted for during calculation. For the XPS spectra, it is noticeable that the background intensity at high binding energies increases as a result of inelastically scattered electrons. In addition, a spin-orbit splitting is observed on all the core levels, which have an orbital angular momentum quantum number, l, ≥ 1 (p, d, f,...). This behaviour is due to the spin-orbit coupling with higher angular momentum state, for example the d-orbital has the angular momentum quantum number 2 and a spin quantum number (s) that equals to ½ a vector, giving a coupling constant (j) value of 3/2 and 5/2. The one with the maximum j gives the lowest energy final state. Figure 2.16 illustrates the signal of a Au 4*f* XPS spectrum.

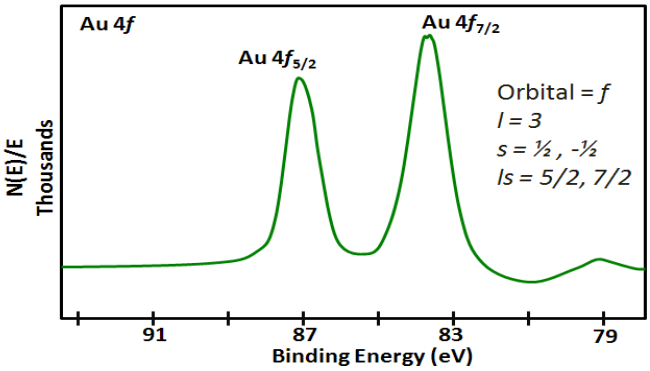

Figure 2.16 XPS spectrum of Au 4*f*.

An X-ray photoelectron spectrometer is composed of an X-ray source, electron energy analyser, Ar ion gun, neutraliser, vacuum system, electrical controls and a computer system. The experiment is operated under an ultrahigh vacuum system (<10^{-9} Torr or <10^{-7} Pa) in order to detect the electrons and to prevent surface reaction and contamination. The system setup of instruments is shown in Figure 2.17.

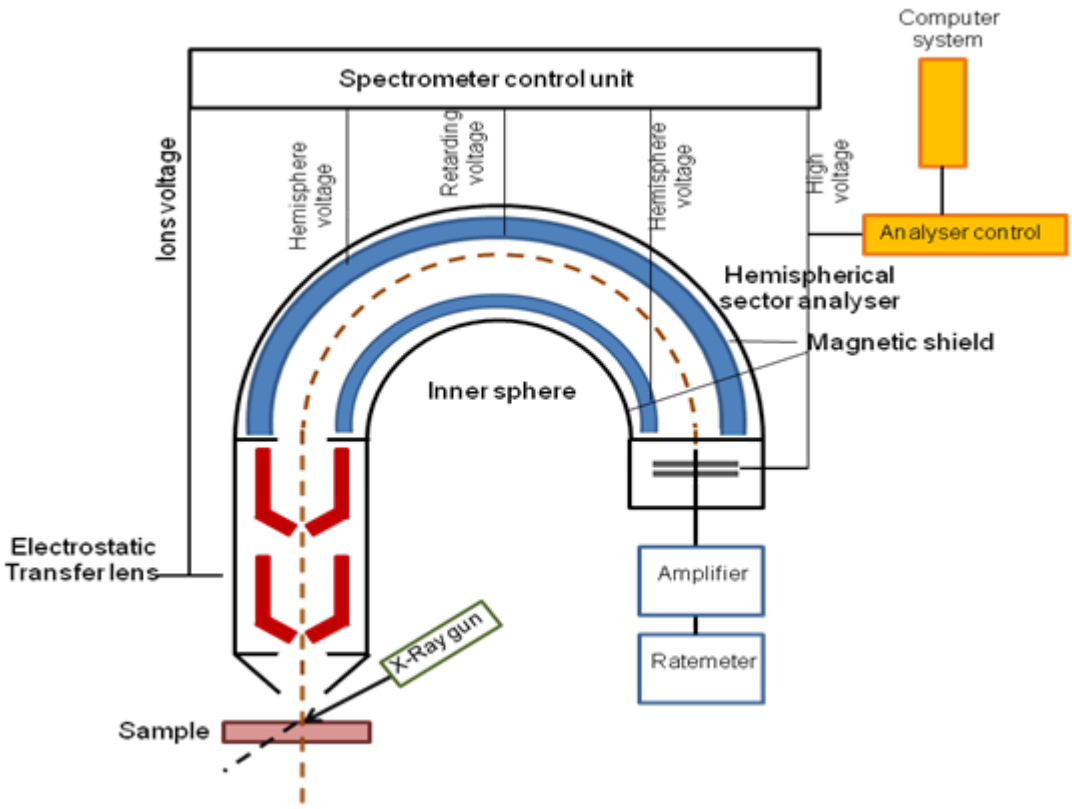

Figure 2.17 Schematic of X-ray photoelectron spectrometer.

2.8 Electron Microscopy (EM)

Transmission electron microscopy (TEM) is a standard method that yields structural information about topography and morphology of a material. The principle of TEM operation is same as that of a light microscope but electrons are used as the light source. The much lower wavelength of the electron beam results in a much higher resolution of TEM compared

with that of the light microscope. The electron beams are formed in a high vacuum and they are accelerated through a thin-section of specimen material. Metal apertures and magnetic lens are employed in order to confine and focus the electron beams. The electron beams are magnified by a system of electromagnetic lens. A three-lens system is commonly used in TEM, as shown in Figure 2.18. There are three different interactions of electron beams:[15,20] transmission, diffraction and inelastic scattering. TEM can also be connected to another analysis, such as an EDX (Energy Dispersive X-ray spectroscopy), EELS (Electron Energy Loss Spectroscopy), EFTEM (Energy Filtered Transmission Electron Microscopy) etc.

The resolution of the microscope is defined by the closest spacing of two points, which can be seen as two distinct entities represented by the formula:[20]

$$D = 0.61\lambda/n\sin\alpha \qquad (2.38)$$

where D is the closest spacing of two points, which can be seen as two distinct entities. λ is the wavelength of the incident radiation, n is the refractive index and α is the half-angle subtended by the aperture.

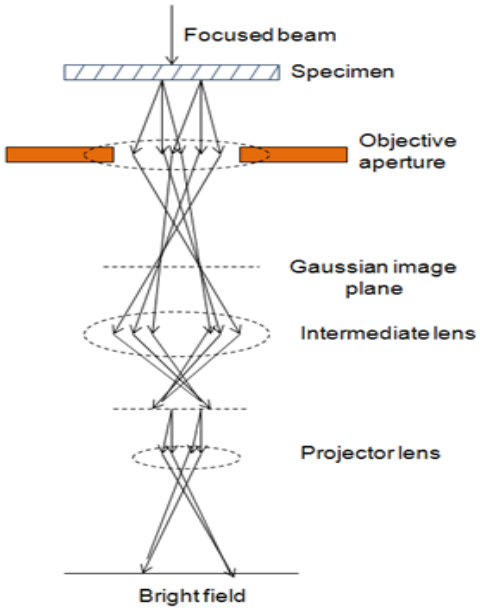

Figure 2.18 A three-lens system of TEM and ray paths in a reference transmission electron microscope with high resolution magnification imaging mode.[20]

Scanning transmission electron microscopy (STEM) employs the scanning principle of scanning electron microscope (SEM) and the high-resolution of TEM. A fine electron beam is scanned over the sample in a two-dimensional raster. STEM signals can be obtained by either bright-field or dark-field signals derived from the elastic scattering of electrons in the specimen.

Annular dark-field (ADF) imaging is an illumination technique used to observe unstained samples. The unscattered beam is excluded from the image, resulting in a dark background around the bright specimen. The particular detector geometry in STEM is positioned in the optical far field beyond the specimen.[21] First, light enters the microscope for illumination of the sample. The condenser lens focuses the light towards the sample. Most light is transmitted (unscattered) to the sample and some is scattered from the sample. The scattered light is collected at an objective lens, while the transmitted light misses the objective lens and is not collected. The image is formed by only the scattered light. The ADF is atomic number (Z)-dependent, leading to a so-called Z-contrast in the image. ADF is used to detect heavy-atom particles in a light-atom matrix. However, if the light-atom material is microcrystalline, the variation of diffraction intensities causes large fluctuation in the ADF. It is suggested that this effect can be avoided when a high-angle annular dark-field (HAADF) is used. This results in good Z-contrast.[20]

2.9 Energy-Dispersive X-ray Spectroscopy (EDS)

X-ray microanalysis is a technique that used for analysing microscopic samples. There are two kinds of X-ray analysis: one is wavelength-dispersive spectroscopy (WDS), which uses

the wavelength of X-rays, the other is energy-dispersive spectroscopy (EDS), which uses the energy of the X-rays. Wavelength and energy are related by the formula:[22]

$$E = \frac{hc}{\lambda} = \frac{12.4}{\lambda} \qquad (2.39)$$

EDS analysis is based on the use of the x-ray spectrum emitted by a solid sample bombarded with a focused beam of electrons to obtain a localised chemical analysis. It is commonly equipped in analytical scanning electron microscopes (SEM). Better resolution is obtainable with ultra-thin (~100 nm) specimens, which can be analysed with a scanning transmission electron microscope (STEM). The process of X-ray emission is shown in Figure 2.19.

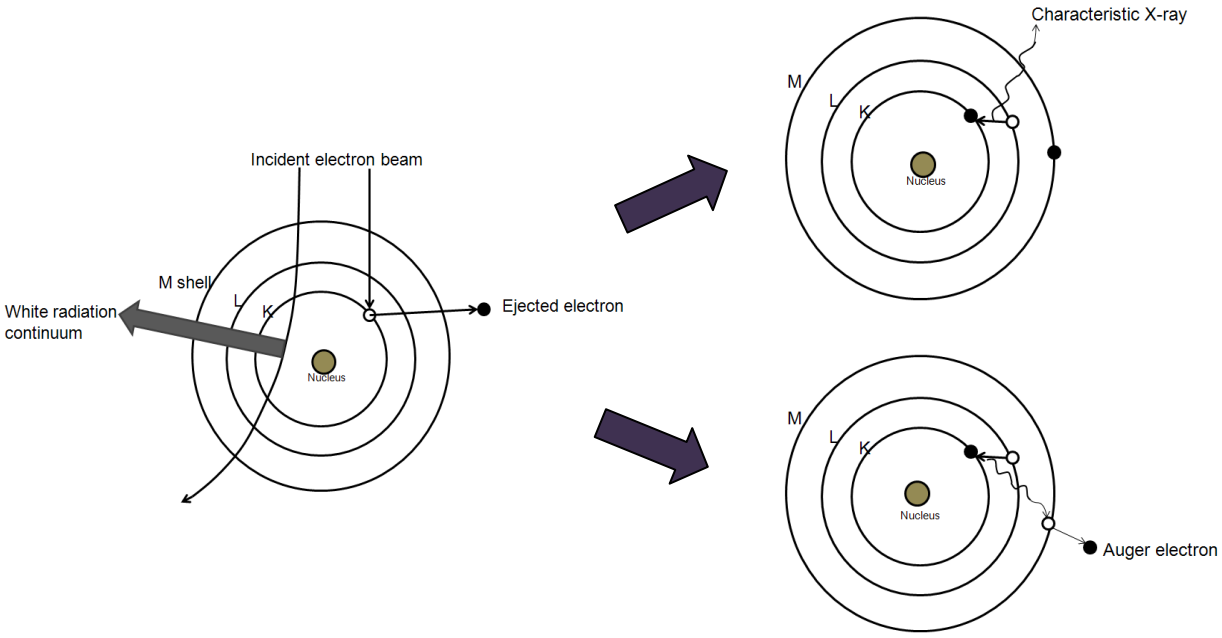

Figure 2.19 The process of X-ray and Auger electron emission and.[23]

First the primary electron beam of the electron microscope ejects an electron from the inner shell of the sample atom, resulting in a vacancy. The vacancy is then filled by another electron from a higher energy shell in the atom. The dropping of this electron to the lower energy shell means that some energy must be emitted. This can be in the form of electromagnetic radiation known as X-rays.[24] The atom excited by the primary electron beam

canalso be relaxed by an alternative procedure. Instead of X-ray emission, the X-ray is reabsorbed by a third electron from a further outer shell in the same atom, ejecting a lower-energy electron and creating an outer vacancy. This ejected electron is called an Auger electron and it contains specific chemical information about the atom from which it originated. Hence, the original X-ray cannot be detected. Instead, a secondary X-ray may be emitted because the outer vacancy is filled. The fluorescent yield is a measurement of the relative quantity of x-ray and Auger electrons produced by excitation. The deexcitation of an ionized atom may occur by either the emission of an Auger electron or the emission of a characteristic x-ray. This fact is reflected in the fluorescent yield, which depends primarily on the atomic number of the excited atom. For low atomic numbers, the process of Auger emission is favoured and the fluorescent yield is low. Conversely, atoms with higher atomic numbers favour the emission of characteristic x-rays. The dispersion of the X-ray occurs by using a pulse-height amplification, pile-up rejection of possible coincidence of pulses and sorting by a multichannel analyser. The analyser analyses the measured pulse height to the energy of the incoming photon.[20] X-ray lines can be identified with a capital Roman letter (K, L or M) which it representing the shell containing the inner vacancy. A Greek letter refers to the group of the lines in an order of decreasing importance (α, β etc.). A number represents the intensity of the line in the same group in an order of (1, 2 etc.).[23] Thus, the most intense K line is $K\alpha_1$.

An electron is held in the atom by its binding energy. In order to eject an electron, the energy of the electron beam must be greater than that binding energy. The critical excitation energy E_c is the minimum energy which the electron beam must have to eject the orbital electron.[22,23] The incident light (E_0) must exceed E_c and should be twice as higher as E_c to provide sufficiently high excitation efficiency. The qualitative analysis of EDS consists of

identifying the lines in the spectrum acquired from a measurement by using tables of energies or wavelengths. The quantitative analysis involves measuring the line intensities corresponding to each element in the samples and making a calibration from the standards of known composition. The line intensities are measured by counting the pulses generated in the X-ray detector. The EDS spectra are presented by in a digitised form where the x-axis represents X-ray energy and the y-axis represents the number of count per channel. This technique can be called by either EDS or EDX.

2.10 Thermo Gravimetric/Differential Thermal Analysis (TG/DTA)

Thermal Analysis (TA) is a group of techniques that studies the change of material properties as a function of temperature. TA provides informative data on enthalpy, thermal capacity, mass changes, the coefficient of heat expansion, thermal degradation etc.[25] TA includes several different methods, which can be separated based on properties measured.

Thermo gravimetric/Differential Thermal Analysis (TG/DTA**)** is a technique which combines the methods of Differential Thermal Analysis (DTA) and Thermo Gravimetric Analysis (TGA). The temperature difference and mass changes are measured at the same time. TGA relies on a high precision measurement of weight loss, temperature and temperature change. Thus, a highly precise balance equipped with a sample pan and a programmable furnace are required. A derivative or weight loss is used to show the temperature point, where the weight loss is most apparent. The TGA curve is influenced by several factors, such as heating rate, sample size, sample particle size, gas flow rate, crucible shape etc. DTA measures an identical thermal cycle of the sample with respect to an inert reference. The temperature difference between the sample and reference is recorded as a function of temperature. Figure 2.20 shows a model of a TG/DTA instrument.

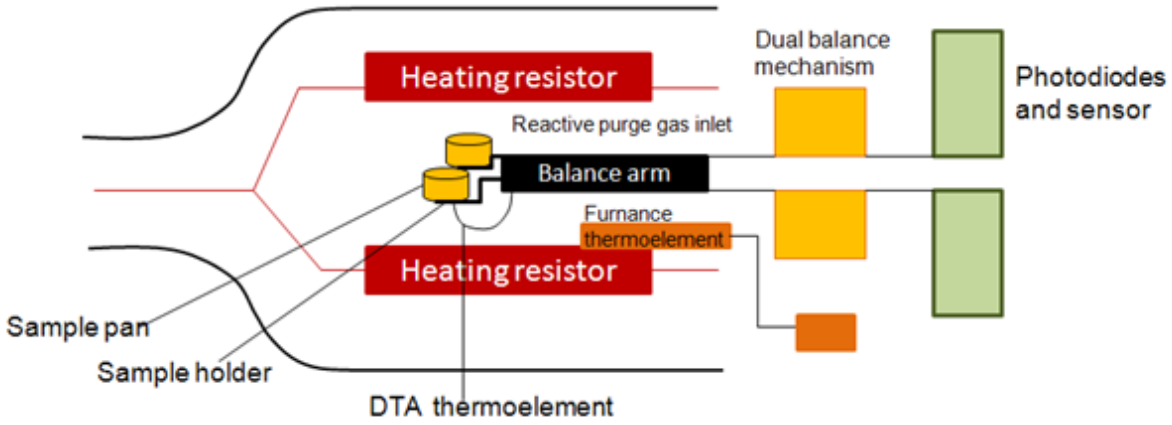

Figure 2.20 Schematic of TG/DTA.[25]

2.11 On-line Electrochemical Mass Spectrometry (OLEMS)

On-line Electrochemical Mass Spectrometry (OLEMS) can be used to identify volatile species and intermediates during an electrochemical reaction by combining the principle of electrochemistry and mass spectrometry. This technique is based on the common procedure of Differential Electrochemical Mass Spectrometry (DEMS), which was first introduced by Bruckenstein and Gadde in 1971.[26] The gaseous products are collected in a vacuum system prior to being analysed by mass spectrometry (MS). MS was the first technique, which could detect and analyse a relative small amount of volatile products produced from electrode surfaces. This technique was then further developed to obtain an on-line detection and to be applied to a small surface area electrode. The DEMS has been widely used in several reactions.[27-30]

In this study, the OLEMS system based on the system of Wonders *et al.*[31], as shown in Figure 2.21. Teflon-base tip is employed to collect gaseous products by placing it very close to the electrode surface (10-20 µm). Due to its hydrophobic properties, only gaseous products can penetrate through it to the MS. The ultra high vacuum (UHV) system is necessary for the performance of OLEMS, both in terms of efficiency and sensitivity. The MS consists of three

major parts: ion source, the mass analyser and the detector. The MS works by changing the molecules to ions so that the ions can be manipulated by an external electric and magnetic field. The charged molecules are measured according to their mass to charge ratio. The MS determines ion intensity (I_i) as represented by Eq. (2.40). The I_i value is directly proportional to the incoming flow J_i given by Faradaic current. K^0 contains all settings of the mass spectrometer and the ionization probability of the corresponding species.[28]

$$I_i = K^0 J_i \qquad (2.40)$$

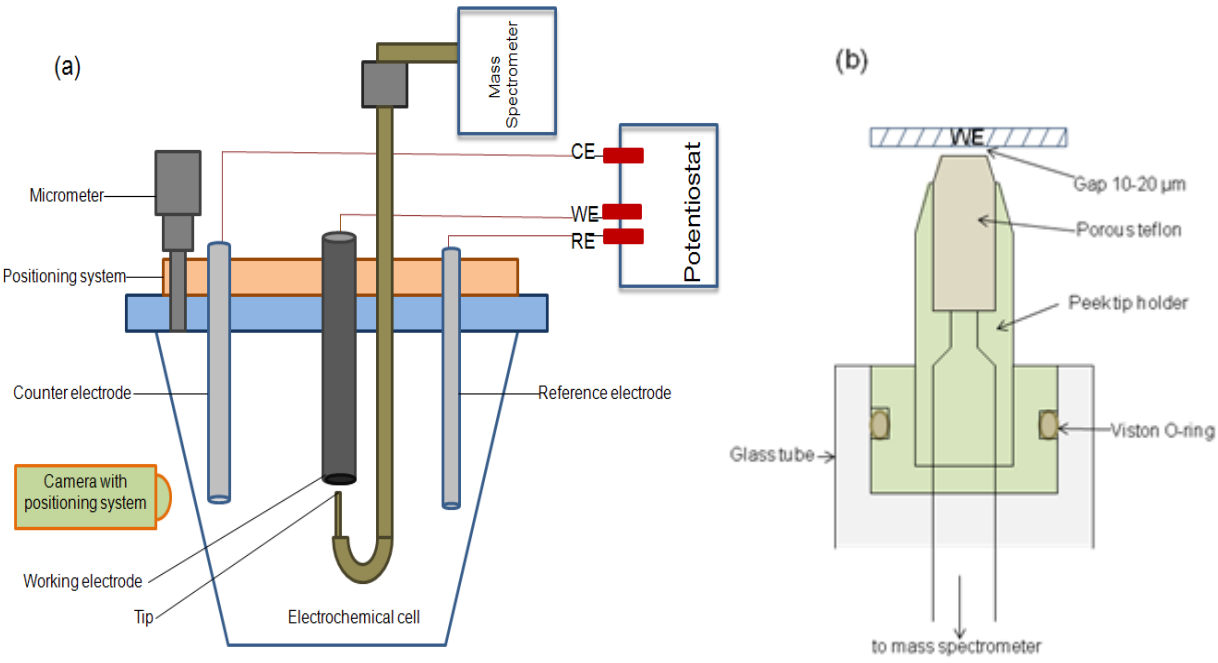

Figure 2.21 Schematic of (a) on-line electrochemical mass spectrometry (OLEMS) set up and (a) OLEMS tip.[31]

2.12 Ion Chromatography (IC)

Ion Chromatography (IC) is another technique that can be combined with electrochemistry. IC is one of the members of the chromatographic methods used to separate mixtures of substances. The separation is based on the contribution of a stationary phase and a mobile phase. IC retains analyte molecules in the column based on electrostatic forces between ions and functional groups on solid substances.[32] The most widely application of IC is the investigation of an aqueous system, such as an analysis of drinking water and analysis of species contaminated in the environment. IC can be carried out as cationic exchange ion chromatography or with anionic exchange ion chromatography.[33] The cationic exchange ion chromatography retains the positive charge analytes due to negative charge functional groups in the stationary phase, while the opposite occurs for the anion exchange ion chromatography, as shown in Eq. (2.41) and (2.42).

Cation exchange chromatography

$$R - X^{-}C^{+} + M^{+}B^{-} \rightleftarrows R - X^{-}M^{+} + C^{+} + B^{-} \quad (2.41)$$

Anion exchange chromatography

$$R - X^{+}A^{-} + M^{+}B^{-} \rightleftarrows R - X^{+}B^{-} + M^{+} + A^{-} \quad (2.42)$$

where the ionic compound consists of the cationic species M^{+} and the anionic species B^{-}. $R - X^{-}C^{+}$ and $R - X^{+}A^{-}$ are the stationary phase with functional groups.

The separation is based on the differences in the electrostatic forces of individual analytes. The separation clearly demonstrates when the distribution coefficients (*D*) of each component can be sufficiently distinguished from one another. The value of *D* can be defined as the ratio of the concentration of analyte A in the stationary phase to that of in mobile phase, as shown in Eq. (2.43). The analyte with higher values of *D* are retained strongly in the stationary phase.

$$D_A = \frac{[A]_S}{[A]_M} \quad (2.43)$$

A chromatogram is recorded in the form of a detection signal or a concentration as a function of time. The residence time or gross retention time t_R of a substance on the stationary phase is obtained by adding the net retention time t_S, which corresponds to the actual residence time on the migration path, and the flow time of the mobile phase without any interaction, the dead time t_M, as shown in Eq. (2.44).

$$t_R = t_S + t_M \quad (2.44)$$

2.13 References

(1) Pletcher, D. A. *First Course in Electrode Processes*; Second Edition ed.; RSC Publishing, 2009.

(2) Bond, A.M., Compton, R. G, Fiedler, D.A., Inzelt, G., Kahlert, H., Komorsky-Lovric, S., Lohse, H., Lovric, M., Marken, F., Nudeck, A., Retter, U., Scholz, F. and Stojek, Z. *Electroanalytical Methods: Guide to Experiments and Applications*; 2nd, revised and extended edition ed.; Springer: New York, 2010.

(3) Von Helmholtz, H. L. F. *Ann. Physik* **1879**, *7*, 337.

(4) Greef, R., Peat, R., Peter, L. M., Pletcher, D. and Robinson, J *Instrumental Methods in Electrochemistry*; Ellis Horwood: Great Britain, 1990.

(5) Chapman, D. L. *Phil. Mag* **1913**, *25*, 475.

(6) Gouy, G. *Compt. Rend.* **1910**, *149*, 654.

(7) Gouy, G. *J. Phys. Radium* **1910**, *9*, 457.

(8) Fisher, A. C. *Electrode Dynamics*; Oxford University Press: New York, 2009.

(9) Stern, O. *Z. Electrochem* **1924**, *30*, 508.

(10) Grahame, D. C. *Chem. Rev* **1947**, *41(3)*, 441.

(11) Grahame, D. C. *Ann. Rev. Phys. Chem.* **1956**, *6*, 337.

(12) Bockris J. O., Devanathan M. A. V., Muller K. *Proc. R. Soc. London Ser. A* **1963**, *274 (1356)*, 55.

(13) Bard, A.J., Faulkner, L. R. *Electrochemical Methods, Fundamentals and Applications*; Second Edition; John Wiley and Sons: New York, 2001.

(14) Pletcher, D. A. *First Course in Electrode Processess*; 2 ed.; The Royal Society of Chemistry: Cambrige, 2009.

(15) Faust, B. *Modern Chemical Techniques*; Royal Society of Chemistry: Unilever, 1997.

(16) Stewart, M. E.; Anderton, C. R.; Thompson, L. B.; Maria, J.; Gray, S. K.; Rogers, J. A.; Nuzzo, R. G. *Chemical Reviews* **2008**, *108*, 494.

(17) Myroshnychenko, V.; Rodriguez-Fernandez, J.; Pastoriza-Santos, I.; Funston, A. M.; Novo, C.; Mulvaney, P.; Liz-Marzan, L. M.; de Abajo, F. J. G. *Chemical Society Reviews* **2008**, *37*, 1792.

(18) Sharma, V.; Park, K.; Srinivasarao, M. *Materials Science & Engineering R-Reports* **2009**, *65*, 1.

(19) Briggs, D. and Seah, M. P. *Pratical Surface Analysis* Second ed.; Vol. Volume 1-Auger and X-Ray Photoelectron Spectroscopy

(20) Amelinckx, A., Van Dyck, D., Van Landuyt, J., Van Tendeloo, G. *Electron Microscopy Principles and Fundamentals*; VCH A Wiley company: Weinheim, 1997.

(21) Nellist, P. D.; Pennycook, S. J. *Advances in Imaging and Electron Physics, Vol 113* **2000**, *113*, 147.

(22) Reed, S. J. B. *Electron Microprobe Analysis*; 2nd ed.; Cambridge University Press: Cambridge, 1993.

(23) Goldstein, J. I., *et al*. *Scanning Electron Microscopy and X-ray Micronalysis*; 3rd ed.; Plenum Press: New York, 2003.

(24) Vaughan, D. *ENERGY-DISPERSIVEX-RAY MICROANALYSIS An Introduction*; NORAN Instruments Middleton, Wisconsin, 1999.

(25) Coats, A. W.; Redfern, J. P. *Analyst* **1963**, *88*, 906.

(26) Bruckens.S; Raogadde, R. *Journal of the American Chemical Society* **1971**, *93*, 793.

(27) Abd-El-Latif, A. A.; Xu, J.; Bogolowski, N.; Konigshoven, P.; Baltruschat, H. *Electrocatalysis* **2012**, *3*, 39.

(28) Baltruschat, H. *Journal of the American Society for Mass Spectrometry* **2004**, *15*, 1693.

(29) Jusys, Z.; Massong, H.; Baltruschat, H. *Journal of the Electrochemical Society* **1999**, *146*, 1093.

(30) Mostafa, E.; Abd-El-Latif, A. A.; Ilsley, R.; Attard, G.; Baltruschat, H. *Physical Chemistry Chemical Physics* **2012**, *14*, 16115.

(31) Wonders, A. H.; Housmans, T. H. M.; Rosca, V.; Koper, M. T. M. *Journal of Applied Electrochemistry* **2006**, *36*, 1215.

(32) Eith, C., Kolb, M., Seubert, A., Henning Viehweger, K. *Practical Ion Chromatography An Introduction* Metrohm Monograph: Switzerland, 2001.

(33) Peter. J., Haddad, P. R. *Ion chromatography: principles and applications*; Elsevier: Amsterdam, 1990.

CHAPTER 3

THE OXYGEN REDUCTION OF RHODIUM COATED GOLD NANORODS AND NANOPARTICLES

3.1 Introduction

The development of alternative energy sources is an issue of worldwide importance. The projected decline in fossil fuel resources means that renewable energy sources are needed, many of which are not in continuous supply (e.g. wind power, solar energy). A means to store energy is thus desirable. Renewable energy could be used to generate hydrogen, which could be stored and used as required. The fuel cell is a device that produces electrical energy from a fuel, such as hydrogen. A fuel cell can be used to synthesise chemicals, if the appropriate reactions are chosen. The basic reactions for a hydrogen-powered fuel cell are the hydrogen oxidation reaction (HOR) on the anode, which is the reverse of the hydrogen evolution reaction (HER), and the oxygen reduction reaction (ORR) on the cathode. Both the HOR and the ORR have been extensively investigated, with platinum (Pt) being the most widely used catalyst. There has been particular interest in the ORR over the past decades because of its efficiency-limiting reaction compared with the HOR. The ORR results in the formation of water (H_2O) *via* a 4-electron pathway or hydrogen peroxide (H_2O_2) *via* a 2-electron pathway, depending on the catalyst. Pt and Pt alloys are currently the most active catalysts for the ORR since they catalyse the reaction almost completely to water in both acidic media and alkaline media;[1-3] however, even with the most promising catalysts there is a large overpotential, which results in a decrease in the fuel cell output.[3] Due to the high cost and scarcity of Pt, alternative transition metals and metallic alloys have long been investigated in a search for a cheaper catalyst.

Among the transition metals, Au is a possible electrocatalyst for the ORR as it supports both 2-electron and 4-electron pathways, depending on the orientation of the surface[4] and experimental conditions.[5-7] Au exhibits less activity for the ORR in acidic media than in alkaline media. El Deab *et al.* published a number of papers on Au substrates for the ORR.[8-14] They reported that electrodeposited Au nanoparticles on Au electrodes present two well-defined reduction peaks for the ORR in sulphuric acid, while bulk Au electrodes present only one peak located at more negative potentials. The two peaks result from two steps of the ORR, which have been assigned to the reduction of O_2 to H_2O_2 and the reduction of H_2O_2 to H_2O.[8] The numbers of electron transferred per oxygen molecule were calculated at 4 for the Au particle electrodeposited on a Au electrode and 3 for the bulk Au electrode. This suggests that more H_2O_2 is reduced to H_2O on the Au nanoparticle electrode.[9] The catalytic activity of the Au nanoparticles was found to decrease as the Au nanoparticle size increased to micrometres.[8] It is known that the ORR is highly sensitive to the crystallographic orientation of the Au electrode, particularly in alkaline media. The oriented Au particles were electrodeposited on a glassy carbon electrode.[11] The oriented Au (100)-like nanoparticles showed a high electrocatalytic activity for the ORR, corresponding to previous reports of the reaction at Au (100) facets.[15] The effect of substrate nature and the effect of electrodeposition condition on catalytic activity of Au nanoparticles have also been studied.[12] The particles deposited on glassy carbon electrodes in the presence of cysteine showed a high catalytic activity. The Au particles deposited on electro-oxidised highly oriented pyrolytic graphite (HOPC) yielded higher current density than those deposited on untreated HOPG.[12]

Sarapuu *et al.* prepared Au thin-films on a GC electrode and studied the ORR in both acidic and alkaline media.[5] The catalytic activities of thin-film electrodes were found to be similar to the catalytic activity of a bulk Au electrode. The specific activities (SA) of the Au

films in acidic media were independent of the film thicknesses, while the SA in alkaline media decreased as the film thickness decreased. Erikson *et al.* studied the effect of a Au/C catalyst layer thickness on the kinetics of O_2 reduction and compared the kinetics with that on a bulk Au electrode in both acidic media and alkaline media.[6] It was found that the diffusion of O_2 was effective when the layer thickness was between 1.5-10 μm. Jirkovsky´*et al.* studied the kinetics of the ORR on Au/C nanoparticles.[16] The H_2O_2 selectivities of Au/C catalysts obtained from RDE and RRDE techniques are in good agreement, suggesting that both techniques are suitable for measuring the H_2O_2 selectivity. The increase of Au loading decreases the selectivity towards H_2O_2, as a result of the further reduction of H_2O_2 to H_2O. The ORR depends on Au particle size with a size of 5.7 nm being found to give the highest electrocatalytic activity.

The size and structure of catalyst can be controlled during preparation using defined methods, to learn more about any influence of morphology on catalytic activity. Much research has been carried out on spherical Au particles (Au NPs),[6,16] Au nanorods (Au NRs),[17-23] nanocubes,[24,25] nanowires[26] etc.[27,28] Several methods have been proposed for the synthesis of well-defined Au NRs, such as template methods,[29,30] electrochemical methods,[31] seeded growth methods[20,22]. The seeded growth method uses metal seeds to induce the nucleation and growth of larger metal particles. Jana *et al.* developed this method by varying reducing agents and conditions; however, a low uniformity of rod-shaped particles was obtained.[21] They found that additional nucleation can be avoided by controlling the rate of reducing agent addition and the chemical reduction potential of the reducing agent. They were then able to synthesis Au NRs by using sodium borohydride as a reducing agent to obtain 3-5 nm Au seeds and preparing the growth stage solution of an optimum concentration of a cationic surfactant, hexadecyltrimethylammonium bromide (CTAB).[22] It was found that the

addition of $AgNO_3$ affects the yield, aspect ratio and crystal structure of Au NRs. Nikoobakht *et al.* prepared Au NRs which had a higher aspect ratio by using a binary surfactant mixture of CTAB and benzyldimethylhexadecylammonium chloride (BDAC).[18]

Due to its relative inertness in acidic media, Au can be used as a support for other metals, such as Pt,[32-34] Pd,[35-38] and Rh[39-41] to form alloy or core-shell structures. This idea has been extended to study the deposition of other transition metals such as, Pt,[42-45] Pd,[46,47] or Ag[48] onto Au NRs form core/shell structures. He *et al*. prepared Pt–Ag nanoislands on Au NRs and studied methanol oxidation on the resulting catalysts.[44] Pt deposited on Au NRs can guide Pt−Ag nanoalloy formation since Pt has a strong catalytic activity, which can control the reduction of Ag^+ by ascorbic acid. Wang *et al.* reported that Pt was successfully deposited on Au NRs and exhibited a high catalytic activity for formic acid oxidation.[49] In addition to Au alloy NRs, smaller alloy particles have also been widely researched; for example, Jirkovsky *et al.* studied the ORR on metal nanoalloys, with the aim of forming H_2O_2 rather than H_2O.[37] DFT modelling suggested that alloy formation of Pd, Pt and Rh on Au surfaces can improve the selectivity of H_2O_2 production compared with carrying out the ORR on pure Au.

Rhodium is one of the transition metals that have been studied for the ORR.[50-55] The kinetics of the ORR on Rh over a wide pH range was studied by Martinovic *et al.*[51] However, Rh is an expensive metal. Therefore, electrodeposition of Rh thin films[39-41] and deposition of Rh on other metals[56,57] have been made and investigated their catalytic properties in order to find a way to reduce the loading of Rh whilst maintaining activity. Arbib *et al.* studied the nucleation and growth of Rh on Au (100) substrates and polycrystalline Au electrodes.[39] It was found that the nucleation and growth of 3D Rh clusters proceeded on the top of a 2D Rh phase. Zelenay *et al.* studied sulphate/bisulphate anion adsorption on a single crystal Rh

electrode and a polycrystalline Rh electrode.[58] It was revealed that the adsorption of sulphate on Rh (111) is more stable than on other Rh surfaces. The strong adsorption of sulphate on Rh (111) not only prevents the adsorption of the other ions but also shifts hydrogen adsorption to more negative potentials. Thus, sulphate/bisulphate adsorption is undesirable in catalysis. The surface oxide formation and reduction of Rh have been investigated by many authors.[50,54,57,59-62] Jerkiewicz *et al.* studied the formation and the reduction of surface oxide films at polycrystalline Rh electrodes and the oxygen evolution reaction (OER) at these surfaces.[59,60] The anodic polarisation of Rh in sulphuric acid produces the thin Rh oxide film of nominal composition $Rh(OH)_3$ at high potential. The thickness of the film is not in excess of three monolayers. There are two linear regions for Tafel slopes, which are 60 mV at low current density and 120 mV at high current density. The oxide film on Rh electrode markedly affects the OER in several ways, (a) the reaction energetic at the double layer region is affected, (b) the electronic properties of the metal surface are affected, (c) a barrier to charge transfer through the surface oxide film is formed, (d) the adsorption of reaction intermediates and/or products at the catalyst surface is affected. Lukaszewski *et al.* studied the electrochemical behaviour of polycrystalline Rh layers on Au electrodes with cyclic voltammetry and a quartz crystal microbalance (EQCM).[57] The desorption of hydrogen takes place along with the simultaneous adsorption of HSO_4^- ions. Dissolution of Rh increases with increasing positive potential limit and decreasing scan rate.

In this present work, the electrochemical reduction reaction of oxygen for Rh on differently shaped Au supports and different methods of Rh deposition has been studied. Au NRs have been used because they provide a well-defined surface crystallographic orientation, therefore allowing the growth of Rh on the Au substrate to be investigated. The smaller particles have been compared to study the size and shape-dependent catalytic activities of Au

and Rh nanoparticles. The different types of synthesis have been compared in order to study the formation of Au–Rh alloys and Rh-rich phases and the effect of Au-Rh distribution on catalytic activities.

3.2 Experimental

3.2.1 Chemicals and Reagents

All reagents used were analytical grade or better and were used as received. Cetyltrimethylammonium bromide (CTAB) and L-ascorbic acid were purchased from Acros. Sodium borohydride ($NaBH_4$) was obtained from Riedel-de Haën. Silver nitrate ($AgNO_3$) and Nafion solution (5% wt) were purchased from Sigma Aldrich. Hydrogen tetrachloroauric acid ($HAuCl_4 \cdot 3H_2O$) and sodium hexachlororhodate ($Na_3RhCl_6 \cdot 12H_2O$), both Premion grade, were obtained from Alfa Aesar. Sulphuric acid, 96% suprapur, was from VWR. Copper (II) sulphate pentahydrate, 99.99% were from Fluka. Ultrapure water (purified with a Milli-Q tandem Elix-Gradient A10 system: resistivity 18.2 MΩ cm, TOC ≤ 5 ppb) was used throughout. All glassware used was first cleaned by heating in a mixture of concentrated nitric and sulphuric acids for 1.5 h, followed by rinsing with copious quantities of ultrapure water and soaking overnight in ultrapure water.

3.2.2 Preparation of Au NRs

The Au NRs were synthesised using a seed-mediated, sequential growth method, following the method of Nikoobakht *et al.*[18], as modified by He *et al.*[44] A brief description is provided below.

Seed Solution

7.5 mL 0.1 M CTAB aqueous solution was mixed with 100 μL 0.025 M $HAuCl_4 \cdot 3H_2O$ and diluted with water to 9.4 mL. 0.6 mL ice-cold 0.01 M $NaBH_4$ was then added all at once into the solution and sonicated for 1 min. The solution was kept at 25 °C for 2-5 h until it became brownish in colour. The solution was used immediately as seed solution.

Growth Solution

100 mL 0.1 M CTAB was mixed with 2.0 mL 0.025 M $HAuCl_4 \cdot 3H_2O$. 0.5 mL 0.5 M H_2SO_4, 1 mL 10 mM $AgNO_3$ and 0.8 mL 0.1 M ascorbic acid were then added dropwise and the mixture was sonicated for 1 min. The solution changed from yellow to colourless. 240 μL freshly prepared seed solution was then added dropwise. The solution was kept at 25 °C without sonication or agitation for 24 h. The colour of the solution changed from colourless to purple-red.

3.2.3 Deposition of Rh on Au NRs by varying molar ratio of Au NRs:Rh (10:1, 7:3, 1:1 and 1:2)

9 mL of the growth solution (4.5×10^{-6} mol Au) was centrifuged at 6000 rpm for 1 h to remove excess CTAB and nanospheres. The supernatant was carefully removed with a pipette. The Au NRs precipitate was redispersed in ultrapure water and made up to 3 mL. The centrifuging step was repeated to complete the removal of surfactant from Au NRs surfaces. The Au NRs precipitate was redispersed in 0.5 mL ultrapure water. To study the effect of different amounts of Rh on Au, the same amount of Au was used for each preparation. The molar ratio of Au NRs:Rh was varied by mixing 0.5 mL Au NRs solution with different

volumes of 0.002 M $Na_3RhCl_6 \cdot 12H_2O$ reagent (0.225, 0.965, 2.25, and 4.5 mL), giving samples with molar ratios Au NRs:Rh of 10:1, 7:3, 1:1 and 1:2. 1 mL 0.2 M ascorbic acid was added, and the total volume of each sample was adjusted to 6.0 mL. The mixture was sonicated for 2 h at 40 °C. After sonication, the mixture was kept at 25 °C for 24 h.

The catalyst suspension was prepared by mixing 1 mL of the obtained Au NRs–Rh mixture with 0.35 mg cleaned carbon black (Vulcan XC-72R, refluxed in HNO_3 for 2 h and washed by Milli-Q water until neutral pH) under sonication for 2 h, whilst keeping the loading of Au on carbon black at 30 wt%.

3.2.4 Au−Rh nanoparticles prepared by sequential reduction and by co-reduction

Au−Rh nanoparticles were prepared by sequential reduction of Au followed by Rh, "sequentially reduced particles", and by co-reduction of Au and Rh salts, "co-reduced particles". Sequentially reduced and co-reduced Au–Rh nanoparticles were prepared in the same concentration and molar ratio as Au NRs:Rh. To prepare sequentially reduced particles, $HAuCl_4$ aqueous solution was added into 3 mL 0.1 M CTAB and the Au salt was reduced by adding 1.5 mL 0.1 M $NaBH_4$. The particles were sonicated for 2 h at room temperature and left for 24 h. The obtained Au particles were mixed with 0.02 M $Na_3RhCl_6 \cdot 12H_2O$ (0.0225, 0.0965, 0.225 and 0.45 mL) and the Rh salt was reduced with ascorbic acid at 40 °C with 2 h sonication. The sample was then kept at 25 °C for 24 h. To synthesise co-reduced particles, $HAuCl_4$ and $Na_3RhCl_6 \cdot 12H_2O$ were added together into CTAB in the same quantities as for sequentially reduced particles. 1.5 mL 0.1 M $NaBH_4$ was used as a reducing agent. The total volume of each sample was adjusted to 6.0 mL.

In order to obtain the catalyst suspensions of co-reduced and sequentially reduced Au–Rh nanoparticles, 1 mL catalyst suspension was mixed with cleaned carbon powder under sonication for 2 h (The carbon powder was cleaned by refluxing in nitric acid for 1.5 h and thorough rinsing in Milli-Q water). 1 mL ethanol was added to remove the excess CTAB.[49] The catalyst was then centrifuged at 6000 rpm for 1 h. The supernatant was carefully removed. The Au:Rh/C precipitates were redispersed in ultrapure water and made up to 3 mL. The centrifuging step was repeated to complete the removal of surfactant from catalyst surfaces. The precipitates were redispersed in 1 mL of H_2O to form a catalyst ink.

3.2.5 Nanoparticle and Nanorod characterisation

UV–visible absorption measurements were carried out with a Camspec M550 double-beam spectrophotometer with wavelength resolution 0.1 nm. Scanning transmission electron microscopy (STEM) images were obtained with a Jeol 2100F STEM, fitted with a CEOS spherical aberration corrector and a high-angle annular dark field (HAADF) detector, operated at an accelerating voltage of 200 kV. The microscope is also equipped with a Bruker XFlash 4030 SDD detector enabling EDX measurements. Samples for STEM were prepared by dropping the aqueous samples onto carbon-coated copper grids and leaving to dry under ambient conditions for at least 24 h prior to imaging. STEM measurements were performed by Ruth Chantry (School of Physics). Some additional TEM measurements were made by Dr Zoe Schnepp on a JEOL 2100 with 200keV acceleration voltage and a CCD camera. X-ray photoelectron spectroscopy (XPS) was employed using an Escalab 250 system (Thermo VG Scientific, UK) and a custom-built instrument with an Al Kα X-ray source to provide a monochromatic X-ray beam. The Au NRs–Rh aqueous mixture was deposited on Si substrates and the sample was then measured in ultrahigh vacuum at a pressure of 1×10^{-8} mbar.

3.2.6 Electrochemical measurement for oxygen reduction reaction (ORR)

Cyclic voltammetry and rotating disk electrode (RDE) measurements were performed for oxygen reduction in a three-electrode glass cell at room temperature with an Autolab PGStat12 potentiostat (Ecochemie, NL) that was controlled with General Purpose Elecrochemical System (GPES) software. The glassy carbon working electrode (0.071 cm^2, Radiometer, Copenhagen) was polished using aqueous alumina slurries of increasingly finer grain size (1.0, 0.3 and 0.05 μm, Buehler, USA), followed by sonication in ultrapure water for 5 min. 20 μL of catalyst suspension was pipetted on to the glassy carbon electrode surface and dried in air. The Au loading on the glassy carbon electrode was 41 μg cm^{-2}. After drying the catalyst, 3 μL of Nafion solution (5% wt, Aldrich) was dropped on to the catalyst layer and the electrode was dried in air. The counter and reference electrodes were a Pt wire and a saturated calomel electrode (SCE), respectively. The potentials in this work are presented *vs* SCE. Cyclic voltammetry (CV) was used to investigate the electrochemical surface properties of each catalyst. The electrode was activated in 0.5 M H_2SO_4 saturated with Ar by scanning the potential from -0.24 and 1.3 V at scan rate of 0.1 V s^{-1} for 10 scans.

All samples were subjected to copper under potential deposition (Cu upd) to remove the surfactant on the catalyst surface. The activated electrode was immersed into the electrochemical cell containing Ar-saturated 1 mM $CuSO_4$ in 0.5 M H_2SO_4 electrolyte under potential control at -0.165 V (*vs* SCE) for 10 min. After 10 min, the electrode was rinsed and protected with a droplet of Milli-Q water during transfer to another cell containing Ar-saturated 0.5 M H_2SO_4 electrolyte. The electrode was immersed into the electrolyte and the potential was maintained at 0.45 V for 10 min to ensure the removal of Cu. After 10 min at this potential, the electrode was transferred to Ar-saturated clean electrolyte and CV was performed between limits of -0.24 and 0.6 V, at a scan rate of 0.05 V s^{-1}, so that the real

surface area of the Rh could be calculated from the hydrogen desorption waves. The cyclic voltammograms presented in this study is the tenth scan.

ORR measurements were performed in oxygen-saturated 0.5 M H_2SO_4 electrolyte at a scan rate of 0.01 V s^{-1}, with rotation rates 400, 900, 1600 and 2500 rpm. The background currents measured in Ar-saturated electrolyte were subtracted from single-wave polarisation curves acquired for oxygen reduction.

3.3 Results and Discussion

3.3.1 Characterisation of Au NRs:Rh and Au:Rh nanoparticles

3.3.1.1 Transmission electron microscopy (TEM) and scanning transmission electron microscopy (STEM)

The TEM and STEM images were kindly provided by Ruth Chantry, School of Physics and Astronomy, University of Birmingham and Dr Zoe Schnepp, School of Chemistry, University of Birmingham. Figure 3.1 shows representative scanning transmission electron microscopy (STEM) and high angle annular dark field (HAADF) images of Au NRs. The average length and width of the Au NRs are 35 nm and 10 nm, respectively. A relatively uniform size distribution and high monodispersity of Au NRs are obtained although a small proportion of other shapes is also observed. The Au NRs exhibit smooth surfaces with rounded-end appearance. Au NRs obtained from the seeded growth method are single crystalline structures, which are composed of low Miller index facets. Atomic scale characterisation was performed in order to investigate the detailed structure of the Au NRs. Different structures are observed for the ends of the NRs, perhaps as a result of different orientation of NRs on the grid. The

ends appear as “more-rounded” or “less-rounded”, with angles between facets of 135° and 125°, corresponding to {110} and {111} facets, respectively, as shown in Figure 3.2.[63] The rod end terminates with a (001) face. The bodies of the Au NRs are composed of alternate {100} and {110} facets. The facet structure of Au NRs in this study is consistent with the Au NRs model of Wang *et al*., whose model consists of four {110} and four {100} facets at the body of the rods, suggesting a cylindrical shape.[64]

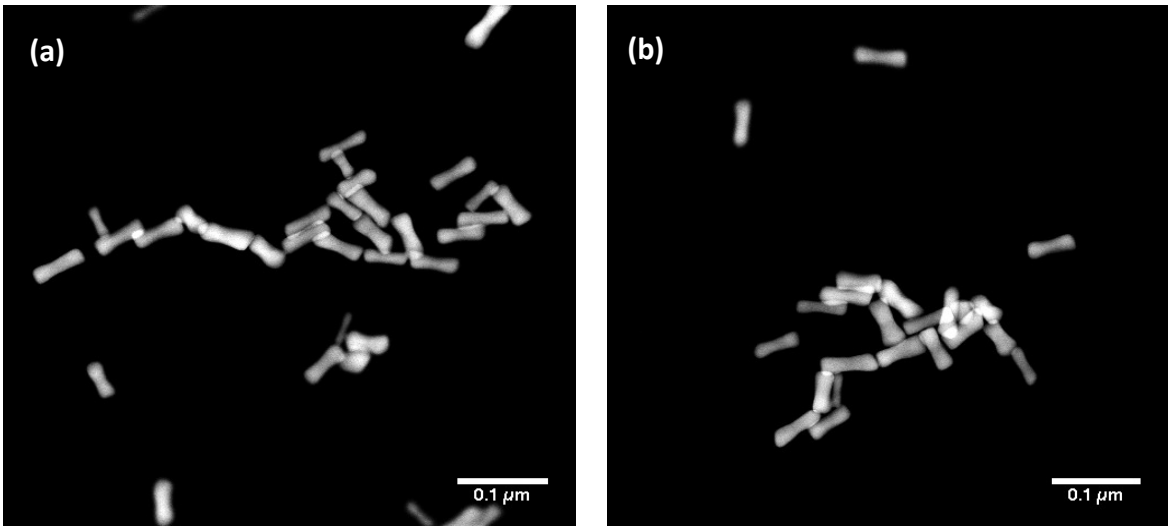

Figure 3.1 STEM-HAADF images of Au NRs.

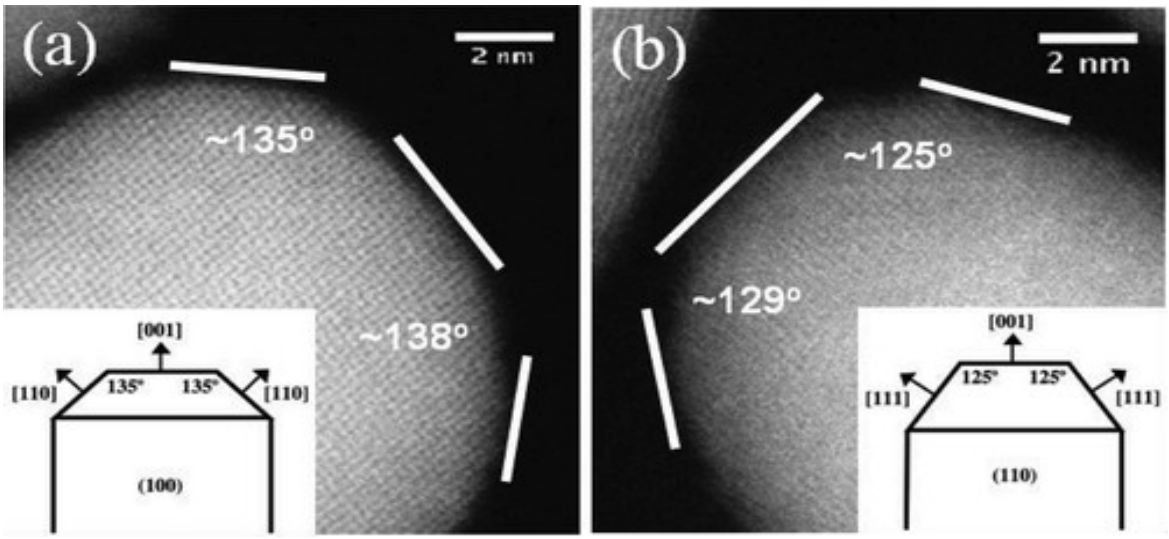

Figure 3.2 STEM-HAADF images of two Au nanorods: (a) the more-rounded end and (b) the less-rounded end.[63]

The structure of Au NRs is sensitive to several factors. In this work, the temperature of the growth solution was controlled at 25 °C. At temperatures lower than 25 °C, the formation of spherical-shaped particles occurs because the temperature is not high enough to induce a sufficient collision of Au seeds and the recrystallisation of CTAB at low temperature hinders the formation of a soft template to form rod-shaped particles. At temperatures higher than 25 °C, the aspect ratio of Au NRs decreases because the growth rate of the length is slower than the growth rate of the diameter. This suggests that the diameter growth is confined at low temperatures.[21] The concentration of ascorbic acid (AA) also has an effect on the structure of Au NRs. The molar ratio of AA:Au in the growth solution is 1.6:1 in this work. A high concentration of AA decreases the aspect ratio of Au NRs and increases the number of spherical-shaped particles formed.[23]

The nanorod solution was centrifuged in order to separate the Au NRs from the spherical-shaped particles and in order to stop the progress of the reaction. Centrifugation of the Au NRs solution also removes the CTAB excess before Rh deposition on Au NRs. Figure 3.3 compares STEM images of Au NRs:Rh of 10:1 ratio, for two situations, one in which Au NRs were centrifuged **once** to remove excess CTAB and one in which Au NRs were centrifuged **twice** to remove and wash CTAB on the Au NRs surface before Rh deposition. The deposition of Rh on Au NRs is clearly seen, with a contrast between the Au NRs core and the Rh outer layer consistent with the sequential reduction procedure.[46,65] This contrast arises from the difference between the atomic numbers of Au and Rh.[63] On the once-centrifuged Au NRs in Figure 3.3(a) and (b), a little Rh has deposited with uneven morphology on the Au NRs surface. Rh nanoislands can be observed on the rod-side and Rh overgrowth is mostly seen at rod-ends. The Rh deposited on twice-centrifuged Au NRs appears as a thicker and smoother Rh shell with less rounded ends, suggesting that CTAB removal increases the

collision frequency between Rh^{3+} and Au NRs surfaces, while without CTAB removal, Rh^{3+} forms micelles with CTAB, which slows the collision frequency.

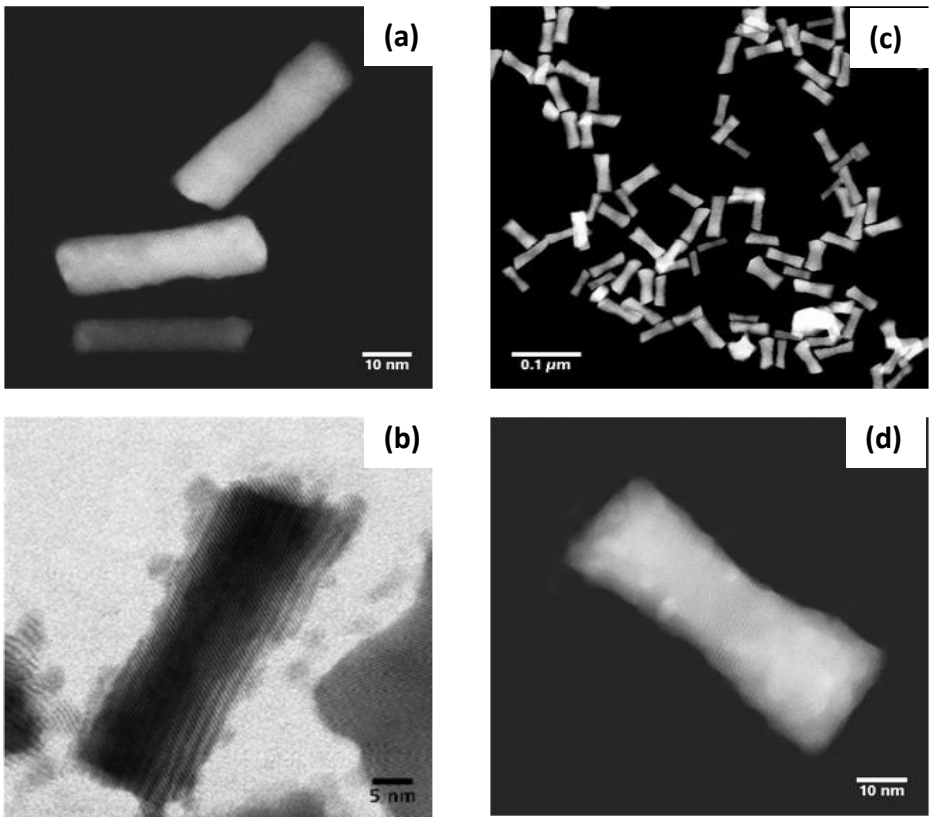

Figure 3.3 STEM-HAADF images of (a) once-centrifuged Au NRs:Rh 10:1 ratio and (b) bright field[63], STEM-HAADF images of (c) and (d) twice-centrifuged Au NRs:Rh 10:1 ratio.

After the Au NR solution has been centrifuged, it is possible that the presence of Ag^{+} ions has an effect on Rh deposition. Ag^{+} residues are observed on the once centrifuged Au NRs and to a lesser extent on the twice centrifuged Au NRs, as confirmed by EDX results in Figure 3.4.[63] This may explain the preferential growth of Rh on the ends of Au NRs in the presence of Ag^{+}, while Rh can cover the sides of the Au NRs surface in the absence of Ag^{+}. The surface energy of Au-Ag at the tip is lower than on the side.[34,63,66] Also, Ag^{+} stabilises the soft template of CTAB at the rod-sides,[18] which reduces the collision rate of Rh^{3+} on Au NRs, resulting in preferential coating of the ends. These results are consistent with those observed

for Pt deposition on Au NRs in the presence and absence of Ag^{+}.[34,66] It is noteworthy that Ag^{+} ions in bulk solution are not able to be reduced by ascorbic acid in acidic conditions.[67,68]

In this work, the Rh deposited on twice-centrifuged Au NRs have been chosen for further characterisation and electrochemical measurement because they displayed higher catalytic activity than the once-centrifuged Au NRs.

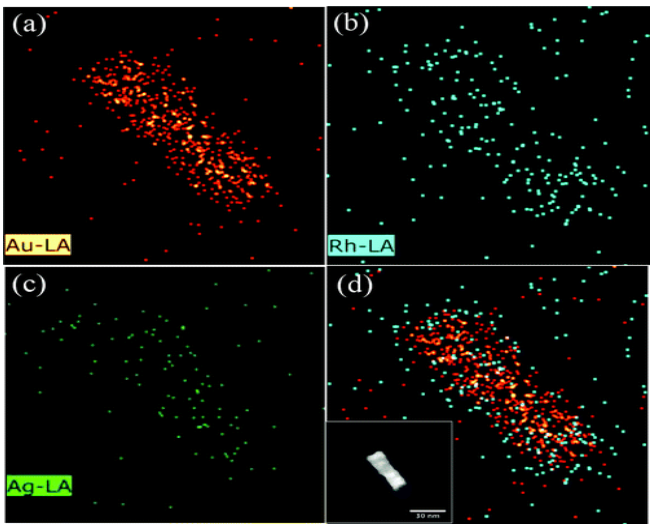

Figure 3.4 EDX maps of (a) Au, (b) Rh, and (c) Ag, with (d) an overlay of panels a and b, showing the relative locations of the Au and Rh signals, with corresponding STEM-HAADF image inset of once-centrifuged Au NRs.[63]

Figure 3.5 presents TEM images of Au−Rh NRs of 10:1, 7:3, 1:1 and 1:2 Au:Rh ratios. The successful deposition of Rh on Au NRs is visible from the surface roughness compared with the smooth surface of Au NRs. Rh deposition starts from the stage that Rh^{3+} ions are reduced by ascorbic acid on the Au NRs surface. At 10:1 ratio, Rh dispersed on the Au NRs and forms nanoislands. This 10:1 ratio have a dumbbell shape. The Au NRs are not completely coated by Rh. At 7:3 ratio, Rh starts to growth on Au NR surface and continue to overgrowth at 1:1 ratio. At 1:2 ratio, the Au NR surface is completely coated by Rh. Au NRs:Rh of 1:2 ratio appear to be more cylindrical with less rounded ends. The Rh overgrowth

on Au NRs increases with increasing Rh content. When Rh salt content increases, the collision frequency of Rh^{3+} with Au NRs surface increases, resulting in either overgrowth or complete overcoating with smooth coverage.[34]

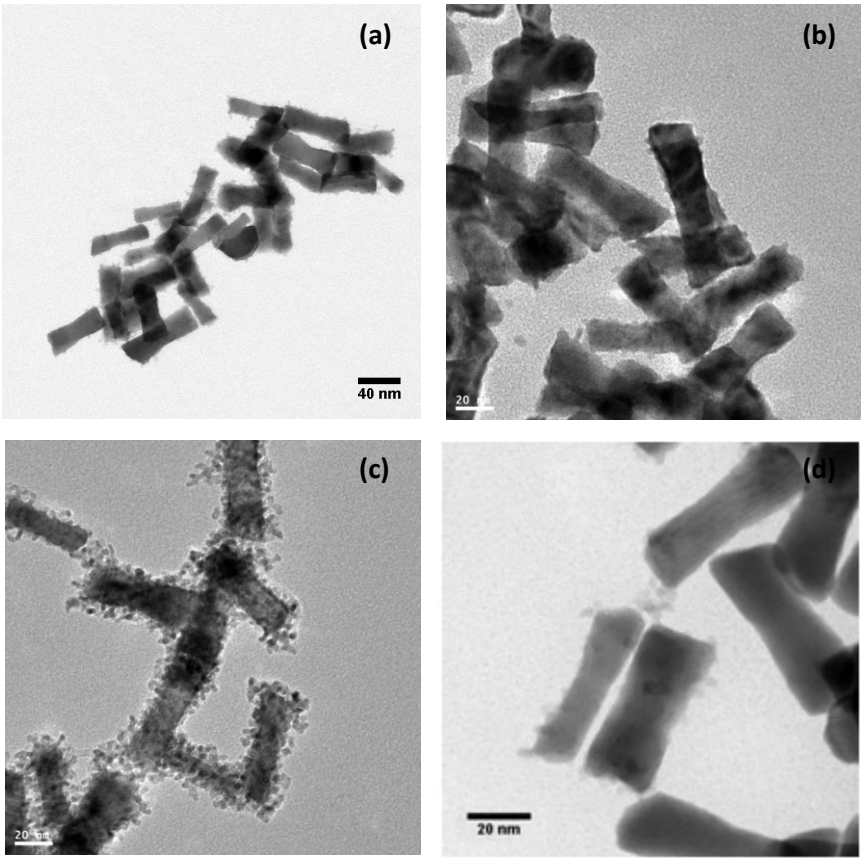

Figure 3.5 TEM images of Au NRs:Rh (a) 10:1, (b) 7:3, (c) 1:1 and (d) 1:2 ratios.
N.B. (a) and (d) were provided by Ruth Chantry, (b) and (c) were provided by Dr Zoe Schnepp.

There is preferential deposition of Rh on the tips compared to the sides because the different curvature on Au NRs presents faster potential decays and mass transport at rod-ends than rod-sides.[69] The uneven surface at the high content of Rh can be influenced by several factors. The different Rh growth rates depend on the atomic facets. The surface energy and cohesive energy of Rh are higher than those of Au, which causes a tendency for Rh to cluster on Au surfaces at room temperature in order to minimise their surface energy.[40] The key parameters of Au and Rh are compared in Table 3.1.

Table 3.1 Comparison of the key parameters of Au and Rh elements.[40,70]

	Au	Rh	Au *vs* Rh (%)
Atomic number	79	45	
Lattice spacing (nm)	0.288	0.269	7%
Surface energy (J/m^2)	1.626	2.828	-74%
Cohesive energy (eV/atom)	3.8	5.8	-53%

The miscibility of bimetallic particles has been taken into account in order to derive the possibility to combine the properties of two constituent metals and to control their properties. AuRh nanoparticles have been primarily studied by surface science techniques on systems formed *via* thermal evaporation.[71,72] Au and Rh are immiscible in the bulk under equilibrium conditions because of the large lattice mismatch between Au and Rh.[73-75] Kibler *et al.*, using scanning tunnelling microscopy, reported that Rh deposited on Au followed an island mode after initial formation of bilayers.[77] It was reported that AuRh systems on TiO_2, formed by sequential deposition of Rh and then Au, results in a $Rh_{core}Au_{shell}$ structure which is consistent with their relative surface energy.[72] In contrast, in our study, the $Au_{core}Rh_{shell}$ structure is able to be prepared by chemical synthesis. This difference may because of the effect of TiO_2 support and the temperature during Rh vapour deposition.[72] The $Au_{core}Rh_{shell}$ NRs are stable in solution stored in the dark and in ambient conditions.[63] There is no clear sign of degradation of these particles when kept for more than 1 year. The $Au_{core}Rh_{shell}$ NRs deposited on thin carbon films also retained their core-shell structure, even after annealing at 120 °C. These results demonstrate the long-term stability of $Au_{core}Rh_{shell}$ NRs.

The details of deposition and growth pattern were studied at the atomic level for the AuRh nanoparticles prepared in this work. Aberration-corrected scanning transmission

electron microscopy (AC-STEM), together with energy dispersive X-ray spectroscopy (EDX) can provide atomically resolved elemental and structural information. These results were provided by Ruth L. Chantry, School of Physics, University of Birmingham. Figure 3.6 shows HAADF and BF images of Au NRs:Rh of 10:1 ratio. Figure 3.6 (a) and (b) show a random of intensity variation through the interfacial region, indicated by arrows in Figure 3.6 (a). Figure 3.6 (c) presents the line intensity profiles of two regions in Figure 3.6 (a). The profiles taken over four atomic columns show a progressive change in intensity because of the averaging of random column to column. The randomness in imaging intensity apparent is typical of this RhAu NRs. This behaviour is different from that of PdAu NRs, whose line intensity profiles clearly change, suggesting phase segregation in this core-shell structure.[76] The randomness intensity of Rh Au NRs indicates a randomly mixed interfacial alloy layer in this $Au_{core}Rh_{shell}$ system. The mixed alloy layer, some 4–5 atomic layers thick between completely bulk immiscible Au and Rh, facilitates fully epitaxial overgrowth for the first few atomic layers of Rh. At the area where the Rh deposition is thicker, a smaller lattice spacing, similar to the Rh bulk value, is observed because of the extensive Rh outgrowth.[76]

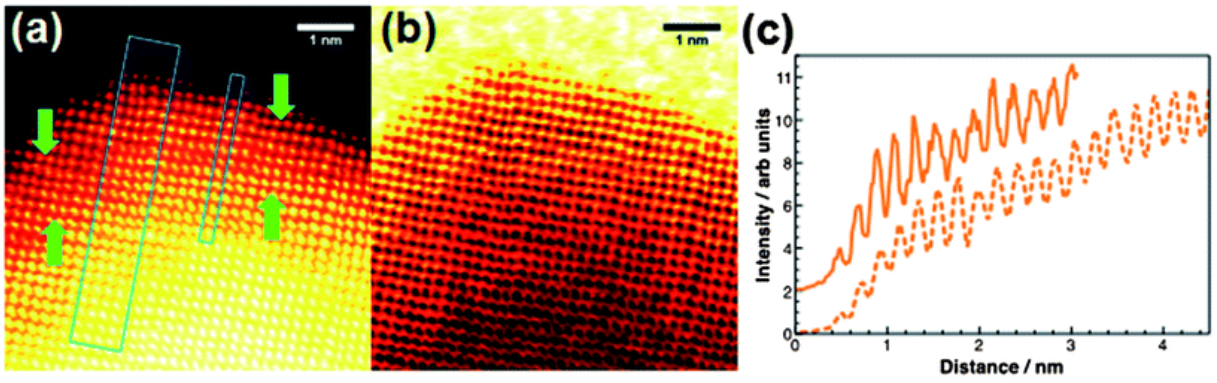

Figure 3.6 Simultaneously acquired (a) HAADF-STEM and (b) BF-STEM images of an $Au_{core}Rh_{shell}$ nanorod, with (c) line intensity profiles taken as indicated in (a) over a width 16 pixels, or one atomic column (solid line) and over 70 pixels, or approximately 4 atomic columns (dotted line).[76]

Molecular dynamics simulations were carried out to investigate the initial step of Rh growth on Au (111) and Au (100) surfaces at temperature between 300 K and 500 K. These simulations were performed by Dr Ivailo Itanasov, School of Chemistry, University of Birmingham. The simulations do not show a mixed AuRh interface in the initial stage of overgrowth. This may because the formation of Rh clusters is critical to the formation of a mixed interface. It was found that at the initial stage mobile Au atoms from the exposed Au regions of substrate can migrate to the surface of a Rh cluster. These can then be buried by further Rh deposition.

Figure 3.7 presents STEM-HAADF images of co-reduced Au:Rh particles of 10:1, 7:3, 1:1 and 1:2 ratios. The co-reduced particles were prepared by borohydride reduction at room temperature in aqueous solution containing metal salts and CTAB. The images show some small particles and a few much larger particles. The small particles have average size 3-5 nm and the EDX data indicate that they contain both Au and Rh with Rh-rich phase. The large particles, however, appear to contain only Au.

Figure 3.8(a) presents an EDX spectrum of a bare Au particle sample. The sharp peak at 2.16 keV arises from the signal of Au element. In Figure 3.8(b), only a Au signal can be detected for particles of Au:Rh of 10:1 ratio. Figure 3.8(c), (d) and (e) show the EDX spectra of Au:Rh of 7:3, 1:1 and 1:2 ratios, respectively. Signals of both Au and Rh are observed. The spectra show that the area containing agglomerated particles are Au and Rh particles; the signals show Au at 2.160 keV and Rh at 2.696 keV. The relative strength of the Rh:Au signals increases as Rh content in the synthesis increases. The signal of Na and Cl are from residual reagents in the synthesis. After addition of $NaBH_4$, it is likely that the nucleation of Au takes place first, followed by the formation of Rh, because the redox potential of Au is at more positive potential than that of Rh, as shown in Eq. (3.1) and (3.2).

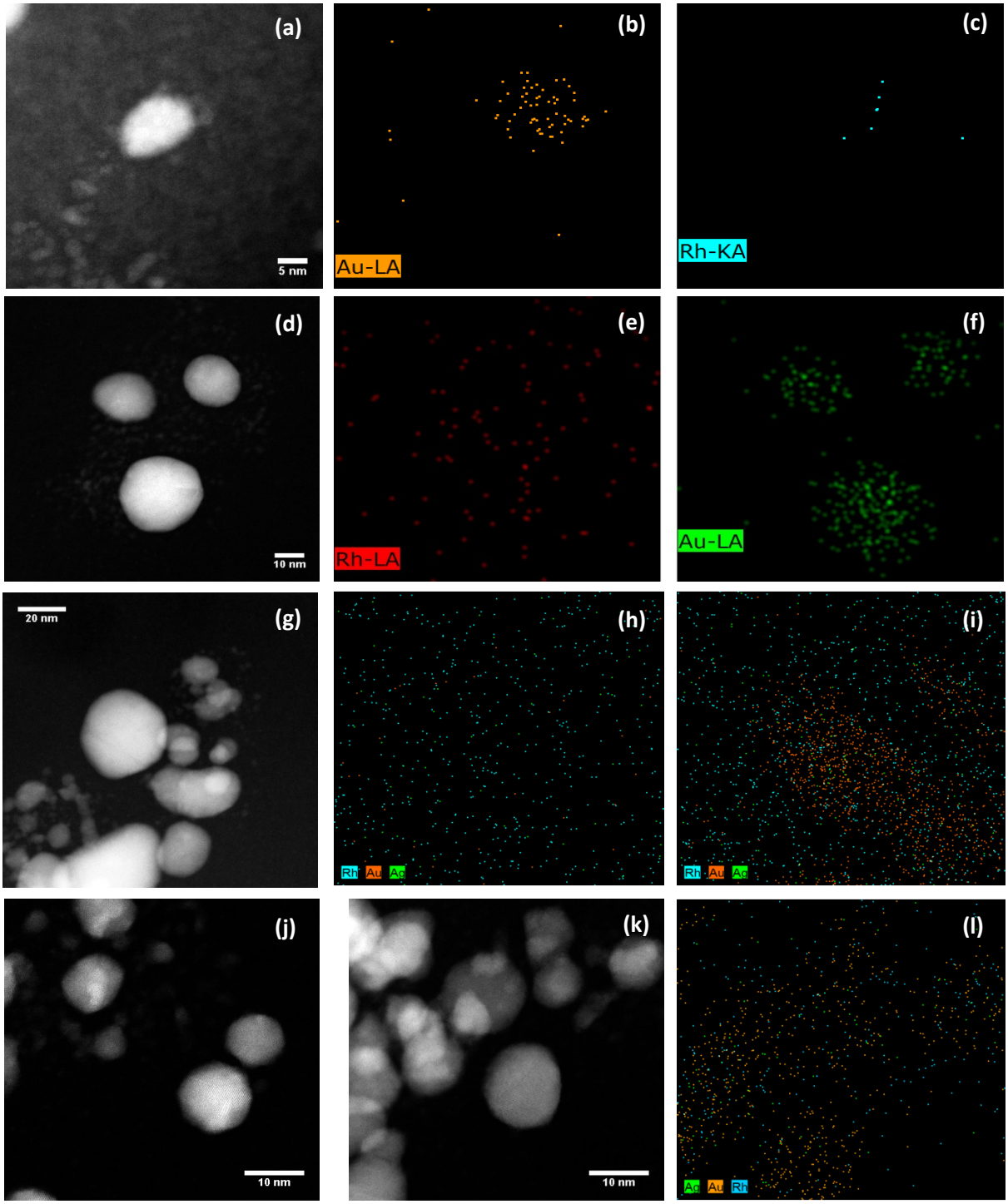

Figure 3.7 STEM-HDAAF images and EDX of co-reduced Au:Rh nanoparticles (a)-(c) 10:1, (d)-(f) 7:3, (g)-(i) 1:1 and (j)-(l) 1:2 ratios.

$$AuCl_4^- + 3e^- \leftrightarrow Au(s) + 4Cl^- \qquad E^0 = +1.002\ V \qquad (3.1)$$

$$RhCl_6^{3-} + 3e^- \leftrightarrow Rh(s) + 6Cl^- \qquad E^0 = +0.44\ V \qquad (3.2)$$

Au has a larger affinity to gain electrons, resulting the faster formation of Au seeds.[78] A Au-rich phase is formed and, on increasing Rh content, more Rh is diffused and incorporated into the particles to form Rh cluster on Au surface, as seen in the sample of Au:Rh 1:2 ratio.

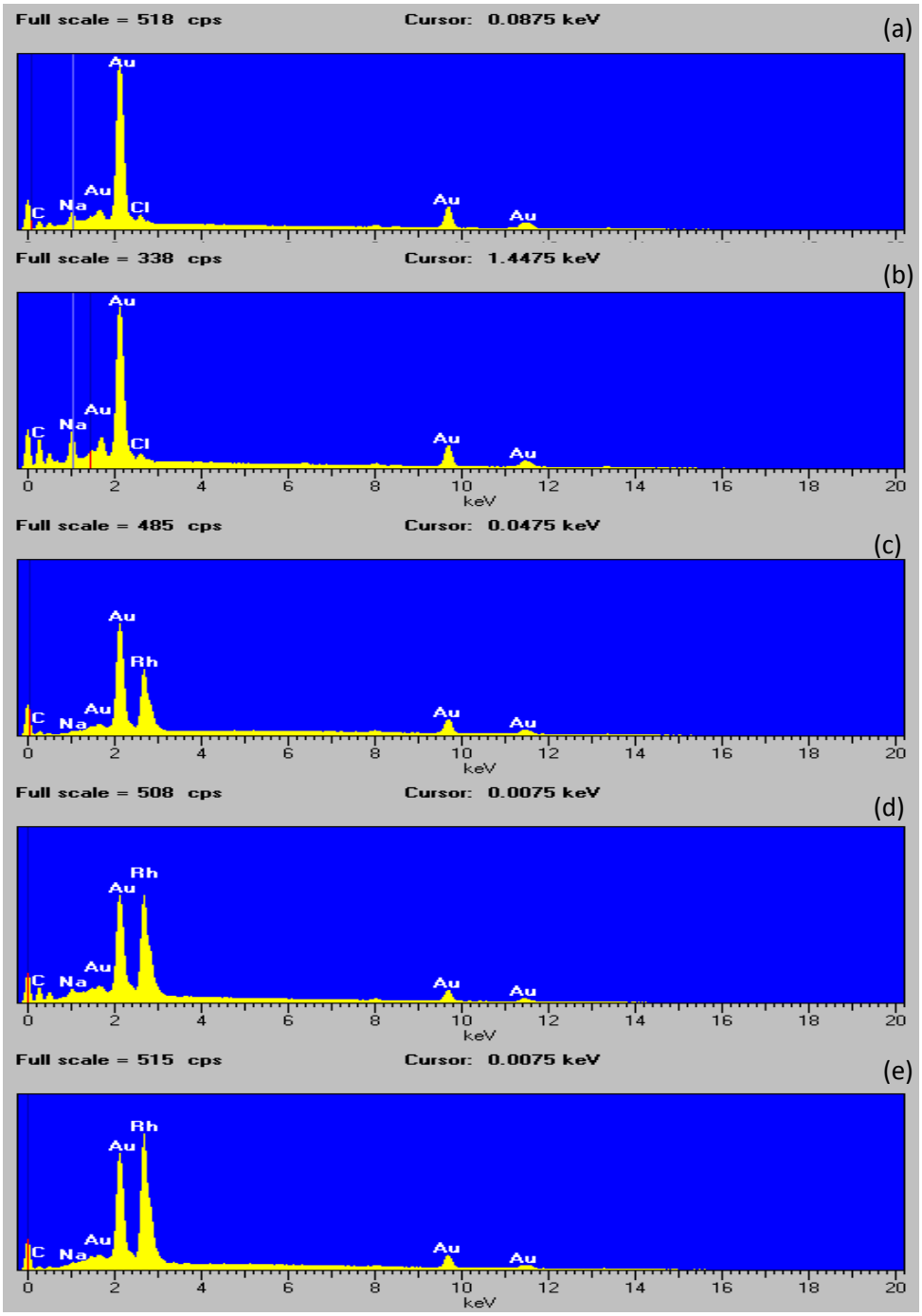

Figure 3.8 EDX spectra of (a) Au particles, co-reduced Au:Rh particles (b) 10:1, (c) 7:3, (d) 1:1 and (e) 1:2 ratios.

In the synthesis of sequentially reduced particles, Au seeds were reduced by borohydride, followed by the reduction of Rh by ascorbic acid. Figure 3.9 displays the STEM-HAADF images and EDX maps of sequentially reduced Au:Rh particles of 10:1 ratio. Most of the particles are small and a small proportion of the particles are large. The average diameter of the small particles is 3 nm and the average diameter of the larger particles is greater than 10 nm. The EDX signals in Figure 3.9(d) are very weak; however, they could suggest that the particles are mostly Au particles with a small number of Rh particles. It is possible that Rh particles are incorporated and diffused into Au surfaces.

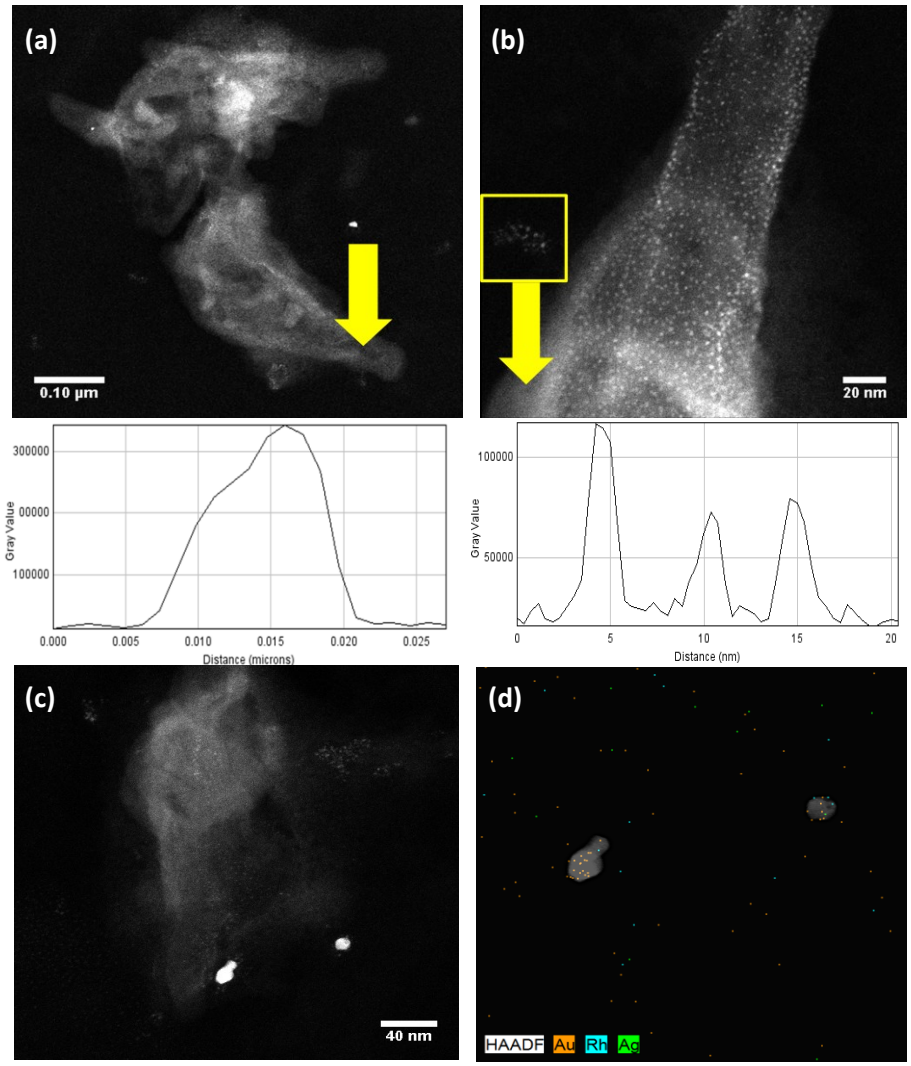

Figure 3.9 STEM-HAADF of sequentially reduced Au:Rh 10:1 nanoparticles with size distribution of (a) large particles, (b) small particles, (c) and (d) image and EDX map of this sample.

Figure 3.10 presents TEM images of sequentially reduced Au:Rh nanopaticles of 10:1, 7:3, 1:1 and 1:2 ratio. The atomically resolved imaging of Au:Rh of 7:3 ratio does not clearly indicate a core-shell structure but the uneven contrast of the particles indicate that they include both Au and Rh and that there is some degree of segregation. In the sample of Au:Rh of 1:2 ratio, the average size of the particles has a range of 10 – 15 nm, which is larger than those of the lower Au:Rh ratios. Some particles appear to be Rh clusters deposited on Au and some core-shell structures, although the Au seeds are not completely coated by Rh. A large degree of particle agglomeration has been observed.

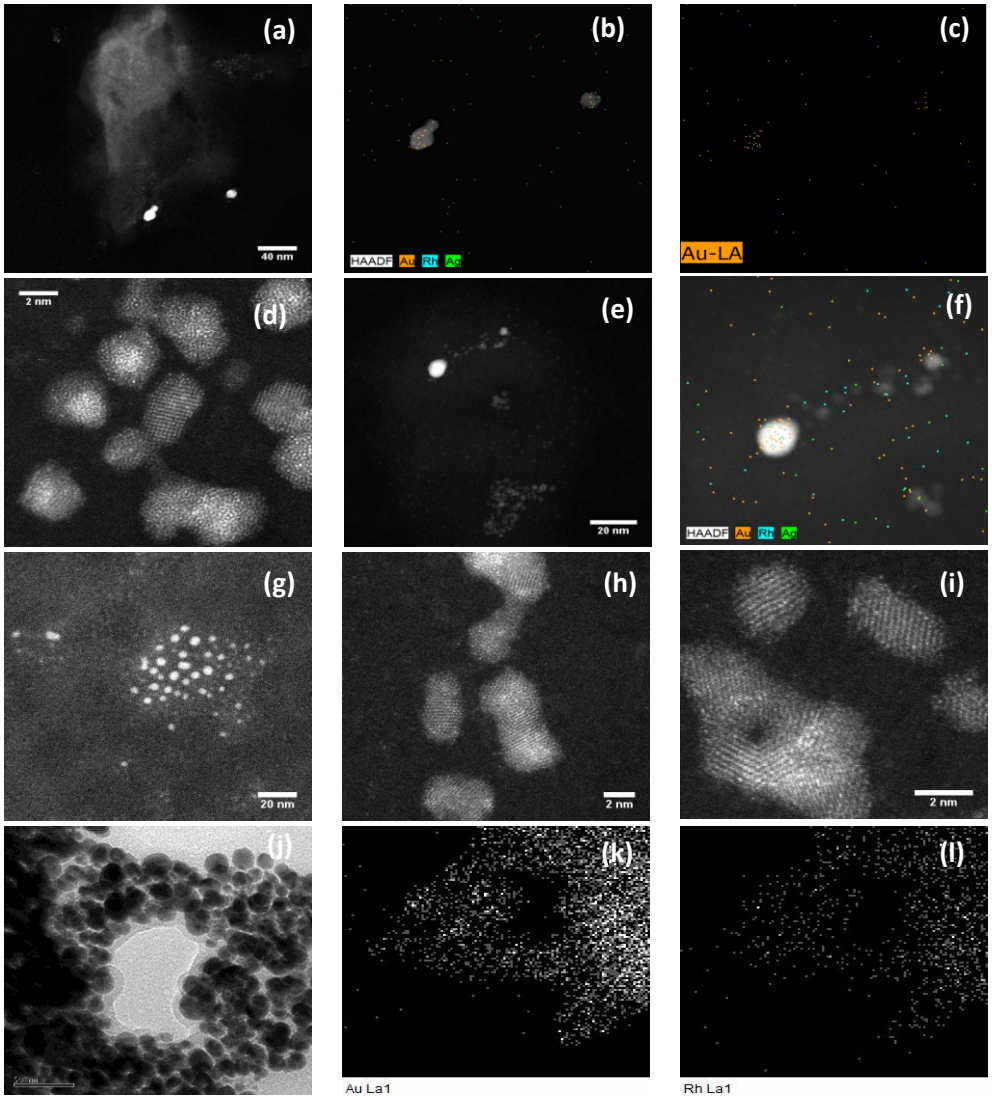

Figure 3.10 STEM-HDAAF images and EDX of sequentially reduced Au:Rh nanoparticles (a)-(c) 10:1, (d)-(f) 7:3, (g)-(i) 1:1 and (j)-(l) 1:2 ratios.

3.3.1.2 UV-visible spectroscopy

The surface plasmon resonance (SPR) of Au NRs is in the visible and near-infrared (vis-NIR) part of the spectrum. Most metals display a SPR absorbance in the ultraviolet (UV). The UV-visible absorption spectrum of Au NRs is presented in Figure 3.11. Au NRs show 2 absorption peaks at 793 nm and 520 nm, corresponding to the longitudinal surface plasmon resonance (LSPR) and the transverse surface plasmon resonance (TSPR), respectively.[19,22] The LSPR of Au NRs embedded in a dielectic medium is more sensitive to the change of aspect ratio (length/width) than the TSPR because the longitudinal peak displays a blue shift (lower wavelength shift) or a red shift (higher wavelength shift), which is not typically seen in the TSPR.[64,69,79] The increase of the Au NRs aspect ratio leads to a red shift of the LSPR.[23,80] The TSPR is related to the width of Au NRs.

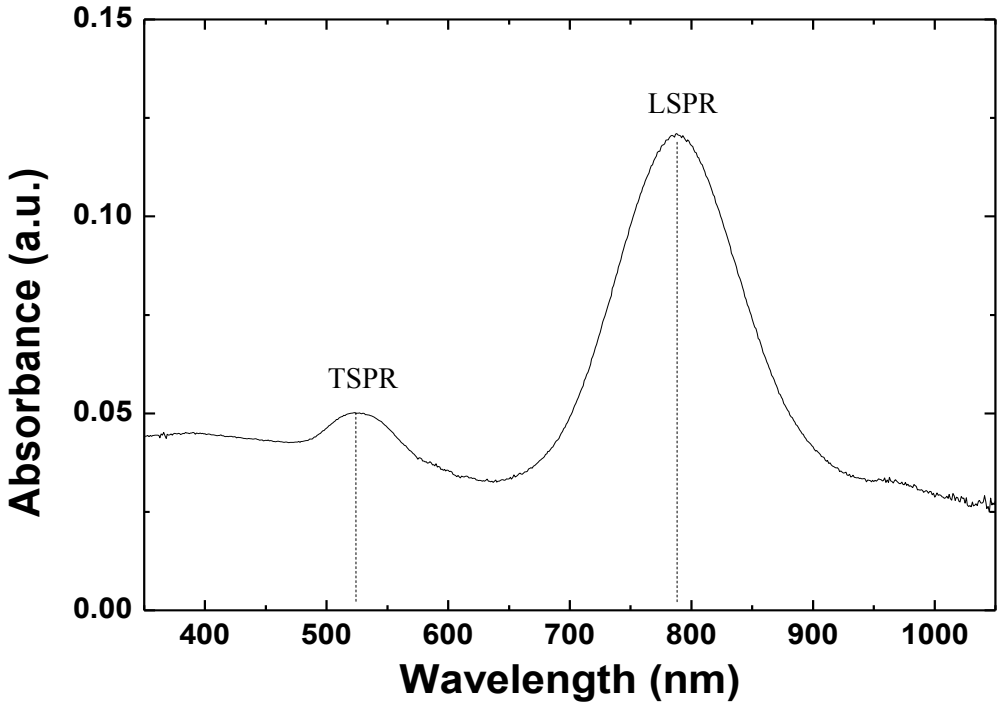

Figure 3.11 UV-visible absorption spectrum of Au NRs presented in Figure 3.1.

The colour of colloidal Au NRs is likely to be size- and shape- dependent; however, the change of absorption spectra cannot be detected by the human eye when the LSPR is

above 700 nm (aspect ratio ~3).[23] It has been reported that the absorption of Au NRs in the visible region of the spectrum is quite sensitive to by-products.[23,80] When there is a large quantity of spherical particles, an additional adsorption peak will appear between 500-600 nm.[81,82]

It is known that the deposition of foreign metals on Au NRs results in a change of optical properties. The SPR of Rh nanoparticles is not in the visible range. Figure 3.12 and 3.13 present the UV-visible absorption spectra of Rh deposited on once-centrifuged Au NRs and on twice-centrifuged Au NRs, respectively. In both cases, the TSPR of Au NRs does not display a red shift; however, the intensity of the TSPR slightly decreases with increasing Rh content. The LSPR of Rh deposited on twice-centrifuged Au NRs is strongly attenuated and has a larger red shift compared with that measured for once-centrifuged Au NRs. This effect begins at lower Rh content for the twice-centrifuged NRs.

Focusing on Rh deposited on twice-centrifuged Au NRs, the Au NRs:Rh 10:1 sample displays a large reduction of LSPR, with a concomitant broadening. At the higher molar ratios of Au NRs:Rh, the LSPR is slightly decreased until it is only weakly observed for Au−Rh NRs of 1:2 Au:Rh ratio. On increasing Rh content, the peak position of the LSPR is gradually shifted to higher wavelength. The tendency of Rh to deposit preferentially on the ends of NRs increases the aspect ratio, which leads to the red shift in the LSPR observed in Figure 3.12.[34,44,63] These results are consistent with our previous report of Rh overgrowth on once-centrifuged Au NRs.[63] The experimental and simulation results presented in that report agree well, demonstrating that the trend in red shift can be attributed to increase of aspect ratio of Au NRs on increasing the amount of Rh. It has also been shown recently that coating an entire Au rod with Pt results in almost complete quenching of both TSPR and LSPR.[83] Rh and Pt have similar absorption behaviour in this wavelength range and so it can be inferred that the

quenching observed in Figure 3.13 for the sample of Au:Rh 1:2 ratio is a consequence of the close to complete coverage of the Au NR, in agreement with the STEM data.

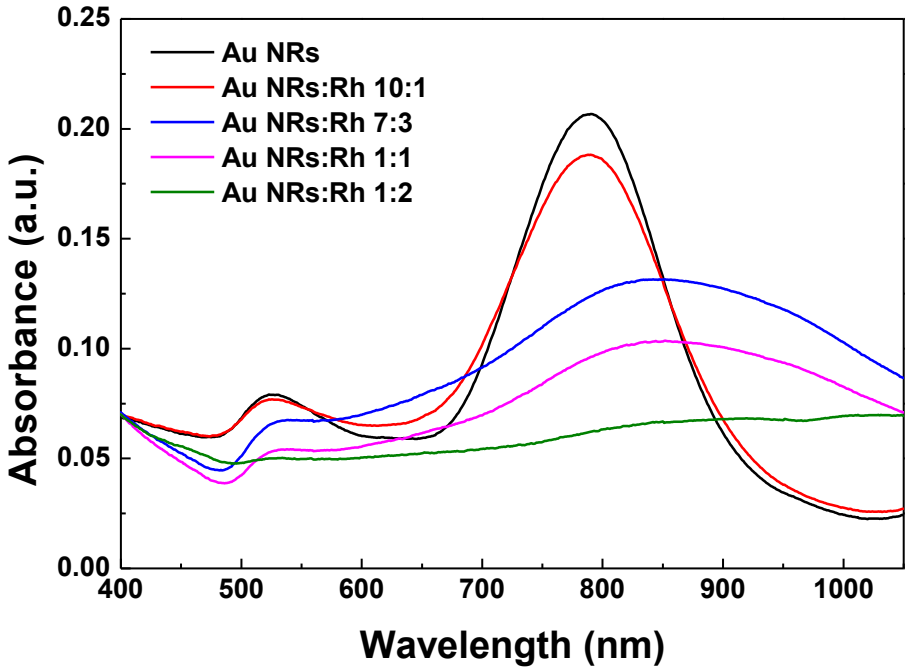

Figure 3.12 UV-visible absorption spectra of once-centrifuged Au NRs and Au NRs:Rh 10:1,7:3, 1:1 and 1:2 ratios.

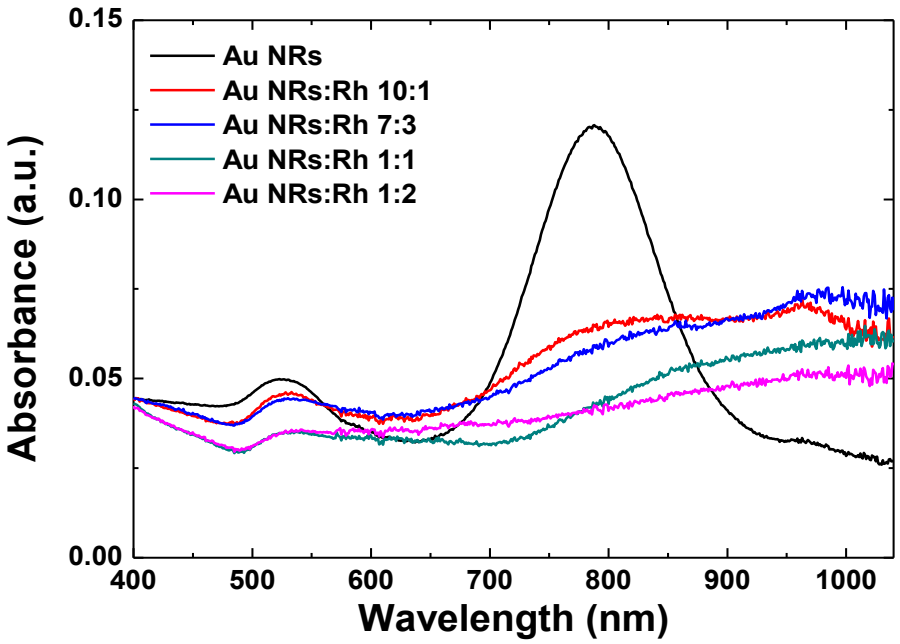

Figure 3.13 UV-visible absorption spectra of twice-centrifuged Au NRs and Au NRs:Rh 10:1,7:3, 1:1 and 1:2 ratios.

Returning to the comparison between once-centrifuged and twice-centrifuged Au NRs, it is possible to use similar arguments to rationalise the different in optical properties. The more even deposition of Rh on twice-centrifuged particles, as seen in STEM images, would at first red shift and broaden the LSPR at low Rh content and then quench it at high Rh content.

The light-scattered colour and the optical properties of nanoparticles are shape- and size-dependent.[84,85] In the present work, the colour of Au nanoparticles in aqueous CTAB solution is ruby red. The wavelength of absorption of spherical Au nanoparticles can appear over a wide range of the visible spectrum, depending on the particles size.[86] Spherical Au nanoparticles (Au NPs) of size 3-5 nm display a single SPR at 535 nm,[78,87] as shown in Figure 3.14.

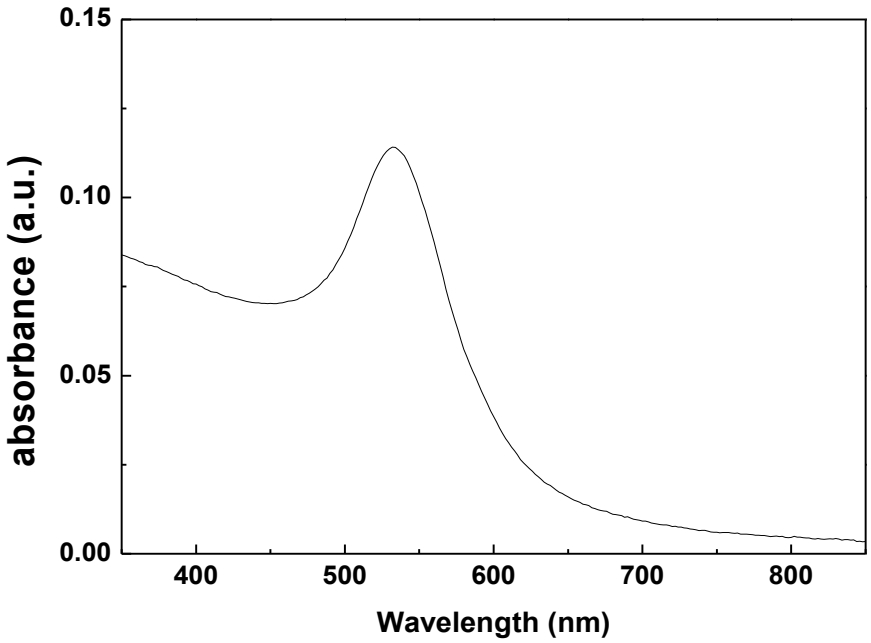

Figure 3.14 UV-visible absorption spectrum of aqueous Au nanoparticles.

The formation of Rh supported on Au also influences the Au SPR. Figure 3.15 presents the absorption spectra of co-reduced Au:Rh nanoparticles. The intensity of the peak arising from Au NPs is decreased from a Au:Rh ratio of 10:1 until 1:2 Au:Rh. Although the

peak is still present for the sample of higher Rh content it is strongly attenuated, which indicating some quenching of the SPR. This observation can be explained by the presence of both Au and Rh in the NPs (dispersed particles or Rh-rich surface of the NPs) of this sample. A red shift is not observed when increasing Rh content, which suggest that most particles are in the form of separated Au and Rh particles in the other samples. This observation is consistent with the STEM results, in which only the highest ratio of Au:Rh appeared to contain particles with a partial core-shell formation.

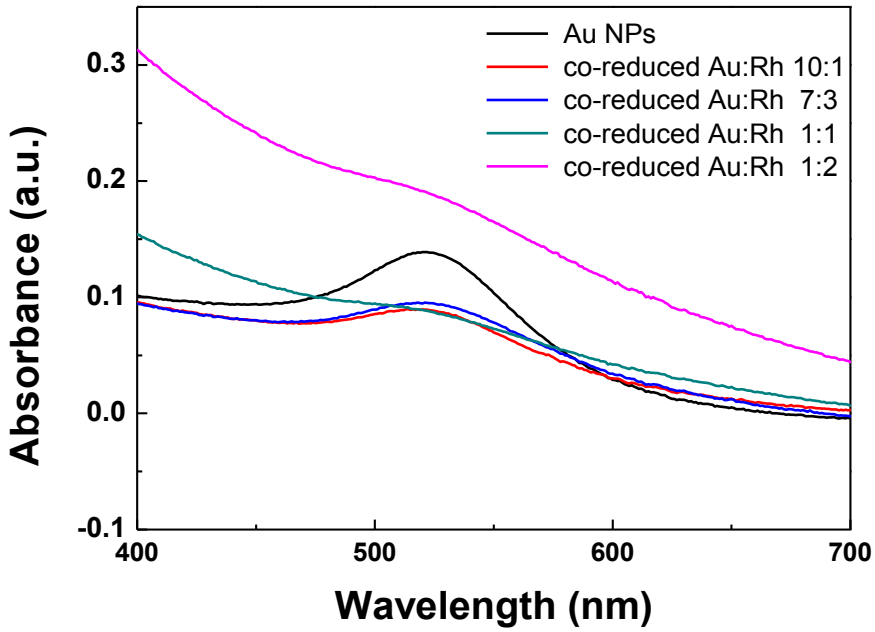

Figure 3.15 UV-visible absorption spectra of Au NPs and co-reduced Au:Rh nanoparticles of 10:1,7:3, 1:1 and 1:2 ratios.

In the spectra acquired for sequentially reduced Au:Rh particles in Figure 3.16, the plasmon band of Au is red shifted and broadened on increasing Rh content of the particles. The red shift may result from either the formation of alloy and core-shell structure or from an increase of Au−Rh particle size. The presence of Au is still observed at the highest ratio of Au:Rh, indicating that some of the Au particles are not completely coated by Rh to form a

core-shell structure. These results are in good agreement with the STEM results of these sequentially reduced nanoparticles.

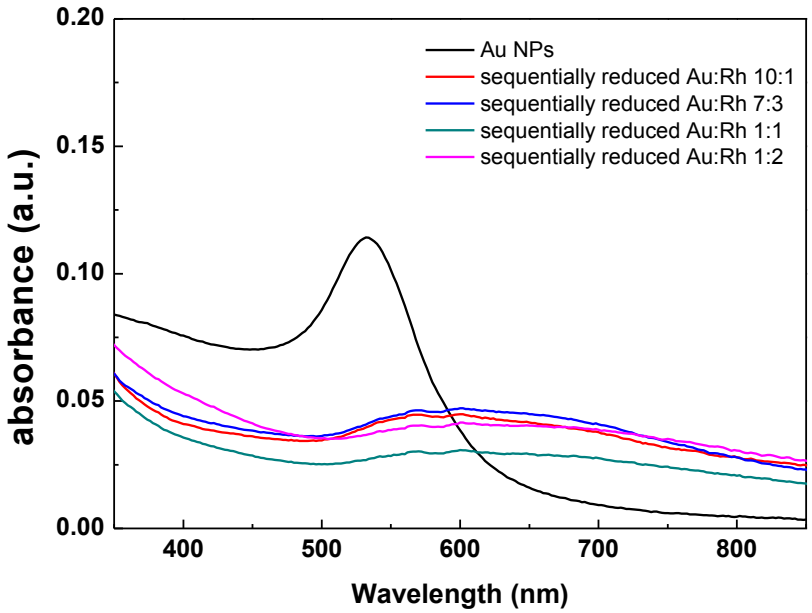

Figure 3.16 UV-visible absorption spectra of Au NPs and sequentially reduced Au:Rh nanoparticles of 10:1,7:3, 1:1 and 1:2 ratios.

3.3.1.3 X-ray photoelectron spectroscopy (XPS)

XPS was used to determine the prsence of Au and Rh on the surface. The XPS survey spectra of Au NRs along with AuRh NRs samples are presented in Figure 3.17. The survey-scan showed signals from Au 4f, Rh 3d, C 1s and O 1s. The C 1s peaks result from the residues of surfactant molecules and from the atmosphere in the chamber. The small peak at 183.4 eV arises from the Si substrate. Au NRs show a strong spin-doublet at 83.8 eV ($Au4f_{7/2}$) and 87.5 eV ($Au\ 4f_{5/2}$), which can be assigned to metallic Au.[44,87] In addition, a Au 3d signal is also visible at higher binding energy.

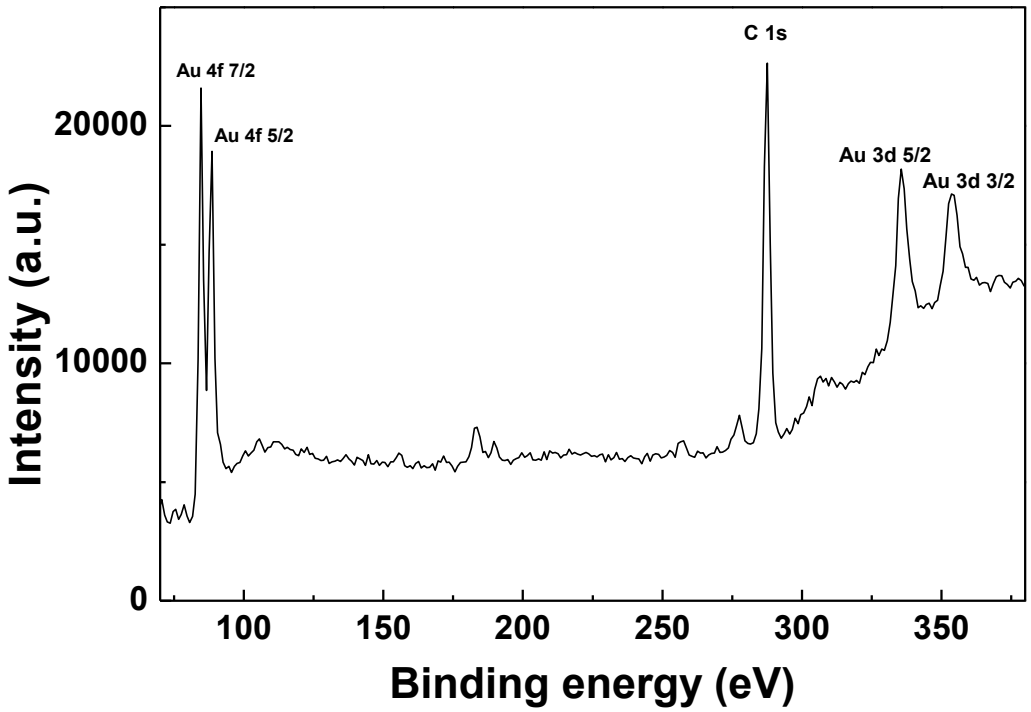

Figure 3.17 XPS spectra of Au NRs on Si substrate.

Figure 3.18 shows the XPS spectra of AuRh NRs of Au 4f, Au 3d, Rh 3d and C 1s. The signals at 307 and 312 eV verify the existence of metallic Rh.[88-90] At a Au:Rh ratio of 10:1, Au spectra and Rh spectra are weakly detected. Au spectra are barely visible and Rh spectra are noticeable on Au NRs:Rh of 7:3 and the higher ratios. The intensity of the signals corresponding to Rh nanoparticles is similar to that of Au NRs:Rh of 1:1 ratio, which has an equal Rh content. The intensities of Au 4f and Au 3d significantly decrease on increasing Rh concentration, indicating the successful deposition of Rh onto the surface of Au NRs. Also the decrease of Au signal on increasing Rh may be according to the diffusion of Rh into the Au surface. These XPS results suggest that Rh surface area increases at the expense of the Au surface area as Rh concentration is increased during the reaction. This observation is consistent with the deposition of Rh on Au inferred from the UV-visible spectra and STEM images.

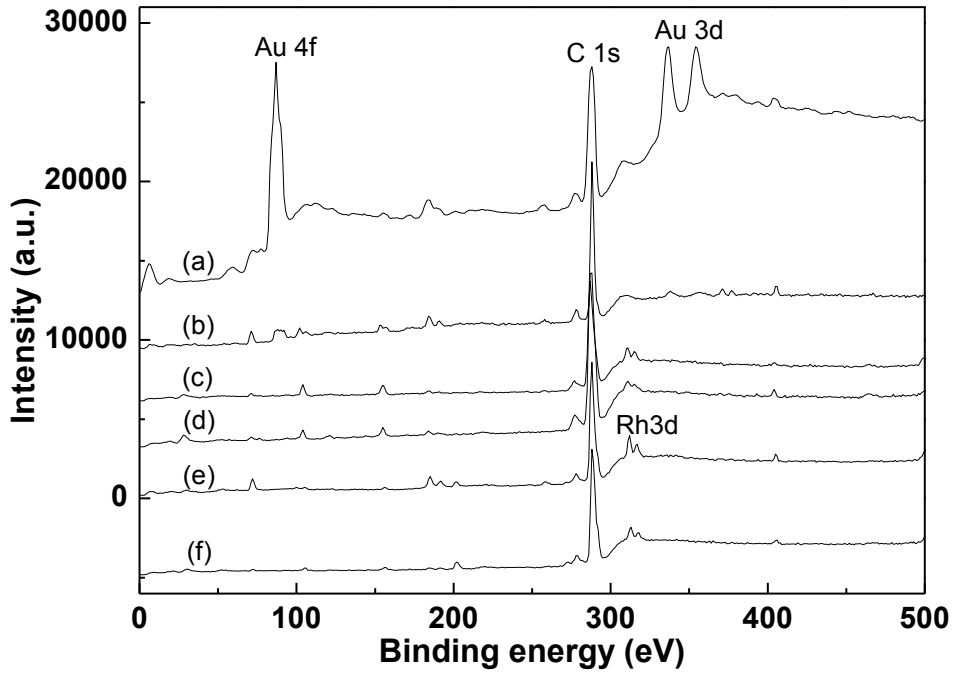

Figure 3.18 XPS spectra of (a) Au NRs, (b) Au NRs:Rh 10:1, (c)7:3, (d) 1:1, (e) 1:2 and (f) Rh nanoparticles.

Figure 3.19 displays the Rh3d features of Au NRs:Rh with different Au:Rh ratios. The data show that the binding energy of Rh3d signals shift to lower binding energy with decreasing Rh content. A chemical shift arises from the change in chemical bonding of elements and electron transfer between elements. The Pauling electronegativities of Au and Rh are 2.54 and 2.28, respectively, indicating that a slight electron transfer should occur from Rh to Au. According to the peak shift to lower binding energy; however, it seems that Rh is an electron acceptor and Au is an electron donor.[91] This may caused by the environment of the particle and the nature of the support. A similar effect, where Rh 3d shifted to lower binding energy, was found by Rasko *et al.*, when Rh was introduced onto a Au surface, which was supported on TiO_2.[92] Possibly the Si substrate has an influence on the binding energy observed in the present study.[92] The chemical shift may also be due to the alloy formation. The Rh3d signal of

Au NRs:Rh 1:2 is similar to position that of Rh particles, as a result of Rh enrichment on Au surface at high Rh content.

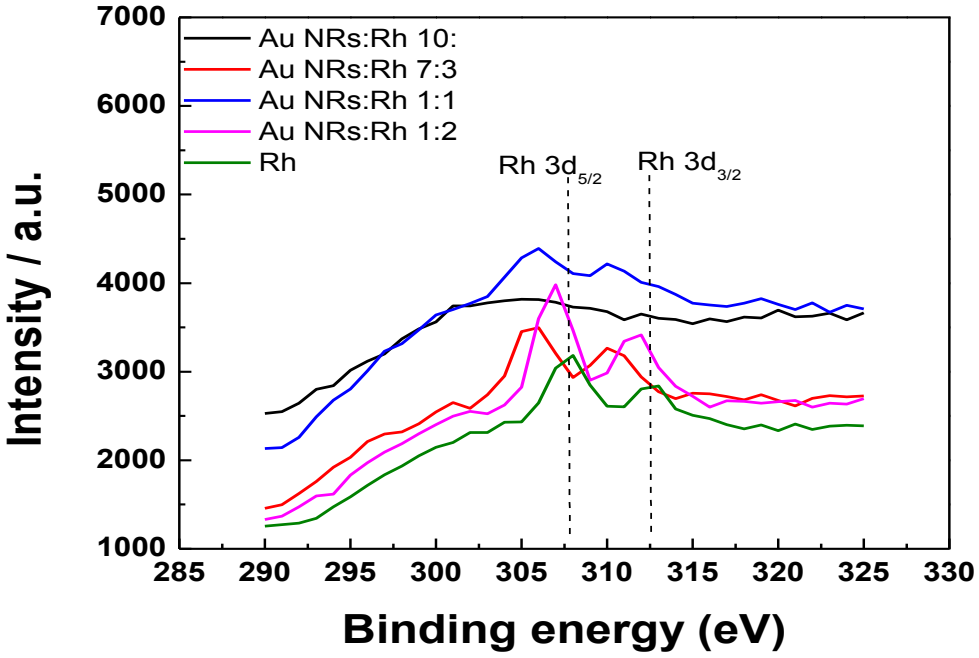

Figure 3.19 The Rh3d features of Au NRs:Rh at different Au:Rh ratios.

3.3.2 Electrochemical characterisation of Au NRs:Rh and Au:Rh nanoparticles

The catalyst suspensions were prepared by the procedure described in section 3.2. It should be noted that the current in this work was normalised by the geometric surface area of the electrode not the real surface area, and the potential is reported *vs* SCE.

3.3.2.1 Cyclic voltammetry

Figure 3.20 compares cyclic voltammograms (CVs) of a polycrystalline Au electrode, Au NRs/C and Au NPs/C electrodes. The CV of the polycrystalline Au electrode has two anodic peaks at > 1.1 V, corresponding to the formation of Au oxide. The cathodic peak at 0.85 V arises from the reduction of Au oxide.[5] Peaks relating to hydrogen adsorption/desorption are not detectable because hydrogen adsorbs too weakly on Au. The

CVs of Au NRs/C and Au/C nanoparticles are different from that of the polycrystalline Au electrode because there is a large capacitance from the carbon support. A pair of redox peaks centred at 0.3 V can be attributed to quinoidal groups on carbon surfaces.[6] Au oxide formation and Au oxide reduction peaks are also present for Au NRs/C and Au/C nanoparticles. The Au oxide reduction peaks of Au NRs/C and Au/C nanoparticles are slightly shifted to more negative potentials compared with that observed for the bulk Au electrode. The Au oxide formation and Au oxide reduction peaks of Au/C nanoparticles are larger than those of Au NRs/C because the surface area of the smaller nanoparticles is greater than that of the larger nanorods at the same loading. It is noticeable that the peaks of quinoidal groups in Au/C particles are smaller than those of Au NRs/C, suggesting that the Au nanoparticles are well distributed and deposited on most of the carbon surface.

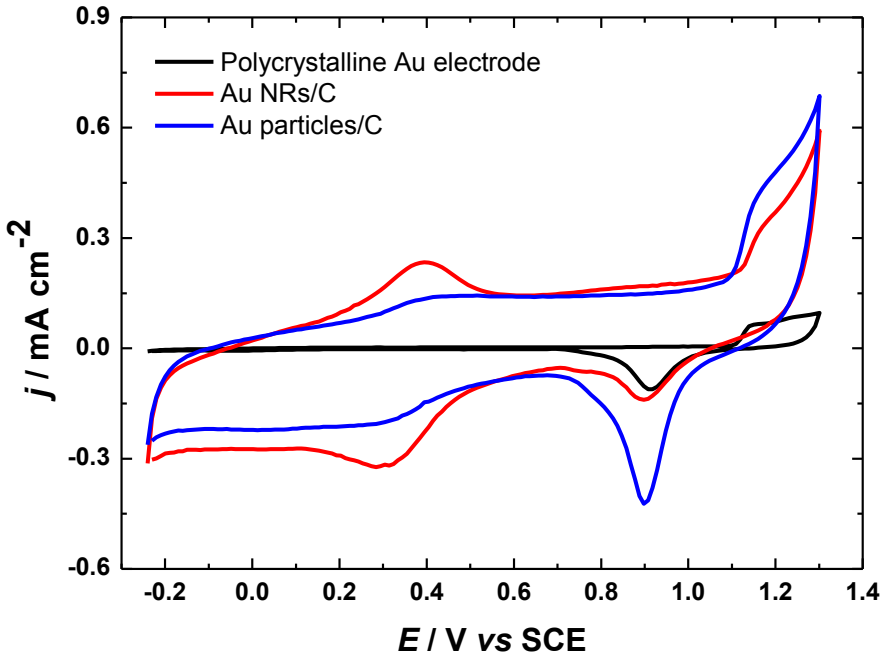

Figure 3.20 Cyclic voltammograms of polycrystalline Au electrode, Au NRs/C and Au NPs/C electrodes in Ar-saturated 0.5 M H_2SO_4. Scan rate 0.05 V s^{-1}.

Figure 3.21 presents an assignment of the features in the CV of Rh/C nanoparticles in Ar-saturated 0.5 M H_2SO_4. On the anodic scan, the hydrogen desorption peak (A) is observed at negative potentials and Rh oxide formation (C and D) occurs at positive potentials. The double layer region (B) is between hydrogen desorption and surface oxide formation. On the cathodic scan, Rh oxide reduction (E) and hydrogen adsorption (F) are shown without the presence of double layer region between.[59-62] The peaks corresponding to the redox of quinoidal species are close to the onset of Rh oxide reduction. In this Rh/C sample, the quinoidal peaks are weak because Rh is well dispersed on the carbon support. The CV features of Rh have some similarity to those of a polycrystalline Pt electrode.[93] The only difference is the smaller double-layer region, especially in the cathodic scan, because of the overlap between hydrogen desorption and Rh oxide reduction.[57,94,95] The large separation between Rh oxide formation (D) and Rh oxide reduction indicates irreversible oxide formation.[61]

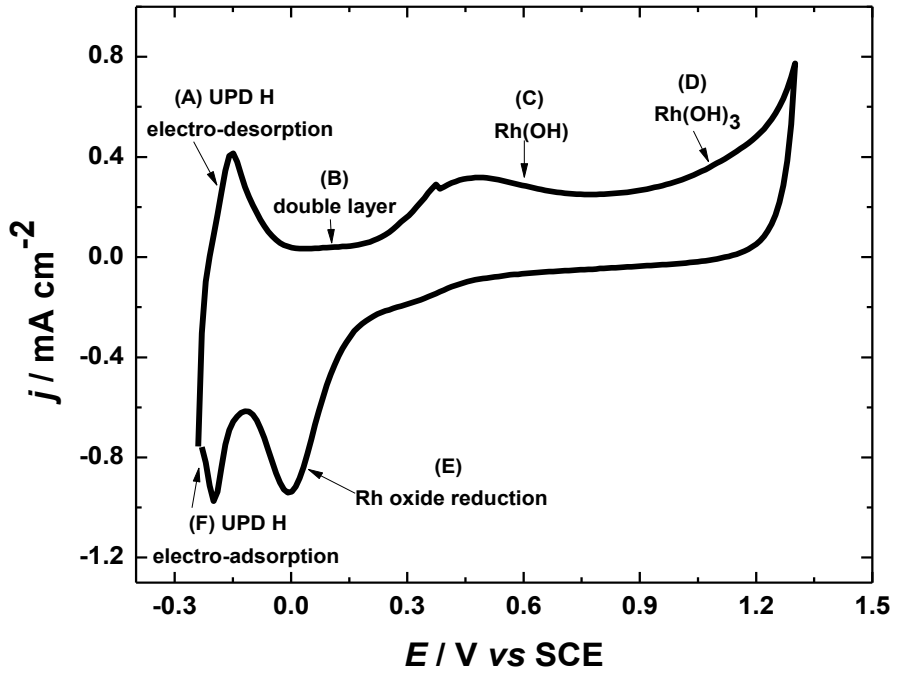

Figure 3.21 Cyclic voltammogram of Rh/C nanoparticles in Ar-saturated 0.5 M H_2SO_4. Scan rate 0.05 V s^{-1}.

The overlap of the Rh oxide electroreduction process and the initial stage of the H electroadsorption reaction typically occur when the upper potential limit is increased because the irreversibility of the oxide formation is extensively enhanced.[57,96,97] The hydrogen evolution starts at potentials negative of 0.1 V (*vs* RHE). The (A) and (F) regions in Figure 3.21 are nearly at the same potential, suggesting reversibility of hydrogen adsorption/desorption. The reversibility occurs since the sulphate adsorption is rapidly decreases from 0.25 V (*vs* RHE) to 0 V (*vs* RHE), thus hydrogen can be adsorbed on the Rh surface.[58,96]

The oxide formation of Rh is related to the electrochemisorption of OH.[60] The oxidation of bulk Rh in 0.5 M H_2SO_4 occurs in the potential range between 0.55 V (*vs* RHE) and 1.40 V, forming Rh(OH) and $Rh(OH)_3$, respectively. The reduction of RhO(OH) is not detectable, suggesting that RhO(OH) is hardly formed at potentials positive of that where $Rh(OH)_3$ is formed. The reactions corresponding to the oxidation and reduction processes are as follows:[60]

Formation

$$Rh + H_2O \rightarrow Rh(OH) + H^+ + e^- \qquad 0.55 - 0.95 \text{ V (}vs\text{ RHE)} \qquad (3.3)$$

$$Rh(OH) + 2H_2O \rightarrow Rh(OH)_3 + 2H^+ + 2e^- \qquad 0.94 - 1.40 \text{ V (}vs\text{ RHE)} \qquad (3.4)$$

$$2Rh(OH)_3 + Rh \rightarrow 3RhO(OH) + 3H^+ + 3e^- \qquad > 1.40 \text{ V (}vs\text{ RHE)} \qquad (3.5)$$

Reduction

$$3RhO(OH) + 3H^+ + 3e^- \rightarrow 2Rh(OH)_3 + Rh \qquad (3.6)$$

$$Rh(OH)_3 + 3H^+ + 3e^- \rightarrow Rh + 3H_2O \qquad (3.7)$$

The reaction schemes show that there are three sequential stages for Rh oxide formation and two stages for reduction. Rh in the anodic scan preferentially forms oxide species in the +3 oxidation state.[59,60] The reaction scheme of Rh is different from that of the

polycrystalline Pt electrode, which forms two different oxidation states differing in their hydration.[59,98,99] Also, there are two hydrogen desorption peaks on the polycrystalline Pt electrode but there is only one hydrogen desorption peak on the Rh electrode. A typical CV of a Pt polycrystalline electrode is shown in Figure 3.22.

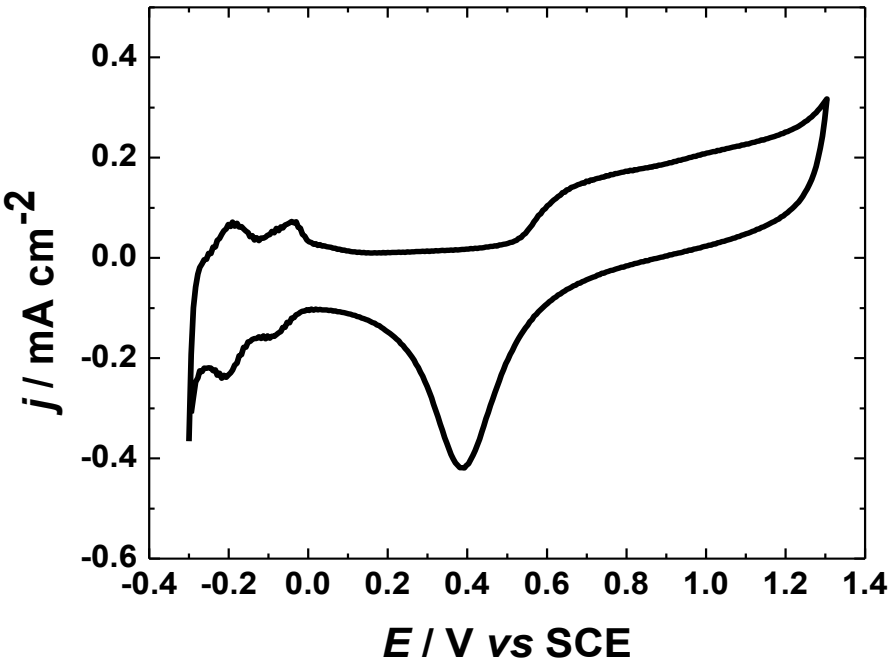

Figure 3.22 Cyclic voltammogram of polycrystalline Pt electrode in Ar-saturated 0.5 M H_2SO_4. Scan rate 0.05 mV s^{-1}.

Cyclic voltammetry (CV) has been used to investigate the surface electrochemical properties of Au NRs:Rh/C and Au:Rh/C nanoparticle electrodes. Figures 3.23 and 3.24 compare CVs of Au NRs/C and Au NRs:Rh/C electrodes in Ar-saturated 0.5 M H_2SO_4 at high and low upper potential limit, respectively. The oxide formation and reduction peaks of Au and Rh are distinguishable. The peaks of quinoidal groups are slightly suppressed with increasing Rh content on Au NRs. The Au oxide formation and Au oxide reduction peaks decrease in size with increasing Rh content of the catalyst. These peaks are still visible for the Au NRs:Rh of 10:1, 7:3 and 1:1 ratios but not for the 1:2 ratio. The Rh oxide formation peak, located at 0.5 V, is not visible for Au NRs:Rh of 10:1 and 7:3 ratios but it is clearly observed

for Au NRs:Rh of 1:1 and 1:2 ratios. The Rh oxide reduction peak at 0.03 V is also only observed for Au NRs:Rh of 1:1 and 1:2 ratios. The hydrogen adsorption/desorption current of the under potentially deposited hydrogen (H_{UPD}) (shown also in Figure 3.24) is just discernible for 10:1 and 7:3 ratios and significantly increased for 1:1 and 1:2 ratios.

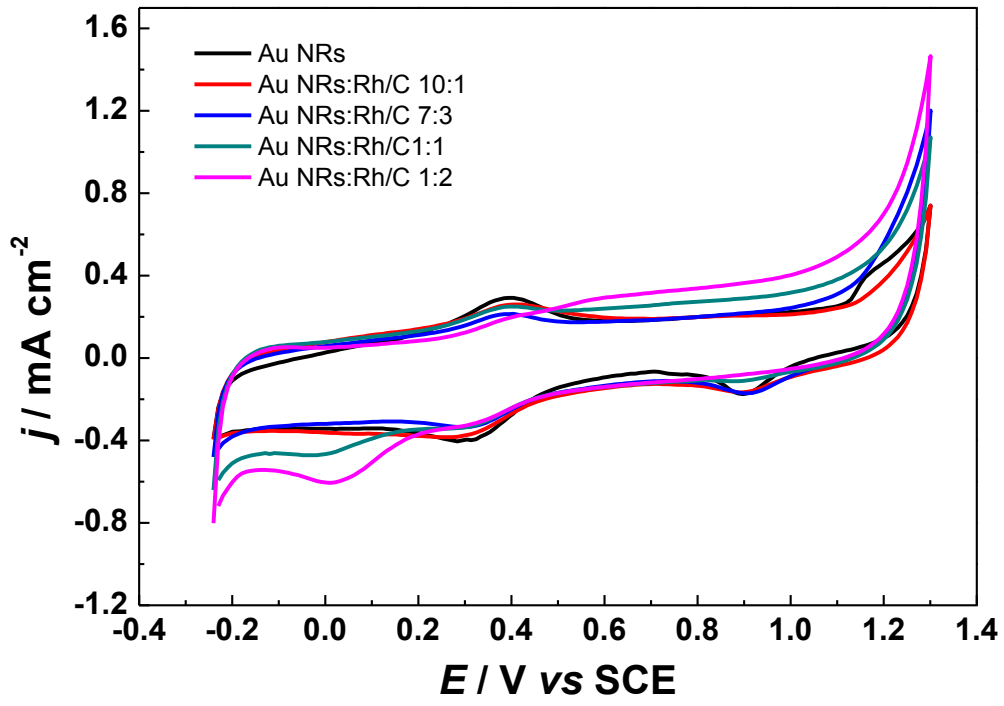

Figure 3.23 Cyclic voltammograms of Au NRs/C and Au NRs:Rh/C in Ar-saturated 0.5 M H_2SO_4. Scan rate 0.05 V s^{-1}.

The absence of Rh oxide reduction and H adsorption/desorption peaks in CVs acquired for Au NRs:Rh/C of 10:1 and 7:3 ratios suggests that the exposed catalyst surface is composed mainly of Au. The Rh atoms may be dispersed on the Au NR surface or beginning to form an alloy. The surface energy of Rh is higher than that of Au, indicating that metal clusters can be formed and covered by Au.[72] As a result, Rh particles could be incorporated and diffused into Au surfaces to form homogenous Au–Rh alloys.[37,40,74] A recent study has shown that Au is incorporated into Rh outgrowths of samples of 10:1 composition.[76] The presence of Rh oxide formation and Rh oxide reduction peaks for Au NRs:Rh of 1:1 and 1:2

ratios suggest that Rh has coated the majority of the Au NR surfaces to form a core-shell structure, with a Rh-rich phase. It is likely that Rh surface segregation takes place only at high Rh content.[74] Therefore, the samples containing less Rh may have electrochemical properties of bare Au NRs and Au–Rh alloy formation, while the higher containing Rh samples may have properties related to Rh-rich phase behaviour.[76]

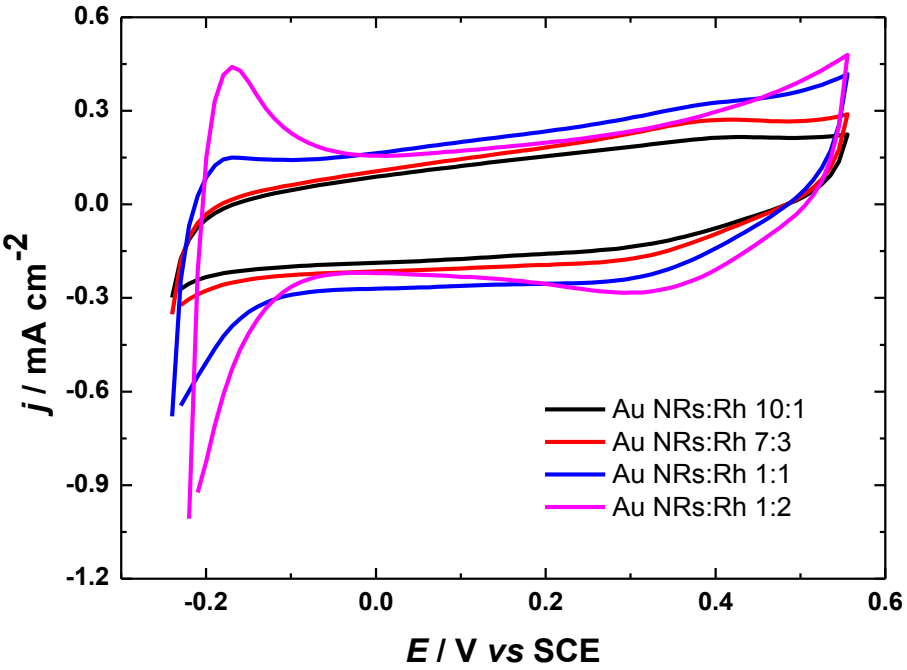

Figure 3.24 Cyclic voltammograms of Au NRs:Rh/C in Ar-saturated 0.5 M H_2SO_4 with upper potential at 0.55 V. Scan rate 0.1 V s^{-1}.

The real surface area of Au was quantified from the CVs by the integration of the charge under the Au oxide reduction peak, as shown in Figure 3.23. The charge for the reduction of the Au oxide monolayer is 400 μC cm^{-2}.[5,6] The real surface area of Rh was calculated by the integration of the hydrogen desorption peak of H_{UPD} in Figure 3.24, using the value of 220 μC cm^{-2} for a full monolayer of H_{UPD}.[59,61] The hydrogen adsorption has not been used to estimate the real surface area of Rh due to the influence of co-adsorption from

electrolyte anions[58,100,101] and the overlapping of H adsorption and Rh oxide reduction, indicating that the real surface area is prone to systematic error.

Table 3.1 and 3.2 present the charges corresponding to the reduction of Au oxide and H desorption for each sample. The Au oxide reduction is observed on Au NRs:Rh/C of 10:1, 7:3 and 1:1 ratios, while it is not observed on that of 1:2 ratio, suggesting full Rh coverage. The charges attributed to Au oxide reduction decrease on increasing the amount of Rh, suggesting the decrease of Au surface area. The charges from H desorption increase; however, they only begin to be observed on Au NRs:Rh/C of 1:1 ratio, indicating the increase of Rh real surface area. The charges due to hydrogen desorption on Au NRs:Rh of 1:2 ratio is dramatically increased, indicating a Rh-rich phase on this sample. The surface area appears low on AuRh NRs of 10:1 and 7:3 Au:Rh ratios perhaps because of the incorporation and diffusion of Rh into the Au surface.[37]

Table 3.1 The charge and the real surface area of Au NRs:Rh samples, corresponding to the reduction of Au oxide.

Sample	Position (V)	Charge due to Au surface oxide reduction (μC)	Surface area of Au on nanorod surface (cm^2)	% Area of Au on nanorod surface
Au NRs	0.88	20.6	0.052	100
Au NRs:Rh 10:1	0.88	15.0	0.038	73
Au NRs:Rh 7:3	0.89	11.0	0.028	54
Au NRs:Rh 1:1	0.89	6.94	0.017	32
Au NRs:Rh 1:2	-	-	-	-

Table 3.2 The charge and the real surface area of Au NRs:Rh samples, corresponding to the hydrogen desorption.

Sample	Position (V)	Charge due to hydrogen desorption (μC)	Surface area of Rh (cm^2)	Metal (Au + Rh) loading at electrode / $\mu g\ cm^{-2}$
Au NRs	-	-	-	42
Au NRs:Rh 10:1	-	-	-	44
Au NRs:Rh 7:3	-	-	-	51
Au NRs:Rh 1:1	-0.18	3.15	0.014	64
Au NRs:Rh 1:2	-0.17	16.2	0.073	86

The inability to quantify the Rh area for some of the samples means that the real surface area cannot be calculated without large error, for this reason currents were normalised to geometric surface area. The co-reduced and sequentially reduced Au:Rh/C nanoparticles were also electrochemically characterised by cyclic voltammetry. Figure 3.25 compares CVs of co-reduced Au:Rh/C nanoparticles. Au oxide formation decreases as the Rh content increases. Au oxide formation disappears when the Au:Rh ratio is 1:1 and 1:2. The Au oxide reduction is decreased on increasing Rh until it is hardly observed at the highest Rh:Au ratio. The peaks corresponding to Rh oxide reduction and hydrogen desorption increase until the Au:Rh 1:1 ratio and then decrease for the 1:2 ratio. Figure 3.26 compares CVs of co-reduced Au:Rh/C nanoparticles measured with an upper potential at 0.5 V. The hydrogen desorption and Rh oxide reduction peaks increase until the Au:Rh 1:1 ratio and decrease for the 1:2 ratio. The decrease of Rh oxide reduction and hydrogen desorption current density on co-reduced Au:Rh/C nanoparticles of 1:2 ratio may be explained by the formation of Au−Rh alloys, the increase of particle size and the decrease of metal surface area.

The real surface area of co-reduced Au:Rh/C nanoparticles determined by the charge integration in Figures 3.25 and 3.26 are presented in Table 3.3 and 3.4. The surface area of Au nanoparticles decreases when increasing Rh content; however, the Au surface area decrease may result from the incorporation of Au into a few large particles (of relatively low surface area), instead of Au−Rh alloy formation, since most Au and Rh particles are separated particles. The sharp Au surface area decrease at the highest Rh contents arises from the alloy formation and the particles size increase, as observed with STEM. Interestingly, the Rh oxide reduction peak in Figure 3.26 is at a more positive potential than that observed in Figure 3.25. The negative shift of Rh oxide reduction peak of the higher upper potential limit is because of the irreversibility of Rh oxide reduction.

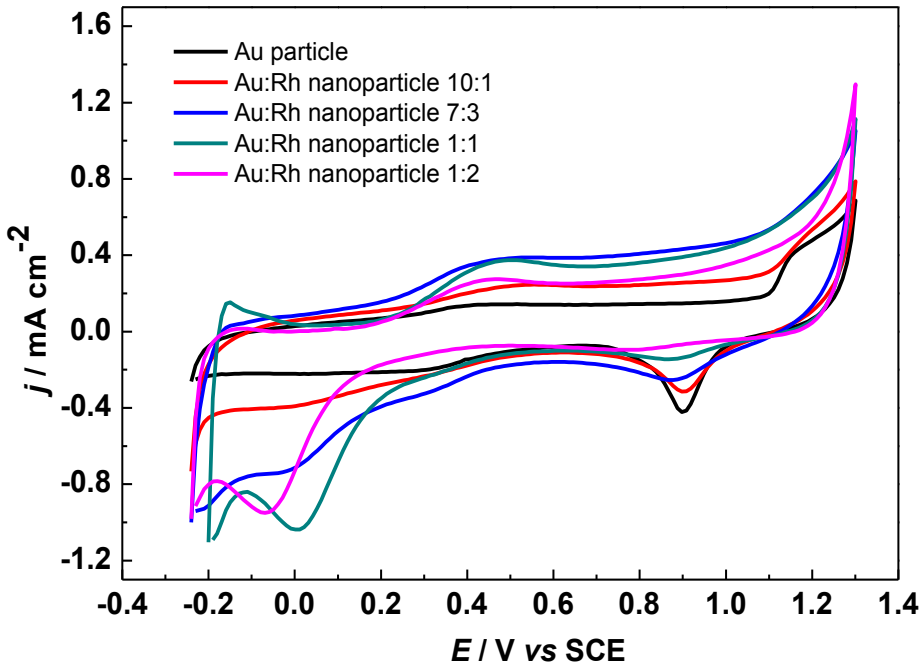

Figure 3.25 Cyclic voltammograms of Au/C nanoparticles and Au:Rh/C co-reduced nanoparticles in Ar-saturated 0.5 M H_2SO_4. Scan rate 0.05 V s^{-1}.

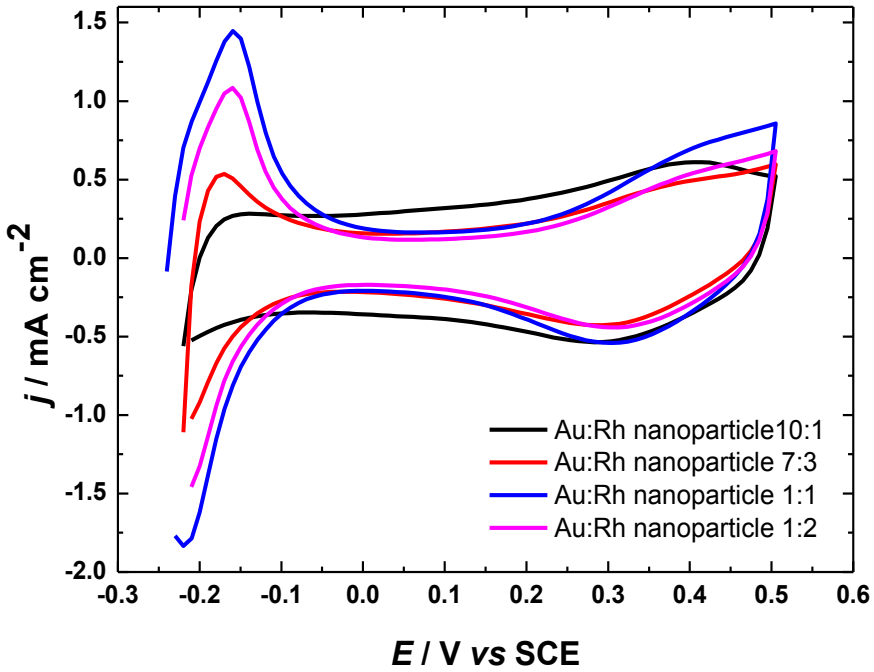

Figure 3.26 Cyclic voltammograms of co-reduced Au:Rh/C nanoparticles in Ar-saturated 0.5 M H_2SO_4 with upper potential at 0.5 V. Scan rate 0.1 V s^{-1}.

Table 3.3 The charge and the real surface area of co-reduced Au:Rh nanoparticle samples, corresponding to the reduction of Au oxide.

Sample	Position (V)	Charge due to Au surface oxide reduction (μC)	Surface area of Au on nanoparticle surface (cm^2)	% Area of Au on nanoparticle surface
Au nanoparticles	0.89	57.6	0.144	100
Au:Rh 10:1	0.90	36.5	0.091	63
Au:Rh 7:3	0.89	18.9	0.047	32
Au:Rh 1:1	0.88	6.49	0.016	11
Au:Rh 1:2	-	-	-	-

Table 3.4 The charge and the real surface area of co-reduced Au:Rh nanoparticle samples, corresponding to the hydrogen desorption.

Sample co-reduced nanoparticles	Position (V)	Charge due to hydrogen desorption (μC)	Surface area of Rh nanoparticle surface (cm^2)
Au:Rh 10:1	-0.15	1.17	0.01
Au:Rh 7:3	-0.22	20.2	0.09
Au:Rh 1:1	-0.16	88.0	0.40
Au:Rh 1:2	-0.16	61.3	0.28

Figure 3.27 and 3.28 present CVs of Au/C nanoparticles and sequentially reduced Au:Rh/C nanoparticles with high and low upper potential limits, respectively. The Au oxide reduction peak is diminished until a minimum is reached at a Au:Rh/C ratio of 1:1 and increased for the 1:2 ratio. The Rh oxide reduction begins to appear from Au:Rh/C of 7:3 ratio and increases until reaching a maximum at the 1:1 ratio, followed by a decrease for the 1:2 ratio. The hydrogen desorption can be observed for the 1:1 composition and decreases on that of 1:2 ratios. The presence of Rh oxide reduction and hydrogen desorption for high Rh content agree well with the results of Rh deposited on Au NRs and indicate that a Rh-rich phase is formed for particles of high Rh content, while an alloy may be formed for particles of low Rh content.

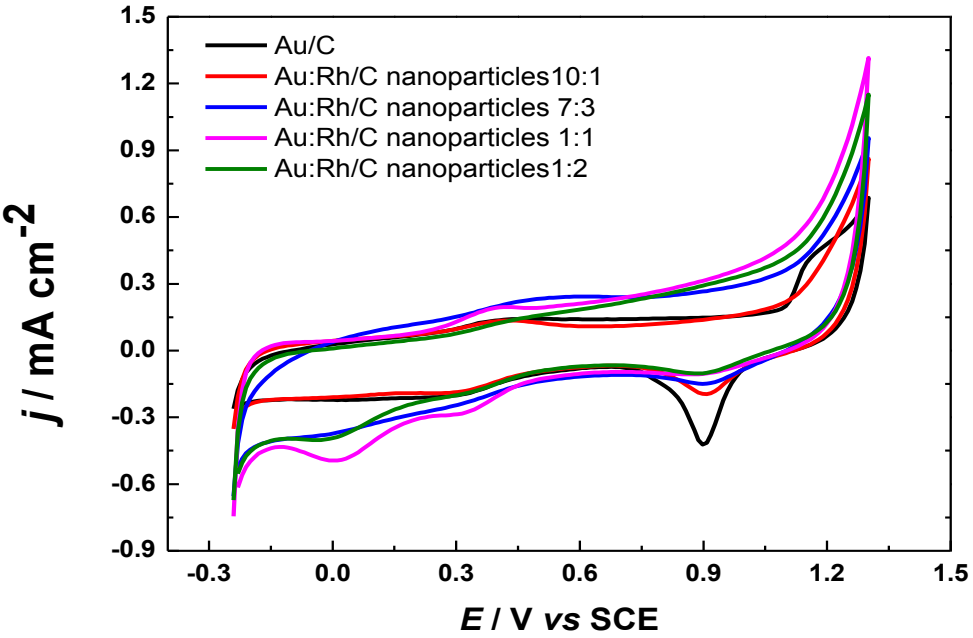

Figure 3.27 Cyclic voltammograms of Au/C nanoparticles and Au:Rh/C sequentially reduced nanoparticles in Ar-saturated 0.5 M H_2SO_4. Scan rate 0.05 V s^{-1}.

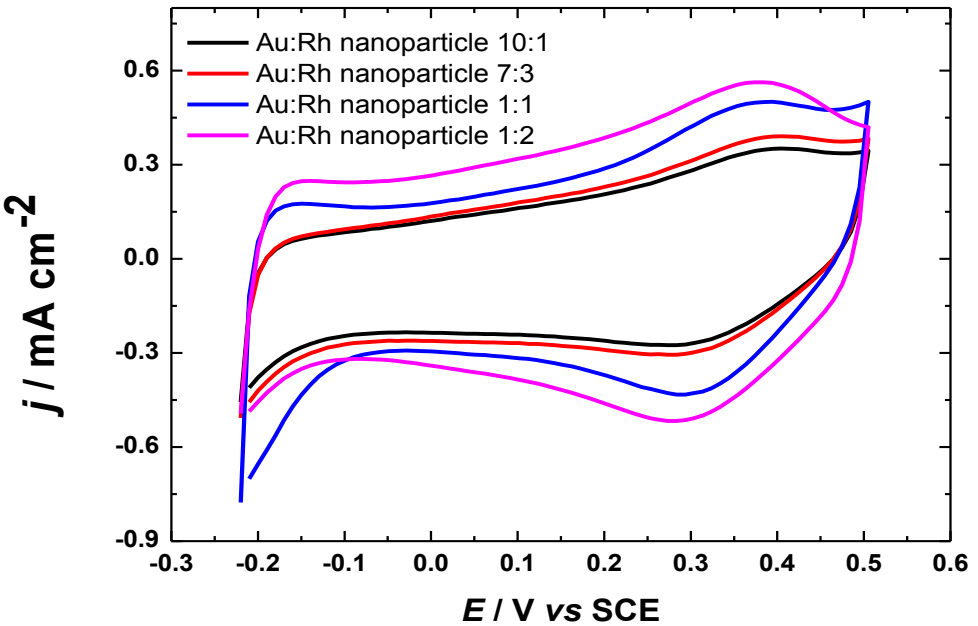

Figure 3.28 Cyclic voltammograms of sequentially reduced Au:Rh/C nanoparticles in Ar-saturated 0.5 M H_2SO_4 with upper potential at 0.5 V. Scan rate 0.1 V s^{-1}.

The real surface areas of sequentially reduced Au:Rh nanoparticles determined by the charge integration in Figure 3.27 and 3.28 are presented in Table 3.5 and 3.6., respectively. The surface area of Au nanoparticles diminishes until reaching a minimum for Au:Rh of 1:1

ratio, followed by a slight increase for the Au:Rh of 1:2 ratio. The surface area of Rh from charge integration of hydrogen desorption enables the area of the Au:Rh of 1:1 and 1:2 ratios. The smaller surface area of the 1:2 ratio sample is because the aggregation of particles at high Rh content increases the average particle size and reduce surface area. It is noticeable that the hydrogen desorption at sequentially reduced Au:Rh nanoparticles is lower than that of co-reduced Au:Rh nanoparticles, suggesting that the Rh surface area of the particles is lower for sequentially reduced nanoparticles. STEM images of sequentially reduced nanoparticles show that the average particle size of sequentially reduced Au:Rh nanoparticles is larger than that of co-reduced nanoparticles, which explains the decrease in surface area. The electrocatalytic activity of the three types of samples toward oxygen reduction will be discussed in the next section.

Table 3.5 The charge and the real surface area of sequentially reduced Au:Rh nanoparticles, corresponding to the reduction of Au oxide.

Sample	Position (V)	Charge due to Au surface oxide reduction (μC)	Surface area of Au on nanoparticle surface (cm^2)	% Area of Au on nanoparticle surface
Au nanoparticles	0.89	57.6	0.144	100
Au:Rh 10:1	0.91	25.8	0.063	36
Au:Rh 7:3	0.92	18.1	0.045	31
Au:Rh 1:1	0.91	10.6	0.026	21
Au:Rh 1:2	0.91	15.3	0.038	27

Table 3.6 The charge and the real surface area of sequentially reduced Au:Rh nanoparticles.

Sample sequentially reduced nanoparticles	Position (V)	Charge due to hydrogen desorption (μC)	Surface area of Rh nanoparticle surface (cm^2)
Au:Rh 10:1	-	-	-
Au:Rh 7:3	-	-	-
Au:Rh 1:1	-0.17	10.95	0.050
Au:Rh 1:2	-0.16	4.13	0.019

3.3.3 Oxygen reduction reaction in 0.5 M H_2SO_4

The electrocatalytic activities toward the ORR of Au NRs, Au nanoparticles, co-reduced and sequentially reduced Au:Rh nanoparticles were obtained using a rotating disc electrode (RDE) in oxygen-saturated 0.5 M H_2SO_4. The anodic going sweep has been used for the data analysis. The background current has been substracted from the RDE curves for the ORR on each electrode.

The RDE polarisation curves (with 400, 900, 1600 and 2500 rpm) of the polycrystalline Au electrode are presented in Figure 3.29. Figure 3.30 shows RDE polarisation curves for Au NRs/C and Au NRs:Rh/C samples. The RDE curves of Au NRs/C are presented in Figure 3.30 (a); the characteristics of the curves are identical to those of the curves acquired for a typical Au electrode, as shown in Figure 3.29.[5,6,102] Both Au and carbon support have low ORR electrocatalytic activity in acidic electrolyte. The onset potential of the ORR (the starting potential of the ORR) for Au NRs/C is at 0.17 V. The diffusion-limited current plateau was not found for this sample, suggesting a mixed control of diffusion and kinetic limitations of the reaction.[8,102] The reduction current of the ORR continued to increase at cathodic potentials: the reduction current of the Au NRs/C commences at 0.2 V and increases as the potential is negatively scanned to -0.3 V. The current densities of the polarisation curves increase with increasing rotating rate of electrode, indicating that the ORR at the Au NRs/C depends on rotation rate, whilst the polarisation curves of Au NRs/C in Ar-saturated 0.5 M H_2SO_4 (background, not shown here) are independent of electrode rotation rate. The polarisation curves of Au NRs:Rh/C of 10:1, 7:3 and 1:1 ratios have onset potentials at 0.3 V, 0.45 V and 0.5 V, respectively, and also exhibit no limiting current, as shown in Figure 3.30(b), (c) and (d), respectively. The polarisation curves of those samples have similar attributes to those of the Au NRs/C; however, the electrocatalytic activities and reduction

currents of Au NRs:Rh samples in the kinetically controlled region are higher than for the Au NRs/C sample. A well-defined limiting current is obtained only on Au NRs:Rh of 1:2 ratio and the onset potential is 0.55 V, as shown in Figure 3.30(e), suggesting that the reaction kinetics is faster for the sample containing a Rh-rich phase. Figure 3.30(f) compares the polarisation curves acquired for Au NRs/C and Au NRs:Rh/C of different ratios, at a rotation rate of 1600 rpm. It is clearly seen that the onset potential of the ORR is sequentially shifted to more positive potential with increasing Rh content of Au NRs. It is likely the presence of Rh on Au NRs dramatically increases the catalytic activity because the catalytic activity of Au NRs for the ORR is lower than that of Rh. The ORR at the Au NRs/C starts at 0.2 V. The ORR at potentials positive of 0.3 V is catalysed by Rh or alloyed Au–Rh.[36,54] The presence of additionally dispersed Rh small particles (apart from the Rh on Au NRs) was observed in STEM images of the Au NRs:Rh 1:2 ratio. However, the catalytic activity of this sample mostly shows from Rh on Au NRs because the catalytic activity of Rh small particles on the ORR would be expected to be higher (even at low Rh content, as seen in co-reduced Au−Rh particles).

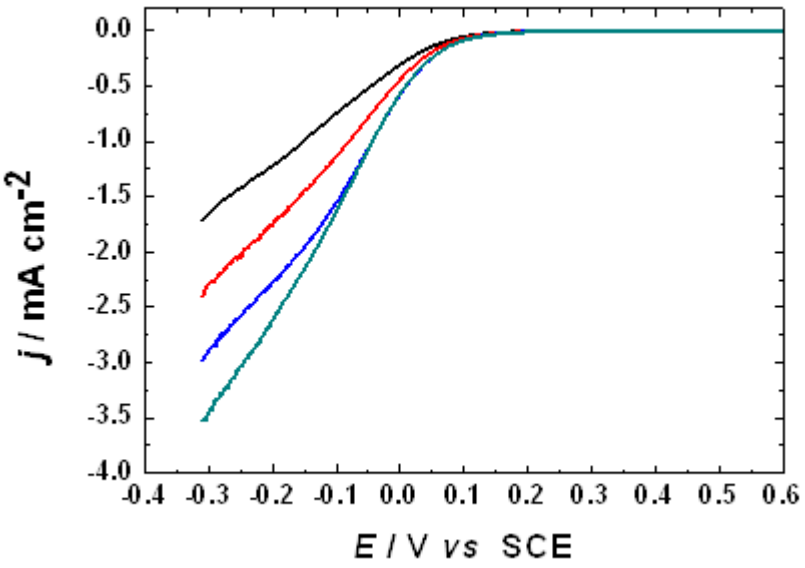

Figure 3.29 RDE polarisation curves for the ORR on a polycrystalline Au electrode in oxygen-saturated 0.5 M H_2SO_4. Scan rate 0.01 V s^{-1}.

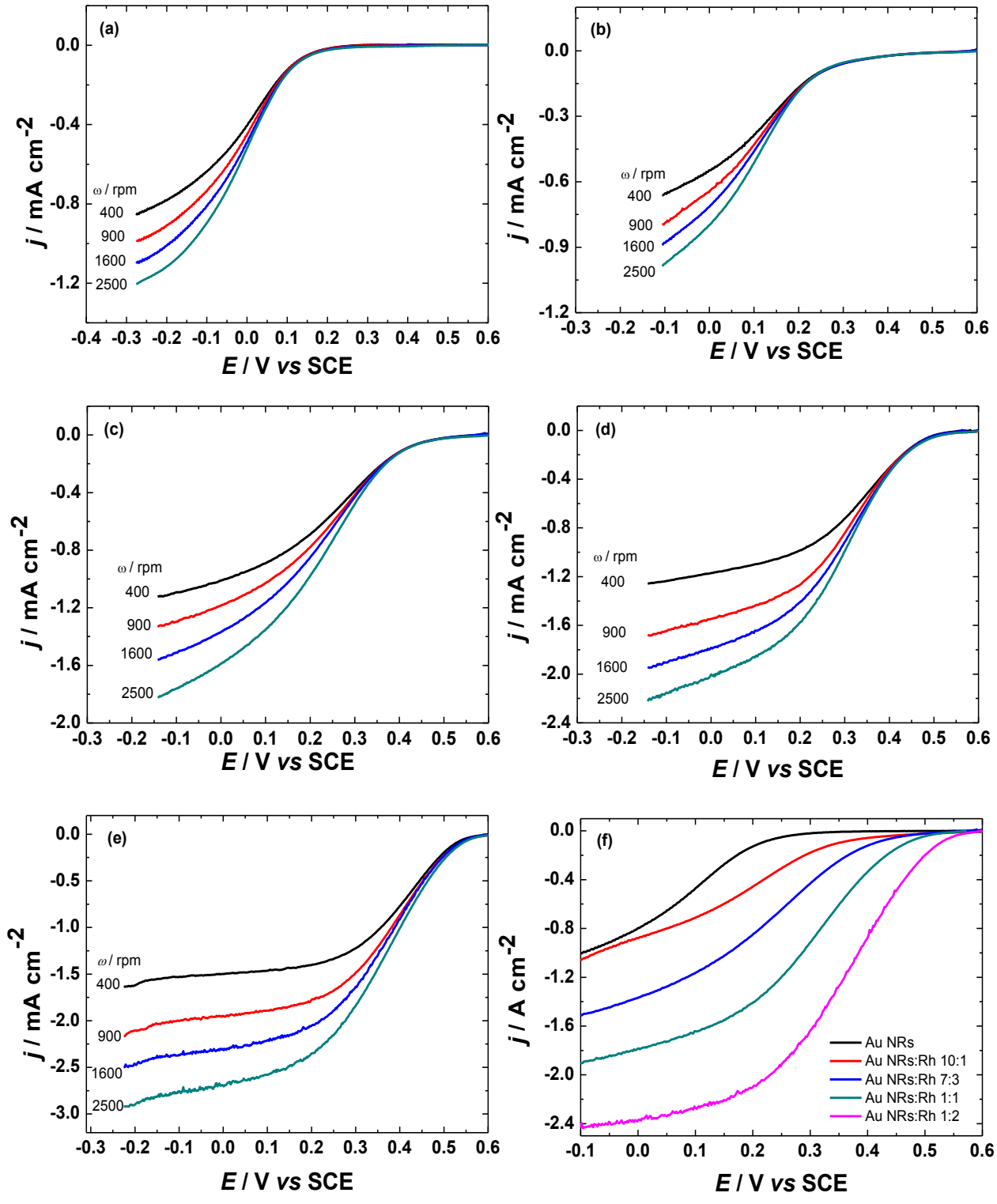

Figure 3.30 RDE polarisation curves for the ORR on (a) Au NRs/C, Au NRs:Rh/C (b) 10:1, (c) 7:3, (d) 1:1, (e) 1:2 and (f) comparison of Au NRs/C and Au NRs:Rh/C samples at rotation rate of 1600 rpm, all measured in oxygen-saturated 0.5 M H_2SO_4. Scan rate 0.01 V s^{-1}.

Figure 3.31 presents the RDE curves for Au/C, Rh/C and co-reduced Au:Rh/C nanoparticles. The onset potential observed for Au/C particles in Figure 3.31(a) is at 0.24 V, which is slightly shifted to more positive potential compared with Au NRs/C. This may be interpreted by not only shape dependence but also by surface area dependence of catalytic activities. The RDE curve for Rh/C nanoparticles displayed in Figure 3.31(b) has an onset potential at 0.57 V, indicating that Rh/C particles are very active towards the ORR. The reduction current of the Rh/C nanoparticles is dramatically higher than that of Au/C particles and the limiting current is reached at *ca* 0.15 V. The onset potentials of Au:Rh of 10:1, 7:3 and 1:2 ratios are close to potential at 0.55 V, while that of the 1:1 ratio is at 0.6 V. The limiting current is apparent for Rh concentrations from Au:Rh 7:3 ratio. It is noticeable that there is a shallow peak at 0.15 V for the Au:Rh/C 1:2 ratio, which may result from the reduction of hydroxyl (oxide) species from the Rh[55], as seen in Figure 3.31(f). This may suggest that Au−Rh alloy formation or particle aggregation at high Rh content enables the reduction of hydroxyl species during the ORR.

From the comparison in Figure 3.32, it can be seen that the limiting current of the ORR on the Au:Rh 1:1 ratio sample is reached at a more positive potential than the other samples. However, most of the Au and Rh in the co-reduced nanoparticle sample are in separate nanoparticles, except for the 1:2 ratio. Thus, the increase of catalytic activities for co-reduced Au:Rh samples may result from the increase of the amount of Rh nanoparticles instead of the modification of surface structure.[55] The current decrease and the negatively shifted onset potential of the co-reduced Au:Rh 1:2 sample occurs as a result of Au−Rh alloy formation and decrease of surface area.

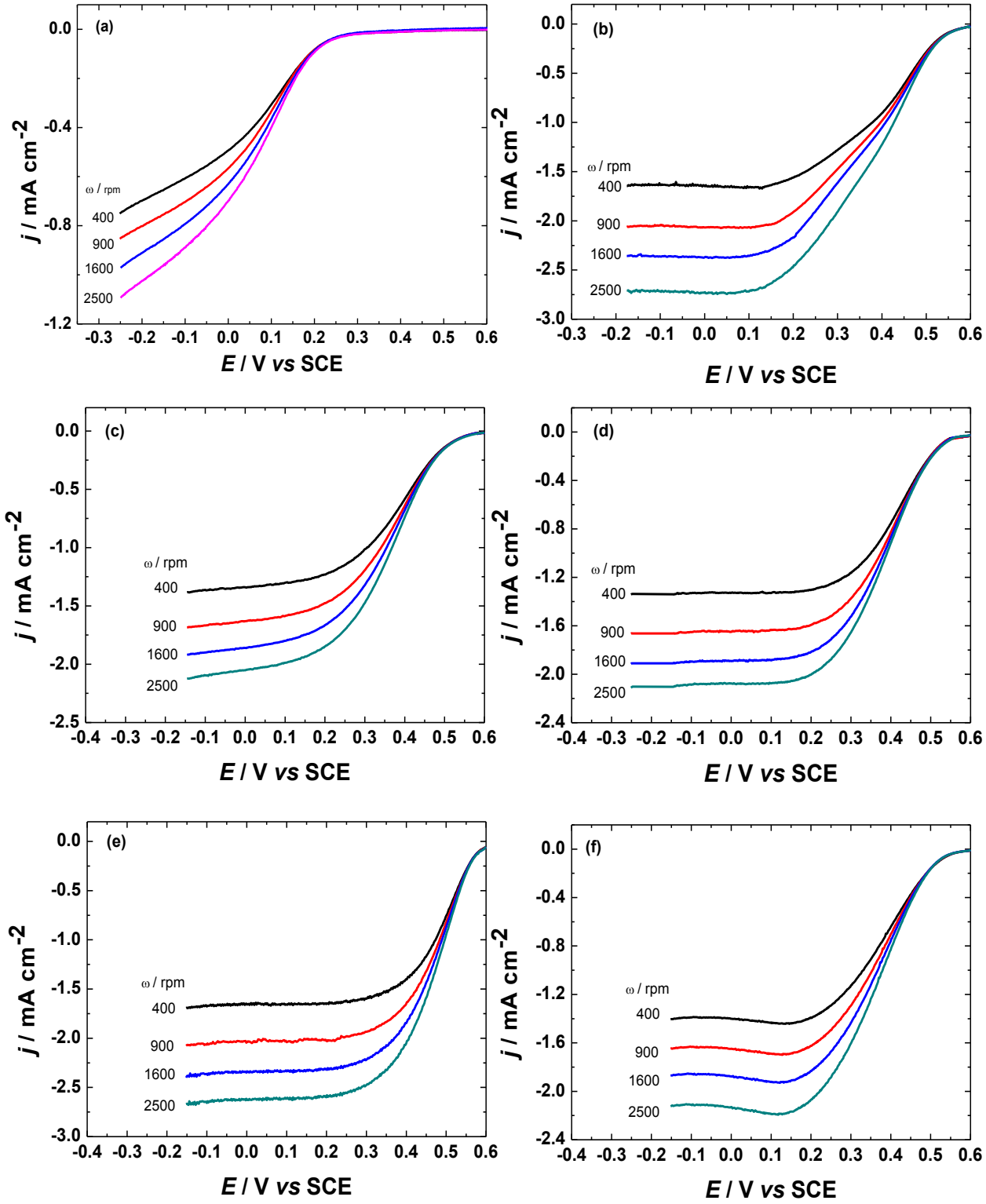

Figure 3.31 RDE polarisation curves for the ORR on (a) Au/C, (b) Rh/C, co-reduced Au:Rh/C (c) 10:1, (d) 7:3, (e) 1:1and (f) 1:2 nanoparticles, all measured in oxygen-saturated 0.5 M H_2SO_4. Scan rate 0.01 V s^{-1}.

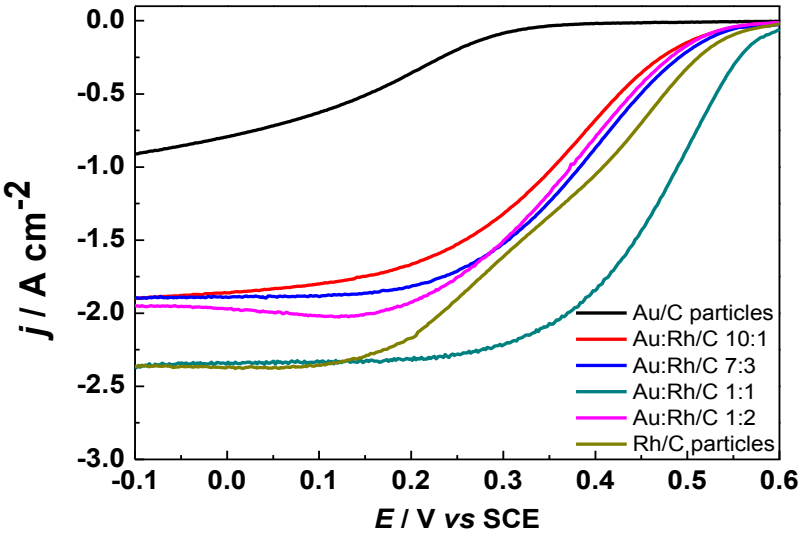

Figure 3.32 Comparison of Au/C, Rh/C and co-reduced Au:Rh/C nanoparticles at rotation rate of 1600 rpm in oxygen-saturated 0.5 M H_2SO_4. Scan rate 0.01 V s^{-1}.

Figure 3.33 illustrates the corresponding RDE curves acquired for the ORR at sequentially reduced Au:Rh/C nanoparticles. The polarisation curves of the Au:Rh/C 10:1 ratio sample have similar features as those of Au/C nanoparticles; however, the reduction current is higher than that of Au/C and the onset potential is at a more positive potential. A limiting current is observed at Au:Rh ratios of 7:3 and above. The data for the 7:3, 1:1 and 1:2 ratios reach limiting currents at -0.1 V, 0.2 V and 0.1 V, respectively. The reduction current is decreased and the onset potential is negatively shifted for the highest Rh content. A comparison of the data acquired for sequentially reduced Au:Rh nanoparticles is presented in Figure 3.34. It is clearly observed that a decrease of overpotential is obtained when increasing Rh content. The current density is drastically enhanced on Au:Rh for 7:3 and the above ratios. It is likely that the lowest Rh content tends to display catalytic activity similar to the bare Au/C nanoparticles because Rh is incorporated into the Au surface.[37] After this ratio, the growth of Rh on Au nanoparticle is induced and a Rh-rich phase is formed on Au particles, as shown in STEM images. However, the Au seeds have not been completely coated by Rh, as the UV-vis spectra still show a SPR (corresponding to Au) and the Au oxide reduction peak

still can be observed in the CV. Some aggregation of the particles can be observed at high Rh content, which may explain the decrease in ORR activity for this sample.

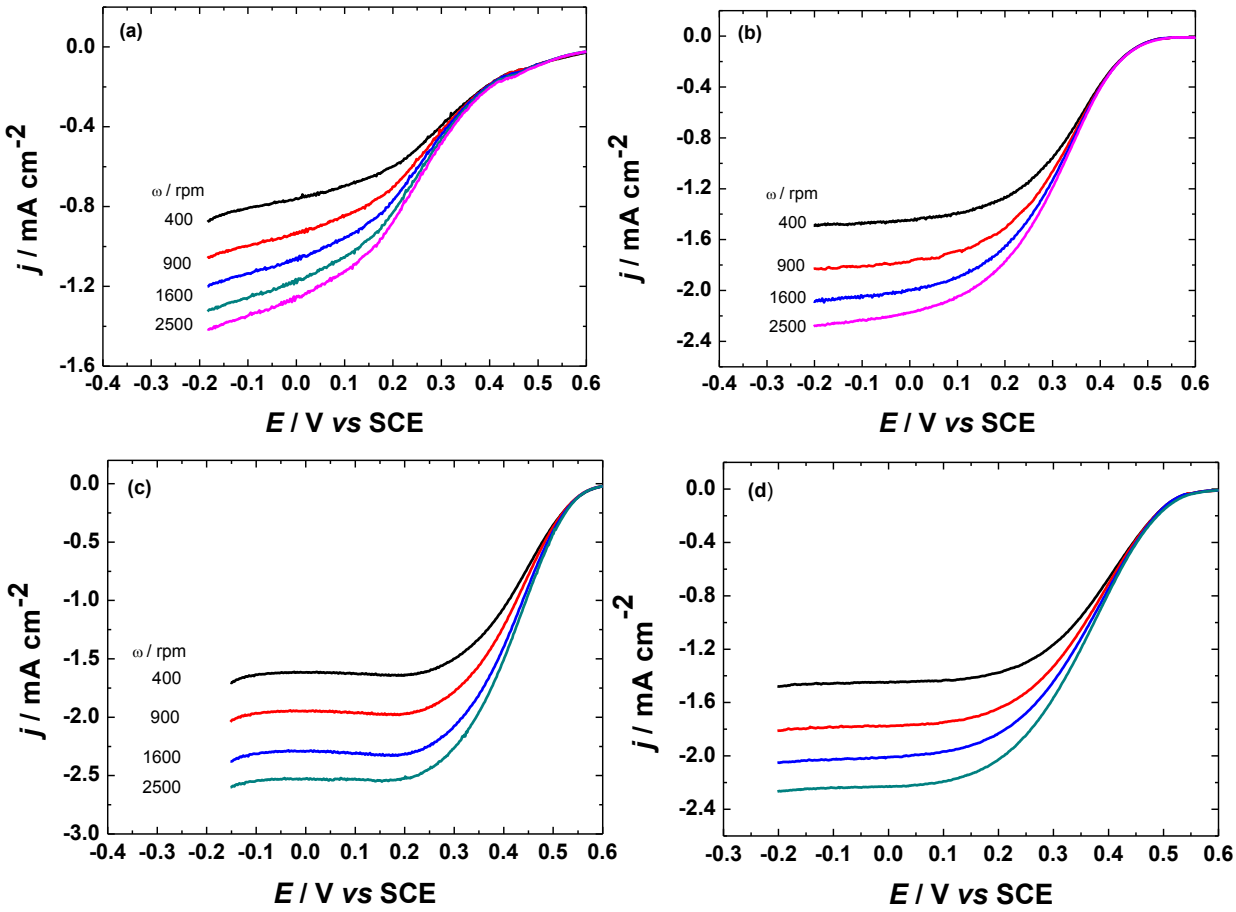

Figure 3.33 RDE polarisation curves for ORR on sequentially reduced Au:Rh/C (a) 10:1, (b) 7:3, (c) 1:1 and (d) 1:2 in oxygen-saturated 0.5 M H_2SO_4. Scan rate 10 mV s^{-1}.

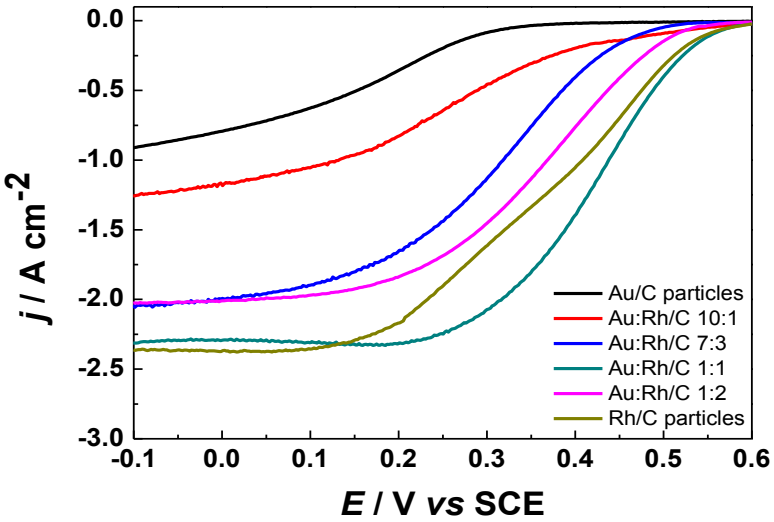

Figure 3.34 Comparison of Au/C, Rh/C and sequentially reduced Au:Rh/C nanoparticles at rotation rate of 1600 rpm in oxygen-saturated 0.5 M H_2SO_4. Scan rate 0.01 V s^{-1}.

It is evident from the comparison of the three types of sample that the overpotentials of co-reduced and sequentially reduced nanoparticles are smaller than those measured for rod-shaped nanoparticles. These features can be attributed to shape dependence of catalytic activity and to the difference in surface area of the particles. Comparing co-reduced and sequentially reduced particles, the overpotential needed to drive the ORR on sequentially reduced particles is higher than that with the former. The co-reduced nanoparticles mostly consist of mixed Au and Rh particles, with some partial alloy formation at high Rh content, whilst the sequentially reduced particles contain particles with an alloy phase and a Rh-rich phase. This suggests that the catalytic activity of sequentially reduced Au:Rh nanoparticles is more controllable by the composition of Rh on Au surfaces than that of co-reduced Au:Rh nanoparticles.

It is clear that there is a major enhancement of Au catalytic activity toward the ORR *via* the modification of Au nanorods and nanoparticles by sufficient Rh content, which is higher than 10% of Rh on Au. The deposition of Rh starts on Au (111), as proposed on Au NRs.[63] The diluted Rh alloy of 10% of Rh on Au NRs and Au particles shows similar catalytic activity to that of the pure Au. Thus, it is proposed that a Au-rich surface with a minority of Rh atoms results in behaviour similar to pure Au. A previous report on Au–Pd nanoalloys revealed that a surface alloy of Au and Pd is formed for samples of Pd content below 15% and present the catalytic activity on the ORR similar to that of Au nanoparticles.[37]

3.3.4 Koutecky-Levich analysis of Au NRs:Rh and Au:Rh nanoparticles

The RDE data can be analysed to obtain the number of electrons transferred in the reaction using the Koutecky-Levich (K–L) equation.[103]

$$\frac{1}{j} = \frac{1}{j_{\mathrm{k}}} + \frac{1}{j_{\mathrm{d}}} = -\frac{1}{nFkC_{\mathrm{O_2}}^{b}} - \frac{1}{0.62nFD_{\mathrm{O_2}}^{2/3}\nu^{-1/6}C_{\mathrm{O_2}}^{\mathrm{b}}\omega^{1/2}} \qquad (3.8)$$

where j is the measured current density, j_{k} is the current density relating to kinetic limitation, j_{d} is the diffusion-limited current density, F is the Faraday constant (96,485 C mol^{-1}), n is the number of electrons transferred per O_2 molecule, $D_{\mathrm{O_2}}$ is the diffusion coefficient of oxygen (1.8×10^{-5} cm^2 s^{-1}),[6] $C_{\mathrm{O_2}}$ is the concentration of oxygen in the bulk (1.13×10^{-6} mol cm^{-3}),[6] ω is the rotation rate of the disc electrode (rad s^{-1}), k is the rate constant for O_2 reduction and ν is the kinematic viscosity of the solution (0.01 cm^2 s^{-1}).[6] Plots of j^{-1} *vs* $\omega^{-1/2}$ (K–L plots) can be made and kinetic parametres determined using Eq. (3.8).

Figure 3.35(a) - (e) presents the K–L plots derived from the RDE data of Au NRs/C and Au NRs:Rh/C at various potentials. The linearity and parallelism of the plots indicate that the number of electrons transferred per O_2 molecule does not significantly change over the potential range of the experiment and confirm that the reaction is first order with respect to oxygen.[104] Figure 3.35(f) compares the K-L plots obtained from data measured for Au NRs/C and Au NRs:Rh/C samples at -0.1 V. It is noticeable that the slope of the plot for Au NRs/C is lower than that of Au NRs:Rh/C of 10:1 ratio, while the slopes of the other samples decrease with increasing Rh content.

Figure 3.36 and 3.37 display the K–L plots of co-reduced and sequentially reduced Au:Rh/C nanoparticles, respectively. Linear and parallel lines are obtained for these samples, similar to those of Au NRs:Rh/C samples. The K−L plot comparison of co-reduced nanoparticles at 0.0 V in Figure 3.36(f) shows that the slope of the plot for Au/C is reasonably higher than those co-reduced Au:Rh nanoparticles. The slope of the plot for Au/C is similar to that for the sequentially reduced Au:Rh 10:1 nanoparticles, as seen in Figure 3.37(f),

indicating that the catalytic selectivity of sequentially reduced Au:Rh nanoparticles of 10:1 ratio tends toward that of Au/C nanoparticles.

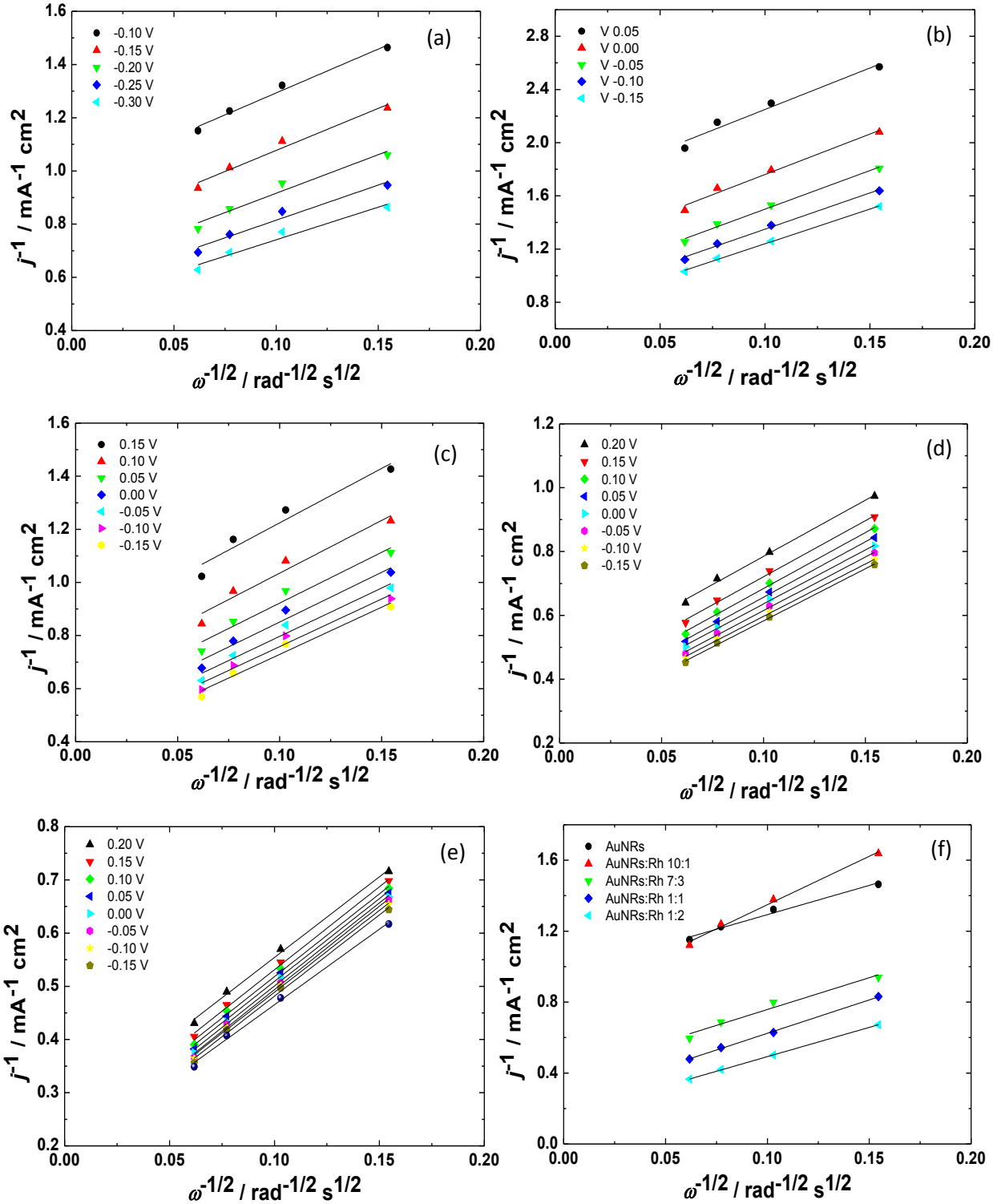

Figure 3.35 Koutecky-Levich plots for the ORR on (a) Au NRs/C nanoparticles, Au NRs:Rh/C (b) 10:1, (c) 7:3, (d) 1:1, (e) 1:2 and (f) Au NRs/C and different ratio of co-reduced Au NRs:Rh/C electrodes at -0.1 V.

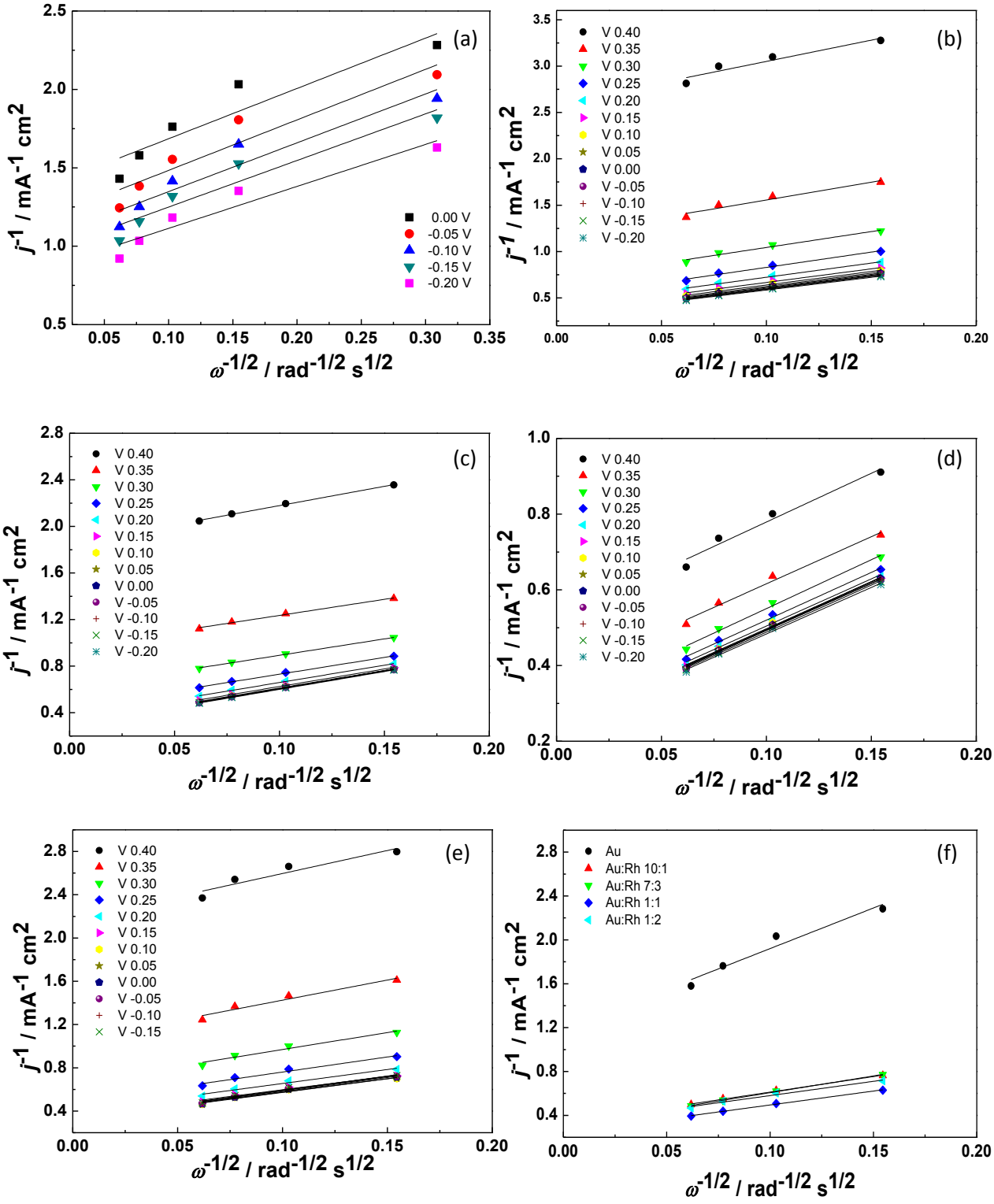

Figure 3.36 Koutecky-Levich plots for the ORR on (a) Au/C nanoparticles, co-reduced Au:Rh/C (b) 10:1, (c) 7:3, (d) 1:1, (e) 1:2 and (f) Au/C and different ratio of co-reduced Au:Rh/C electrodes at 0.0 V.

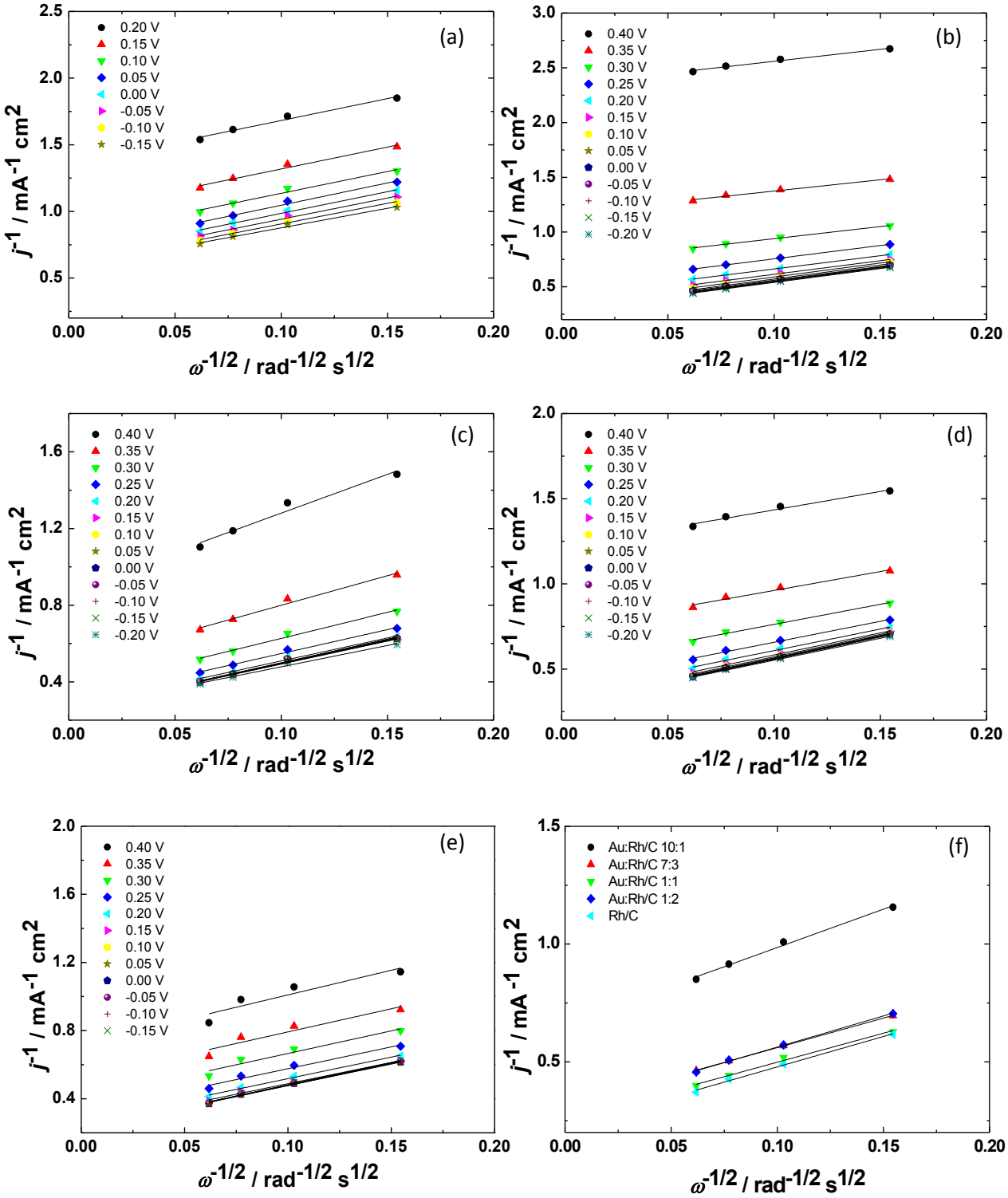

Figure 3.37 Koutecky-Levich plots for the ORR on sequentially reduced Au:Rh/C (a) 10:1, (b) 7:3, (c) 1:1, (d) 1:2, (e) Rh/C and (f) Au/C and different ratio of sequentially reduced Au:Rh/C electrodes at 0.0 V.

The number of electrons transferred per oxygen molecule (n) was calculated from the slopes of the K–L plots and Eq. (3.8). Figure 3.38(a) is a plot of *n* as a function of potential for Au NRs/C and Au NRs:Rh/C at different ratios. The number of electrons transferred at Au NRs catalysts increases as a function of potential and reaches a number close to 2 at the foot of the polarisation curve, suggesting that H_2O_2 is the main product at these potentials. The *n* values tend to be higher than 2 at more negative potentials, indicating the further reduction of H_2O_2 to H_2O. Interestingly, the *n* value obtained on Au NRs:Rh of 10:1 ratio is also close to 2; however, the *n* values at potentials negative of 0.0 V are less than those of Au NRs, which would indicate higher selectivity towards H_2O_2. The current densities and the *n* values on the above Au NRs:Rh of 10:1 ratio gradually increases with increasing Rh content, indicating that H_2O is the main reduction product when a Rh-rich phase is present on Au NRs.

The decrease of *n* value for Rh loading up to 10% on Au NRs is a result of the formation of Au−Rh alloys, which seems to enable suppression of the further reduction of H_2O_2 at more negative potentials and increases selectivity towards H_2O_2 production. The H_2O_2 production enhancement is related to the incorporation of Rh atoms on Au surfaces. The alloy formations inhibit the O−O bond breaking. This behaviour is similar to that in a previous report on Au−Pd alloys, based on DFT modelling and surface composition analysis by CVs, that Pd loading up to 10% on Au surface suppresses the further reduction of H_2O_2.[37] The DFT modelling suggested that alloying formation of Pd, Pt and Rh on Au surface should improve the selectivity of H_2O_2 production compared with pure Au, although the effect of Rh was predicted to be smaller than that of Pd and Pt. Figure 3.38(b) compares the n values obtained for the ORR at Au/C nanoparticles and at co-reduced Au:Rh/C nanoparticles. The n value for Au/C nanoparticles is *ca* 3, which is higher than that for Au NRs/C.

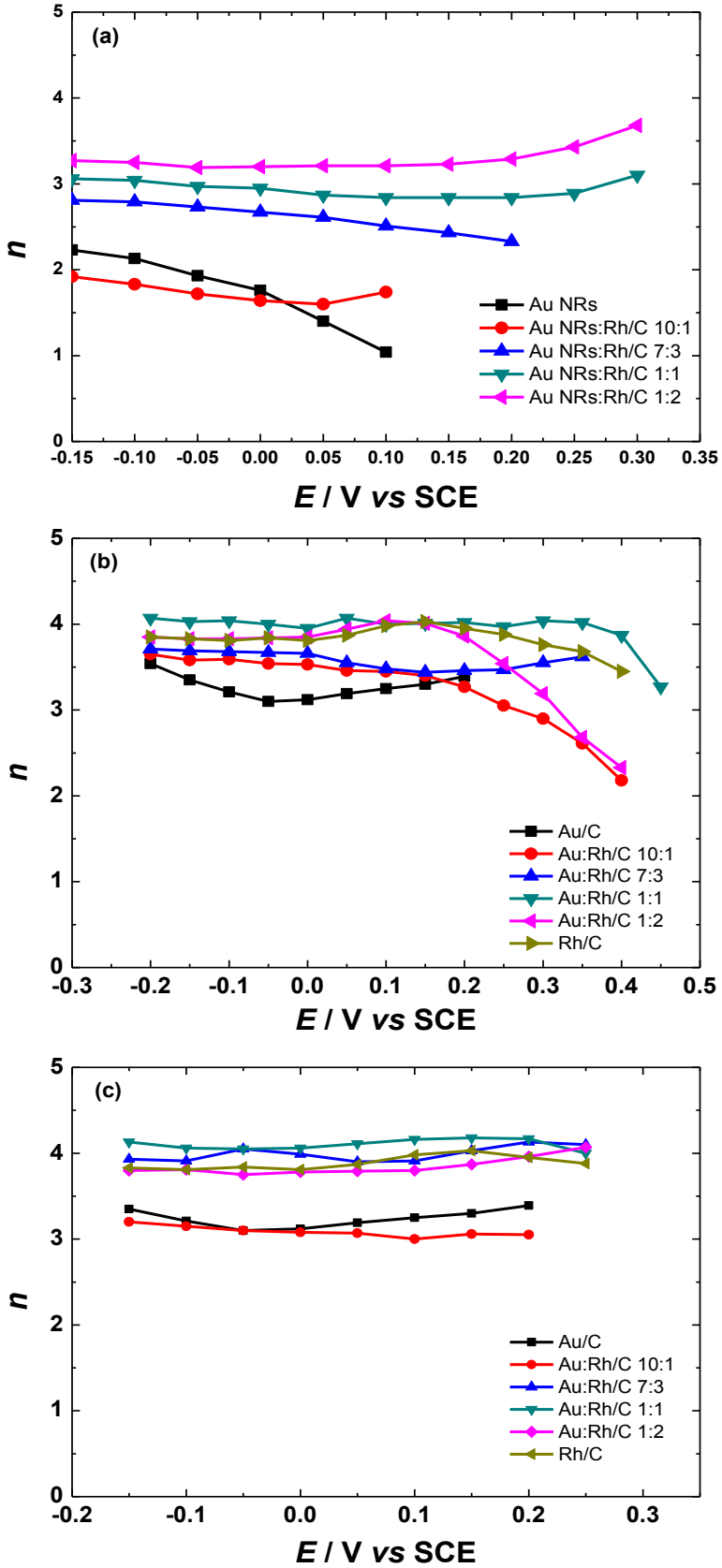

Figure 3.38 Potential dependence of *n* for (a) Au NRs/C and different ratio of Au NRs:Rh/C electrodes (b) Au/C nanoparticles and different ratio of co-reduced Au:Rh/C nanoparticles and (c) Au/C nanoparticles and different ratio of sequentially reduced Au:Rh/C nanoparticles.

Values of $3 > n > 2$ in acidic media have been reported for various thicknesses of Au film on glassy carbon electrode[5,36] and for different loadings of Au on carbon substrates.[16,37] A value of n of *ca* 2 was obtained for Au (100) and Au (110) single crystal electrodes higher than for Au (111).[102] The higher number of electrons measured in the ORR on Au/C nanoparticles compared with that for Au NRs/C may arise from the different surface structures of Au. The n value increases on increasing Rh content until a maximum for the 1:1 ratio, decreasing for the 1:2 ratio, which is the only sample where partial alloy formation was observed. It is seen that the n values obtained for the ORR at co-reduced Au:Rh/C of 10:1 ratio are considerably higher than those for Au NRs:Rh/C 10:1 samples because the electrocatalytic activity of the co-reduced particles is mostly from separate Au and Rh particles. Figure 3.38(c) shows that the n values measured for sequentially reduced Au:Rh/C nanoparticles are drastically increased for the Au:Rh 7:3 sample and slightly increased after that ratio. The Au:Rh 1:1 sample yields the highest n value. The n values determined for sequentially reduced Au:Rh/C 10:1 are slightly lower than those for Au/C nanoparticles, similar to the case for Au NRs.

3.3.5 Analysis of electrode kinetics by Koutecky-Levich and Tafel Equations

The rate of electron transfer or current density for a reaction depends on several parameters, such as standard rate constant and concentration, transfer coefficient and applied overpotential.

The kinetic current density, j_k, can be estimated from an intercept of the K–L plot at different potentials, in accordance with Eq. (3.8). From Eq. (3.8), the rate constant (k) can be

expressed in terms of j_k using Eq. (3.9).[50] The results for each sample at -0.1 V are given in Table 3.7.

$$k = \frac{j_k}{nFC_{O_2}} \quad (3.9)$$

It is known that the rate constant also can be expressed by Eq. (3.10). This equation describes the rate constant as a function of potential measured *vs* a reference electrode.[50]

$$k = k_0 \exp\left(-\frac{\alpha n_a F}{RT} E\right) \quad (3.10)$$

where k_0 stands for a purely chemical rate constant, indicating the activity of the surface for oxygen reduction in the absence of an electric field, α is the transfer coefficient (or symmetry factor), n_a is the number of electrons transferred in the rate-determining step (RDS), which is the slowest step of the ORR, R is the gas constant (8.314 J K^{-1} mol^{-1}), T is the absolute temperature (K). The values k_0 and αn_a can be calculated from the intercept and the slope of the log k *vs* E plot, respectively. Values of k were estimated from j_k using Eq. (3.9) and log k *vs* E was plotted for each sample. Values of k_0 and αn_a were estimated from the plots using Eq. (3.10) and the results are shown in Table 3.7. The rate constant, k, calculated from the intercept of the K−L plot at 0.0 V, increases with increasing Rh content, except for the highest ratio of Rh for co-reduced and sequentially reduced nanoparticles, whose ORR rate constants are decreased. The values of k_0 obtained for Au NRs:Rh samples are in similar sequence to their k. The values of k_0 calculated for co-reduced and sequentially reduced nanoparticles are in similar trend to their k, although there is a fluctuation at the lowest Rh content.

Table 3.7 Values of j_k, k, k_0, αn_a and Tafel slope.

Samples	j_k / mA cm^{-2}	k cm s^{-1} at 0.0 V	k_0 cm s^{-1}	αn_a	Tafel slope lcd / mV dec^{-1}	Tafel slope hcd/ mV dec^{-1}
Au NRs/C	1.02	2.43×10^{-3}	2.24×10^{-3}	0.20	-	170
Au NRs:Rh/C 10:1	1.07	2.45×10^{-3}	5.37×10^{-3}	0.18	-	183
Au NRs:Rh/C 7:3	2.31	5.30×10^{-3}	1.66×10^{-2}	0.17	97	128
Au NRs:Rh/C 1:1	3.36	7.70×10^{-3}	7.24×10^{-2}	0.18	83	132
Au NRs:Rh/C 1:2	5.31	1.22×10^{-2}	3.90×10^{-2}	0.17	60	110
Au/C	0.92	3.85×10^{-3}	6.92×10^{-3}	0.22	-	136
Rh/C	4.54	1.04×10^{-2}	3.17×10^{-2}	0.14	86	126
Co-reduced Au:Rh/C 10:1	3.10	7.11×10^{-3}	2.40×10^{-1}	0.27	93	136
Co-reduced Au:Rh/C 7:3	3.34	7.66×10^{-3}	9.77×10^{-2}	0.23	80	137
Co-reduced Au:Rh/C 1:1	4.11	9.42×10^{-3}	2.57×10^{-1}	0.24	71	134
Co-reduced Au:Rh/C 1:2	3.06	7.02×10^{-3}	5.89×10^{-2}	0.19	84	112
Sequentially reduced Au:Rh/C 10:1	3.10	7.11×10^{-3}	1.07×10^{-2}	0.16	-	158
Sequentially reduced Au:Rh/C 7:3	3.30	7.57×10^{-3}	3.09×10^{-3}	0.24	87	135
Sequentially reduced Au:Rh/C 1:1	3.96	9.08×10^{-3}	7.08×10^{-3}	0.18	67	117
Sequentially reduced Au:Rh/C 1:2	3.35	7.68×10^{-3}	2.34×10^{-3}	0.22	75	128

The electrode kinetics can also be obtained with the Tafel equation in Eq. (3.12), which is written as Eq. (3.11).[50,103,105] The mass transport-corrected Tafel equation was applied in order to analyse the kinetic current density. The value of j_k is estimated by revising Eq. (3.8) to Eq. (3.13). The Tafel equation can be rearranged in the form of Eq. (3.14).

$$j_k = j_0 e^{\frac{-\alpha n_a F \eta}{RT}} \tag{3.11}$$

$$\eta = \frac{2.303RT}{\alpha n_a F} log\, j_0 - \frac{2.303RT}{\alpha n_a F} log\, j_k \tag{3.12}$$

where j_0 is the exchange current density and η is the overpotential ($E - E_{eq}$).

$$j_k = \frac{j_d j}{j_d - j} \tag{3.13}$$

$$\eta = \frac{2.303RT}{\alpha n_a F}\left(log\, j_0 - log j_{\mathrm{d}} - log\, \frac{j}{j_{\mathrm{d}} - j}\right) \quad (3.14)$$

From Eq. (3.11), it can be seen that the current density depends on the applied potential and the electron-transfer activity at the equilibrium potential.

Figure 3.39, 3.40 and 3.41 present mass transfer-corrected Tafel plots obtained from the RDE data of Au NRs/C, Au NRs:Rh/C, Au/C nanoparticles, co-reduced and sequentially reduced Au:Rh nanoparticles. For the x-axis values of $\left(\frac{j}{j_{\mathrm{d}} - j}\right)$, j is taken from the current density of the polarisation curve of each surface when the RDE is rotated at 1600 rpm. The value of j_{d} for each surface is calculated from the K-L equation. The Tafel slopes of each sample are presented in Table 3.7. For Au NRs/C, Au/C nanoparticles, 10:1 Au NRs:Rh/C and 10:1 sequentially reduced Au:Rh nanoparticles, one Tafel slope is obtained. For the Rh/C nanoparticle, Au NRs:Rh/C, co-reduced and sequentially reduced Au:Rh/C nanoparticle at high Rh content, two Tafel slopes are obtained, at the high current densities (hcd) and low current densities (lcd). The Tafel slopes of Au NRs/C and Au/C are close to 170 mV dec^{-1} and 136 mV dec^{-1}, respectively. These values depend on the morphology of nanoparticles.[8,9,12-14,25,106,107] The Tafel slopes of 10:1 Au NRs:Rh/C and 10:1 sequentially reduced Au:Rh nanoparticles are close to those observed for the ORR at Au NRs/C and Au/C nanoparticles. The values indicate that the first electron transfer from Au surface to oxygen is the rate-determining step. Tafel slope values higher than 120 mV dec^{-1} have been reported in the literature for Au (111) electrode and Au nanoparticles.[5,6] Tafel slopes higher than -120 mV dec^{-1} have been explained by a potential distribution at the interface affected by the accumulation of peroxide.[108] This could arise from a higher degree of sulphate adsorption on Au (111). The high Tafel slope value for the Au NRs could be further evidence that there are some Au (111) sites on the Au NR and Au NPs surfaces.

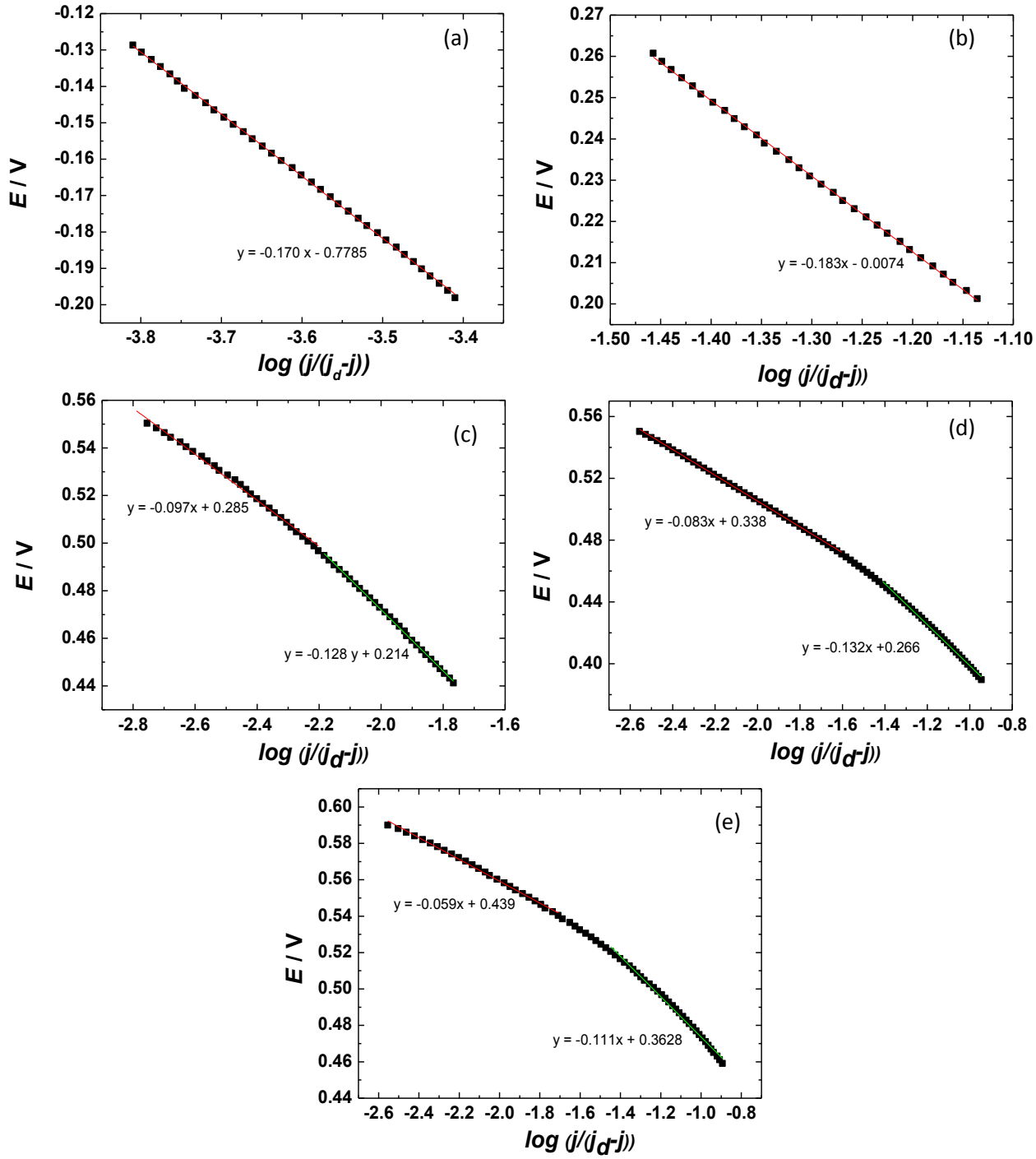

Figure 3.39 Tafel plots for the ORR on (a) Au NRs/C, Au NRs:Rh/C (b) 10:1, (c) 7:3, (d) 1:1 and (e) 1:2.

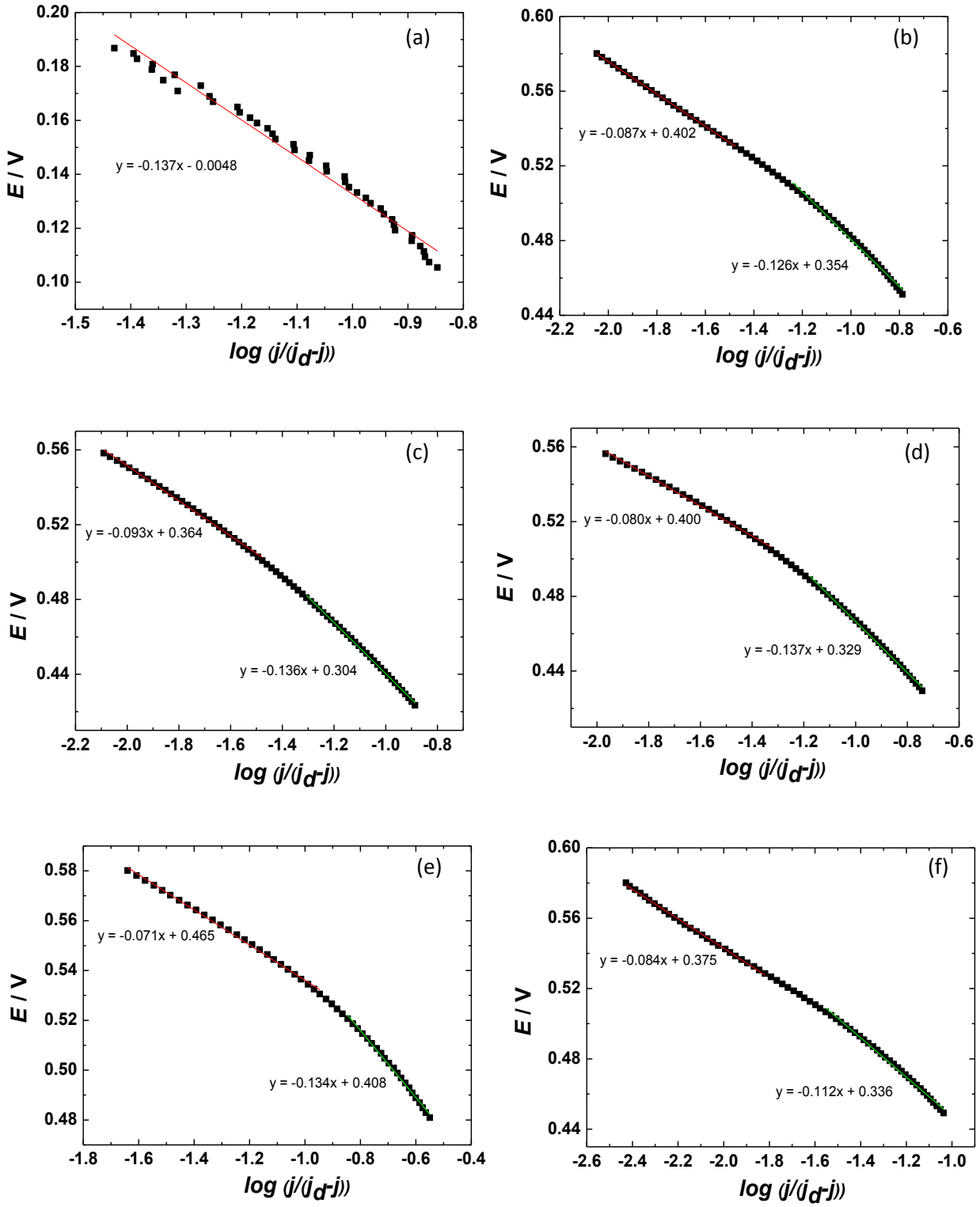

Figure 3.40 Tafel plots for the ORR on (a) Au/C, (b) Rh/C, co-reduced Au:Rh/C (c) 10:1, (d) 7:3, (e) 1:1 and (f) 1:2 nanoparticles.

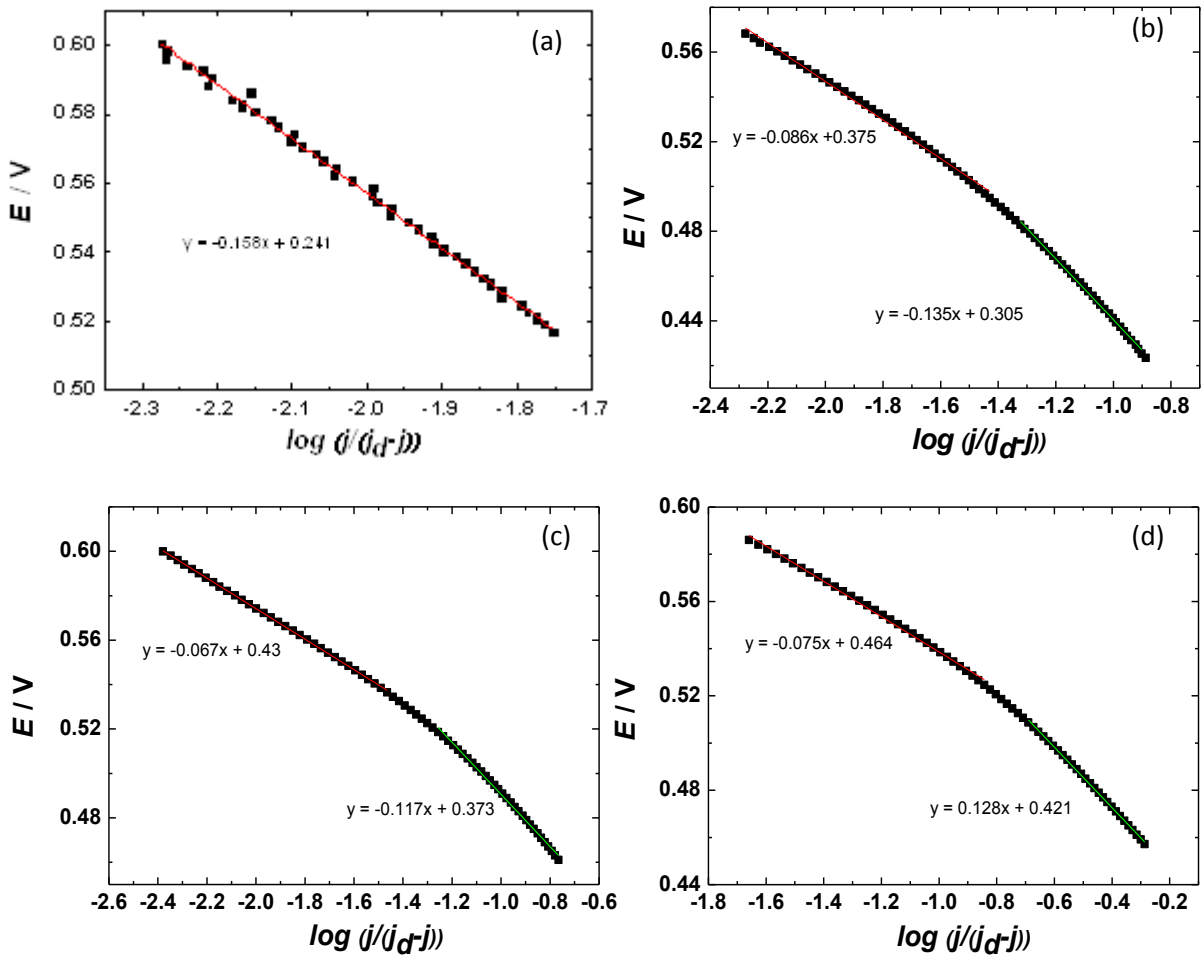

Figure 3.41 Tafel plots for the ORR on sequentially reduced Au:Rh/C (a) 10:1, (b) 7:3, (c) 1:1 and (d) 1:2 nanoparticles.

The Tafel slopes for Au:Rh samples tend to 60 mV dec^{-1} and 120 mV dec^{-1} for lcd and hcd, respectively, similarly to the reports of Pt/Au[33] and Pd/Au[36]. It is likely that the Tafel slope changes with the Rh loading, indicating that the Tafel slope is sensitive to Rh composition on Au surface. The change of slope as a function of potential can be ascribed to the potential dependence of surface oxides coverage, which changes the adsorption of O_2, reaction mechanism and IR drop in the oxide layer. Similar effects have been reported for Pt,[33] Ru[109] and Rh[50,109] surfaces. The thin layer of Rh oxide can cause an increase of Tafel slope at lcd. Thicker Rh oxide layers increase further the Tafel slope at hcd.[50,109]

In order to determine the dependence of electrocatalytic activity on Au−Rh nanoparticle size and morphology, the specific activity (SA) and the mass activities (MA) of O_2 was calculated using the Eqs. (3.15) and (3.16).

$$\mathrm{SA} = \frac{I_\mathrm{k}}{\mathrm{A_r}} \tag{3.15}$$

$$\mathrm{MA} = \frac{I_\mathrm{k}}{\mathrm{m_{Au+Rh}}} \tag{3.16}$$

where I_k is the kinetic current, A_r is the real surface area of Au and Rh and $\mathrm{m_{Au+Rh}}$ is the mass of Au and Rh in this catalyst layer. The SA and MA values acquired for Au−Rh catalysts at 0.4 V (*vs* SCE) are given in Table 3.8 and are presented graphically as a function of composition in Figures 3.42 and 3.43. At this potential, the catalytic activity of the carbon powder and the Au substrate is low and the reduction of O_2 is catalysed only by Rh or the Rh−Au alloy. The specific activity and mass activities determined for Au−Rh catalysts are largely dependent on Rh loadings, size and shape of nanoparticles. The SA values obtained for the Au NRs:Rh catalyst increase upon increasing the Rh loadings. As the size of Au NRs-Rh rods increases with increasing Rh, the specific surface area of rod-shaped catalysts increases, resulting in the increase of specific activities, as shown in Figure 3.42(a). The mass activities of Au−Rh NRs catalysts also increase with increasing Rh loading, suggesting that the increase of catalytic activity depends on Rh loading, as seen in Figure 3.43(a). The specific activity and mass activities of co-reduced Au:Rh nanoparticles are plotted in Figure 3.42(b) and 3.43(b). The specific activity slightly decreases for the samples of 10:1, 7:3 and 1:1 Au:Rh ratio and dramatically decreases for sample of 1:2 Au:Rh ratio, reflecting the fact that the surfaces are Rh-rich for this sample. The mass activities also show a descending trend similar to the trend of specific activity. The specific activity and mass activity of sequentially reduced Au:Rh nanoparticles are plotted in Figure 3.42(c) and 3.43(c). Both SA and MA

values increases until reach a maximum for the sample of 1:1 Au:Rh ratio, suggesting that SA and MA values increase with increasing particle size. The decrease of activity on the sample of 1:2 Au:Rh ratio may result from the increase of particle size and aggregation of particles. The mole activities of the catalysts were also calculated and presented in Figure 3.43(d)-(f).

Table 3.8 Kinetic parameters of oxygen reduction on Au−Rh catalysts at 0.4 V (*vs* RHE).

Catalyst	A_r (cm^2)	m_{Au+Rh} (μg)	SA (mA cm^{-2})	MA (A g^{-1})
Au NRs	0.052	2.97	0.002	0.030
Au NRs:Rh 10:1	0.038	3.12	0.039	0.480
Au NRs:Rh 7:3	0.028	3.73	0.308	2.310
Au NRs:Rh 1:1	0.031	4.51	0.759	5.220
Au NRs:Rh 1:2	0.073	6.05	1.036	12.51
Au	0.144	2.97	0.015	0.710
Rh	0.500	1.54	0.195	63.16
Co-reduced Au:Rh 10:1	0.101	3.12	0.609	19.73
Co-reduced Au:Rh 7:3	0.137	3.73	0.526	19.30
Co-reduced Au:Rh 1:1	0.416	4.51	0.462	42.62
Co-reduced Au:Rh 1:2	0.280	6.05	0.240	11.10
Sequentially reduced Au:Rh 10:1	0.063	3.12	0.207	4.190
Sequentially reduced Au:Rh 7:3	0.045	3.73	1.131	15.82
Sequentially reduced Au:Rh 1:1	0.076	4.51	1.878	31.65
Sequentially reduced Au:Rh 1:2	0.057	6.05	0.994	9.370

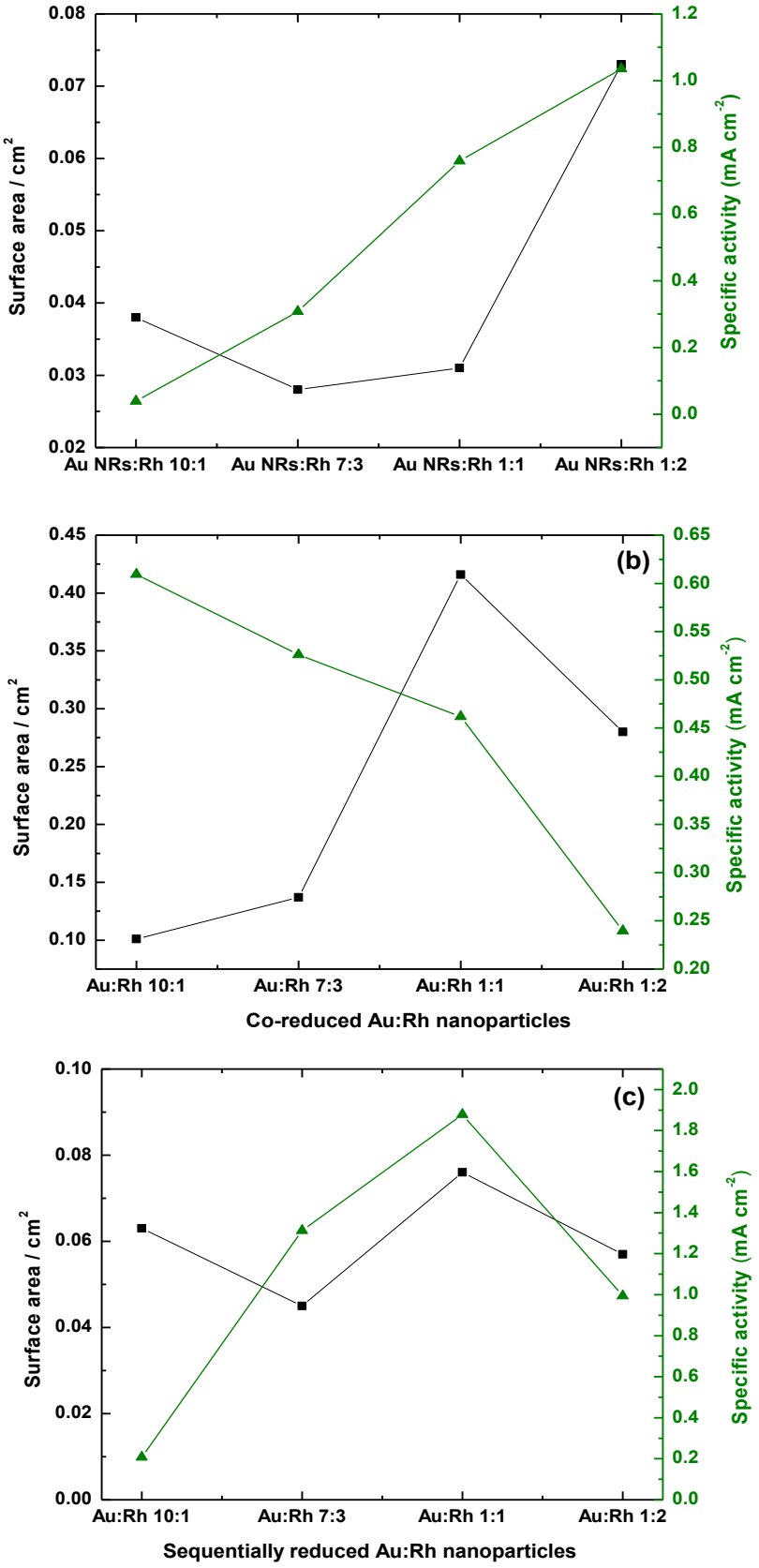

Figure 3.42 Specific surface area (black) and specific activity (green) measured at 0.4 V for (a) Au−Rh NRs (data from Figure3.30), (b) co-reduced Au−Rh nanoparticles (data from Figure3.31) and (c) sequentially reduced Au−Rh nanoparticles (data from Figure3.33).

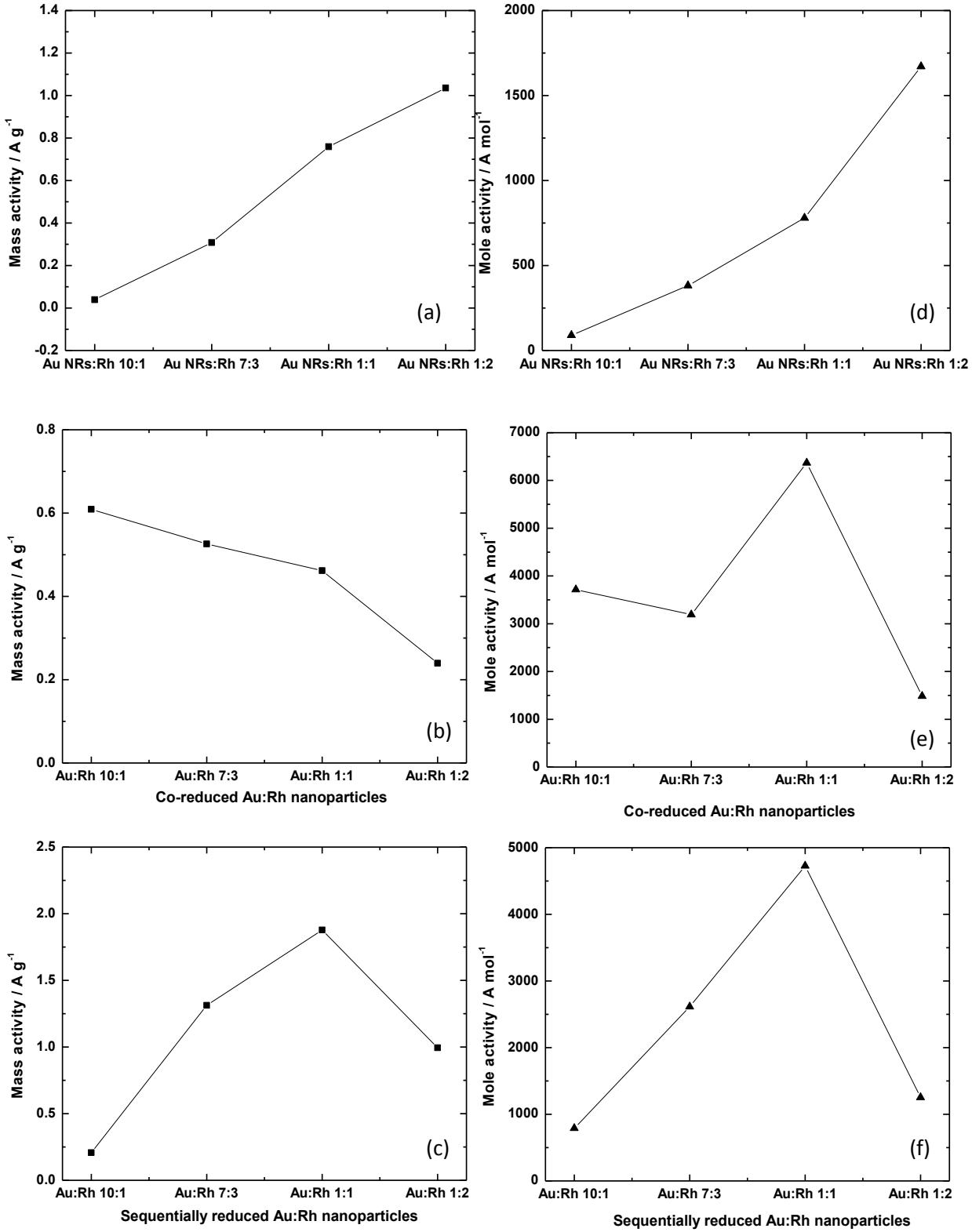

Figure 3.43 Mass activity measured at 0.4 V for (a) Au−Rh NRs (data from Figure3.30), (b) co-reduced Au−Rh nanoparticles (data from Figure3.31) and (c) sequentially reduced Au−Rh nanoparticles (data from Figure3.33). Mole activity measured at 0.4 V for (d) Au−Rh NRs, (e) co-reduced Au−Rh nanoparticles and (f) sequentially reduced Au−Rh nanoparticles.

Different and sometimes contrary observations of specific activity and mass activity have been reported by different research groups. Kinoshita *et al.* attributed the specific activity and mass activity dependency described in: (a) mass activity increase, reaches a maximum and then decreases as the crystallite size increase, (b) specific activity increases as a particle size increase.[110] Watanabe *et al.* reported that: (c) mass activity decreases as the particles size increases, (d) specific activity is independent of the crystallize size.[111] The specific activity and mass activity of Au−Rh NRs and sequentially reduced Au−Rh nanoparticles have similar trend. For Au NRs:Rh catalysts, the SA and MA values increase with increasing Rh content. For sequentially reduced Au:Rh nanoparticles, the SA and MA increase as Rh contents increase but the SA and MA values decrease when big particles (lower surface area) appear. Both trends of Au NRs:Rh and sequentially reduced Au:Rh nanoparticles are supported by the report of Kinoshita *et al.* For co-reduced Au:Rh nanoparticles, the mole activity values is similar to the surface area trend but the trend of mole activity is opposite with the trend of specific surface area. This may explain by the report of Watanabe *et al.* However, the co-reduced Au:Rh of 1:2 ratio sample is an alloy, probably it will present different electronic properties.

3.4 Conclusions

Comparing three types of Au:Rh catalysts, the Rh deposited on Au NR catalyst has lower catalytic mass activity towards the ORR. The lower catalytic activity results from the larger size of Au NRs. The smaller Au seeds have higher surface area, higher curvature and number of defect sites for the Rh deposition. However, if the sizes of Au NRs and Au nanoparticles were comparable, the one-dimensional nanostructure of Rh deposited on Au NRs might present certain advantages over the spherical nanoparticles. For the ORR *via* 4-electron

pathway, the smaller particles containing a Rh-rich phase have higher mass activity than rod-shaped particles. For H_2O_2 generation, Au NRs and Rh deposited on Au NRs display higher selectivity towards H_2O_2 production than the smaller particles, as seen from the number of electrons transferred. The Au NRs:Rh 10:1 catalyst is the most likely candidate for H_2O_2 generation. It is a significant finding that manipulating the composition of the Rh on Au surface enables control of the selectivity of the ORR.

3.5 References

(1) Markovic, N. M.; Schmidt, T. J.; Stamenkovic, V.; Ross, P. N. *Fuel Cells* **2001**, *1*, 105.

(2) Schmidt, T. J.; Paulus, U. A.; Gasteiger, H. A.; Behm, R. J. *Journal of Electroanalytical Chemistry* **2001**, *508*, 41.

(3) Norskov, J. K.; Rossmeisl, J.; Logadottir, A.; Lindqvist, L.; Kitchin, J. R.; Bligaard, T.; Jonsson, H. *Journal of Physical Chemistry B* **2004**, *108*, 17886.

(4) Prieto, A.; Hernandez, J.; Herrero, E.; Feliu, J. M. *Journal of Solid State Electrochemistry* **2003**, *7*, 599.

(5) Sarapuu, A.; Nurmik, M.; Mandar, H.; Rosental, A.; Laaksonen, T.; Kontturi, K.; Schiffrin, D. J.; Tammeveski, K. *Journal of Electroanalytical Chemistry* **2008**, *612*, 78.

(6) Erikson, H.; Jurmann, G.; Sarapuu, A.; Potter, R. J.; Tammeveski, K. *Electrochimica Acta* **2009**, *54*, 7483.

(7) Tang, W.; Lin, H. F.; Kleiman-Shwarsctein, A.; Stucky, G. D.; McFarland, E. W. *Journal of Physical Chemistry C* **2008**, *112*, 10515.

(8) El-Deab, M. S.; Ohsaka, T. *Electrochemistry Communications* **2002**, *4*, 288.

(9) El-Deab, M. S.; Ohsaka, T. *Electrochimica Acta* **2002**, *47*, 4255.

(10) El-Deab, M. S.; Ohsaka, T. *Journal of Electroanalytical Chemistry* **2003**, *553*, 107.

(11) El-Deab, M. S.; Okajima, T.; Ohsaka, T. *Journal of the Electrochemical Society* **2003**, *150*, A851.

(12) El-Deab, M. S.; Sotomura, T.; Ohsaka, T. *Electrochimica Acta* **2006**, *52*, 1792.

(13) El-Deab, M. S.; Sotomura, T.; Ohsaka, T. *Electrochemistry Communications* **2005**, *7*, 29.

(14) El-Deab, M. S.; Sotomura, T.; Ohsaka, T. *Journal of the Electrochemical Society* **2005**, *152*, C1.

(15) Adzic, R. R.; Markovic, N. M.; Vesovic, V. B. *Journal of Electroanalytical Chemistry* **1984**, *165*, 105.

(16) Jirkovsky, J. S.; Halasa, M.; Schiffrin, D. J. *Physical Chemistry Chemical Physics* **2010**, *12*, 8042.

(17) Nikoobakht, B.; El-Sayed, M. A. *Langmuir* **2001**, *17*, 6368.

(18) Nikoobakht, B.; El-Sayed, M. A. *Chemistry of Materials* **2003**, *15*, 1957.

(19) Nikoobakht, B.; Wang, J. P.; El-Sayed, M. A. *Chemical Physics Letters* **2002**, *366*, 17.

(20) Jana, N. R. *Chemical Communications* **2003**, 1950.

(21) Jana, N. R.; Gearheart, L.; Murphy, C. J. *Journal of Physical Chemistry B* **2001**, *105*, 4065.

(22) Jana, N. R.; Gearheart, L.; Murphy, C. J. *Advanced Materials* **2001**, *13*, 1389.

(23) Sharma, V.; Park, K.; Srinivasarao, M. *Materials Science & Engineering R-Reports* **2009**, *65*, 1.

(24) Wu, H. L.; Tsai, H. R.; Hung, Y. T.; Lao, K. U.; Liao, C. W.; Chung, P. J.; Huang, J. S.; Chen, I. C.; Huang, M. H. *Inorganic Chemistry* **2011**, *50*, 8106.

(25) Hernandez, J.; Solla-Gullon, J.; Herrero, E.; Aldaz, A.; Feliu, J. M. *Journal of Physical Chemistry C* **2007**, *111*, 14078.

(26) Wei, H.; Hao, F.; Huang, Y. Z.; Wang, W. Z.; Nordlander, P.; Xu, H. X. *Nano Letters* **2008**, *8*, 2497.

(27) Xu, J. G.; Wilson, A. R.; Rathmell, A. R.; Howe, J.; Chi, M. F.; Wiley, B. J. *Acs Nano* **2011**, *5*, 6119.

(28) Xia, Y. N.; Li, W. Y.; Cobley, C. M.; Chen, J. Y.; Xia, X. H.; Zhang, Q.; Yang, M. X.; Cho, E. C.; Brown, P. K. *Accounts of Chemical Research* **2011**, *44*, 914.

(29) van der Zande, B. M. I.; Bohmer, M. R.; Fokkink, L. G. J.; Schonenberger, C. *Langmuir* **2000**, *16*, 451.

(30) vanderZande, B. M. I.; Bohmer, M. R.; Fokkink, L. G. J.; Schonenberger, C. *Journal of Physical Chemistry B* **1997**, *101*, 852.

(31) Yu, Y. Y.; Chang, S. S.; Lee, C. L.; Wang, C. R. C. *Journal of Physical Chemistry B* **1997**, *101*, 6661.

(32) Maye, M. M.; Kariuki, N. N.; Luo, J.; Han, L.; Njoki, P.; Wang, L. Y.; Lin, Y.; Naslund, H. R.; Zhong, C. J. *Gold Bulletin* **2004**, *37*, 217.

(33) Luo, J.; Njoki, P. N.; Lin, Y.; Wang, L. Y.; Zhong, C. J. *Electrochemistry Communications* **2006**, *8*, 581.

(34) Grzelczak, M.; Perez-Juste, J.; de Abajo, F. J. G.; Liz-Marzan, L. M. *Journal of Physical Chemistry C* **2007**, *111*, 6183.

(35) Naohara, H.; Ye, S.; Uosaki, K. *Electrochimica Acta* **2000**, *45*, 3305.

(36) Sarapuu, A.; Kasikov, A.; Wong, N.; Lucas, C. A.; Sedghi, G.; Nichols, R. J.; Tammeveski, K. *Electrochimica Acta* **2010**, *55*, 6768.

(37) Jirkovsky, J. S.; Panas, I.; Ahlberg, E.; Halasa, M.; Romani, S.; Schiffrin, D. J. *Journal of the American Chemical Society* **2011**, *133*, 19432.

(38) Edwards, J. K.; Ntainjua, E.; Carley, A. F.; Herzing, A. A.; Kiely, C. J.; Hutchings, G. J. *Angewandte Chemie-International Edition* **2009**, *48*, 8512.

(39) Arbib, M.; Zhang, B.; Lazarov, V.; Stoychev, D.; Milchev, A.; Buess-Herman, C. *Journal of Electroanalytical Chemistry* **2001**, *510*, 67.

(40) Altman, E. I.; Colton, R. J. *Surface Science* **1994**, *304*, L400.

(41) Casella, I. G.; Contursi, M. *Journal of Electroanalytical Chemistry* **2007**, *606*, 24.

(42) Liu, C. W.; Wei, Y. C.; Liu, C. C.; Wang, K. W. *Journal of Materials Chemistry* **2012**, *22*, 4641.

(43) He, D. S.; Han, Y.; Fennell, J.; Horswell, S. L.; Li, Z. Y. *Applied Physics Letters* **2012**, *101*.

(44) He, W. W.; Wu, X. C.; Liu, J. B.; Zhang, K.; Chu, W. G.; Feng, L. L.; Hu, X. A.; Zbou, W. Y.; Me, S. S. *Journal of Physical Chemistry C* **2009**, *113*, 10505.

(45) Feng, L. L.; Wu, X. C.; Ren, L. R.; Xiang, Y. J.; He, W. W.; Zhang, K.; Zhou, W. Y.; Xie, S. S. *Chemistry-a European Journal* **2008**, *14*, 9764.

(46) Wang, A. N.; Peng, Q.; Li, Y. D. *Chemistry of Materials* **2011**, *23*, 3217.

(47) Zhang, K.; Xiang, Y. J.; Wu, X. C.; Feng, L. L.; He, W. W.; Liu, J. B.; Zhou, W. Y.; Xie, S. S. *Langmuir* **2009**, *25*, 1162.

(48) Khlebtsov, B. N.; Khanadeev, V. A.; Khlebtsov, N. G. *Optics and Spectroscopy* **2010**, *108*, 59.

(49) Wang, S. Y.; Kristian, N.; Jiang, S. P.; Wang, X. *Electrochemistry Communications* **2008**, *10*, 961.

(50) Gobal, F.; Arab, R. *Electrocatalysis* **2011**, *2*, 42.

(51) Martinovic, J. M.; Sepa, D. B.; Vojnovic, M. V.; Damjanovic, A. *Electrochimica Acta* **1988**, *33*, 1267.

(52) Jin, C.; Xia, W.; Nagaiah, T. C.; Guo, J. S.; Chen, X. X.; Bron, M.; Schuhmann, W.; Muhler, M. *Electrochimica Acta* **2009**, *54*, 7186.

(53) Ziegelbauer, J. M.; Gatewood, D.; Gulla, A. F.; Guinel, M. J. F.; Ernst, F.; Ramaker, D. E.; Mukerjee, S. *Journal of Physical Chemistry C* **2009**, *113*, 6955.

(54) Neergat, M.; Gunasekar, V.; Singh, R. K. *Journal of the Electrochemical Society* **2011**, *158*, B1060.

(55) Cao, D. X.; Wieckowski, A.; Inukai, J.; Alonso-Vante, N. *Journal of the Electrochemical Society* **2006**, *153*, A869.

(56) Poirier, J. A.; Stoner, G. E. *Journal of the Electrochemical Society* **1995**, *142*, 1127.

(57) Lukaszewski, M.; Siwek, H.; Czerwinski, A. *Electrochimica Acta* **2007**, *52*, 4560.

(58) Zelenay, P.; Horanyi, G.; Rhee, C. K.; Wieckowski, A. *Journal of Electroanalytical Chemistry* **1991**, *300*, 499.

(59) Jerkiewicz, G.; Borodzinski, J. J. *Langmuir* **1993**, *9*, 2202.

(60) Jerkiewicz, G.; Borodzinski, J. J. *Journal of the Chemical Society-Faraday Transactions* **1994**, *90*, 3669.

(61) Karschin, A.; Katsounaros, I.; Klemm, S. O.; Meier, J. C.; Mayrhofer, K. J. J. *Electrochimica Acta* **2012**, *70*, 355.

(62) Villiard, F.; Jerkiewicz, G. *Canadian Journal of Chemistry-Revue Canadienne De Chimie* **1997**, *75*, 1656.

(63) Chantry, R. L.; Siriwatcharapiboon, W.; Horswell, S. L.; Logsdail, A. J.; Johnston, R. L.; Li, Z. Y. *Journal of Physical Chemistry C* **2012**, *116*, 10312.

(64) Wang, Z. L.; Mohamed, M. B.; Link, S.; El-Sayed, M. A. *Surface Science* **1999**, *440*, L809.

(65) Li, Z. Y.; Yuan, J.; Chen, Y.; Palmer, R. E.; Wilcoxon, J. P. *Applied Physics Letters* **2005**, *87*.

(66) Grzelczak, M.; Perez-Juste, J.; Rodriguez-Gonzalez, B.; Liz-Marzan, L. M. *Journal of Materials Chemistry* **2006**, *16*, 3946.

(67) Liu, M. Z.; Guyot-Sionnest, P. *Journal of Physical Chemistry B* **2005**, *109*, 22192.

(68) Huang, C. C.; Yang, Z. S.; Chang, H. T. *Langmuir* **2004**, *20*, 6089.

(69) Perez-Juste, J.; Liz-Marzan, L. M.; Carnie, S.; Chan, D. Y. C.; Mulvaney, P. *Advanced Functional Materials* **2004**, *14*, 571.

(70) Kittel, C. *Introduction to Solid State Physics*; 7th ed.; John Wiley & Sons: New York, 1996.

(71) Kukovecz A., P. G., Oszko A., Konya Z., Erdohelyi A. and Kiss J. **2011**, *605*, 1048.

(72) Ovari, L.; Bugyi, L.; Majzik, Z.; Berko, A.; Kiss, J. *Journal of Physical Chemistry C* **2008**, *112*, 18011.

(73) Kusada, K.; Yamauchi, M.; Kobayashi, H.; Kitagawa, H.; Kubota, Y. *Journal of the American Chemical Society* **2010**, *132*, 15896.

(74) Essinger-Hileman, E. R.; DeCicco, D.; Bondi, J. F.; Schaak, R. E. *Abstracts of Papers of the American Chemical Society* **2011**, *242*.

(75) Peng, Z.; Yang, H. *Journal of Solid State Chemistry* **2008**, *181*, 1546.

(76) Chantry, R. L.; Siriwatcharapiboon, W.; Horswell, S. L.; Khanal, B. P.; R., Z. E.; I., A.; L., J. R.; Y., L. Z. *Nanoscale* **2013**, *5*, 7452.

(77) Kibler, L. A. K., M.; Kolb, D. M. *J. Electroanal. Chem.* **1999**, *467*, 249−257.

(78) Ferrer, D.; Torres-Castro, A.; Gao, X.; Sepulveda-Guzman, S.; Ortiz-Mendez, U.; Jose-Yacaman, M. *Nano Letters* **2007**, *7*, 1701.

(79) Link, S.; Burda, C.; Wang, Z. L.; El-Sayed, M. A. *Journal of Chemical Physics* **1999**, *111*, 1255.

(80) Park, K., Georgia Institute of Technology, 2006.

(81) Gou, L. F.; Murphy, C. J. *Chemistry of Materials* **2005**, *17*, 3668.

(82) Orendorff, C. J.; Murphy, C. J. *Journal of Physical Chemistry B* **2006**, *110*, 3990.

(83) Fennell, J.; He, D.; Tanyi, A. M.; Logsdail, A. L.; Johnston, R. L.; Li, Z. Y.; L., H. S. *J. Am. Chem. Soc. 135* **2013**, *135*, 6554.

(84) El-Sayed, M. A. *Accounts of Chemical Research* **2001**, *34*, 257.

(85) Orendorff, C. J.; Sau, T. K.; Murphy, C. J. *Small* **2006**, *2*, 636.

(86) Mahendia, S.; Tomar, A. K.; Chahal, R. P.; Goyal, P.; Kumar, S. *Journal of Physics D-Applied Physics* **2011**, *44*.

(87) Zeng, J. H.; Yang, J.; Lee, J. Y.; Zhou, W. J. *Journal of Physical Chemistry B* **2006**, *110*, 24606.

(88) Di Noto, V.; Negro, E.; Vezzu, K.; Toniolo, L.; Pace, G. *Electrochimica Acta* **2011**, *57*, 257.

(89) Grass, M. E.; Zhang, Y. W.; Butcher, D. R.; Park, J. Y.; Li, Y. M.; Bluhm, H.; Bratlie, K. M.; Zhang, T. F.; Somorjai, G. A. *Angewandte Chemie-International Edition* **2008**, *47*, 8893.

(90) Toth, M.; Kiss, J.; Oszko, A.; Potari, G.; Laszlo, B.; Erdohelyi, A. *Topics in Catalysis* **2012**, *55*, 747.

(91) Li Z., G. F., Wang Y., Calaza F., Burkholder L., Tysoe W. T. *Surface Science* **2007**, *601*, 1898.

(92) Raskó J., K. Á., Baánb K. and Kissb J. *React.Kinet.Catal.Lett.* **2007**, *90*, 187.

(93) Ohashi, K.; Sasaki, K.; Nagaura, S. *Bulletin of the Chemical Society of Japan* **1966**, *39*, 2066.

(94) Wasberg, M.; Horanyi, G. *Journal of Electroanalytical Chemistry* **1995**, *386*, 213.

(95) Sverdlova, N. D.; Schafer, W.; Mansurov, G. N.; Petrii, O. A. *Russian Journal of Electrochemistry* **1995**, *31*, 227.

(96) Florit, M. I.; Bolzan, A. E.; Arvia, A. J. *Journal of Electroanalytical Chemistry* **1995**, *394*, 253.

(97) Losiewicz, B.; Jurczakowski, R.; Lasia, A. *Electrochimica Acta* **2011**, *56*, 5746.

(98) Tremiliosifilho, G.; Jerkiewicz, G.; Conway, B. E. *Langmuir* **1992**, *8*, 658.

(99) Conway, B. E.; Tremiliosifilho, G.; Jerkiewicz, G. *Journal of Electroanalytical Chemistry* **1991**, *297*, 435.

(100) Shingaya, Y.; Ito, M. *Journal of Electroanalytical Chemistry* **1999**, *467*, 299.

(101) Shingaya, Y.; Ito, M. *Journal of Electroanalytical Chemistry* **1994**, *372*, 283.

(102) Adzic, R. R.; Strbac, S.; Anastasijevic, N. *Materials Chemistry and Physics* **1989**, *22*, 349.

(103) A.J. Bard, L. R. F. **1980**.

(104) Metikos-Hukovic, M.; Babic, R.; Jovic, F.; Grubac, Z. *Electrochimica Acta* **2006**, *51*, 1157.

(105) Pletcher, D. *A First Course in Electrode Processess*; 2 ed.; The Royal Society of Chemistry: Cambrige, 2009.

(106) Hernandez, J.; Solla-Gullon, J.; Herrero, E. *Journal of Electroanalytical Chemistry* **2004**, *574*, 185.

(107) Hernandez, J.; Solla-Gullon, J.; Herrero, E.; Aldaz, A.; Feliu, J. M. *Journal of Physical Chemistry B* **2005**, *109*, 12651.

(108) Yeager, E. *J Electrochem Soc* **1984**, *128*, 160.

(109) Anastasijevic, N. A.; Dimitrijevic, Z. M.; Adzic, R. R. *Journal of Electroanalytical Chemistry* **1986**, *199*, 351.

(110) Kinoshita, K. *Journal of the Electrochemical Society* **1990**, *137*, 845.

(111) Watanabe, M.; Sei, H.; Stonehart, P. *Journal of Electroanalytical Chemistry* **1989**, *261*, 375.

CHAPTER 4

COBALT-BASED CATALYSTS TOWARDS HYDROGEN PEROXIDE FORMATION DURING OXYGEN REDUCTION

4.1 Introduction

Around 1.2 million tons of H_2O_2 are being manufactured every year. H_2O_2 was first manufactured in 1818 by Louis Jacques Thenard by reacting barium peroxide with nitric acid. The production has been improved and has been used industrially since the mid-19th century. The current method to produce H_2O_2 is an auto-oxidation process, which is an indirect process, based on sequential hydrogenation and oxidation of an anthraquinone. Disadvantages, such as the fact that production cannot be implemented at the point of use, high energy consumption and waste generation, have had a negative effect on the sustainability and on product cost. The necessity of a simple production process, which can be implemented at the point of use, is the goal for the industries concerned.

One of the most extensively studied reactions in electrochemistry is the oxygen reduction reaction (ORR), which results in the formation of H_2O_2 or the formation of H_2O. It is known that the ORR is the major limit on the performance of the proton exchange membrane fuel cell (PEM fuel cell). Pt has been widely used to catalyse the ORR. As a result of the high cost of Pt, approaches to reduce Pt loading on the catalyst and to seek an alternative catalyst for the ORR have been intensively studied. In the short-term, metallic alloys of Pt/X catalysts, where X is usually a transition metal, have been considered as alternative catalysts. In the long-term, non-precious metal catalysts, such as Fe and Co, could be a sustainable solution. Non-precious metal catalysts for the ORR have been studied over several decades, as they present remarkable catalytic activity and selectivity. Fe and Co can

form metal complexes with nitrogen-containing precursors, such as polyacrylonitrile,[1,2] pyrrole polymer,[3-6] ammonia,[7] acetonitrile[8] etc.[9] Metal-N_4 macrocycles are good candidates for a nitrogen source.[10-19] Co-N_4 macrocycles catalyse the oxygen reduction with both $2e^-$ and $4e^-$ pathways depending on preparation conditions, whereas the ORR on Pt proceeds *via* the $4e^-$ pathways.[20-23] Thus, selectivity may be turned towards H_2O_2 production or H_2O production. However, the activity and stability of these catalysts are still lower than those of Pt. The activity, stability and selectivity of the catalyst depend on the synthesis method, metal precursor, ligand, carbon support, heat treatment etc.

Jasinski *et al.* were the first authors to report a non-precious metal with nitrogen-containing macrocycle as a catalyst for the ORR.[24] It was found that Co-phthalocyanine exhibited catalytic activity for the ORR. The major obstacle for exploiting this catalyst is its low stability in acidic media because fuel cell technology is created around acidic conditions.[9,25,26] The low stability of this catalyst may a result of loss of active sites. Hydrogen peroxide produced during the ORR can destroy the active sites.[27-29] In order to increase the stability and catalytic activity, heat treatment has been introduced into the preparation conditions of metal-N_4 macrocycles under an inert atmosphere.[30] Yeager found heat treatment to be important in yielding better catalytic stability and activity using cobalt tetramethoxyphenyl porphyrin (TMPP).[31-36] The heat treatment has an effect on the formation of catalytic sites. The M-N_4 active sites may be partially or fully decomposed to form M-N_2 or to form new active sites, which are no longer M-N_x. The long-term stability issues and the tendency of these materials to promote hydrogen peroxide as a two-electron reduction product are considered for their use in mainstream fuel cell technology.

Most preparations of Co-N_x catalysts have related to the impregnation of Co-N_x complexes into carbon supports and pyrolysis. A metal precursor, N-containing ligand, carbon

support and heat treatment are required to form the active sites. For N-containing ligands, Gupta *et al.* initiated the first catalyst for the ORR from polyacrylonitrile, a N-containing polymer, instead of from N_4 macrocycles.[37] Gouérec *et al*. studied Co-based ORR electrocatalysts using three types of tetraphenylporphyrin (TPP) as electron donor and acceptor, followed by heat treatment.[19,38] After heat treatment up to 600°C, Co oxide formation was found, depending on the type of TPP ligands. They also studied a cobalt tetraazaannulene, CoTAA, which exhibited good activity and stability with heat treatment at 600°C. Okada *et al*.[39] and Lin *et al.*[40] studied the selectivity towards H_2O_2 of Co with aza complexes, with aminophenylmoiety and with tetraphenyl porphyrin (CoTPP) catalysts.

The role of the metallic centre is still unclear. It may form the active site with a ligand or may act as catalyst to promote the active site formation. Ohms *et al.* prepared catalysts from various metal MSO_4 precursors, such as Fe, Co, Mn, Ni, Cu and also $ZnCl_2$, with polyacrylonitrile.[41] They reported that the activity for the ORR depends on the metals. Fe catalyses the reaction *via* a quasi-four electron pathway. Ohms also suggested that Fe-N_x can catalyst the ORR and generate water as the main product.

The metal loading effect on the catalytic activity is determined by other factors, such as metal precursor, carbon support and heat treatment conditions. Typical results of metal loading show that the activity increases until reaching a maximum at saturation and decreases after that level. In the case of Fe, metal overloading leads to the formation of metallic and/or carbidic metal clusters, which have low activity for the ORR.[42-44] Metal loading also affects the surface area of the carbon support by blocking the pores in the surface.[45] Guillet *et al.* studied a pyrolyzed cobalt-based catalyst (CoPP) and reported that the catalytic performance depended on the loading of cobalt.[46] They also assumed that a fraction of H_2O_2 produced on

the catalytic site may be reduced at another catalytic site before leaving the catalytic layer. Li *et al*. found similar results using cobalt with tripyridyltriazine (CoTPTZ).[47]

The carbon support is a key factor for the activity and stability of the metal macrocycle catalysts. Different carbon supports have different attributes, for example, porosity, crystallinity, conductivity, surface area etc. Carbon black, activated carbon and graphite have been normally used as supports, particularly, Vulcan XC-72R[48-52] and Black Pearls 2000[12,13,53-56]. Black Pearls 2000 (BP 2000) and Vulcan XC-72R have a high conductivity with specific surface areas of ca. 1400 m^2/g and ca. 250 m^2/g, respectively.[57] The dispersion of catalyst on the support is sensitive to the carbon support surface, for example, the distribution of Pt/Ru particles on Vulcan XC 72R is more uniform than on BP 2000. It has also been reported that the N concentration in the carbon support is one of the factors affecting the catalytic activity on the ORR[58-61]. High N-concentration in the carbon support yields high ORR electrocatalytic activity. On Co-N_x catalysts, it was observed that heat treatment can decompose oxygen species in the carbon surface to CO_2 or CO, improving the deposition of N on the surface. It was observed that the oxygen groups in the surface decrease the disruption of chelate structure by heat treatment, which would otherwise lead to retarding the formation of active sites[62,63]. Metal impurities in the carbon surface also need to be controlled because they can influence the catalytic activity.

The influence of heat treatment on metal N-containing catalysts is still unclear. Possible models for this effect include:[64] (a) heat treatment enhances the dispersion of the chelate structures, (b) heat treatment catalyses the formation of active sites, (c) heat treatment produces M-N_x active sites, (d) heat treatment promotes and modifies the electronic structure of the active sites so that their abilities to transfer electron are improved. Lalande *et al*. investigated the effect on heat treatment on tetracarboxylic Co phthalocyanide.[65] The nature of

the active sites changed with treatment temperature. A polymerisation reaction competition happens at 400 °C. The formation of a Co-phthalocyanine polymer is stable at a temperature between 500-600 °C. The fragmentation of the chelate structure starts at around 700 °C, generating Co bound to C and N on the surface. It has been noticed that only Co and Co (II) are detectable on the support when the materials were heated to above 700 °C. When the treatment temperature was raised to 1000 °C, Co was still found but the Co (II)-N macrocycle was not detected. Many papers reveal that an M-N_4 moiety can still remain at the lower temperature and that it tends to produce hydrogen peroxide in the ORR.[65-69] At medium temperatures, M-N_4 is gradually transformed to M-N_2, which tends to produce water in the ORR. The existence of M-N_x is negligible at high temperature and metal particles are instead detected. It is agreed that the metal particle is formed inside a graphite shell, depressing the catalytic activity. In accordance with many studies,[70,71] the final active sites of the catalysts after heat treatment should be similar, even if different metal precursor(s) or N-source(s) have been used. The heat treatment also increases the stability of the catalyst with the formation of the carbon layer surrounding the metal particles.[65]

Zhang *et al*. published a number of studies of Co catalyst with the metal centre coordinated by aliphatic nitrogen ligands.[20-23,72,73] The values of *n*, the number of electrons transferred per oxygen molecule turn-over during reduction, vary between two and four and turn back towards two as the pyrolysis temperature of the catalyst is increased from 500 °C to 1000 °C.[72] McBeen used EXAFS to analyse the active site left after pyrolysis of ligand-coordinated metal on the carbon support, suggesting that the metal ions substantially interact with retention of square-planar nitrogen coordination;[74] however, the formation of metallic particles was found under their conditions and this complicated the analysis.[75]

In the present work, we prepared Co/TETA/C catalysts with the procedure of Zhang *et al.*[72] and investigated the formation of active sites during heat treatment in more detail compared with the work from Zhang *et al.*[72] The rotating ring disc electrode was used to evaluate the selectivity of the ORR, as well as the kinetics. Hydrogen peroxide reduction at the catalysts was also studied to provide a more complete analysis of the reaction kinetics.

4.2 Experimental

4.2.1 Materials

Cobalt (II) chloride hexahydrate ($CoCl_2 \bullet 6H_2O$), 99.99% was obtained from Alfa Aesar Triethylenetetraamine (TETA), 97%, and hydrogen peroxide, 35%, were purchased from Sigma-Aldrich. Perchloric acid, double-distilled, 70%, was obtained from Veritas. Carbon black (BP2000) was obtained from Cabot (US). Ultrapure water (purified with a Milli-Q tandem Elix-Gradient A10 system: resistivity 18.2 MΩ cm, TOC ≤ 5 ppb) was used throughout. All glassware used was first cleaned by heating in a mixture of concentrated nitric and sulphuric acids for 1.5 h, followed by rinsing with copious quantities of ultrapure water and soaking overnight in ultrapure water.

4.2.2 Catalyst preparation

The Co/TETA/C catalysts were prepared according to the method reported by Zhang *et al.*[20,23] with a nominal loading of 10% w/w metal. In this study, we used a typical loading of 5% (w/w). Co 6.06 g cobalt (II) chloride was dissolved in 300 mL of absolute ethanol at room temperature. 15 ml 6 mM TETA was added to this solution to form the Co-TETA chelate. 15 g carbon support (BP 2000) was added to the mixture and stirred for 1 h. The suspension was filtered and dried to remove ethanol by rotary evaporator. The resulting powder was

divided and heat-treated in Ar atmosphere at various temperatures, including 300, 500, 700 and 1000 ºC, for 90 min at a heating rate of 10 ºC min^{-1}. The final loading of 5% (w/w) Co, after heat treatment, was confirmed by inductively coupled plasma mass spectrometry (ICP-MS). The catalyst preparation is shown in Scheme 4.1. The TETA/C control catalysts were prepared by the same route. TETA/C and C powder were heat-treated in the same way. 2% of Co/C commercial grade was used as a control against our catalyst.

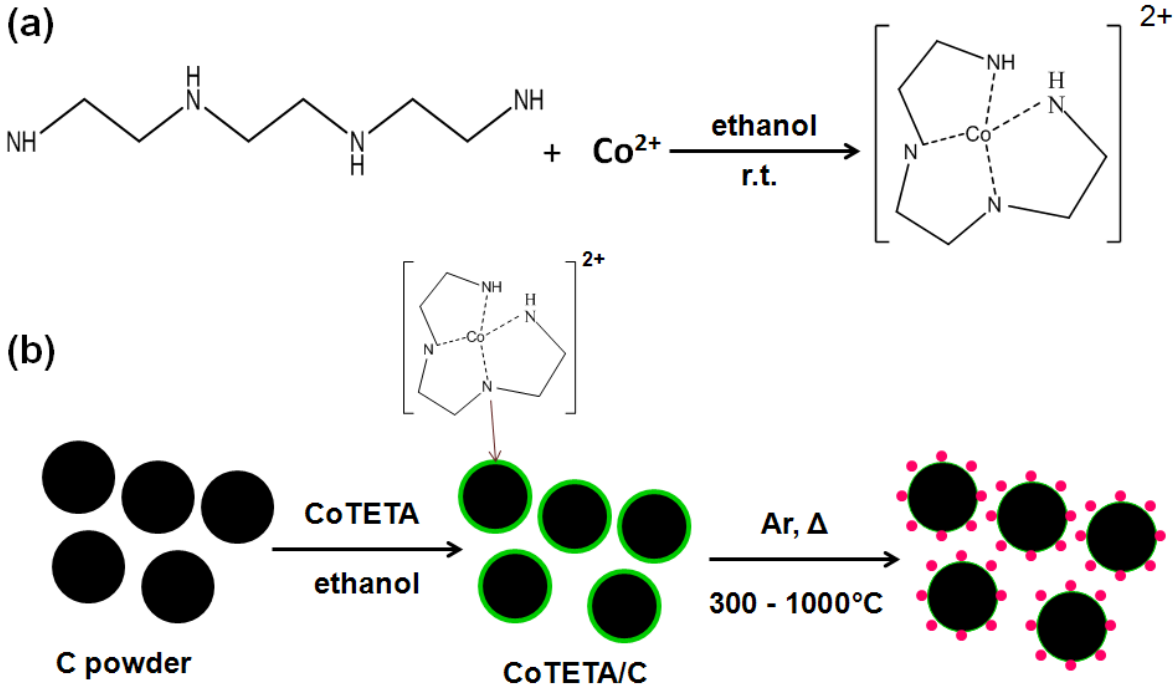

Scheme 4.1 Schematic illustration of (a) the reaction equation of the Co/TETA and (b) the preparation of Co/TETA/C catalysts.[20]

4.2.3 Electrocatalyst characterisation

Samples for Transmission Electron Microscopy (TEM) were prepared by dusting a crushed sample of the catalyst onto a holey carbon/Cu grid. TEM images were obtained by a Tecnai F20 Transmission Electron Microscope, with an acceleration voltage of 200 kV. A C_2 aperture of 30 µm or 50 µm was used; both bright field (BF)[76,77] and high angle annular dark field (HAADF)[78] modes of imaging were employed. High resolution HAADF images for the Co-

containing catalysts were acquired with an aberration correction of 1.2 mm. Energy dispersive X-ray spectroscopy (EDX) was employed to ascertain the distribution of cobalt across the samples. Powder X-ray diffraction (XRD) measurements were carried out with a Bruker AXS D-500 diffractometer using a stationary X-ray source Cu Kα and a movable detector, which scans the intensity of the diffracted radiation as a function of the angle between the incoming and the diffracted beams ($10° < 2\theta < 90°$). The sample powder is spread over a glass holder and then pressed to obtain a flat coverage. The data were interpreted by the ICDD database (PDF-2, Release 2003). Thermogravimetric analysis was performed with a TA Instruments SDT Q600 device.

4.2.4 Electrochemical measurements

Three sets of electrochemical measurements were performed including cyclic voltammetry (CV), rotating disk electrode (RDE) measurements for hydrogen peroxide reduction and rotating ring disk electrode (RRDE) measurements for oxygen reduction.

CV and RDE measurements were performed with a glassy carbon rotating disk electrode (0.071 cm^2, Radiometer, Copenhagen) and an Autolab PGStat12 potentiostat (Ecochemie, NL), controlled by the General Purpose Elecrochemical System (GPES) software. The counter and reference electrodes were a Pt coil and a saturated calomel electrode (SCE), respectively. RRDE measurements were obtained using an Autolab PGStat 30 potentiostat and a rotating ring disk set-up (Pine Company, Grove City, PA, US) with glassy carbon disk of area 0.247 cm^2 and Pt ring, controlled with a Modulated Speed Rotator. For RRDE measurements, the ring potential was set at 1.2 V for the quantitative detection of the peroxide produced at the disk. A collection efficiency of 0.4 was determined from independent measurements of potassium hexacyanoferrate (III) reduction. The counter and

reference electrodes used were a Pt coil and a reversible hydrogen electrode (RHE). All potentials quoted in this work are referenced to the RHE. Measurements were carried out with a controlled atmosphere and temperature (298 K). The electrolyte was 0.1 M $HClO_4$.

The working electrode was prepared according to the method described in reference.[79] The catalyst ink was deposited on the working electrode and dried in air. Typically, 1 mg of catalyst was added to 1 mg of deionised water and subsequently sonicated for three minutes at 0 ºC. 13 μL of the resulting black suspension was pipetted onto the surface of the glassy carbon disc, which was then dried under an infrared lamp for 10 min. This procedure produced loadings on the disc of 13 μg of catalyst, corresponding to a loading of approximately 5 μg per cm^2 disc. The working electrode was activated in Ar-saturated electrolyte solution by scanning the potential between 0.0 V and 1.2 V at a scan rate of 0.02 V s^{-1}. Oxygen reduction reactions (ORR) were then performed in oxygen-saturated electrolyte or hydrogen peroxide reduction measurements were carried out in argon-saturated electrolyte with a concentration of 20 mM H_2O_2. The potential scan rate employed was 0.02 V s^{-1}. For oxygen reduction, background currents measured in N_2 were subtracted from single-wave polarisation curves on rotating disc electrode.

4.3 Results and Discussion

4.3.1 Electrocatalyst characterisation

The XRD data was provided and analysed by Dr. Hoy Dobson, Johnson Matthey Technology Centre. Figure 4.1 presents XRD patterns of 2% Co/C, heat-treated at different temperatures. The ICDD database (PDF-2, release 2003) was used to interpret the data. The broad peak at 2θ=25° is observed in all the samples and arises from C (002) reflections of carbon supports, determined by comparative XRD patterns of carbon supports. An untreated Co/C sample shows only broad peaks of Co_3O_4, while the sample treated at 500 ºC presents cubic CoO and Co_3O_4 features, as shown in Figure 4.1(a) and (b). The face-centered cubic (fcc) crystalline α-Co phase is detected in the sample treated at 900 ºC in Figure 4.1(c).

Figure 4.2 shows the XRD pattern of Co/TETA/C heat-treated at different temperatures. The broad peak at 2θ=25° is weaker in comparison to those observed in Co/C samples, suggesting the presence of TETA on the surface. The crystalline fcc cubic Co is not visible in the sample heat-treated at 300 ºC and 500 ºC. Fcc cubic Co is detected in the samples treated at 700 ºC and 1000 ºC. The trends observed in non TETA-containing and TETA-containing samples are similar. The sharp peaks of Co(111), Co(200) and Co(220) on the XRD pattern increase with the treating temperature, which suggests that metallic Co aggregation occurs at high temperature.[72,80]

The crystallite size of each sample was determined by Scherrer's equation.[81]

$$B(2\theta) = \frac{K\lambda}{Lcos\theta} \qquad (4.1)$$

where, B is the peak width at half the maximum intensity, K is Scherrer's constant, λ is the wavelength of X-ray, L is the is the mean size of the ordered (crystalline) domains, θ is half of the diffraction angle. The peak width is inversely proportional to the crystallite size. The crystallite size values obtained from Co (111) peak of Co/TETA/C 1000 °C and 700 °C are

5.5 and 3.0 nm, respectively. These values present that the crystallite size of metallic Co increases with increasing treated temperature.

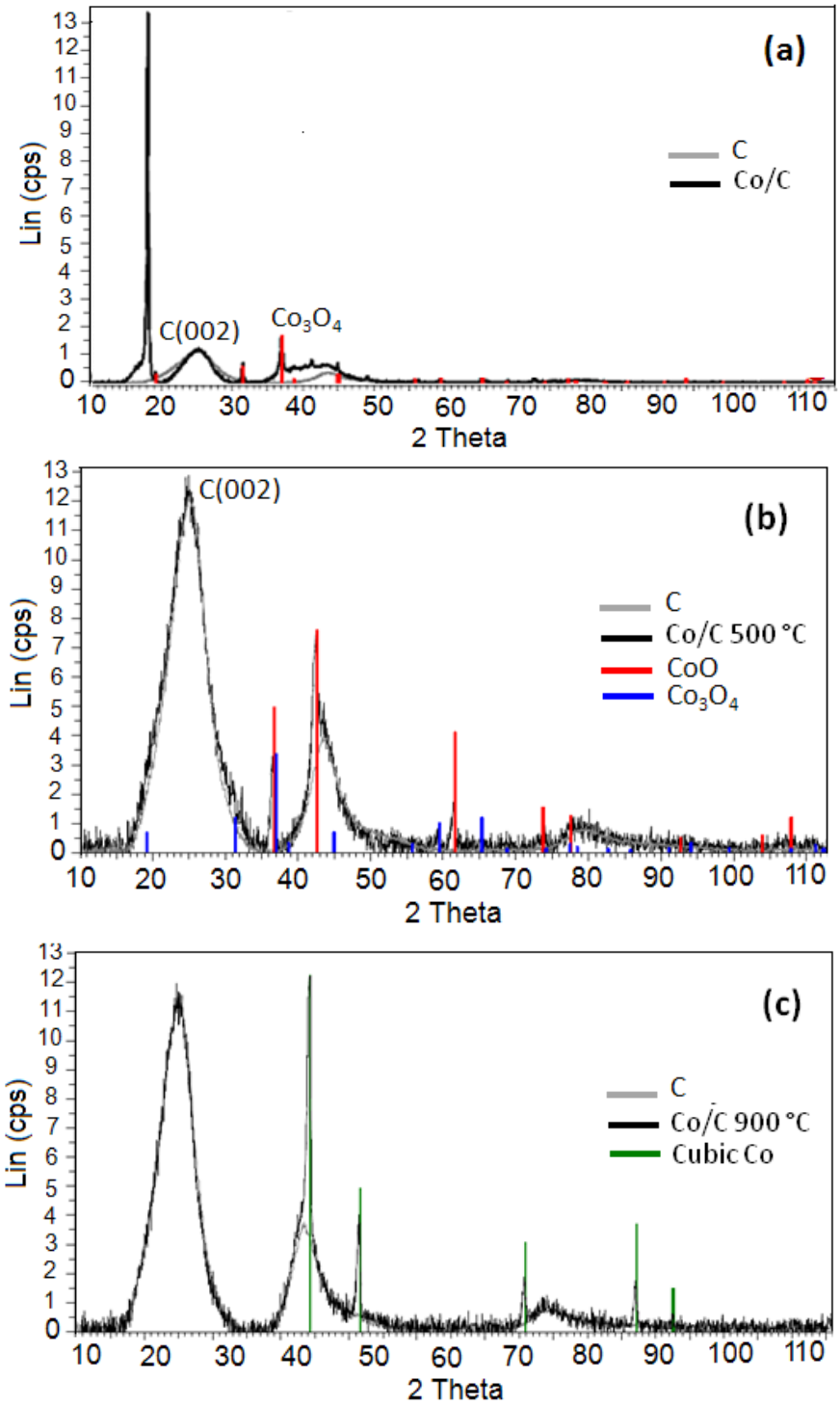

Figure 4.1 X-ray diffraction patterns of Co/C catalysts (a) untreated (b) heat-treated at 500 °C and (c) 900 °C.

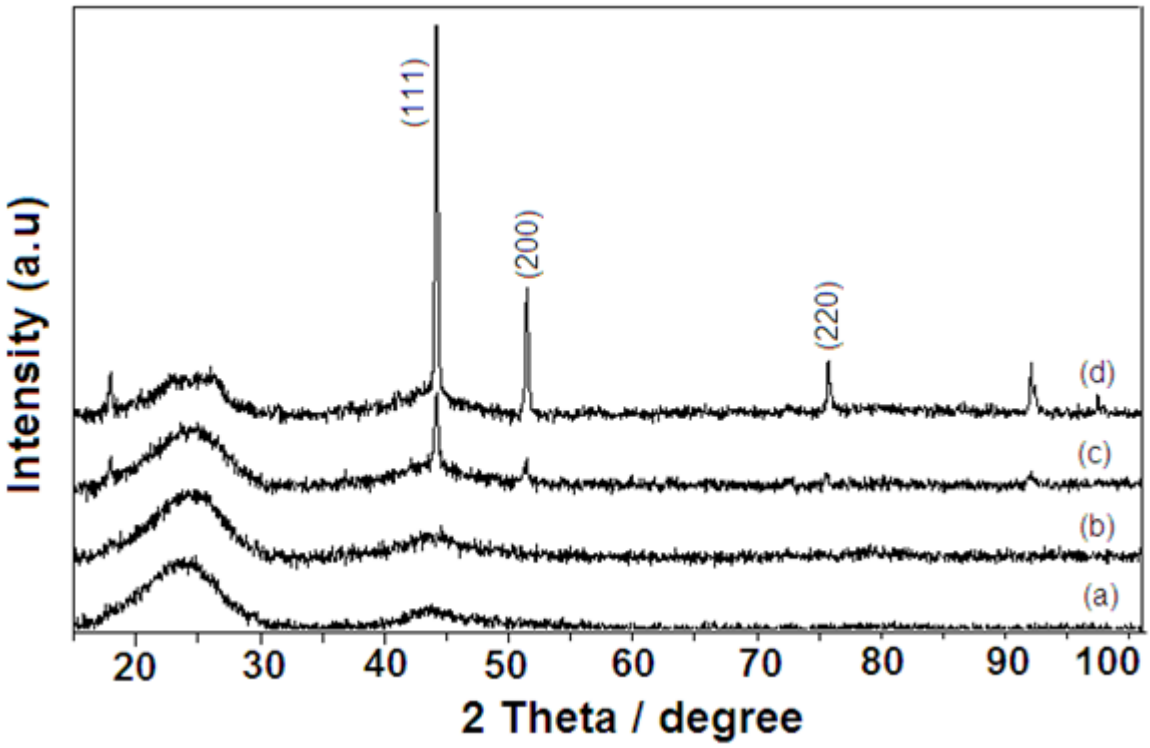

Figure 4.2 X-ray diffraction patterns of Co/TETA/C catalysts (a) heat-treated at 300 °C, (b) 500 °C, (c) 700 °C and (d) 1000 °C.

The morphology of the catalysts were analysed by TEM. The TEM images were provided and analysed by Dr. Sarennah Longworth, Johnson Matthey Technology Centre. Figure 4.3 presents the TEM image of C-only sample. Figures 4.4(a) – 4.11(a) show TEM images of Co/TETA/C and TETA/C samples treated at different temperatures. The large areas observed in all samples are attributes of functional carbon from the carbon support, which is similar to the C-only sample. Charging behaviour under the electron beam was observed from all Co/TETA/C samples. This effect may be due to the presence of TETA on the carbon support, as is observed for the TETA/C samples. The charging behaviour appears to worsen with increasing treatment temperature. A small amount of black particles diffusely distributed on carbon support are observed in Co/TETA/C samples. These particles might be the presence of a Co phase on carbon surfaces. In order to obtain a better understanding of the particle distribution on the carbon support, HAADF was used in the STEM mode. At high resolutions,

HAADF imaging reveals the atomic structure as a function of atomic number. Representative HAADF for the Co/TETA/C and TETA/C are shown in Figures 4.4-4.7(b) and Figures 4.8-4.11(b), respectively. The Co/TETA/C samples treated at various temperatures (300 °C, 500 °C and 700 °C) show the distributed Co particles while the dark field image of 1000 °C Co/TETA/C sample shows large particles, which cannot be observed in the other heat-treated samples or the TETA/C sample treated at 1000 °C. EDX was used to confirm the presence of Co at the area containing distributed small and large particles. Results verified that the large particles observed from 1000 °C Co/TETA/C were indeed Co. There is a significantly higher Co content present in the area containing large particles in comparison with the area containing distributed small particles, as shown on the EDX pattern in Figure 4.4-4.7(c). Both EDX and XRD suggest that the sharp peak for the fcc cubic Co in the 1000 °C Co/TETA/C sample is attributed to the aggregation of metallic Co. Basically, the metallic Co and Co oxide have low catalytic activity toward the ORR.[20] In order to prevent the Co metallic and Co oxide formations, the Co/TETA/C samples should not be heat treated at a temperature higher than 800 °C.[47] Some Ca contamination was found in the TETA/C samples, as shown from EDX in Figure 4.8-4.11(c).

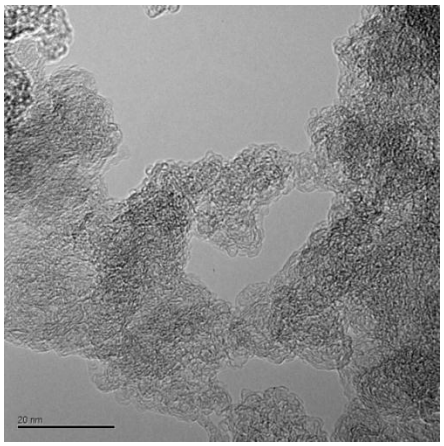

Figure 4.3 TEM image of carbon substrate.

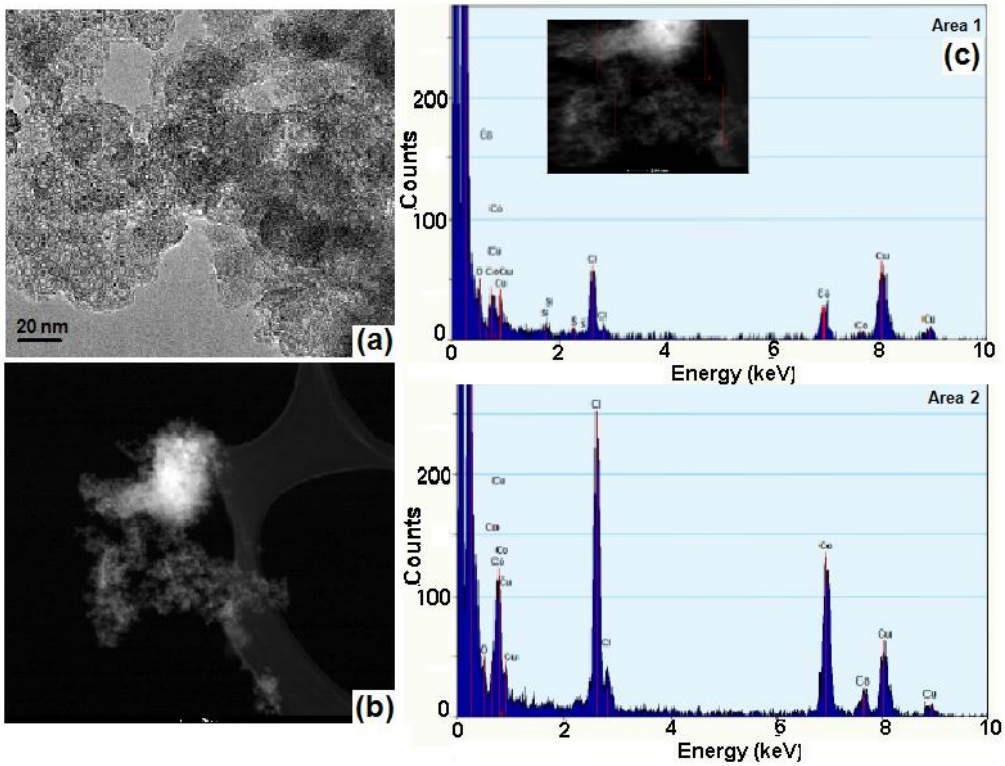

Figure 4.4 (a) TEM image of Co/TETA/C catalyst heat-treated at 300 °C, (b) HAADF image and (c) EDX analysis of Area 1 and Area 2.

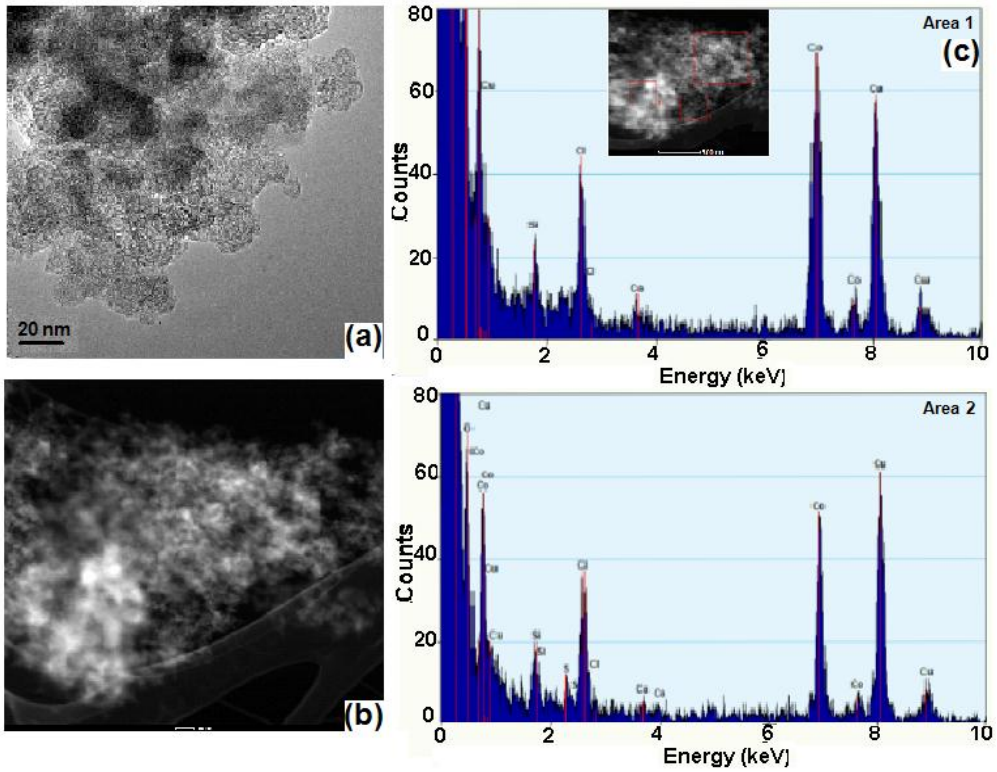

Figure 4.5 (a) TEM image of Co/TETA/C catalyst heat-treated at 500 °C, (b) HAADF image and (c) EDX analysis of Area 1 and Area 2.

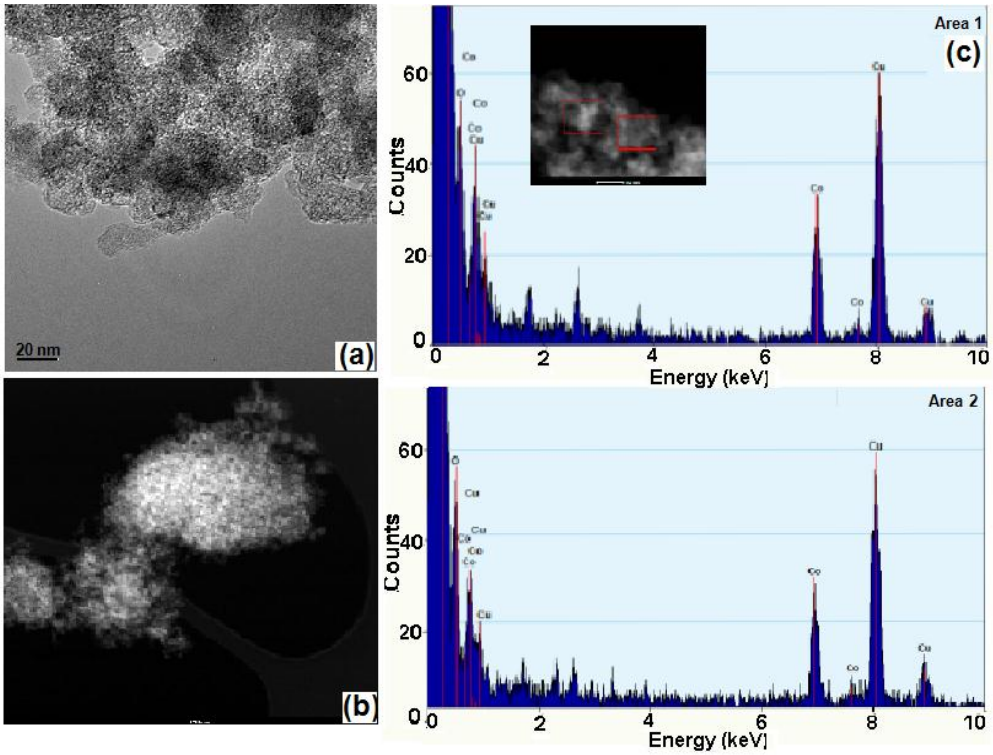

Figure 4.6 (a) TEM image of Co/TETA/C catalyst heat-treated at 700 °C, (b) HAADF image and (c) EDX analysis of Area 1 and Area 2.

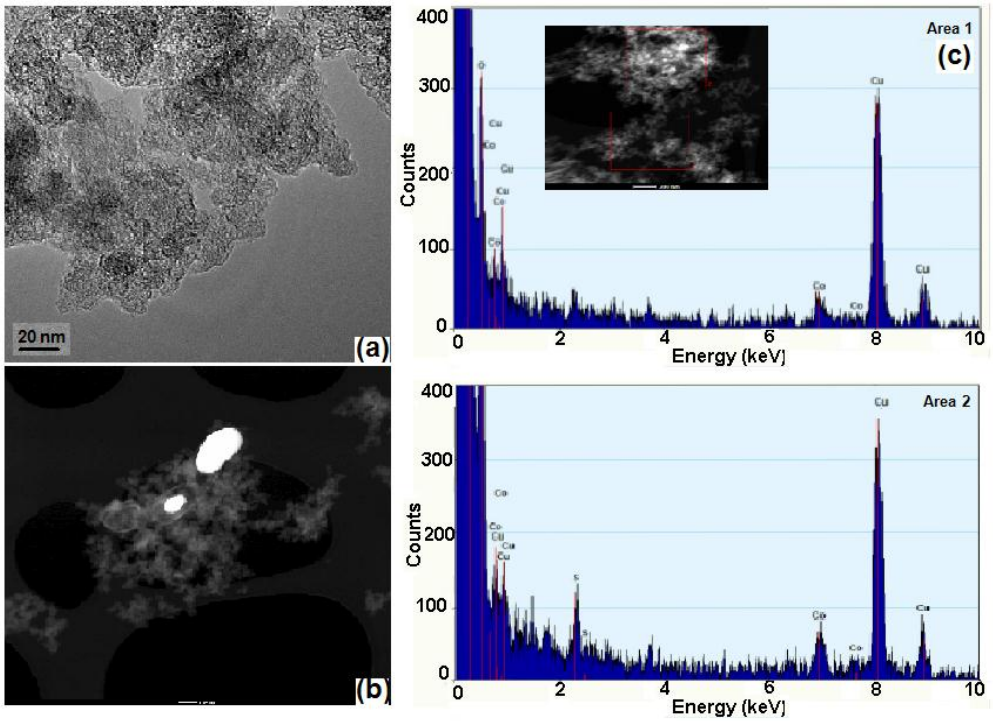

Figure 4.7 (a) TEM image of Co/TETA/C catalyst heat-treated at 1000 °C, (b) HAADF image and (c) EDX analysis of Area 1 and Area 2.

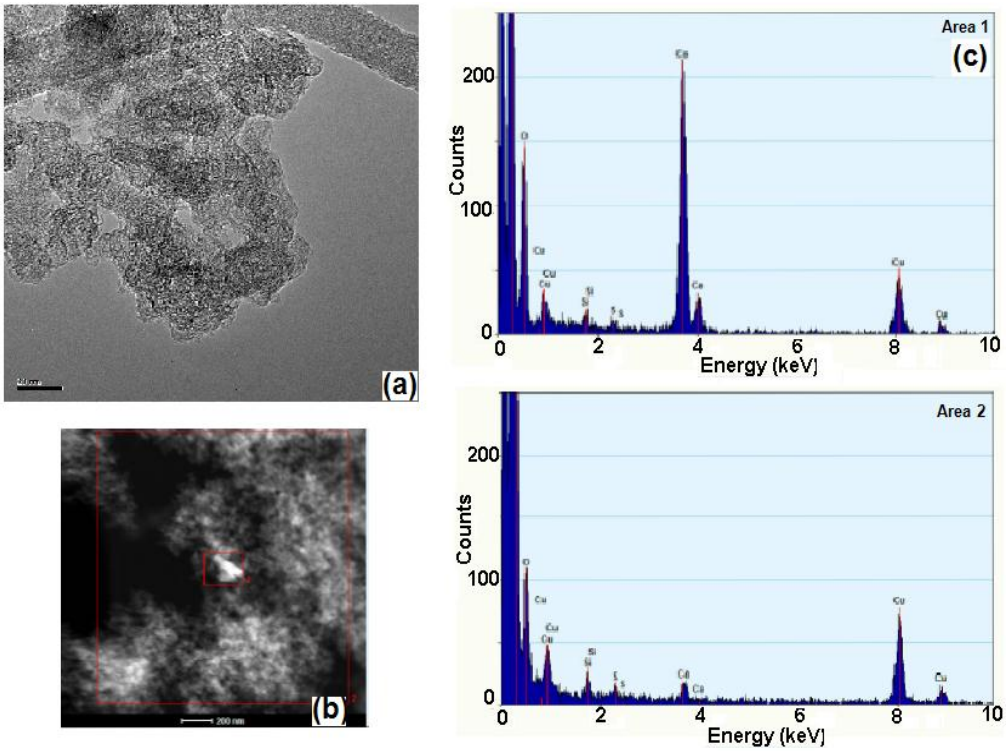

Figure 4.8 (a) TEM image of TETA/C catalyst heat-treated at 300 °C, (b) HAADF image and (c) EDX analysis of Area 1 and Area 2.

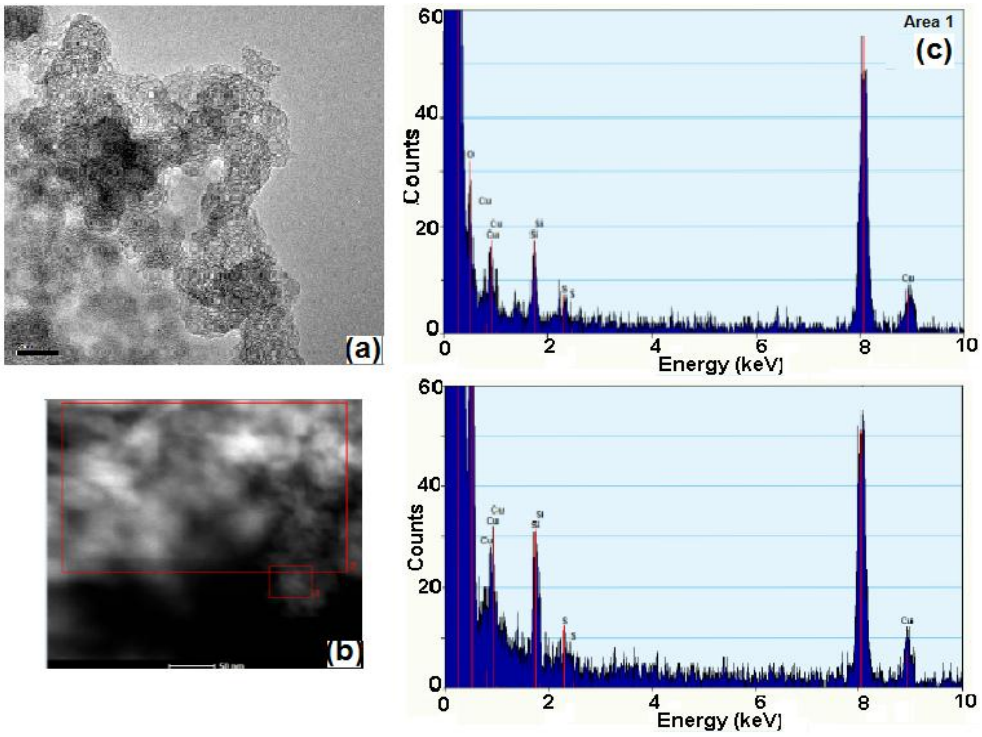

Figure 4.9 (a) TEM image of TETA/C catalyst heat-treated at 500 °C, (b) HAADF image and (c) EDX analysis of Area 1 and Area 2.

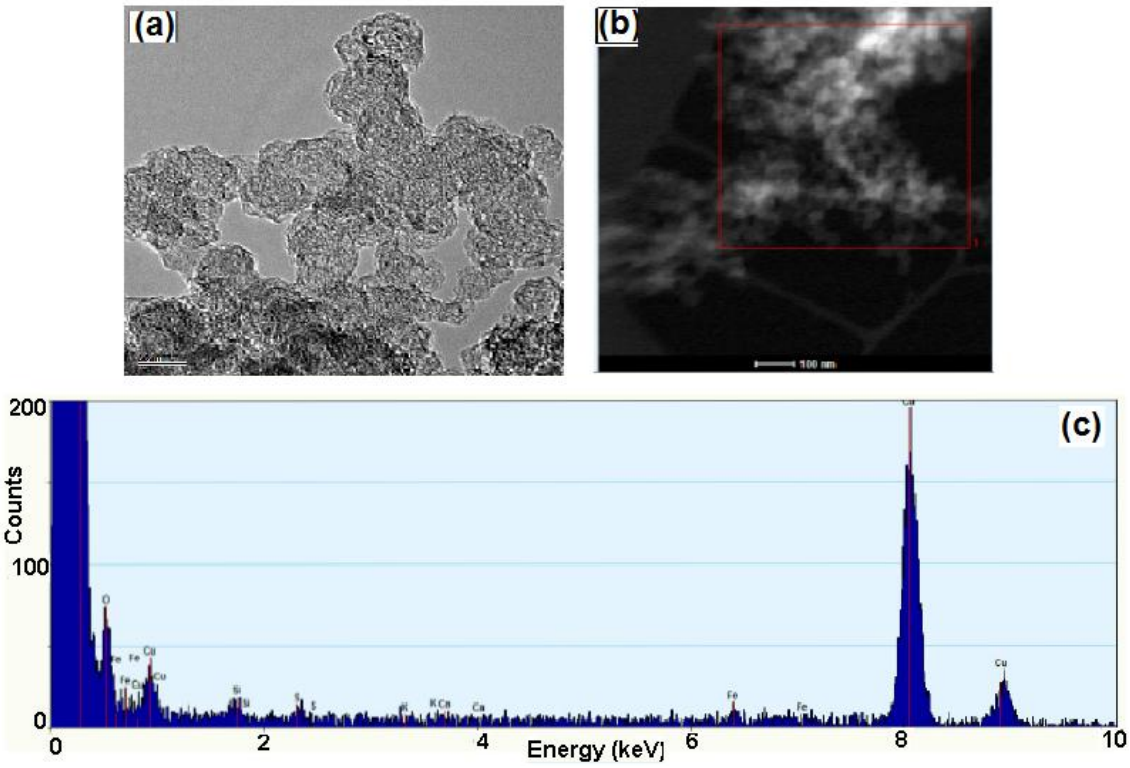

Figure 4.10 (a) TEM image of TETA/C catalyst heat-treated at 700 °C, (b) HAADF image and (c) EDX analysis of Area 1.

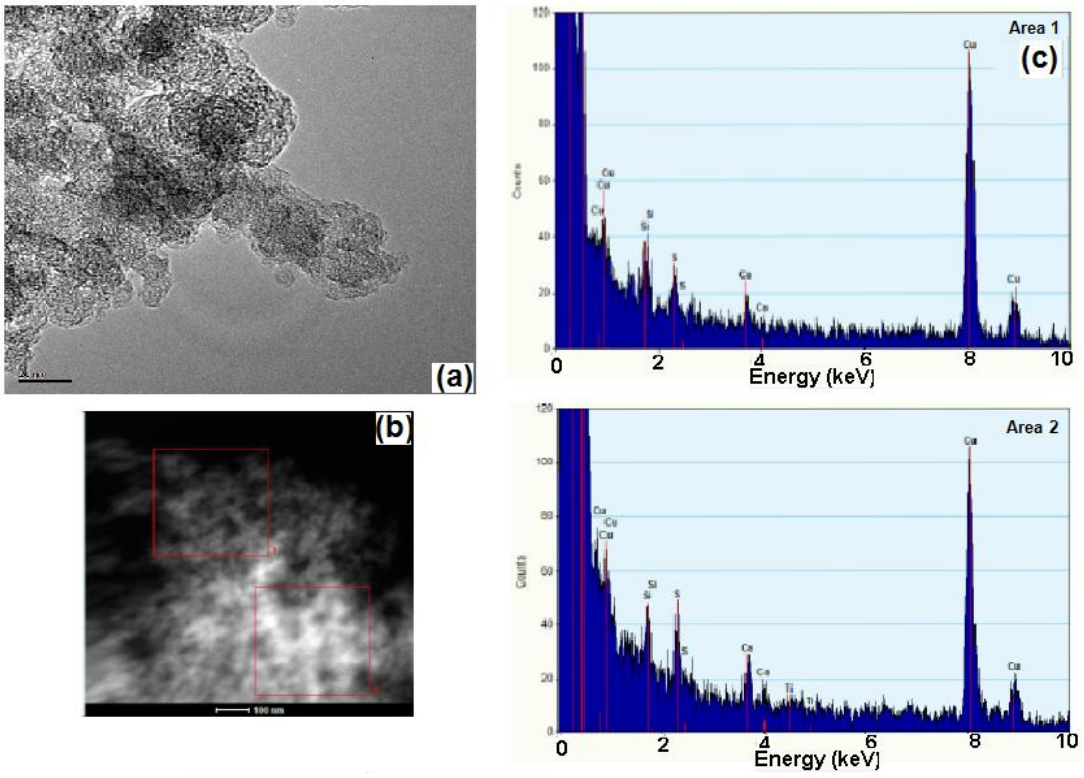

Figure 4.11 (a) TEM image of TETA/C catalyst heat-treated at 1000 °C, (b) HAADF image and (c) EDX analysis of Area 1 and Area 2.

Figure 4.12 presents TG/DTA for the Co/TETA/C and TETA/C samples. A ratio of 2:1 TETA:Co was used, as in ref[72], and the same loading was used for all samples. The weight loss profiles are rather similar and are in agreement with the data presented for Co/TETA/C by Zhang *et al*.[72] The first step in the loss of mass was observed at temperatures below 100 °C and corresponds to the loss of adsorbed ethanol on the surface of catalyst. The major loss in the mass occurs when the temperature is over the range of 100-500 °C. The steep loss at ~200 °C may correspond to the boiling temperature of TETA (267 °C). The temperature range of 300 °C to 700 °C involves the release of Co/TETA on the carbon support. The loss at temperatures above 700 °C is related to the decomposition of the Co chelate.[72,79] The similar curve observed in Co-containing and Co-free samples suggest that there is no additional stabilisation of the TETA by Co. The percentages of weight loss of Co/TETA/C and TETA/C samples at different temperature ranges are shown in Table 4.1.

Table 4.1 The percentage of weight loss of Co/TETA/C and TETA/C.

Sample / Weight %	Up to 300°C	300 to 500°C	500 to 700°C	700 to 1000°C	Total
Co/TETA/C	17.4	19.1	4.64	6.75	47.9
TETA/C	13.9	19.6	4.08	6.19	43.8

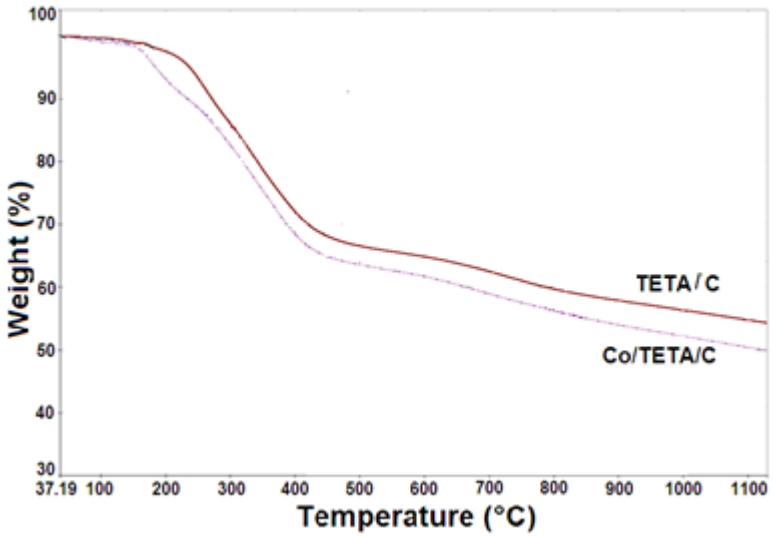

Figure 4.12 TG-DTA analysis of Co/TETA/C and TETA/C catalysts.

4.3.2 Cyclic voltammetry measurements

The Co/TETA/C, TETA/C, C-only and 2% Co/C samples were characterised by using CV, RDE and RRDE. Figure 4.13 compares Co/TETA/C, TETA/C, C-only and 2% Co/C heat-treated at various temperatures in Ar-saturated 0.1 M $HClO_4$. The C-only samples illustrate that the nature of the carbon support changes with heat-treating temperature, as can be seen in Figure 4.13(c). The C-only without heat-treatment produces a pair of peaks centred at ~0.4-0.5 V which can be attributed to the quasi-reversible redox process of quinoidal groups on carbon surfaces.[79] The unheated C-only sample shows a weaker double layer capacitive charging current when compared with the different heated C-only samples, which have increased charging current with pyrolysis temperature. The reversible redox peaks of the quinodal group can still be observed in all of the samples. Figure 4.13(a) and (b) present the CV of Co/TETA/C and TETA/C samples. When compared with the C-only samples, the double layer capacitance of the TETA/C samples show a decrease on introducing TETA onto the carbon surface and an even further decrease with addition of Co. The Co/TETA/C samples have relatively low capacitance, possibly due to the presence of metallic Co and TETA on the carbon surface. The reversible redox peaks are not visible in the unheated, 300 °C, 500 °C of TETA/C and of Co/TETA/C samples, while they can be observed in 700 °C and 1000 °C of both samples.

Although the XRD, TEM and EDX data confirm the presence of metallic Co in 700 °C and 1000 °C Co/TETA/C and 2% Co/C samples, no distinct oxidation and reduction current peaks of metallic Co are observed in this region under these conditions, suggesting that metallic Co has no electrochemical activity over this potential range. Therefore, the feature is more likely to be related to quinone functionality rather than Co redox activity. It is likely that the Co or Co (II) in Co/TETA/C and Co/C samples remained Co(II) or Co in this potential

range.[47] The CV of 2% Co/C is shown in Figure 4.13(d). According to previous literature, these results of Co–N/C are different from the Fe–N/C catalysts in that the redox couple of Fe(II)/Fe(III) can be identified in this potential range. The redox couple of Fe(II)/Fe(III) is at ~0.65 V (*vs* RHE) while Co(III)/Co(II) is at ~1.68 V (*vs* RHE) in aqueous solution.[72]

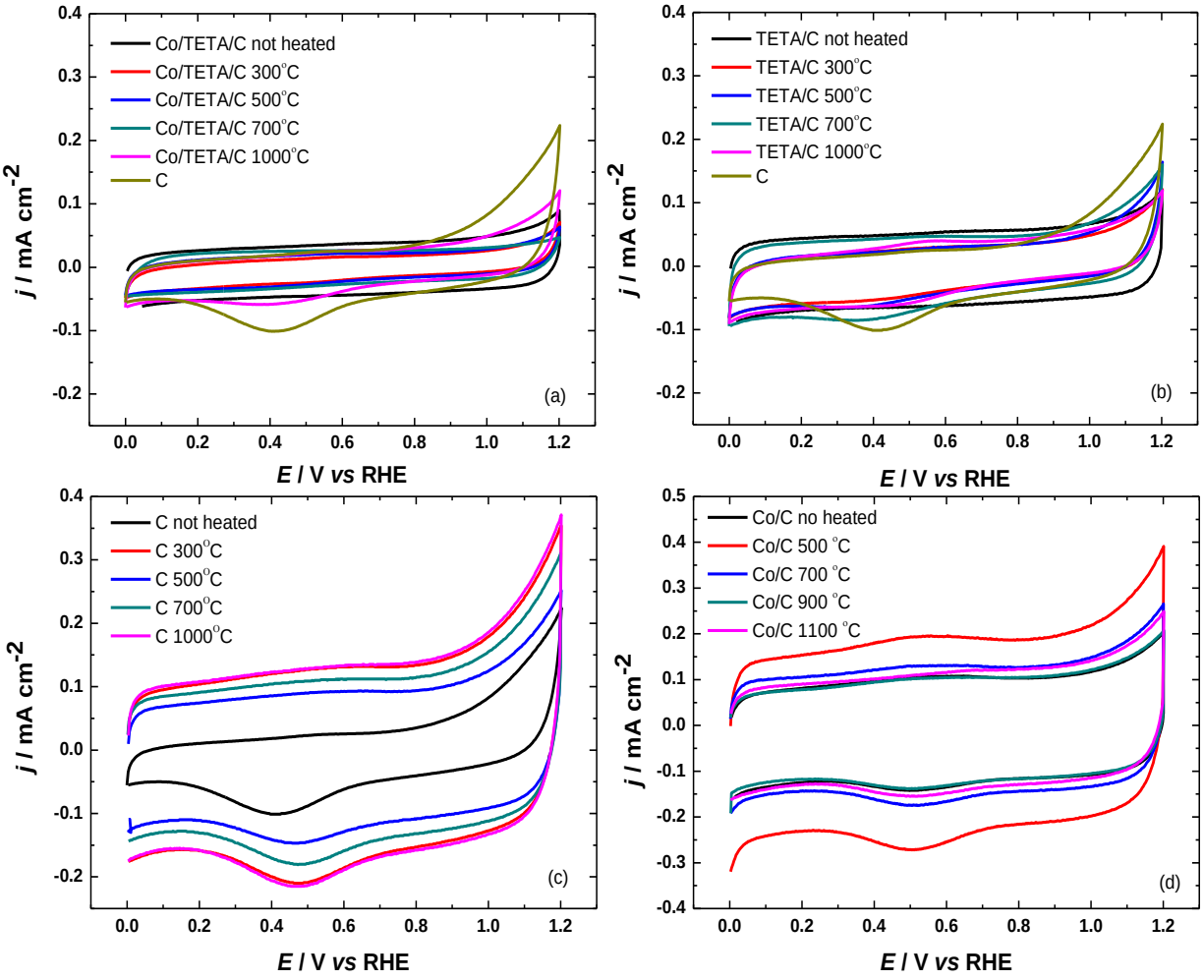

Figure 4.13 Cyclic voltammograms in Ar-saturated 0.1 M $HClO_4$ for (a) Co/TETA/C, (b) TETA/C, (c) C-only and (d) 2% Co/C catalysts heat-treated at different temperatures. Scan rate = 0.02 V s^{-1}.

4.3.3 Selectivity towards hydrogen peroxide reduction

The ORR was studied for all samples in O_2-saturated $HClO_4$, in order to study the effect of heat treatment on the catalytic activity towards the ORR of Co/TETA/C. Figures 4.14 – 4.16 show the RRDE data at different rotation speeds (400, 900, 1600 and 2500 rpm) of Co/TETA/C, TETA/C and C-only samples which are unheated, heated at 300 °C, 500 °C, 700 °C and 1000 °C. In Figure 4.14, the onset potentials of untreated Co/TETA/C, heated at 300 °C, 500 °C, 700 °C and 1000 °C, are 0.28 V, 0.38 V, 0.60 V, 0.70 V and 0.75 V, respectively. The onset potentials at the ring are similar to those at the disc. The current densities of each Co/TETA/C sample increases with rotating speed.

In Figure 4.15, the onset potentials of untreated TETA/C, heated at 300 °C, 500 °C, 700 °C and 1000 °C TETA/C are 0.22 V, 0.25 V, 0.32 V, 0.29 V and 0.4 V, respectively. The current densities of TETA/C heated at 300 °C, 500 °C and 1000 °C result in an increase when increasing the rotating speed, whereas the sample heated at 700 °C shows only scatter. In Figure 4.16, the onset potentials and current densities of C-only samples show no trend. Figure 4.17 shows the RRDE data acquired for 2% Co/C samples unheated, heated at 500 °C, 700 °C, 900 °C and 1100 °C. The onset potentials and current densities of these samples also show no trend, similarly to TETA/C and C-only results.

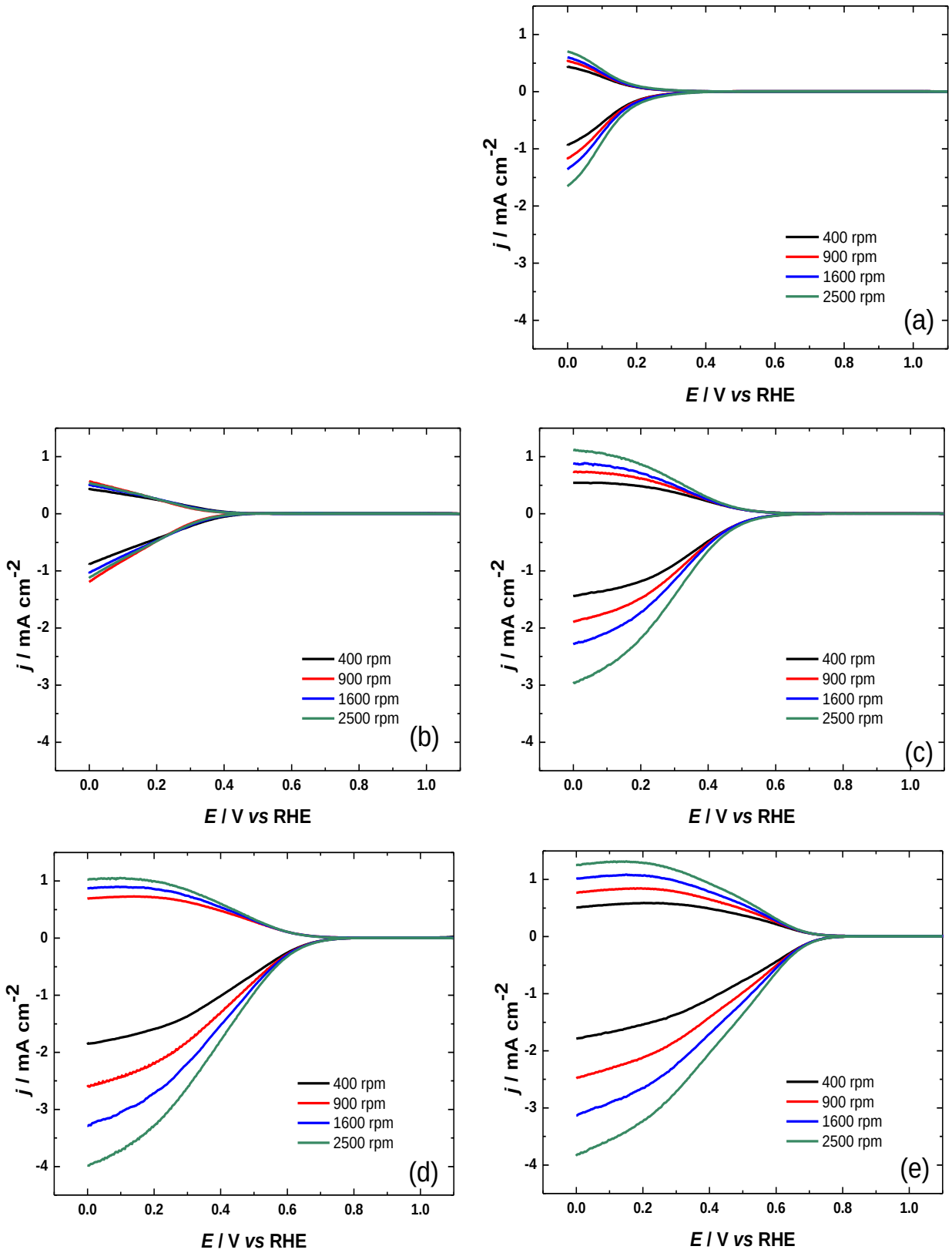

Figure 4.14 RRDE polarisation curves of the oxygen reduction reaction in 0.1 M $HClO_4$ for Co/TETA/C (a) unheated, heated at (b) 300 °C, (c) 500 °C, (d) 700 °C and (e) 1000 °C. Scan rate = 0.02 V s^{-1}.

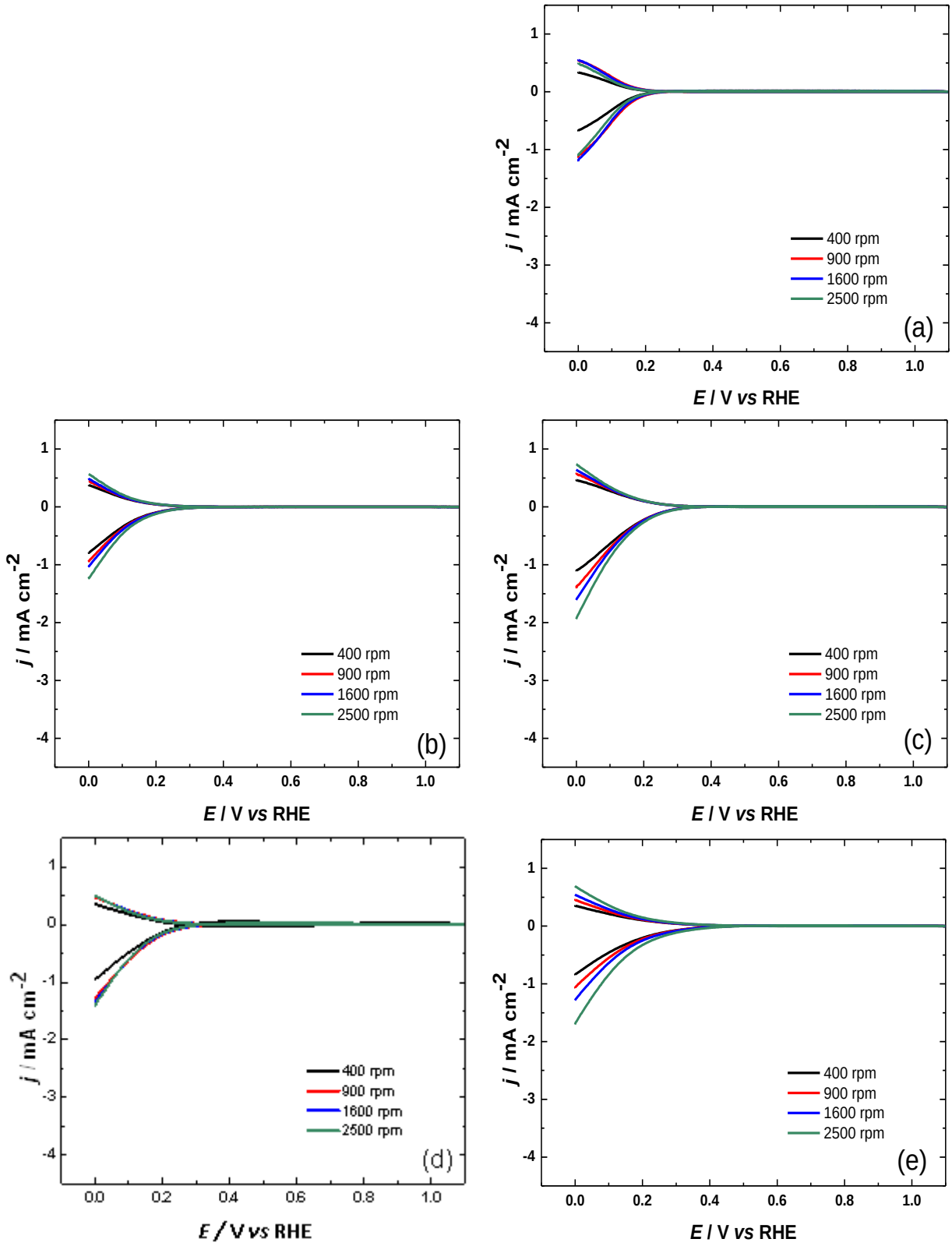

Figure 4.15 RRDE polarisation curves of the oxygen reduction reaction in 0.1 M $HClO_4$ for TETA/C (a) unheated, heated at (b) 300 °C, (c) 500 °C, (d) 700 °C and (e) 1000 °C. Scan rate = 0.02 V s^{-1}.

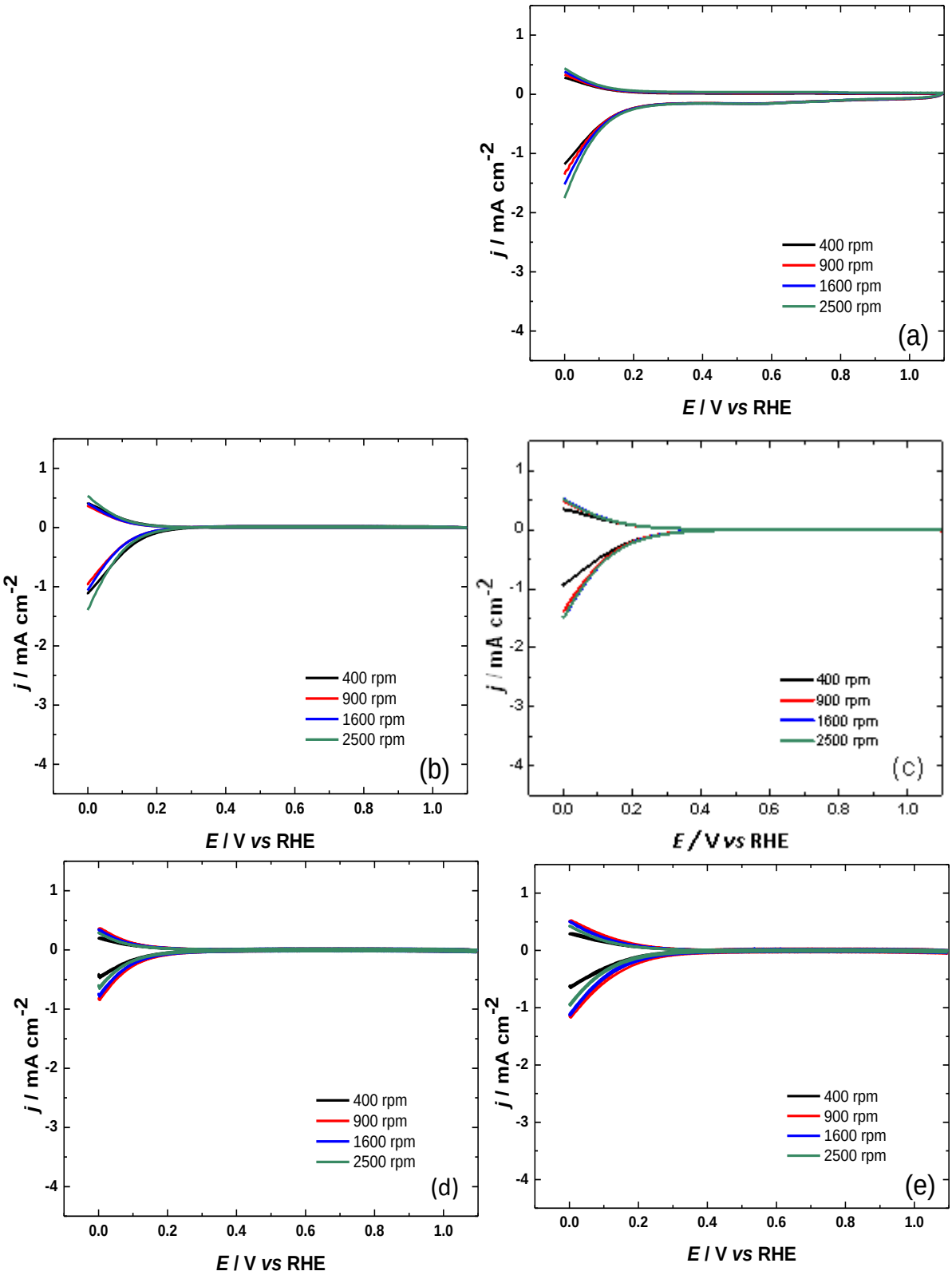

Figure 4.16 RRDE polarisation curves of the oxygen reduction reaction in 0.1 M $HClO_4$ for C-only (a) unheated, heated at (b) 300 °C, (c) 500 °C, (d) 700 °C and (e) 1000 °C. Scan rate = 0.02 V s^{-1}.

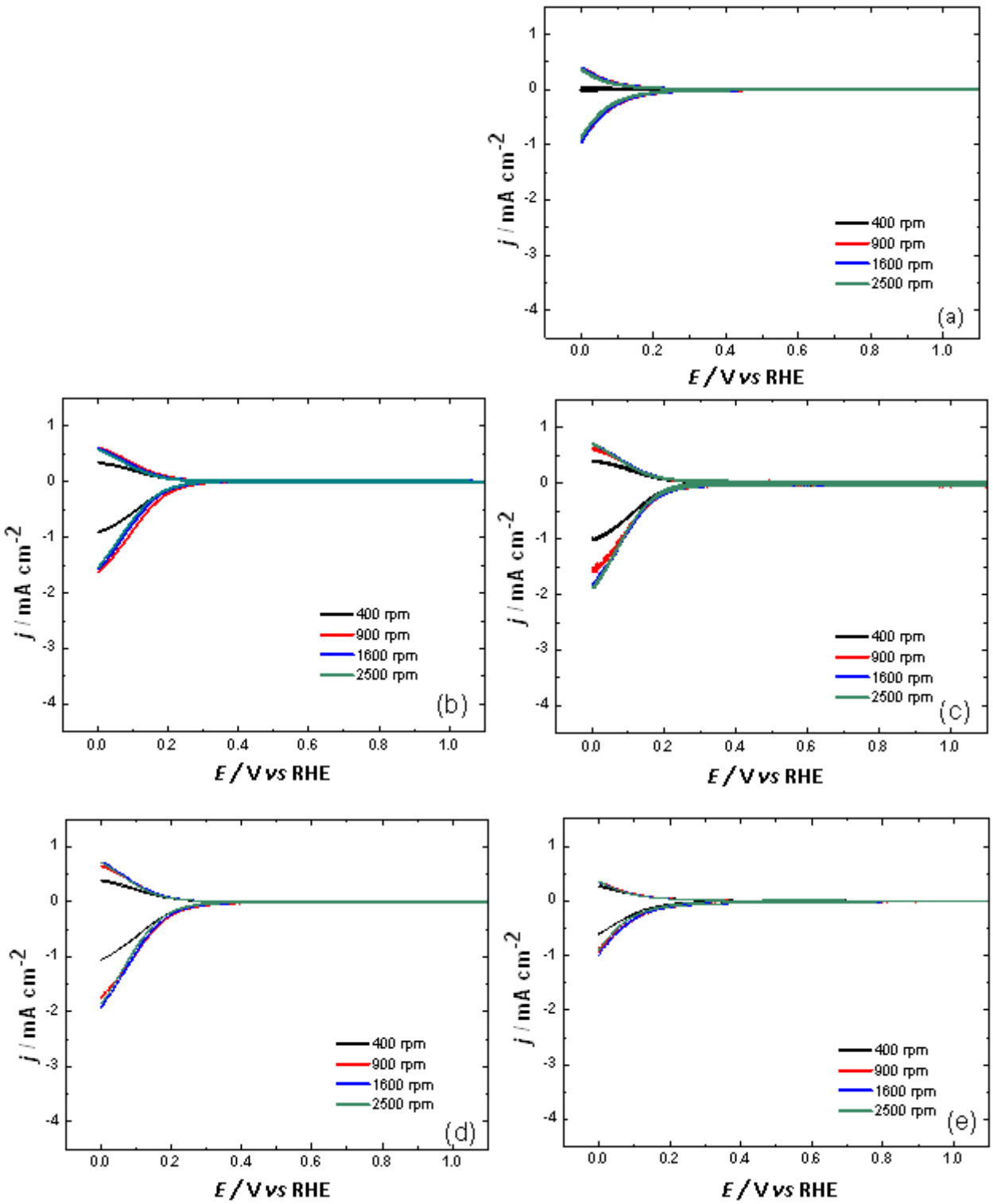

Figure 4.17 RRDE polarisation curves of the oxygen reduction reaction in 0.1 M $HClO_4$ for 2 % Co/C (a) unheated, heated at (b) 500 °C, (c) 700 °C, (d) 900 °C and (e) 1100 °C. Scan rate = 0.02 V s^{-1}.

Figure 4.18 compares the RRDE data at 1600 rpm between Co/TETA/C, TETA/C and C-only samples which were heat-treated at different temperatures. As shown in Figure 4.18(a), the catalytic activity towards the ORR was significantly enhanced for Co/TETA/C samples treated at 300 °C, 500 °C and 700 °C but a slight decrease was observed for the sample treated at 1000 °C. The highest disc current density is obtained for the Co/TETA/C heated at 700 °C. The ring current relates to the oxidation of H_2O_2 produced at the disc electrode. The ring currents increase in the order of unheated, heated at 300 °C, 500 °C and 1000 °C, while the sample heated at 700 °C produces a lower ring current than the 1000 °C sample. A clear trend for the onset potential of the ORR is evidently present. The onset potential has significantly shifted to more positive potential for the samples treated at 300 °C, 500 °C and 700 °C and slightly more for 1000 °C. A positively shifted onset potential can imply that an overpotential decrease is obtained. The trend observed in Figure 4.18(a) suggests that the overpotential decreases as the pyrolysis temperature is increased. The TETA/C samples in 4.18(b) show a similar trend of onset potentials as those in Co/TETA/C with a lesser extent, whereas C-only samples show scatter as shown in Figure 4.18(c). For TETA/C and C-only samples, the ring current is relatively low and scattered. The Co/C heated at 500 °C and 700 °C samples yield the highest catalytic activities compared with unheated, 900 °C and 1100 °C, as seen in Figure 4.18(d). This behaviour probably results from aggregation of Co metal at high pyrolysis temperatures.

In all cases, a limiting current plateau was not observed but only a change in the slope of the polarisation curves. This characteristic has also been reported for carbon-supported transition metal catalysts. Inclined current plateaux have been attributed to a less uniform distribution of active sites and porosity or slow reaction kinetics related to mass transport.[79] It

is known that the porosity of the electrode surface has an effect on the activity and stability of the electrode.

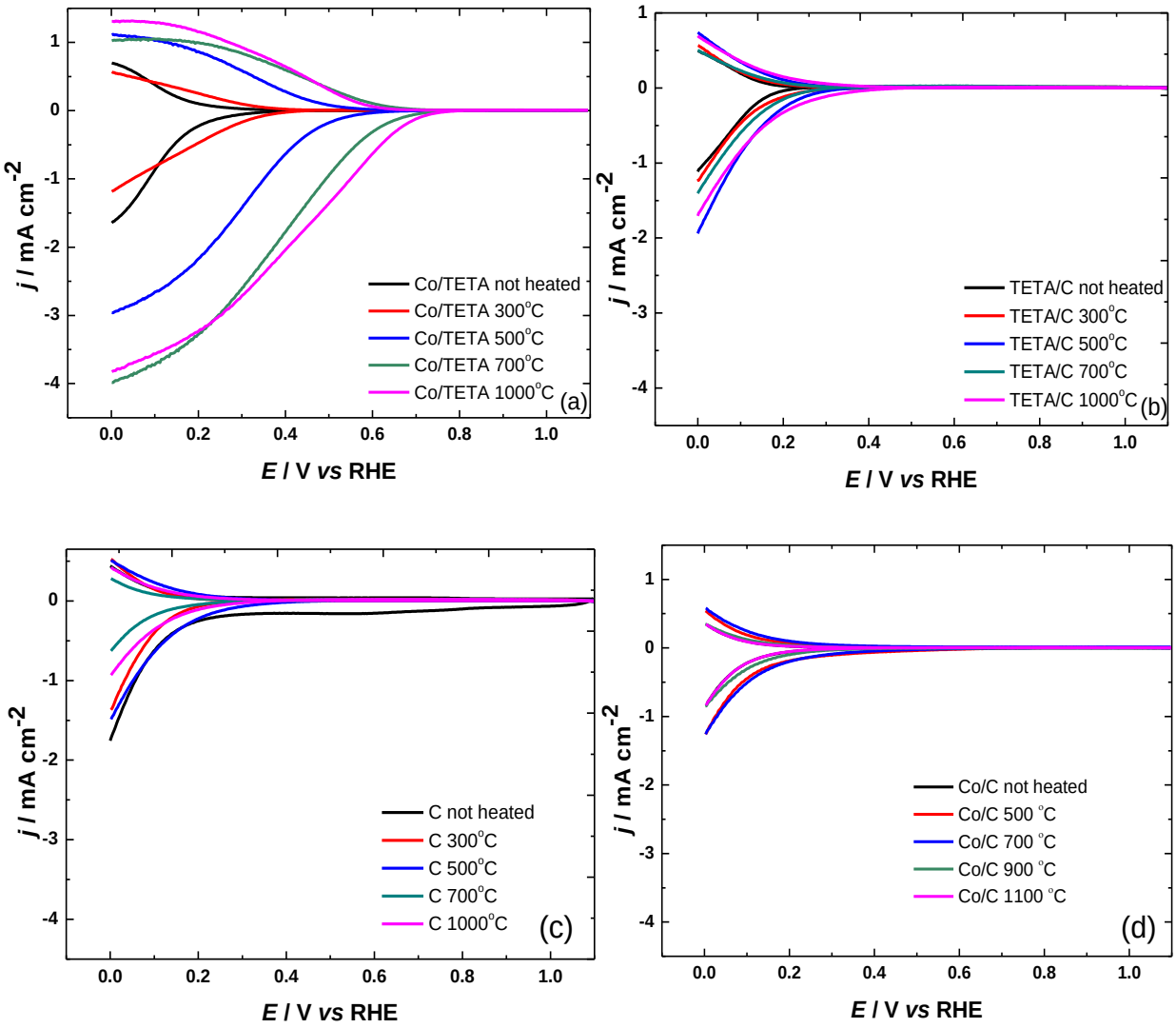

Figure 4.18 RRDE polarisation curves of the oxygen reduction reaction in 0.1 M $HClO_4$ for (a) Co/TETA/C, (b) TETA/C, (c) C-only and (d) Co/C catalysts heat-treated at different temperature. Scan rate = 0.02 V s^{-1}.

In this work, an experiment was also carried out with hexacyanoferrate (III) to check for the effect related to a catalyst distribution. It is noteworthy that the catalyst produces the limiting expected current density for this reaction. It can be assumed that the limiting current

for the ORR on our catalysts do not reach a current plateau possibly due to the mechanism of slow kinetics and/or inhomogeneous distribution of sites rather than electrode porosity alone. The physical characterisations support a change in structure and nature of carbon support with a change in pyrolysis temperature, thus, implicating that heat-treatment leads to marked changes in the porosity of the active layer.[82] The different position of the onset potential suggests that the catalysts heated at different temperatures have different catalytic activities, indicating that the heat treatment strongly influences the catalytic activity of the catalysts for the ORR.

The Co/C, TETA/C and C-only samples provide low catalytic activities towards the ORR. The presence of the cobalt and TETA in the sample, as well as heat-treatment, appears to have a strong influence as it drastically improves the catalytic activity. It is known that the transition metal itself does not primarily take part as an active site for the ORR but rather is involved in creating such active sites. In order for these sites to be formed, transition metal, nitrogen atoms and carbon support are all required. The role of the transition metal as of yet is still unclear; however, it is thought that the transition metal can catalyse the incorporation of nitrogen atoms into the carbon surface during pyrolysis.[83] The main purpose of heat treatment is to create the active sites, which can be accompanied by the formation of radical-promoting polymerisation of nitrogen-containing ligands, including Co, during pyrolysis.[82] The polymerisation of the ligands on the surface enhances the electron transfer on the catalyst surfaces.[83-85] The catalytic sites of Co-N catalysts might be Co-N_x which can either be Co-N_2 or Co−N_4. In this work, the Co/TETA/C yields the highest catalytic activity. It can be postulated that, below 700 °C, the density of Co-N_x active sites shows an increase as a function of pyrolysis temperature. Nevertheless, temperatures above 700 °C have been reported to decrease the density of Co−N_x active sites because the Co-N_x is obviously

converted to metallic Co, as observed in XRD, TEM and EDX. The decrease in active sites leads to the decrease in the ORR activity. The heat treatment also enhances the stability of these catalysts. It has been reported that, during pyrolysis, the metal clusters are surrounded by the protective graphitic layer which can prevent the corrosion in the acidic electrolyte.

The RRDE data can be analysed to obtain the number of electrons transferred in the reaction and the selectivity towards hydrogen peroxide production, as opposed to the production of water. The number of electrons can be found from the relationship between current density and the rotation rate using the Koutecky-Levich equation:[86]

$$\frac{1}{j} = \frac{1}{j_k} + \frac{1}{0.2006 n \mathrm{F} \nu^{-1/6} D_a^{2/3} C_a \omega^{1/2}} \qquad (4.2)$$

In this equation, j is the disc current density, j_k is the current density relating to the kinetic limitations, F is the Faraday constant (96485 C mol^{-1}), n is the number of electrons transferred in the reaction, D is the diffusion coefficient of species a, C_a is the bulk concentration of species a, ν is the kinematic viscosity and ω is the rotation rate (in rpm). The kinematic viscosity is 0.01 cm^2 s^{-1}, the diffusion coefficient and solubility of oxygen are 1.93×10^{-5} cm^2 s^{-1} and 1.26×10^{-6} mol cm^{-3}, respectively, in this electrolyte.[87] The Koutecky-Levich plot is a plot of j^{-1} *vs* $\omega^{-1/2}$, giving a straight line which intercepts the y axis at j_k^{-1} and a slope of $1/(0.2006nFD^{2/3}C\nu^{-1/6})$. The gradient of the resulting straight line of this plot allows the number of electrons (n) transferred in the overall reduction of oxygen (per O_2 molecule) to be obtained.

Figure 4.19 shows Koutecky-Levich (K-L) plots for various applied potentials taken from data acquired for Co/TETA/C unheated, heated at 300 °C, 500 °C, 700 °C and 1000 °C samples. A series of straight and parallel lines can be found for each of the samples. The parallel lines indicate that both the number of electrons transferred per O_2 molecule and the

active surface area for the reaction rate do not change significantly between the potential ranges of the experiment.[23,88] Theoretical K-L plots which have the same gradient as *n* equal to 2 and 4 have been plotted and compared with the series of straight lines of each sample. The gradient of Co/TETA/C heated at 300 °C and 500 °C tends to have the gradient of *n* equal to 2 whereas Co/TETA/C heated at 700 °C and 1000 °C have a tendency for *n* to equal 4.

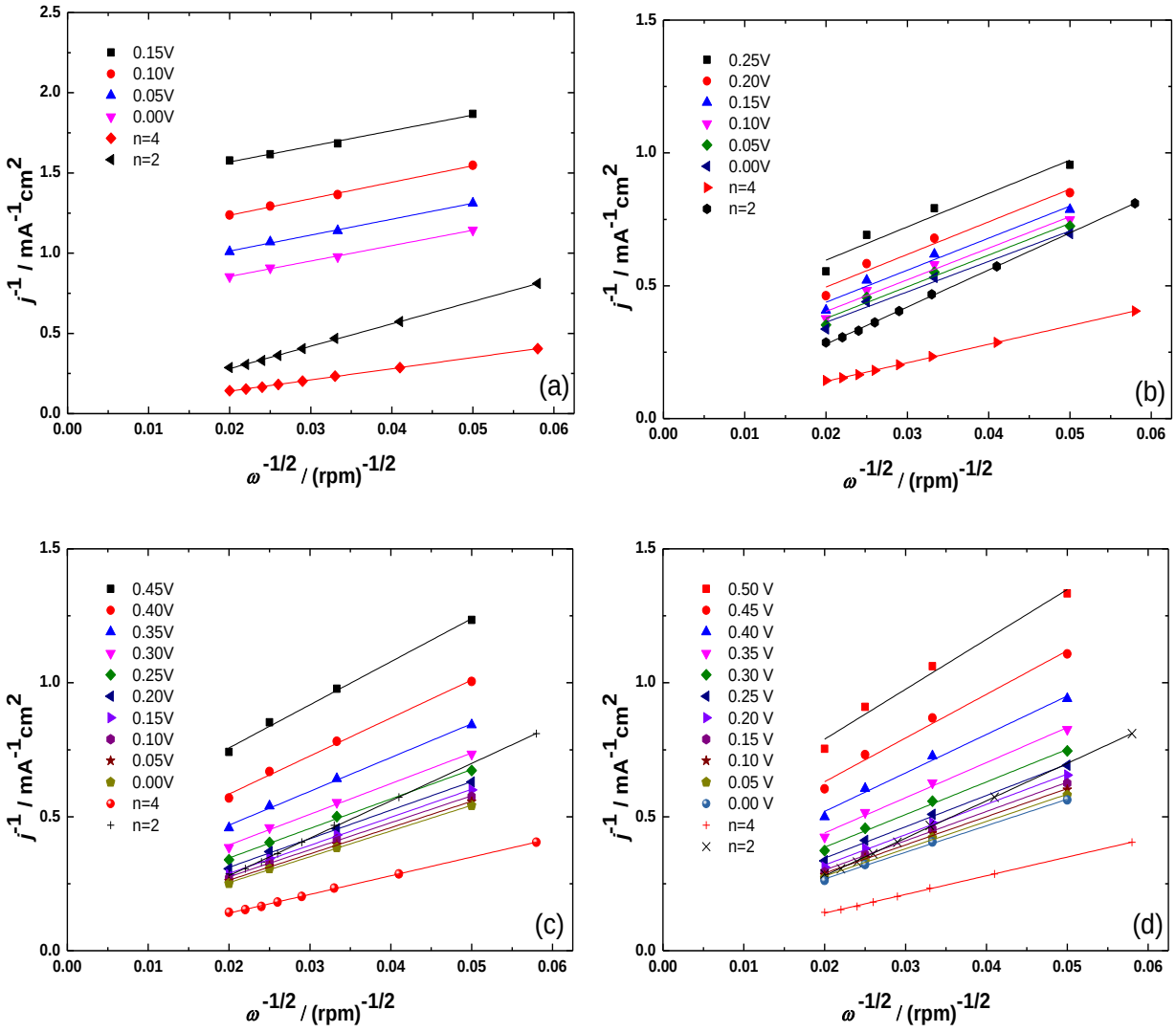

Figure 4.19 Koutechy-Levich plots of the oxygen reduction reaction in 0.1 M $HClO_4$ for Co/TETA/C treated at (a) 300 °C, (b) 500 °C, (c) 700 °C and (d) 1000 °C.

The *n* values of Co/TETA/C analysed from K-L plots are plotted against potential, as shown in Figure 4.20. The *n* values of each sample increase with increasing overpotential. The

n values of these samples are in between 2 and 2.9, suggesting that the ORR is in a mixed process of 2-electron and 4-electron transfer pathways with a degree of uncertainty. The sample heated at 700 °C displays the highest *n* value, close to 3. It has been reported in the literature that the Co-N catalysts tend to undergo the ORR through a 2-electron pathway, producing H_2O_2. For the TETA/C, C-only and Co/C samples, the K-L plots and the *n* values are scattered and ambiguous.

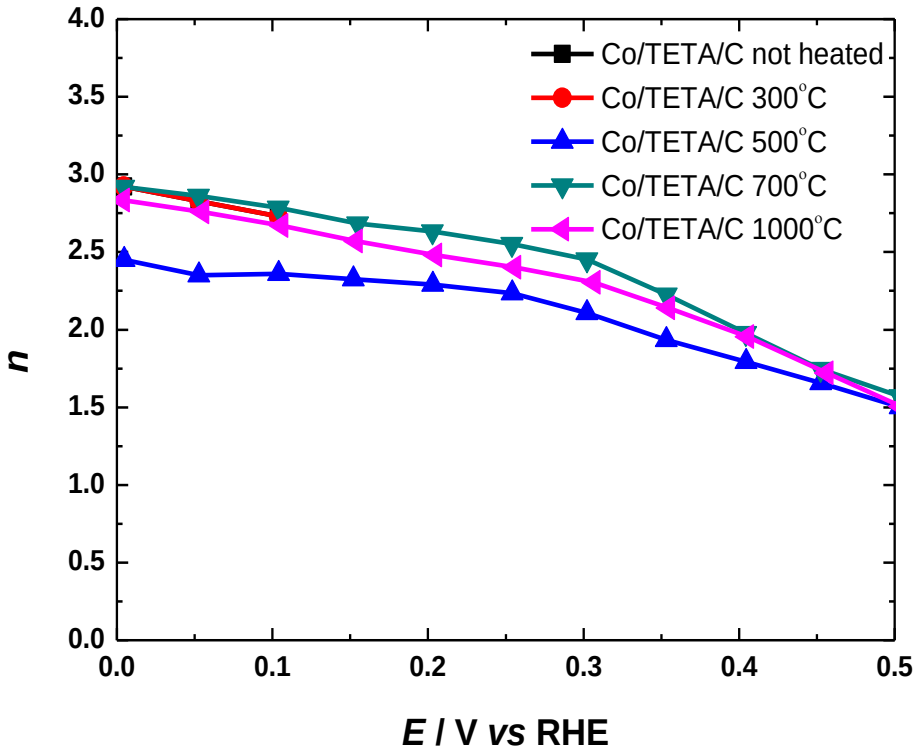

Figure 4.20 The values of *n* from K-L analysis for Co/TETA/C heat treated at different temperatures.

Koutecky-Levich analysis can sometimes subject to a degree of uncertainty. For this reason, the average number of electrons transferred was also quantified by using the RRDE data. An appropriately selected oxidising potential at the ring is applied in order to detect and reoxidise any intermediate of H_2O_2 species escaping from the disc surface. The analysis reported by Claude *et al*. was employed.[89] The *n* value can be determined from the disc and ring currents using Eq. (4.3). This RRDE method is particularly convenient when obtained

disc currents do not level off. This feature can often be found in data acquired from non-precious metal-based catalysts[90] and Au catalysts[91].

$$n = \frac{4I_d}{I_d + I_r/N} \tag{4.3}$$

where I_d is the total disc current (I_d (H_2O) + I_d (H_2O_2)) and I_r is the ring current corresponding to the oxidation of hydrogen peroxide, I_r = I_r (H_2O_2) = N I_d (H_2O_2). N is the collection efficiency, which is 0.4 for this experiment. For 100% selectivity towards reduction of oxygen to water, I_r = N I_d (H_2O_2) = 0 and so n = 4. For 100% selectivity towards reduction of oxygen to hydrogen peroxide, I_d = I_d (H_2O_2) = I_r /N, so that n = 4 I_d (H_2O_2) /2 I_d (H_2O_2) = 2.

Figure 4.21 shows the number of electrons obtained from Eq. (4.3) as a function of potential. In Figure 4.21(a), the n values of Co-containing samples appear to have little changes and variation at negative potential of 0.6 V. The n values increase as a function of pyrolysis temperature, with a value of approximately 2 achieved for untreated samples, a maximum 2.7 for the sample treated at 700 °C and subsequent decrease to 2.5 for 1000 °C. The n values of these samples vary within the range of 2-2.7, which coincides with the previous value obtained using the K-L plot, hence confirming that a 2-electron pathway is the dominant reaction for the Co-containing samples. The n values for TETA/C lie within the range of 2.1 - 2.4 with little changes at the negative potential of 0.3 V, as seen in Figure 4.21(b). A decrease in the values of n can be observed after 0.25 V when increasing the pyrolysis temperature for C-only samples, as shown in Figure 4.21(c). This might suggest that the heat treatment changes the nature of the carbon support. The untreated C has an n value of ca.2.75, which is higher than that of the heated C-only, TETA/C and Co/TETA/C.

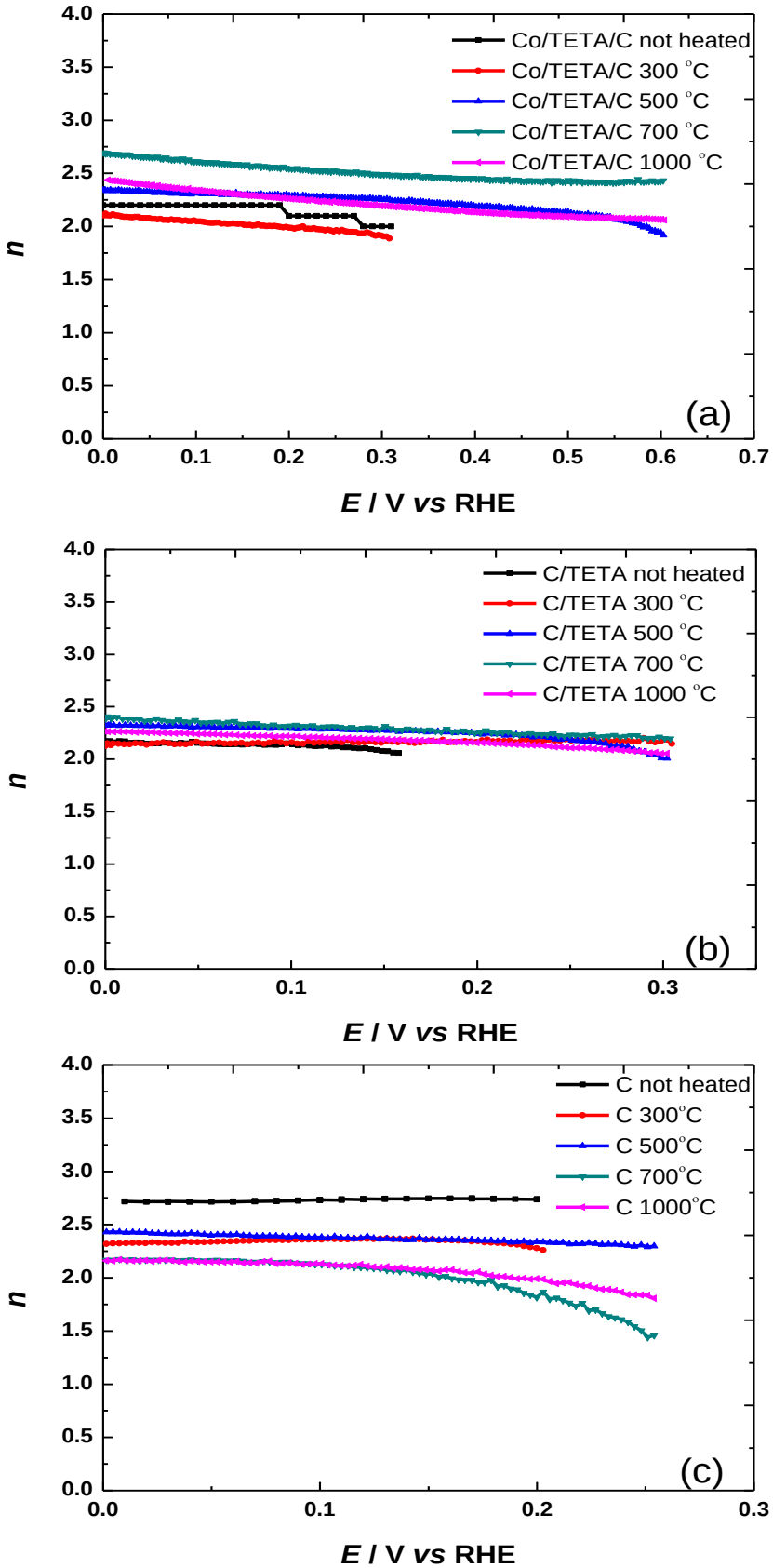

Figure 4.21 Potential dependence of *n* for (a) Co/TETA/C, (b) TETA/C and (c) C-only catalysts heat treated at different temperatures.

The activity of unheated C may arise from some impurities on the carbon surface.[9] The activity change observed in C-only samples may be due to heat treatment and the presence of TETA or Co, which are capable of removing impurities. It has been reported that heat treatment in an inert atmosphere can cause loss of oxygenated groups on carbon supports by their decomposition. It is believed that the loss of those species results in an increase of N concentration on the surface, improving the corrosion resistance of the support.[27,63] The *n* values from K-L analysis and RRDE data are summarised in Table 4.3.

Table 4.3 *n* from Koutecky–Levich analysis and from the RRDE studies at 0.0 V.

n	**Co/TETA/C 300 °C**	**Co/TETA/C 500 °C**	**Co/TETA/C 700 °C**	**Co/TETA/C 1000 °C**
***n* K–L**	2.82	2.36	2.82	2.73
***n* RRDE**	2.1	2.34	2.69	2.43

Figure 4.22 presents a plot of *n* as a function of pyrolysis temperature at 0.0 V for Co/TETA/C, TETA/C and C-only in order to clearly present the *n* value of each sample. The Co/TETA/C samples in our work have a similar *n* value trend to that observed by Zhang *et al*.[72] He reported that the number of electrons for 10% Co/TETA/C catalysts in his work increased as a function of pyrolysis temperature up to a maximum value of 3.6 for the catalyst treated at 800 °C and a decrease to 3.4 for samples treated at 900 °C. However, the *n* values obtained from his study are higher than our present work. It is important to take into consideration the fact that our catalyst loading was lower than that of Zhang.[72] Also, there is a possibility that the difference in higher *n* values may be due to the further reduction of H_2O_2. From our results, it appears that if there is further electro-reduction of hydrogen peroxide to water, it does not appear to make a major contribution to the reaction mechanism.

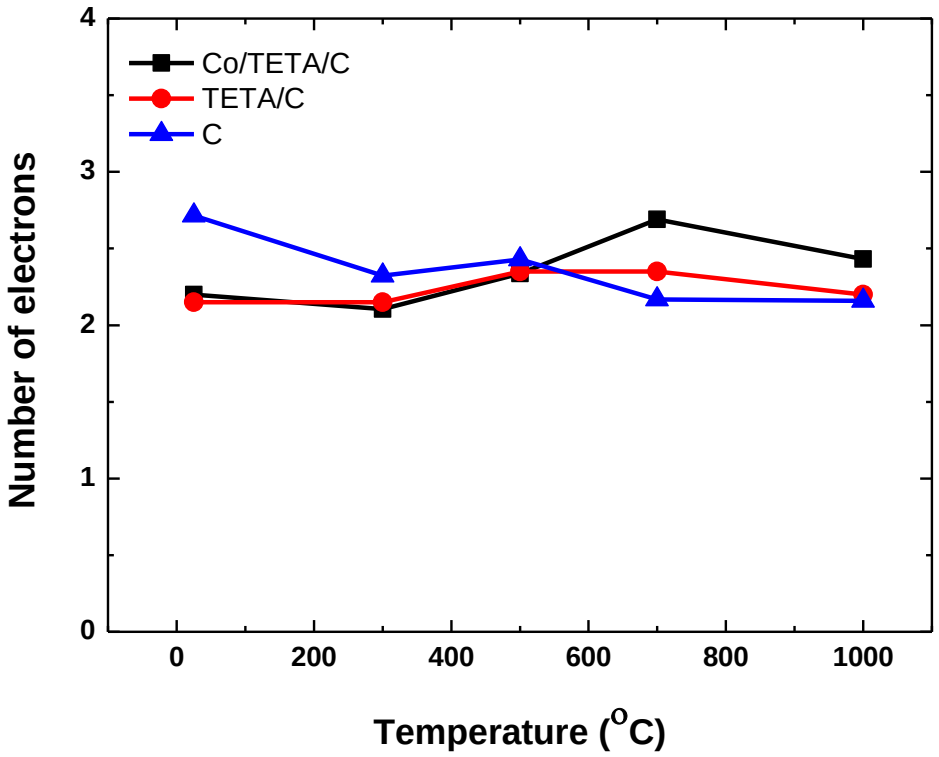

Figure 4.22 Value of *n* for Co/TETA/C, TETA/C and C-only catalysts as a function of heat treatment temperature (applied potential 0.0 V).

From the disc and ring currents, it is possible to analyse the percentage of H_2O_2 released during the ORR, which indicates the selectivity of catalyst towards H_2O_2 generation, using Eq. (4.4).[46]

$$\%H_2O_2 = \frac{2I_r/N}{I_d+(I_r/N)} \times 100 \qquad (4.4)$$

Plots of H_2O_2 selectivity as a function of potential for Co/TETA/C, TETA/C and C-only catalysts are presented in Figure 4.23. The selectivity values of all catalysts are within the range of 60%-100%. The C-only samples show a wide spread of the selectivity as the temperature was varied. The unheated C-only catalyst appears to have the lowest selectivity with a percentage value around 60% at the negative potential of 0.1 V, while the heated C-only catalysts demonstrate higher selectivity. It seems that the nature of the carbon support

changes with heat treatment, as previously described. Such observations may have been caused by the removal of trace functional groups present on the carbon surfaces.

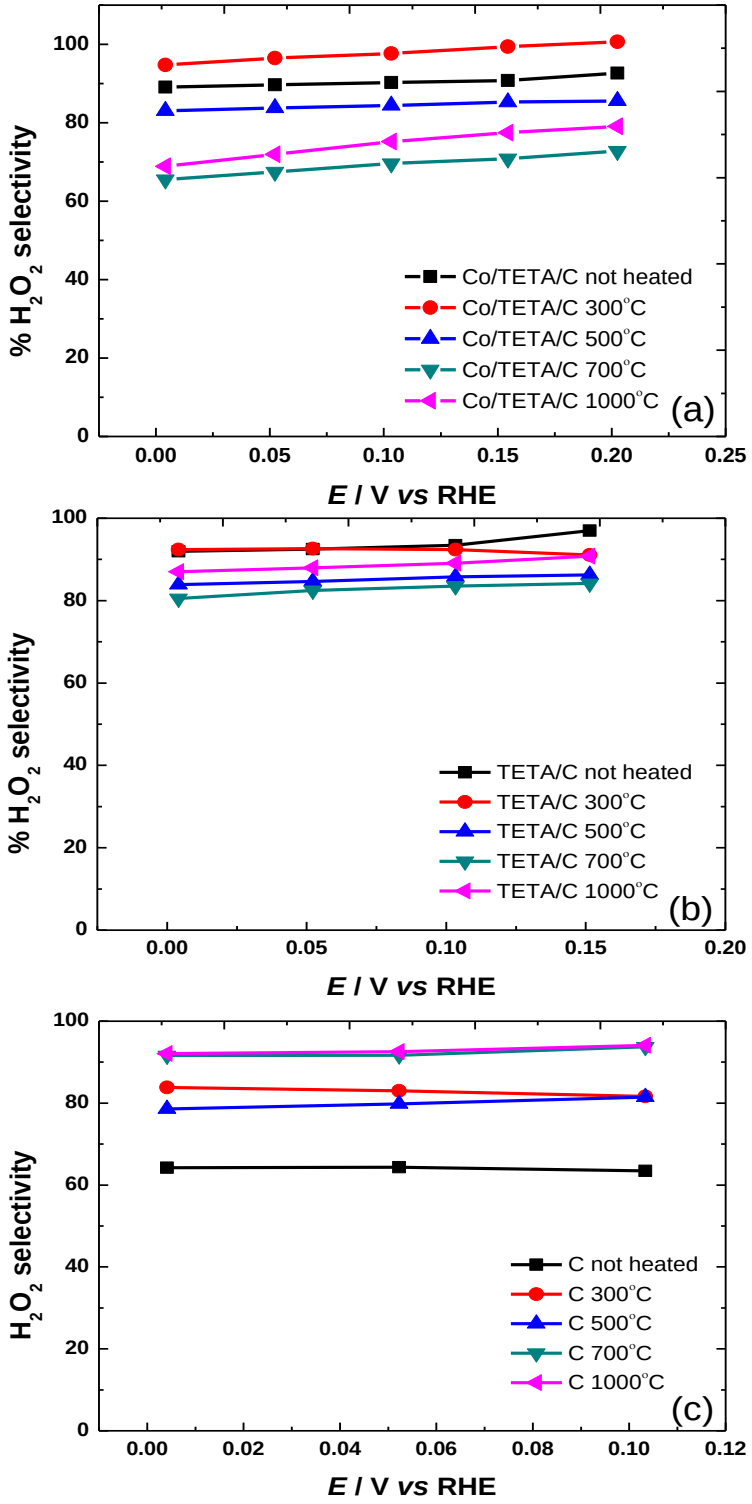

Figure 4.23 The selectivity of H_2O_2 production for (a) Co/TETA/C (b) TETA/C and (c) C-only catalysts heat-treated at different temperatures.

For TETA/C catalysts, the values of selectivity fall into a narrower range of 80% - 100% in comparison with that of the C-only results. The selectivity for TETA/C catalysts decreases in the order of unheated > 300 °C > 1000 °C > 500 °C > 700 °C. The minimum selectivity of 80% was yielded by the 700 °C TETA/C catalyst while the maximum selectivity of ~100% was yielded by the unheated TETA/C catalyst. It seems the presence of TETA on carbon support can control the selectivity of the catalysts to generate primarily H_2O_2. When Co is introduced to the catalysts, the values of selectivity are in between 60% to 100%, which is a wider spectrum than that seen in TETA/C samples. The selectivity of Co-containing catalytic samples decreases in the order of 300 °C > unheated > 500 °C > 1000 °C > 700 °C; the results mimic those observed in Figure 4.21(a). The 300 °C Co/TETA/C catalyst shows the highest selectivity with a value of ~100%.

The 700 °C Co/TETA/C catalyst yields the lowest selectivity towards the two-electron pathway to H_2O_2, which corresponds to the result that the *n* value of this catalyst is higher than the others. The C-only and TETA/C catalysts show the high selectivity towards the generation of H_2O_2; however, it has been produced at a larger negative potential in comparison to Co-containing catalysts. Additionally, the ORR currents measured in non Co-containing samples are dramatically lower than the Co-containing catalysts, indicating a lower H_2O_2 product yield.[46]

4.3.4 Electrode kinetics

The ORR mechanism catalysed by Co/TETA/C catalysts is in the mixed process of 2- and 4-electron pathways, as previously mentioned in the discussion above. The Co/TETA/C catalysts have no electrochemical activity in the potential range of 0.0-1.2 V (*vs* RHE), as shown in the voltammograms. It can be assumed that the Co(II) of Co in the catalyst should

not be reduced during the reaction.[47] An analysis of the rate constants for the ORR was carried out to analyse further the kinetics and selectivity of the reaction. The adsorbed O_2 can be reduced through different pathways depending on the electrode material. Scheme 4.2 presents the different pathways for the ORR proposed by Damjanovic.[92] The model demonstrates that oxygen can be reduced directly to H_2O (rate constant k_1) or to H_2O_2 (rate constant k_2). The H_2O_2 produced after the 2-electron pathway can further be reduced to water (rate constant k_3) or can diffuse away from the electrode surface and dissolve into the solution (rate constant k_4).[47,87] The dissolved H_2O_2 can be detected by the ring electrode of the RRDE set up.

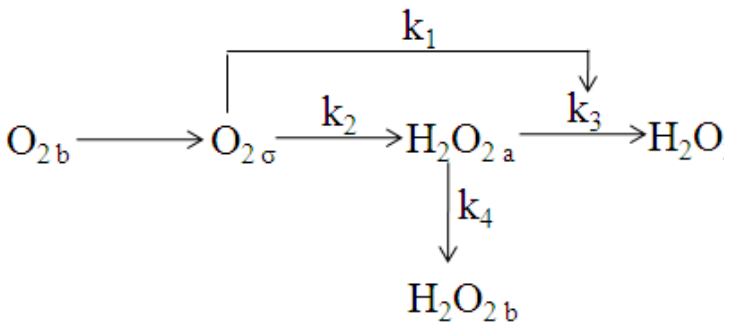

Scheme 4.2 Pathways for the oxygen reduction reaction. The subscripts b and σ refer to species located in the bulk and at the surface, respectively.

Damjanovic *et al*. considered the general case in which the following reactions may occur:

$$Ox + me^- \xrightarrow{k_1} Red \qquad (4.5)$$

$$Ox + (m\text{-}n)e^- \xrightarrow{k_2} Int \qquad (4.6)$$

$$Int + ne^- \xrightarrow{k_3} Red \qquad (4.7)$$

where Ox, Red and Int stand for reactant(s), product(s) and intermediate(s), respectively. m and n are the numbers of electrons involved with the reaction. Diagnostic plots of I_d/I_r *vs* $\omega^{-1/2}$ from RRDE data can be used to distinguish which pathway will be taken and the intermediate products formed during the reaction. The ratio of k_1/k_2 and the rate constant of k_3 can be obtained from the slope and the intercept of the diagnostic plot, respectively. From reactions

(4.5), (4.6) and (4.7), Damjanovic *et al*. assumed that there may be 5 possibilities drawn from the diagnostic plots:

(i) Only reaction (4.5) occurs: it means that no intermediate products are produced during the reaction and there is no ring current to be detected. In this case, the diagnostic plots are not possible.

(ii) Only reaction (4.6) occurs and the intermediate is not further reduced: this means that k_1=0 and k_3≈0. Then, the Eq. (4.8)[92] is reduced to Eq. (4.9):

$$\frac{I_d}{I_r} = \left(x + \frac{1}{N}\right) + \frac{(x+2)k\prime}{N\omega^{-1/2}} \quad (4.8)$$

$$\frac{I_d}{I_r} = \frac{1}{N} \quad (4.9)$$

where N is the collection coefficiency, x is the relative kinetics of reactions, k' is a rate constant. The ratio of $\frac{I_d}{I_r}$ is independent of ω. A straight line parallel to the $\omega^{-1/2}$ axis with an intercept of the $\frac{I_d}{I_r}$axis at $\frac{1}{N}$ should be observed in Figure 4.24(a).

(iii) Only reactions (4.6) and (4.7) occur: This possibility indicates that there is no parallel reaction and the relative kinetics (x) of reactions (4.5) and (4.6) are zero. Thus, the Eq. (4.8) is reduced to Eq. (4.10):

$$\frac{I_d}{I_r} = \frac{1}{N} + \frac{(2k\prime)}{(N\omega^{-1/2})} \quad (4.10)$$

A plot with an intercept at $\frac{1}{N}$ will be observed, as in Figure 4.24(b). The slope of each line is dependent on the potential.

(iv) Only reaction (4.5) and (4.6) occur without reaction (4.7): This means that there are 2 parallel reactions but the intermediate products are not further reduced. Hence, Eq. (4.8) is reduced to Eq. (4.11):

$$\frac{I_d}{I_r} = \frac{(x+1)}{N} \quad (4.11)$$

According to Eq. (4.10), the ratio of $\frac{I_d}{r}$ does not depend on ω; hence straight lines parallel to the $\omega^{-1/2}$ axis are obtained in the same manner as that shown in Figure 4.24(a). However, in this case the intercept is greater than $\frac{1}{N}$ and depends on x.

(v) All three reactions occur: no simplification can be applied to Eq. (4.8). Thus, the slope and the intercept should depend on the potential that is applied; however, the intercept value should be greater than $\frac{1}{N}$ as shown in Figure 4.24(d).

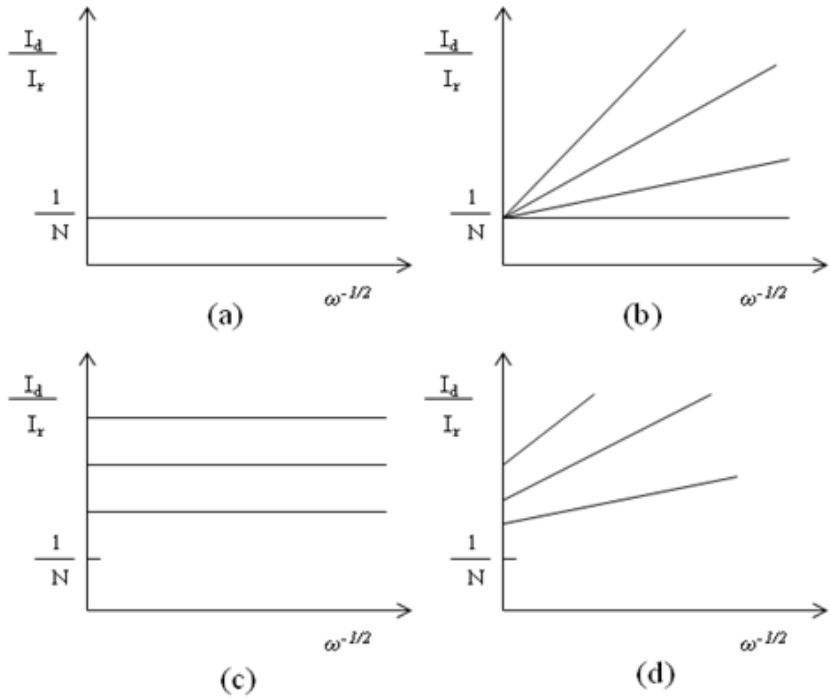

Figure 4.24 I_d/I_r as a function of $\omega^{-1/2}$ from Damjanovic *et al*.[92] (a) Electrode reaction proceeds along a single path with the formation of intermediates which do not really react further, (b) reaction proceeds along a single path with intermediates which readily react further, (c) intermediates are produced in a parallel reaction and do not react further, (d) intermediates are produced in a parallel reaction but do react further.

Based on the results on this study, Figure 4.25 shows diagnostic plots of Co/TETA/C heated at 300 °C, 500 °C, 700 °C and 1000 °C. The diagnostic plots show the straight lines parallel to the $\omega^{-1/2}$ axis and the intercepts are not identical. The dependence of the intercept

on applied potential is not substantial, from which we may conclude that the values of k_1 are small. Also if $\frac{I_d}{I_r}$ is independent of the rotation rate, the values of k_3 for the hydrogen peroxide reduction step can be assumed to be close to zero. These features are in agreement with possible outcomes (ii) and (iv) of Damjanovic's assumptions, indicating that there are two parallel pathways, where oxygen is reduced to water and hydrogen peroxide. This implied that hydrogen peroxide intermediates are produced and are not reduced further to water because the ratio $\frac{I_d}{I_r}$ is not dependent on $\omega^{-1/2}$.

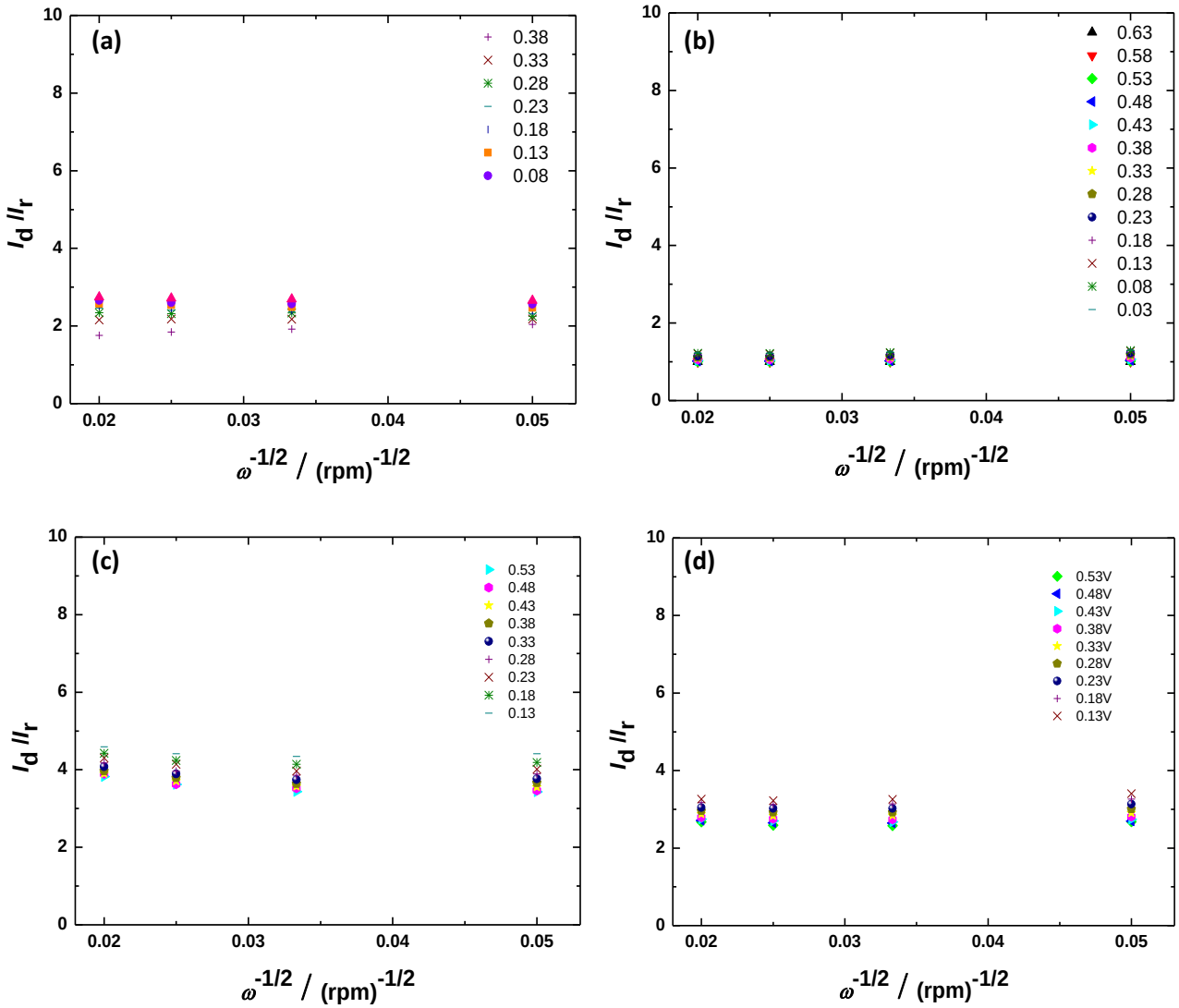

Figure 4.25 $\frac{I_d}{I_r}$ as a function of $\omega^{-1/2}$ for Co/TETA/C heated (a) 300 °C, (b) 500 °C, (c) 700 °C and (d) 1000 °C.

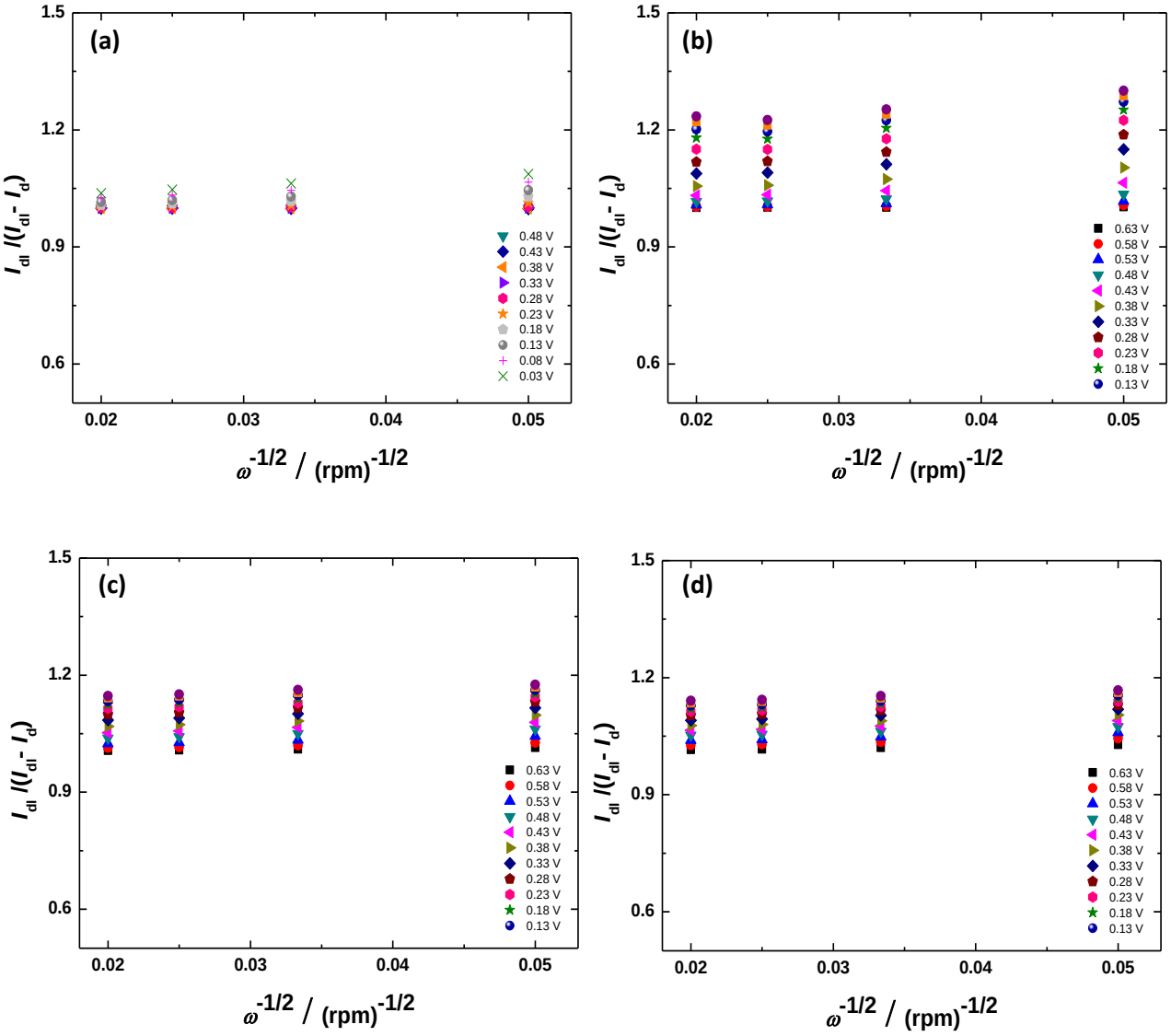

Figure 4.26 $\frac{I_{dl}}{(I_{dl}-I_d)}$ as a function of $\omega^{-1/2}$ for Co/TETA/C heated (a) 300 °C, (b) 500 °C, (c) 700 °C and (d) 1000 °C.

Later, Hsueh and Chin further developed the model based on Damjanovic's work, to determine the rate constant.[93] This model takes into account several presumptions, including (a) that there is no hydrogen peroxide chemical decomposition occurring during the measurement, (b) the adsorption and desorption of hydrogen peroxide proceed rapidly and are in equilibrium, (c) the rate constant for electrochemical oxidation of H_2O_2 is negligible. The rate constants k_1, k_2 and k_3 are calculated from the slope and the intercept of the $\frac{I_d}{I_r}$ *vs* $\omega^{-1/2}$

plot, and the slope and the intercept of $\frac{I_{dl}}{(I_{dl}-I_d)}$ *vs* $\omega^{-1/2}$ plot at the different potentials. Figure 4.26 shows the plots of $\frac{I_{dl}}{(I_{dl}-I_d)}$ *vs* $\omega^{-1/2}$ for the varying potentials from RRDE data of Co/TETA/C heated at different temperatures, which covering the rotation rates from 400 to 2500 rpm. The equations applied to evaluate the rate constants in Scheme 4.2 are given below:[93]

$$\frac{I_d}{I_r} = \frac{1+2k_1/k_2}{N} + \frac{2(1+k_1/k_2)}{NZ_2}\, k_3\omega^{-1/2} \qquad (4.12)$$

$$\frac{I_{dl}/I_r}{I_{dl}-I_d} = 1 + \frac{k_1+k_2}{Z_1}\, \omega^{-1/2} \qquad (4.13)$$

$$k_1 = S_2 Z_1 \left(\frac{I_1 N - 1}{I_1 N + 1}\right) \qquad (4.14)$$

$$k_2 = \frac{2S_2 Z_1}{I_1 N+1} \qquad (4.15)$$

$$k_3 = \frac{S_1 Z_2 N}{I_1 N+1} \qquad (4.16)$$

Eq. (4.12) and (4.13) correspond to the plots in Figure 4.25 and 4.26, respectively.

where I_{dl} = limiting disc current

N = collection efficiency

ω = rotational speed of electrode

S_1 = slope of the plot of I_d/I_r *vs* $\omega^{-1/2}$

S_2 = slope of the plot of $I_{dl}/(I_{dl}-I_d)$ *vs* $\omega^{-1/2}$

I_1 = intercept of the plot of I_d/I_r *vs* $\omega^{-1/2}$

$Z_1 = 0.2006D(O_2)^{2/3}v^{-1/6}$

$Z_2 = 0.2006D(H_2O_2)^{2/3}v^{-1/6}$

In Figure 4.26, the plotted slopes are potential-dependent. The slopes decrease as the applied potentials become more negative. The interception points also depend on the applied

potentials. All intercepted values obtained for each of the catalysts do not equal 1 which would be expected from Eq. (4.13). This may be due to small amounts of chemical decomposition occurring and/or the presence of non-uniform electrical activity produced as a result of a porous or inhomogeneous electrode surface. The straight lines obtained from the plotted graphs suggest that there is no chemical decomposition of hydrogen peroxide occurring during the process, which is expected to yield a non-linear dependence of $I_{dl}/(I_{dl}-I_d)$ *vs* $\omega^{-1/2}$.[93] The slopes and intercepts of the plots seen in Figure 4.26 indicate that the rate constants of k_1 and k_2 may depend on the applied potentials. The slopes of the plots in Figure 4.25 reflect the values of k_3, which are potential-dependent. The values of k_1, k_2 and k_3 were calculated from Eqs. (4.13), (4.14) and (4.15) and are given in Table 4.4.

Table 4.4 The values k_1, k_2 and k_3 at 0.08 V for Co/TETA/C heat-treated at different temperatures.

Samples	$\boldsymbol{k_1}$ (cm s^{-1})	$\boldsymbol{k_2}$ (cm s^{-1})	$\boldsymbol{k_3}$ (cm s^{-1})
Co/TETA/C 300 °C	3.77×10^{-6}	1.47×10^{-4}	1.05×10^{-5}
Co/TETA/C 500 °C	2.15×10^{-5}	1.44×10^{-4}	1.23×10^{-5}
Co/TETA/C 700 °C	1.78×10^{-5}	4.46×10^{-5}	1.97×10^{-5}
Co/TETA/C 1000 °C	2.58×10^{-5}	1.43×10^{-4}	9.32×10^{-5}

The Co/TETA/C catalyst treated at 300 °C provides the lowest k_1 value compared with the other catalysts. The k_2 values of all the catalysts are greater than the values of k_1 and k_3, suggesting that the catalysts may have a preference for reducing O_2 to H_2O_2 *via* the 2-electron pathway. The value of k_2 for Co/TETA/C treated at 700 °C is lower than those of the other catalysts, indicating that its catalytic activity reduces O_2 to H_2O_2 at a relatively slow rate. These features coincide with the *n* values and the H_2O_2 selectivity calculated from I_d and I_r, in that the Co/TETA/C 300 °C catalyst produces the *n* value close to 2 and yields the highest

H_2O_2 selectivity while the Co/TETA/C 700 °C produces the highest *n* value and yields the lowest H_2O_2 selectivity.

From the model of Hsueh *et al*., it is possible that the rate constants contain errors which arise from the intercept values extrapolated from the plots in Figure 4.26 at the most negative potentials. A safer analysis would be to use the intercept of the plots in Figure 4.25 (Eq. 4.12) to determine the ratio of k_1/k_2 and evaluating the k_3^0 from separate experiments of hydrogen peroxide reduction in oxygen–free electrolytes. (Here we assume that the rate of hydrogen peroxide reduction in the solution is similar to the rate of reduction as an intermediate in the ORR; however, in reality this concept may be significantly over-simplified. Nevertheless, the values for k_3 determined from analysing the kinetics of the ORR and hydrogen peroxide reduction in ref.[87] were found to be very similar, which suggests that the assumption is reasonable to a first approximation.)

Figure 4.27 presents the potential-dependent ratio of k_1/k_2 for each Co/TETA/C catalyst. The ratios increase when a larger negative potential value is applied. Nevertheless, it can be observed that the k_1/k_2 ratios of each catalyst increase at different potentials, reflecting the onset potentials order 1000 °C > 700 °C > 500 °C > 300 °C. The Co/TETA/C treated at 300 °C has the lowest ratio with a value below 0.1, suggesting that the 2-electron process is preferential for this sample. The Co/TETA/C catalyst treated at 700 °C exhibits the greatest k_1/k_2 ratio which is approximately double the value for that obtained for the other two catalysts. The larger k_1/k_2 ratio, indicates that the 4-electron reduction can make a larger contribution thus, enabling a slightly larger *n* value and smaller H_2O_2 selectivity.

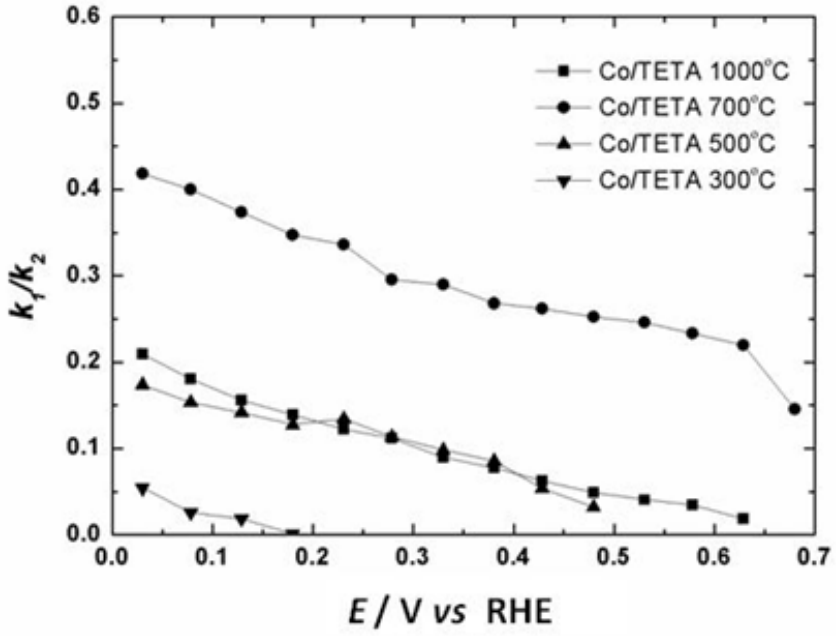

Figure 4.27 Potential dependence of k_1/k_2 for Co/TETA/C catalysts heat-treated at different temperatures.

In order to evaluate the reliability of the k_3^0 value, the H_2O_2 reduction reaction was carried out in 20 mM H_2O_2 in 0.1 M $HClO_4$. Figures 4.28 and 4.29 represent the RDE data for the H_2O_2 reduction reaction for Co/TETA/C and TETA/C catalysts heat-treated at different temperatures, respectively. The diffusion coefficient of H_2O_2 used is 8×10^{-6} cm^{-2} s^{-1}, following the previous studies in ref[86,93]. Non-liner regression analysis of RDE data was performed to fit the data to Eq. (4.1), employing Igor Pro, in order to obtain the reaction kinetic values of the transfer coefficient (αn_a) and k_3^0. n was set to 2, $D_{H_2O_2}$was taken as 8.66×10^{-6} cm^{-2} s^{-1} [87] and the concentration was 20 mM. αn_a and k_3^0 were allowed to vary (although the software restricted αn_a to between 0 and 1 and k_3^0 to positive values). The obtained results were averaged for all rotation rates. The results for k_3^0 and αn_a are presented in Table 4.5.

Table 4.5 The values k_3^0 and αn_a for Co/TETA/C heat-treated at different temperatures.

Samples	k_3^0 (cm s^{-1})	αn_a
Co/TETA/C 300 °C	(3.23 ± 0.14) × 10^{-6}	0.150 ± 0.020
Co/TETA/C 500 °C	(9.27 ± 0.23) × 10^{-6}	0.127 ± 0.005
Co/TETA/C 700 °C	(4.98 ± 0.29) × 10^{-5}	0.120 ± 0.001
Co/TETA/C 1000 °C	(7.98 ± 0.47) × 10^{-6}	0.175 ± 0.001

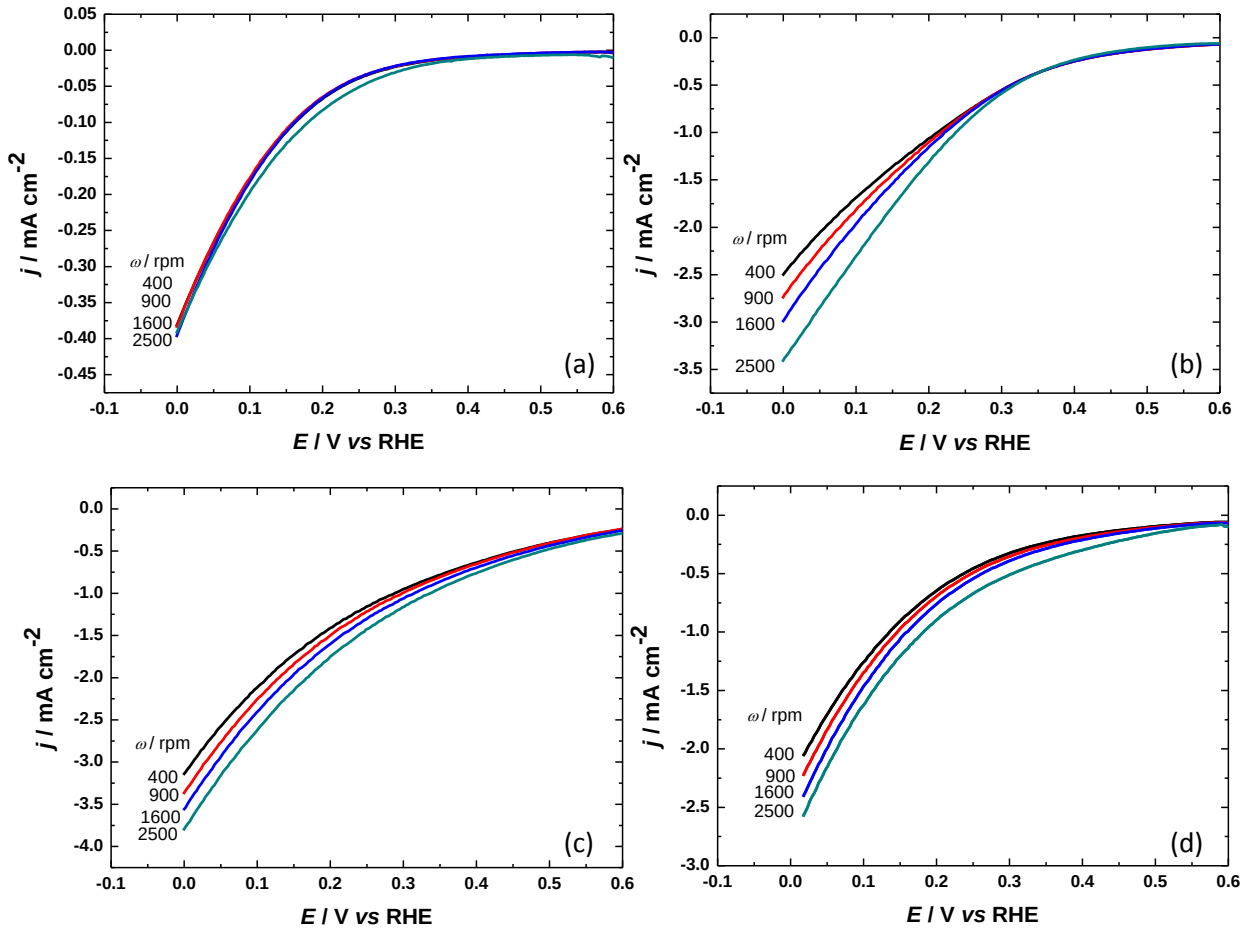

Figure 4.28 RDE polarisation curves of H_2O_2 reduction in Ar-saturated 0.1 M HClO4 + 20 mM H_2O_2 for Co/TETA/C treated at (a) 300 °C, (b) 500 °C, (c) 700 °C and (d) 1000 °C. Scan rate = 0.02 V s^{-1}.

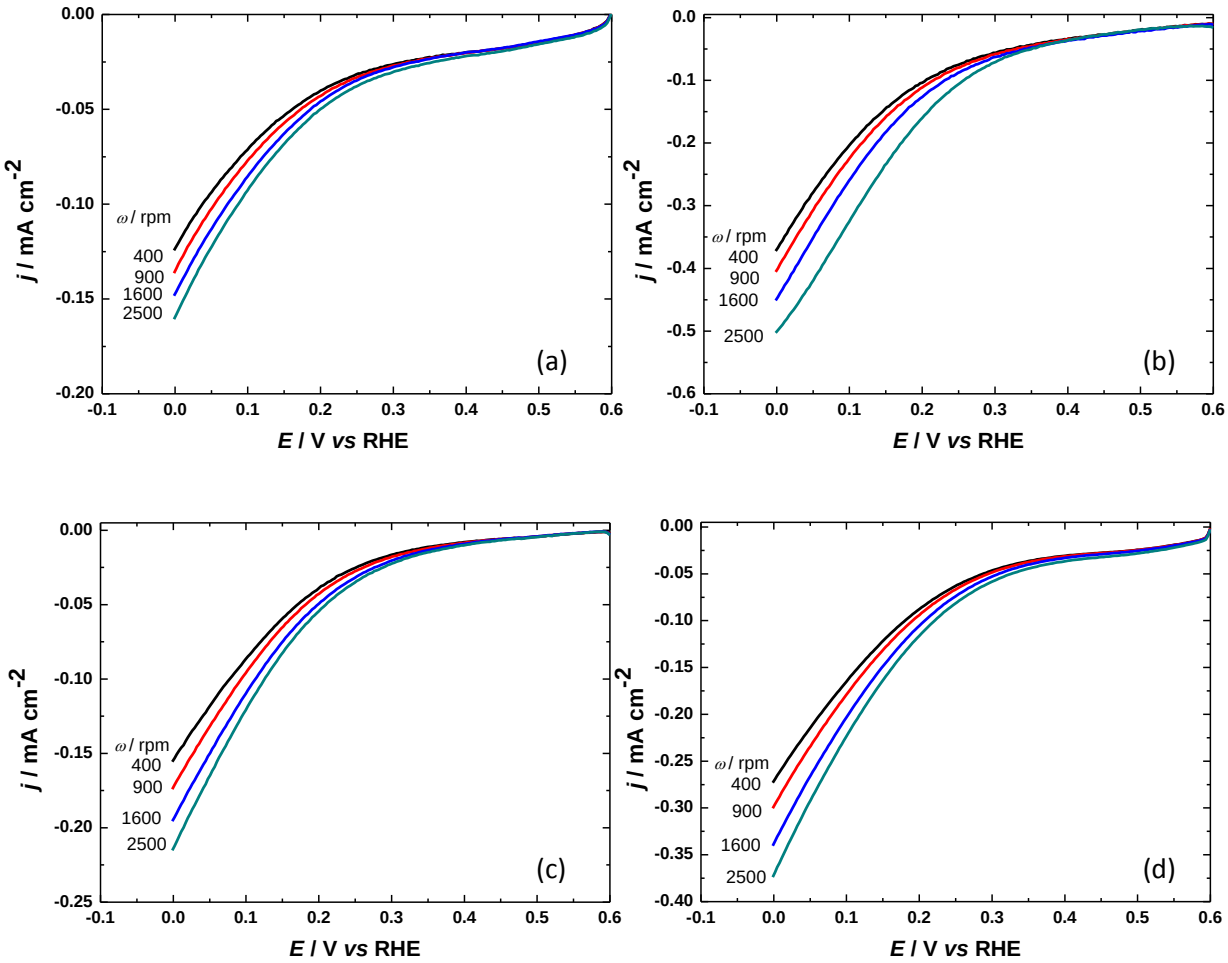

Figure 4.29 RDE polarisation curves of H_2O_2 reduction in Ar-saturated 0.1 M HClO4 + 20 mM H_2O_2 for TETA/C treated at (a) 300 °C, (b) 500 °C, (c) 700 °C and (d) 1000 °C. Scan rate = 0.02 V s^{-1}.

The rate constants for Co-containing catalysts are significantly higher than those for Co-free catalysts, which indicate that the small amounts of H_2O_2 intermediates are further reduced to H_2O in Co-containing catalysts. The k_3^0 values increase as a function of temperature until it reaches the maximum value at 700 °C and subsequently decreases for 1000 °C. The Co/TETA/C catalyst treated at 300 °C shows the lowest k_3^0 value which is similar to that of the Co-free catalyst. The Co/TETA/C catalyst treated at 700 °C has the largest k_3^0 value, which suggests that the H_2O_2 intermediates are rapidly being further reduced to H_2O in comparison with the other catalysts. The k_3^0 value for the 500 °C catalyst is similar to that of the 700 °C sample; however, the reason underlying such observations still remains

unclear. It is feasible to explain that the H_2O_2 reduction for the 500 °C samples corresponds to the co-existence of Co(II) complexes and small Co crystallinities, which are below the detection limit of the analytical techniques. While the heat-treatment increased to 700 °C, the Co(II) complexes decrease and the Co crystallinities increase until a large amount of Co particles were formed in the 1000 °C samples as seen from TEM images. The aggregation of Co crystallites diminishes the catalytic activity of the Co-containing samples when reducing oxygen to water, as can be seen in the decreased value of *n* and the increased selectivity of H_2O_2 obtained by the catalyst treated at 1000 °C.

The overall rate constant is useful to simplify the comparison of rate constants of the catalysts without recognising each pathway of the reaction. Non-linear regression analysis of RDE data was also employed to fit the data of Co/TETA/C catalysts with only one overall value of the standard rate constant, k_{app}^{0} and transfer coefficient (α) from Eq. (4.17).[87]

$$j = 1\Big/\left(\frac{\exp(38.39\alpha(E-E^{0}))}{Fn(E)k_{\mathrm{app}}^{0}c_{O_2}^{b}} + \frac{1}{0.2006n(E)FD_{O_2}^{2/3}\nu^{-1/6}c_{O_2}^{b}\omega^{1/2}}\right) \qquad (4.17)$$

where the potential dependent values of *n*(*E*) were approximated from Koutechy-Levich results as shown in Figure 4.20 and from RRDE data as shown in Figure 4.21(a). The current density in this regression was calculated using the geometric electrode area; thus the k_{app}^{0} is the overall rate constant for oxygen reduction calculated per unit geometric electrode area. The k_{app}^{0} values shown represent the average values taken from all rotation speed with the reduced chi-squared analysis less than 10^{-6}.

The k_{app}^{0} values calculated from both RRDE data and from Koutechy-Levich increase with heat-treatment temperatures. The values from the 700 °C samples are higher than those of the 1000 °C samples in both cases. However, the k_{app}^{0} values calculated from both cases

contain large standard deviation values as they were calculated from the overall oxygen reduction reaction. The values of k^0_{app} and α for each catalyst are shown in Table 4.6.

Table 4.6 The k^0_{app} and α values for Co/TETA/C heat treated at different temperatures.

Samples	k^0_{app} (cm s^{-1})	α
Co/TETA/C 500 °C *n*(*I*d/*I*r)	$(4.63 \pm 3.24) \times 10^{-6}$	0.216 ± 0.037
Co/TETA/C 700 °C *n*(*I*d/*I*r)	$(1.16 \pm 1.12) \times 10^{-5}$	0.224 ± 0.039
Co/TETA/C 1000 °C *n*(*I*d/*I*r))	$(2.51 \pm 2.00) \times 10^{-5}$	0.219 ± 0.038
Co/TETA/C 700 °C *n*(K-L)	$(1.91 \pm 0.287) \times 10^{-4}$	0.125 ± 0.004
Co/TETA/C 1000 °C *n*(K-L)	$(7.54 \pm 0.869) \times 10^{-4}$	0.091 ± 0.004

4.4 Conclusions

It is likely that the lowest k_1/k_2 ratio and k_3 value obtained by the Co/TETA/C 300 °C sample may be results from the formation of Co(II) complexes at low heat-treatment, thus suggesting that the Co (II) complex tends to produce hydrogen peroxide with a low hydrogen peroxide reduction current. The Co/TETA/C 700 °C sample has the greatest k_1/k_2 ratio and k_3 value, indicating that the presence of co-existing Co(II) complex and metallic Co enhances the reduction of oxygen to water and the reduction of hydrogen peroxide. This behaviour results in a lower H_2O_2 selectivity and higher *n* values are obtained. The H_2O_2 yield for Co/TETA/C catalysts is in between 60% to 100%. The yield drops as the heat-treatment temperature exceeds 500 °C, corresponding to the progressive formation of particles of metallic cobalt. It is difficult to separate the effects of remaining pyrolysed ligands from particle-size effects but the relatively high rate constants of oxygen reduction for cobalt particles pyrolysed at 700 °C may simply be a reflection of their very high surface area compared with the large particles found at 1000 °C. We cannot rule out the presence of cobalt metallic-like particles being

formed at 500 °C but they have not been detected by the electron-optic analyses used here. A detailed kinetic analysis does not support any substantial change in mechanism for any of the cobalt-containing catalysts as a function of heat-treatment, whether they be principally metallic or Co(II)-like in form.

Although the 300 ºC catalyst yields the highest H_2O_2 selectivity, it is not an appropriate candidate to be a catalyst for the production of hydrogen peroxide because a low current density is obtained with a large overpotential. Therefore, the 1000 ºC Co/TETA/C catalyst is the best candidate for generating hydrogen peroxide in practical applications, as it gives high current density and selectivity with lower overpotential.

4.5 References

(1) Ye, S. Y.; Vijh, A. K. *Electrochemistry Communications* **2003**, *5*, 272.

(2) Liu, G.; Li, X. G.; Ganesan, P.; Popov, B. N. *Applied Catalysis B-Environmental* **2009**, *93*, 156.

(3) Kawashima, M.; Sato, Y.; Sato, M.; Sakaguchi, M. *Polymer Journal* **1991**, *23*, 37.

(4) Yuasa, M.; Yamaguchi, A.; Itsuki, H.; Tanaka, K.; Yamamoto, M.; Oyaizu, K. *Chemistry of Materials* **2005**, *17*, 4278.

(5) Liu, H. S.; Shi, Z.; Zhang, J. L.; Zhang, L.; Zhang, J. J. *Journal of Materials Chemistry* **2009**, *19*, 468.

(6) Dipojono, H. K.; Saputro, A. G.; Belkada, R.; Nakanishi, H.; Kasai, H.; David, M.; Dy, E. S. *Journal of the Physical Society of Japan* **2009**, *78*.

(7) Jaouen, F.; Dodelet, J. P. *Electrochimica Acta* **2007**, *52*, 5975.

(8) Biddinger, E. J.; Ozkan, U. S. *Topics in Catalysis* **2007**, *46*, 339.

(9) Bezerra, C. W. B.; Zhang, L.; Lee, K. C.; Liu, H. S.; Marques, A. L. B.; Marques, E. P.; Wang, H. J.; Zhang, J. J. *Electrochimica Acta* **2008**, *53*, 4937.

(10) Ziegelbauer, J. M.; Olson, T. S.; Pylypenko, S.; Alamgir, F.; Jaye, C.; Atanassov, P.; Mukerjee, S. *Journal of Physical Chemistry C* **2008**, *112*, 8839.

(11) Olson, T. S.; Pylypenko, S.; Fulghum, J. E.; Atanassov, P. *Journal of the Electrochemical Society* **2010**, *157*, B54.

(12) Gojkovic, S. L.; Gupta, S.; Savinell, R. F. *Journal of Electroanalytical Chemistry* **1999**, *462*, 63.

(13) Gojkovic, S. L.; Gupta, S.; Savinell, R. F. *Electrochimica Acta* **1999**, *45*, 889.

(14) Manzoli, A.; Boccuzzi, F. *Journal of Power Sources* **2005**, *145*, 161.

(15) Kowalewska, B.; Skunik, M.; Karnicka, K.; Miecmikowski, K.; Chojak, M.; Ginalska, G.; Belcarz, A.; Kulesza, P. J. *Electrochimica Acta* **2008**, *53*, 2408.

(16) Wang, P.; Ma, Z. Y.; Zhao, Z. C.; Ha, L. X. *Journal of Electroanalytical Chemistry* **2007**, *611*, 87.

(17) Babic-Samardzija, K.; Sovilj, S. P.; Jovanovic, V. M. *Journal of the Serbian Chemical Society* **2003**, *68*, 989.

(18) Kiros, Y.; Lindstrom, O.; Kaimakis, T. *Journal of Power Sources* **1993**, *45*, 219.

(19) Gouerec, P.; Savy, M. *Electrochimica Acta* **1999**, *44*, 2653.

(20) Zhang, H. J.; Jiang, Q. Z.; Sun, L. L.; Yuan, X. X.; Ma, Z. F. *Electrochimica Acta* **2010**, *55*, 1107.

(21) Zhang, H. J.; Jiang, Q. Z.; Sun, L. L.; Yuan, X. X.; Shao, Z. P.; Ma, Z. F. *International Journal of Hydrogen Energy* **2010**, *35*, 8295.

(22) Zhang, H. J.; Yuan, X. X.; Sun, L. L.; Zeng, X.; Jiang, Q. Z.; Shao, Z. P.; Ma, Z. F. *International Journal of Hydrogen Energy* **2010**, *35*, 2900.

(23) Zhang, H. J.; Yuan, X. X.; Wen, W.; Zhang, D. Y.; Sun, L. L.; Jiang, Q. Z.; Ma, Z. F. *Electrochemistry Communications* **2009**, *11*, 206.

(24) Jasinski, R. *Nature* **1964**, *201*, 1212.

(25) Zhang, L.; Zhang, Y.; Zhou, X. G.; Li, R. X.; Li, X. J.; Tin, K. C.; Wong, N. B. *Journal of Molecular Catalysis a-Chemical* **2006**, *256*, 171.

(26) Bashyam, R.; Zelenay, P. *Nature* **2006**, *443*, 63.

(27) Liu, H. S.; Song, C. J.; Tang, Y. H.; Zhang, J. L.; Zhang, H. J. *Electrochimica Acta* **2007**, *52*, 4532.

(28) Wang, B.; Feng, J.; Gao, C. Y. *Colloids and Surfaces a-Physicochemical and Engineering Aspects* **2005**, *259*, 1.

(29) Fierro, C.; Anderson, A. B.; Scherson, D. A. *Journal of Physical Chemistry* **1988**, *92*, 6902.

(30) Alt, H.; Binder, H.; Sandsted.G *Journal of Catalysis* **1973**, *28*, 8.

(31) Yeager, E. *Electrochimica Acta* **1984**, *29*, 1527.

(32) S. Lopez, R. P. 2009; Vol. WO 2009/081183 A1.

(33) Oloman, C.; Watkinson, A. P. *Journal of Applied Electrochemistry* **1979**, *9*, 117.

(34) Otsuka, K.; Yamanaka, I. *Electrochimica Acta* **1990**, *35*, 319.

(35) Brillas, E.; Alcaide, F.; Cabot, P. L. *Electrochimica Acta* **2002**, *48*, 331.

(36) Alcaide, F.; Brillas, E.; Cabot, P. L. *Journal of the Electrochemical Society* **1998**, *145*, 3444.

(37) Gupta, S.; Tryk, D.; Bae, I.; Aldred, W.; Yeager, E. *Journal of Applied Electrochemistry* **1989**, *19*, 19.

(38) Gouerec, P.; Bilou, A.; Contamin, O.; Scarbeck, G.; Savy, M.; Barbe, J. M.; Guilard, R. *Journal of Electroanalytical Chemistry* **1995**, *398*, 67.

(39) Okada, T.; Gokita, M.; Yuasa, M.; Sekine, I. *Journal of the Electrochemical Society* **1998**, *145*, 815.

(40) Lin, A. S.; Huang, J. C. *Journal of Electroanalytical Chemistry* **2003**, *541*, 147.

(41) Ohms, D.; Herzog, S.; Franke, R.; Neumann, V.; Wiesener, K.; Gamburcev, S.; Kaisheva, A.; Iliev, I. *Journal of Power Sources* **1992**, *38*, 327.

(42) Wang, H.; Cote, R.; Faubert, G.; Guay, D.; Dodelet, J. P. *Journal of Physical Chemistry B* **1999**, *103*, 2042.

(43) Lefevre, M.; Dodelet, J. P.; Bertrand, P. *Journal of Physical Chemistry B* **2000**, *104*, 11238.

(44) Faubert, G.; Cote, R.; Dodelet, J. P.; Lefevre, M.; Bertrand, P. *Electrochimica Acta* **1999**, *44*, 2589.

(45) G.Q. Sun, J. T. W., S. Gupta, R.F. Savinell *Journal of Applied Electrochemistry* **2001**, *31*, 1025.

(46) Guillet, N.; Roue, L.; Marcotte, S.; Villers, D.; Dodelet, J. P.; Chhim, N.; Trevin, S. *Journal of Applied Electrochemistry* **2006**, *36*, 863.

(47) Li, S.; Zhang, L.; Liu, H. S.; Pan, M.; Zan, L.; Zhang, J. J. *Electrochimica Acta* **2010**, *55*, 4403.

(48) Fournier, J.; Lalande, G.; Cote, R.; Guay, D.; Dodelet, J. P. *Journal of the Electrochemical Society* **1997**, *144*, 218.

(49) Faubert, G.; Cote, R.; Guay, D.; Dodelet, J. P.; Denes, G.; Bertrand, P. *Electrochimica Acta* **1998**, *43*, 341.

(50) Matter, P. H.; Ozkan, U. S. *Catalysis Letters* **2006**, *109*, 115.

(51) Matter, P. H.; Zhang, L.; Ozkan, U. S. *Journal of Catalysis* **2006**, *239*, 83.

(52) Wang, X.; Waje, M.; Yan, Y. S. *Journal of the Electrochemical Society* **2004**, *151*, A2183.

(53) Bae, I. T.; Tryk, D. A.; Scherson, D. A. *Journal of Physical Chemistry B* **1998**, *102*, 4114.

(54) Bogdanoff, P.; Herrmann, I.; Hilgendorff, M.; Dorbandt, I.; Fiechter, S.; Tributsch, H. *Journal of New Materials for Electrochemical Systems* **2004**, *7*, 85.

(55) Shentu, B.; Oyaizu, K.; Nishide, H. *Journal of Materials Chemistry* **2004**, *14*, 3308.

(56) Yamazaki, S.; Yamada, Y.; Ioroi, T.; Fujiwara, N.; Siroma, Z.; Yasuda, K.; Miyazaki, Y. *Journal of Electroanalytical Chemistry* **2005**, *576*, 253.

(57) Carmo, M.; Dos Santos, A. R.; Poco, J. G. R.; Linardi, M. *Journal of Power Sources* **2007**, *173*, 860.

(58) Lefevre, M.; Dodelet, J. P.; Bertrand, P. *Journal of Physical Chemistry B* **2002**, *106*, 8705.

(59) Jaouen, F.; Marcotte, S.; Dodelet, J. P.; Lindbergh, G. *Journal of Physical Chemistry B* **2003**, *107*, 1376.

(60) Franke, R.; Ohms, D.; Wiesener, K. *Journal of Electroanalytical Chemistry* **1989**, *260*, 63.

(61) Cheng, X.; Shi, Z.; Glass, N.; Zhang, L.; Zhang, J.; Song, D.; Liu, Z.-S.; Wang, H.; Shen, J. *Journal of Power Sources* **2007**, *165*, 739.

(62) Liu, H.; Song, C.; Tang, Y.; Zhang, J.; Zhang, J. *Electrochimica Acta* **2007**, *52*, 4532.

(63) Gouerec, P.; Savy, M.; Riga, J. *Electrochimica Acta* **1998**, *43*, 743.

(64) Vanveen, J. A. R.; Colijn, H. A.; Vanbaar, J. F. *Electrochimica Acta* **1988**, *33*, 801.

(65) Lalande, G.; Cote, R.; Tamizhmani, G.; Guay, D.; Dodelet, J. P.; Dignardbailey, L.; Weng, L. T.; Bertrand, P. *Electrochimica Acta* **1995**, *40*, 2635.

(66) Widelov, A.; Larsson, R. *Electrochimica Acta* **1992**, *37*, 187.

(67) Faubert, G.; Lalande, G.; Cote, R.; Guay, D.; Dodelet, J. P.; Weng, L. T.; Bertrand, P.; Denes, G. *Electrochimica Acta* **1996**, *41*, 1689.

(68) Lalande, G.; Faubert, G.; Cote, R.; Guay, D.; Dodelet, J. P.; Weng, L. T.; Bertrand, P. *Journal of Power Sources* **1996**, *61*, 227.

(69) Bouwkamp-Wijnoltz, A. L.; Visscher, W.; van Veen, J. A. R.; Boellaard, E.; van der Kraan, A. M.; Tang, S. C. *Journal of Physical Chemistry B* **2002**, *106*, 12993.

(70) Medard, C.; Lefevre, M.; Dodelet, J. P.; Jaouen, F.; Lindbergh, G. *Electrochimica Acta* **2006**, *51*, 3202.

(71) Lefevre, M.; Dodelet, J. P.; Bertrand, P. *Journal of Physical Chemistry B* **2005**, *109*, 16718.

(72) Zhang, H.-J.; Jiang, Q.-Z.; Sun, L.; Yuan, X.; Ma, Z.-F. *Electrochimica Acta* **2010**, *55*, 1107.

(73) Zhang, H.-J.; Jiang, Q.-Z.; Sun, L.; Yuan, X.; Shao, Z.; Ma, Z.-F. *International Journal of Hydrogen Energy* **2010**, *35*, 8295.

(74) McBreen, J. *Extended Abstracts*; The Electrochemical Society: Pennington, NJ, 1987; Vol. 87-1.

(75) Alves, M. C. M.; Dodelet, J. P.; Guay, D.; Ladouceur, M.; Tourillon, G. *Journal of Physical Chemistry* **1992**, *96*, 10898.

(76) Gontard, L. C.; Dunin-Borkowski, R. E.; Ozkaya, D.; Hyde, T.; Midgley, P. A.; Ash, P. In *EMAG-NANO 2005: Imaging, Analysis and Fabrication on the Nanoscale*; Brown, P. D., Baker, R., Hamilton, B., Eds.; Iop Publishing Ltd: Bristol, 2006; Vol. 26, p 367.

(77) Ozkaya, D. *Platinum Metals Review* **2008**, *52*, 61.

(78) Tanaka, N. *Science and Technology of Advanced Materials* **2008**, *9*.

(79) Campos, M.; Siriwatcharapiboon, W.; Potter, R. J.; Horswell, S. L. *Catalysis Today* **2013**, *202*, 135.

(80) Yang, R. Z.; Bonakdarpour, A.; Easton, E. B.; Stoffyn-Egli, P.; Dahn, J. R. *Journal of the Electrochemical Society* **2007**, *154*, A275.

(81) Tong, J. P. K., Langford, C. H. *Can. J. Chem* **1978**, *54*, 706.

(82) Bagotzky, V. S.; Tarasevich, M. R.; Radyushkina, K. A.; Levina, O. A.; Andrusyova, S. I. *Journal of Power Sources* **1978**, *2*, 233.

(83) Oh, H. S.; Kim, H. *Journal of Power Sources* **2012**, *212*, 220.

(84) Kothandaraman, R.; Nallathambi, V.; Artyushkova, K.; Barton, S. C. *Applied Catalysis B-Environmental* **2009**, *92*, 209.

(85) Kundu, S.; Nagaiah, T. C.; Xia, W.; Wang, Y. M.; Van Dommele, S.; Bitter, J. H.; Santa, M.; Grundmeier, G.; Bron, M.; Schuhmann, W.; Muhler, M. *Journal of Physical Chemistry C* **2009**, *113*, 14302.

(86) A.J. Bard, L. R. F. *Electrochemical Methods: Fundamental and Applications*; Wiley: NY, 1980.

(87) Jirkovsky, J. S.; Halasa, M.; Schiffrin, D. J. *Physical Chemistry Chemical Physics* **2010**, *12*, 8042.

(88) Zecevic, S. K.; Wainright, J. S.; Litt, M. H.; Gojkovic, S. L.; Savinell, R. F. *Journal of the Electrochemical Society* **1997**, *144*, 2973.

(89) Claude, E.; Addou, T.; Latour, J. M.; Aldebert, P. *Journal of Applied Electrochemistry* **1998**, *28*, 57.

(90) Ma, Y.; Zhang, H.; Zhong, H.; Xu, T.; Jin, H.; Tang, Y.; Xu, Z. *Electrochimica Acta* **2010**, *55*, 7945.

(91) Jirkovsky, J. S.; Panas, I.; Ahlberg, E.; Halasa, M.; Romani, S.; Schiffrin, D. J. *Journal of the American Chemical Society* **2011**, *133*, 19432.

(92) Damjanov.A; Genshaw, M. A.; Bockris, J. O. *Journal of Chemical Physics* **1966**, *45*, 4057.

(93) Hsueh, K. L.; Chin, D. T.; Srinivasan, S. *Journal of Electroanalytical Chemistry* **1983**, *153*, 79.

CHAPTER 5

RHODIUM AND RHODIUM−GOLD NANOPARTICLES FOR NITRATE REDUCTION AND NITRITE REDUCTION

5.1 Introduction

This chapter describes the investigation of the electrocatalytic activity of Rh, AuRh and modified Rh particles for nitrate reduction and nitrite reduction. Nitrate and nitrite pollution of water is a threat to our human health and to ecological systems. Both nitrate and nitrite are potentially carcinogenic agents and a cause of "blue baby syndrome".[1-3] Nitrite is highly involved in human life since it is widely used in the food industry in order to preserve food and cure meat and to flavour and colour. Nitrate in ground water becomes a risk to the human body after it has been reduced to nitrite by the biological reduction reaction in bacteria *in vivo*. An excess intake of nitrate could then cause deterioration in human health. The EU nitrate directive limits the contaminant level in consumer water such that the concentration of nitrate must not exceed 50 mg/L, which is the same level of nitrate concentration in drinking water is recommended by The World Health Organisation (WHO). The steady accumulation of nitrate in ground water is a result of biological and environmental activity as well as industrial process.[2] In nature, the accumulation takes place from biogeochemical nitrogen cycle, including in the atmosphere, the geomosphere and biomosphere.[1] The intensive use of fertilisers in agriculture and the use of nitrates in several industries, such as iron, paper, electronic and nuclear fuel processes, cause severe water pollution.

Nitrate and nitrite can be removed by several methods, for instance, biological methods and physiochemical methods, including ion exchange[4], membrane separation[5,6], catalytic treatment[7-11]. However, the processes of biological methods are complex and suitable

for nitrate removal only on a small scale. Membrane separation and ion exchange techniques possess various disadvantages, such as the high concentration in secondary brine waste, the formation of toxic by-products and the high process cost. Therefore, much research effort has gone into seeking a feasible process with high selectivity that can convert nitrate into harmless or useful industrial products.

Electrocatalysis for nitrate removal[9,10,12-21] is a promising option, which has been intensively investigated for over four decades due to several advantages, for example, it is environmentally friendly, highly selective, safe and has moderate process costs. The possible oxidation states of nitrogen compounds in acidic media are presented in Figure 5.1.[22-24] The oxidation state diagram plots the volt equivalent (VE, the standard potential × nitrogen oxidation state) of the electrochemical equilibrium between a certain compound and N_2, versus the oxidation state of the compounds.

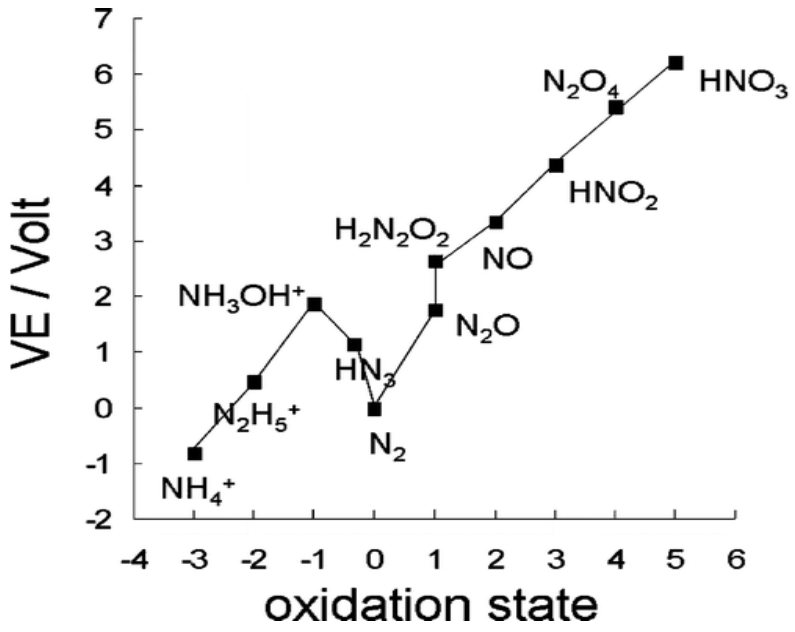

Figure 5.1 Oxidation state diagram of inorganic nitrogen compounds in acidic solution. VE is the "volt equivalent", that is, the standard potential for the conversion to N_2 × the nitrogen oxidation state of the species under consideration.[22-24] (Note that HN_3 refers to azide)

The diagram shows that the ammonia and dinitrogen should be the thermodynamically most stable forms of nitrogen, which mean that they should be the end-products of nitrate reduction.[24] However, this diagram does not consider the kinetics of the reaction and the interaction with the solid-state catalyst, which are necessary considerations for electrocatalysis. Practically, ammonia and nitrous oxide are dominant products in nitrate reduction and the selectivity towards these products depends on electrode nature, pH, electrolyte, electrode potential, experimental conditions etc.

Figure 5.2 presents a reaction of microbial nitrogen cycle in ecosystem, including dinitrogen fixation, nitrification and denitrification. There are several intermediates involved with the nitrogen cycle. The following section describes each compound in the nitrogen cycle.

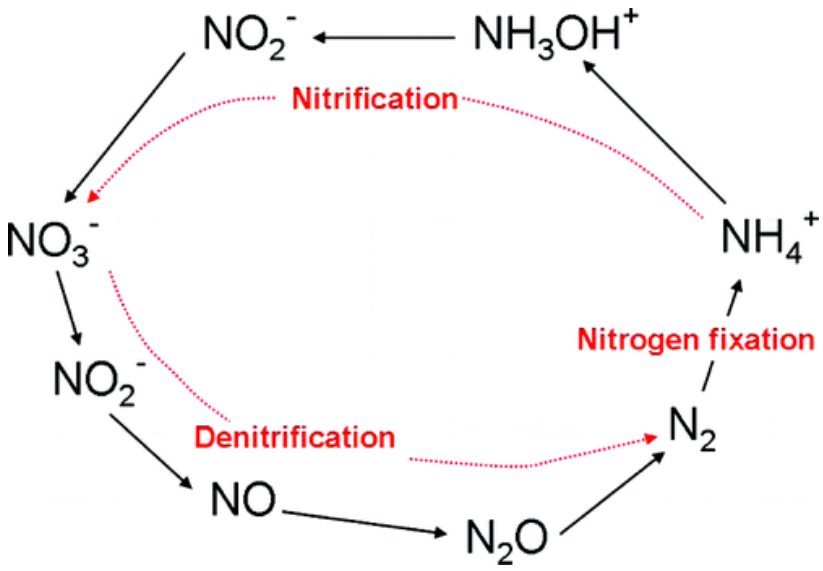

Figure 5.2 Simplified scheme of the "classical" nitrogen cycle.[25,26]

Ammonia (NH_3) can be used as nitrogen source in fertiliser production. NH_3 can be produced as the main product when an electrode capable of cleaving the N−O bond is used, such as Rh[11] or Ru[21].

Hydroxylamine (NH_2OH) is a required material in the production of caprolactam. NH_2OH is a major product of nitrate reduction for various electrodes such as, Pt, Ir, Pd[11,27] or an immobilised Fe porpyrin[28]. It can be produced because those electrodes have less ability to break the last N−O bond of nitrite by electrocatalysis.

Nitrous oxide (N_2O) is a compound used as an anaesthetic in medical applications. N_2O is the main product from nitrite reduction on most precious metal electrodes.[8,27] However, it cannot be found in nitrate reduction, except when a noble metal electrode has been modified by a second metal.[11,29,30] N_2O plays an important role, in that it can be further reduced to N_2 on a few electrodes,[29,31] as shown in the following reaction.

$$N_2O + 2H^+ + 2e^- \rightarrow N_2 + H_2O \qquad (5.1)$$

However, in most cases N_2O is weakly absorbed on electrode surfaces; hence, it escapes from the electrode before further reduction to produce N_2. Pd is the most promising catalyst for nitrite reduction so it is actively able to produce N_2O, even when hindered by sulphate.[32] Differently from the other metals, Pd promotes the mechanism where free sites of Pd can decompose N_2O by adsorbing oxygen atoms on the surface, as shown in reactions (5.2) and (5.3).

$$N_2O_{ads} \rightarrow O_{ads} + N_2 \qquad \text{slow irreversible reaction} \qquad (5.2)$$

$$O_{ads} + 2H^+ + 2e^- \rightarrow H_2O \qquad \text{fast reaction} \qquad (5.3)$$

The decomposition of N_2O has also found on the surface of Pd (110) under Ultra High Vacuum (UHV).[33]

Nitric oxide (NO) is an important key intermediate for nitrate reduction and nitrite reduction. Nitrate is reduced stepwise *via* nitrite formation, leading to an adsorbed NO (NO_{ads}) intermediate. In nitrite reduction, NO adsorbs on the electrode surface and it may yield NO

solution (NO_{aq}), as generated from the pH dependent decomposition of nitrous acid (HNO_2), as shown in reaction (5.4) – (5.6).

$$NO_2^- + H^+ \leftrightarrow HNO_2 \qquad pK_a = 3.35 \qquad (5.4)$$

$$2HNO_2 \leftrightarrow NO + NO_2 + H_2O \qquad (5.5)$$

$$3NO_2 + H_2O \leftrightarrow NO + 2H^+ + 2NO_3^- \qquad (5.6)$$

As seen from the reaction, the decomposition of HNO_2 is promoted when the pH value of the electrolyte decrease and the concentration of nitrite increase. The adsorption of NO on metal surface has been widely investigated. NO adlayers on Pt electrodes, prepared from nitrite in acidic media, can be stripped in blank electrolyte and the Pt electrode completely recovers.[34-36] NO_{ads} on Pt electrodes is preferentially converted to NH_2OH.[11] In contrast, Rh does not recover after NO stripping as there is an irreversible poisoning of N_{ads} from NO_{ads} fragmentation.[20,37]

Nitrite (NO_2^-) is toxic if it contaminates food or water in high concentration. Nitrite reduction has been mostly studies in acidic media in the form of HNO_2, as it can generate NO adlayers on metal electrodes.[37-39] There are much fewer reports in neutral and in alkaline since nitrite reduction is less active and nitrite is mostly converted to ammonia.[19,40] Duca *et al*. have published a number of papers on nitrite reduction[18-21,28,41], showing that the mechanism of nitrite and nitrous acid reduction on platinum electrode is a function of electrode potential and the solution pH. They suggested a general pH-dependent mechanistic scheme, as shown in Figure 5.3.[19] On platinum, nitrite is more easily reduced than nitrate. Several products, such as NH_2OH and NH_3 are detected.[19,20] On rhodium, only NH_3 is detected.[8]

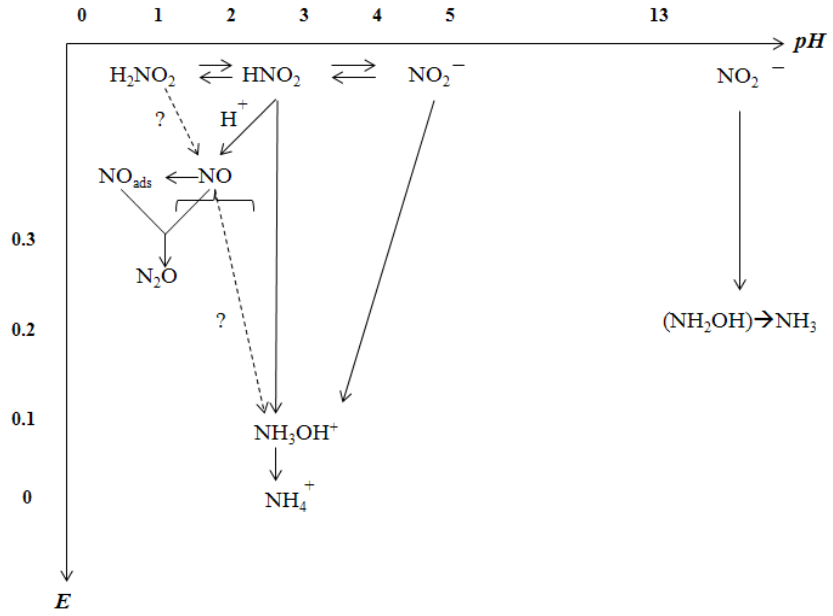

Figure 5.3 Mechanistic pathways for nitrite/nitrous acid reduction as a function of pH and potential.[19]

Nitrate can contaminate ground water. The reduction of nitrate in liquid-phase heterogeneous catalysts can proceed *via* several pathways, indicating that there are several intermediates during the reaction. The list of the products to which nitrate can be reduced and the corresponding equilibrium potentials are given below:[24]

$NO_3^- + 2H^+ + 2e^- \leftrightarrow NO_2^- + H_2O$ $\quad E^0 = 0.835$ V (*vs* NHE) (5.7)

$NO_3^- + 4H^+ + 3e^- \leftrightarrow NO_{(g)} + 2H_2O$ $\quad E^0 = 0.958$ V (*vs* NHE) (5.8)

$NO_3^- + 10H^+ + 8e^- \leftrightarrow N_2O + 5H_2O$ $\quad E^0 = 1.116$ V (*vs* NHE) (5.9)

$NO_3^- + 12H^+ + 10e^- \leftrightarrow N_2 + 6H_2O$ $\quad E^0 = 1.246$ V (*vs* NHE) (5.10)

$NO_3^- + 8H^+ + 6e^- \leftrightarrow NH_3OH^+ + 2H_2O$ $\quad E^0 = 0.727$ V (*vs* NHE) (5.11)

$NO_3^- + 10H^+ + 8e^- \leftrightarrow NH_4^+ + 3H_2O$ $\quad E^0 = 0.875$ V (*vs* NHE) (5.12)

The hydrogen evolution reaction (HER) competes with nitrate reduction in acidic media:

$2H^+ + 2e^- \leftrightarrow H_2$ $\quad E^0 = 0$ V (*vs* NHE) (5.13)

The large number of nitrogen compound intermediates makes the study of nitrate reduction hard. There are many reports about nitrate reduction on noble metal electrodes. Platinum is the most intensively studied. However, Rh has been suggested to be the most promising catalyst.[9,42,43] Palladium shows similar activity to Pt but it is the most active catalyst for nitrite reduction.[10] Au presents very small activity for nitrate reduction, while Cu and Fe present appreciable activity and produce ammonia in acidic media but they are corroded during the reaction.[10,44,45] It is known that nitrate reduction can proceed *via* two different mechanisms: the first mechanism has been practically operated in mild concentration of nitrate and acidity of electrolyte. The second mechanism has been operated in high concentration of nitrate (> 1 M) and high acidity (pH < 0) of supporting electrolyte.[9]

Vijh *et al.* presented the first report, which compared several transition metals for nitric acid and nitrate reduction.[46] Their volcano plot is based on the electroreduction of nitric acid.[47] It has been concluded that a moderate value of interaction energy between metal and oxygen atom presents high reaction rate. Recently, Dima *et al.* investigated nitrate reduction on several metals, along with an anion effect. The activity of transition metals towards nitrate reduction decreases in the order Rh > Ru > Ir > Pd and Pt, and of coinage metals in the order Cu > Ag > Au. No gaseous product was found for Rh and Pt. Rh presents the most catalytic activity and yields both nitrite and ammonia, suggesting it is more effective in stepwise reduction.[7,8] This is in good agreement with reports by Wesberg and Horanyi,[42,43,48] who determined that the diffusion limit is achieved for nitrate reduction on Rh. Dima also determined from the Tafel slope of 120 mV dec^{-1} that the first electron transfer is the rate-determining step, indicating the step of nitrate reduction to nitrite.[10,42,43,49] Also the effect of co-adsorption of anions is more significant on Pt and Pd than on Rh.[10,50,51] Apart from polycrystalline electrodes, Dima *et al.* also studied nitrate reduction on single crystal Pt

electrodes. It has been found that nitrate reduction is a structure-sensitive reaction on single crystal electrodes, controlled by the other species (hydrogen, anion) rather than nitrate itself.[16]

Reddy *et al.* studied nitrate removal from ground water by electrocatalytic reduction under different redox potentials of nitrate and reaction time for Rh, Pd and Pt on carbon supports.[52,53] On Rh, the lower redox potential and longer reaction achieved a substantial decrease in nitrate concentration without the detection of NO_2^-; however, lower redox potential is prior to be considered. While Pt and Pd enable to reduce nitrate but merely in slow rate. It is known that gaseous products cannot be detected from Rh, Pt and Pd electrodes.

Brylev *et al*. studied the direct, quantitative analysis of nitrate reduction in neutral media.[7,8] Rh-modified pyrolytic graphite presents a high nitrite adsorption on its surface and subsequent increases in an ammonium yield. Later, they varied the conditions of the experiment and concluded that the rate constant of the step nitrate to nitrite increases with pH increase, indicating the influence of hydrogen evolution on nitrate removal. The current efficiencies of H_2 and NH_3 increase at more negative potentials. The selectivity to N_2 is not improved on temperature increase. The addition of formate anion has a significantly effect on hydrogen evolution and nitrate reduction rather than the addition of carboxylate and tetraalkylammonium cations.

Witonka *et al.* used Rh/Al_2O_3 and $Rh{-}Cu/Al_2O_3$ for hydrogenation of nitrate in water.[54] The activity of Rh/Al_2O_3 is similarly high to that of $Rh{-}Cu/Al_2O_3$ but the bimetallic catalysts decrease the time to complete nitrate reduction. However, addition of Cu does not increase the selectivity to N_2. The Rh/Al_2O_3 catalyst enables reduction of nitrate to nitrite, although its activity is lower than that of $Rh{-}Cu/Al_2O_3$. In the case of Pt and Pd, the catalysts are less active for nitrate reduction.[55,56] The role of Rh/Al_2O_3 is in the reduction of nitrite to N_2 and NH_4^+. Pronkin *et al*. studied nitrate reduction on Pd/C and Cu-modified Pd/C.[57] The

carbon support does not interfere with the reaction due to its significantly low activity. Cu modification enhances the activity of Pd/C for nitrate reduction. The surface of Pd particles with 4 nm diameter comprises of small contribution of (111) and (100) facets, which decrease with a decrease of particles size, suggesting that the smaller particles presents lower catalytic activity.

Shimazu *et al.* [11,27,30,58-60] published a number of papers involving Sn-modified noble metals for nitrate reduction and nitrite reduction. Sn mainly promotes nitrate reduction by adsorbing one atom of nitrate. The soluble and gaseous products, such as NO_2^-, N_2O, NH_3^+, NH_3OH^+ and N_2, can be detected, depending on the electrode material. The authors quantitatively evaluated the abilities of the electrode to cleave N−O bonds and to form N−N bonds and N−H bonds. The values of ability to cleave N−O bond decrease in the order of Sn/Rh > Sn/Pt > Sn/Ru > Sn/Pd > Sn/Ir. The capability of the selective N_2 production evaluated from the bond formation and bond cleavage decreases in the order of Sn/Pd > Sn/Rh > Sn/Pt > Sn/Ir >> Sn/Ru. Experimentally, Sn/Pt yields the highest amount of N_2 formation. For nitrite reduction, the trends in properties of the electrode opposite to those for nitrate reduction.

Gootzen *et al*. studied Ge-modified Pt, Pd and Pt+Pd electrodes.[12,61] The activity of the electrodes was proportionally related to Ge coverage. GePd generates more hydroxylamine than GePt and GePt+Pd. The formation of NO can be detected from GePd and GePt+Pd. Ge promotes nitrate reduction. Dima *et al.* showed that Ge inhibits anion and hydrogen adsorptions, which compete with nitrate adsorption.[17] Prusse *et al.* investigated the mechanism of nitrate hydrogenation for InPt and InPd catalysts and concluded that the possible mechanism proceeds through the combination of active sites on bimetallic catalysts. [62-64] Several reports form Marchesini investigated the effect of catalyst supports, Al_2O_3 and

SiO_2, on catalytic activity of InPt and InPd.[65-69] Krawczyk *et al.* reported that high selectivity towards N_2 not only depends on catalyst dispersion but also depends on the porosity and the presence of intermetallic PdIn compounds on the surface.[70] However, all reports investigated bimetallic catalysts and the mechanism of nitrate reduction on these catalysts is still unclear.

For nitrate removal from waste water, the nitrate ion is stable and highly soluble so it is not amenable to removal by conventional water treatment processes such as coagulation and precipitation or adsorption and filtration. Hence, specialised processes are necessary. The most common treatment processes used to remove nitrate are reverse osmosis (RO), ion exchange (IE), electro-dialysis (ED) and activated carbon adsorption in conjunction with pH adjustment.[71] However, there are some disadvantages of these methods. IE removes nitrate ions from treated water but it also produces secondary waste from the process of regeneration of the resin, which rich in nitrate ions and difficult to dispose. Complementary methods for denitrification should be combined with nitrate removal processes. Electrocatalytic denitrification has recently been applied successfully when combined with ion exchange.[72,73] The electrochemical method has a high rate of nitrate conversion and applicability to any composition of wastes.

The concentration of nitrate in wastes and water may vary. The concentration of nitrogen compounds in some industrial waste waters is tremendously higher than that in groundwater and surface water.[74-76] The concentration of nitrate influences the rate of nitrate reduction and the distribution of product.[75,76] Industrial waste water contains high concentrations of ions such as nitrate, sulphate, sodium, as well as several metal ions such as copper, lead and zinc. Petrii *et al.* observed a linear dependence of the current density on the nitrate ion concentration in sulfuric acid solutions and studied the cathodic reduction of nitrate in the presence of Cs^+, La^{3+} and Cd^{2+} cations and Cu adatoms.[77,78] For Pt electrodes, the

electroreduction of NO_3^- is pH-independent in that because the reaction takes place at the same potential. However, the electroreduction currents in acid decrease with increasing pH, while the electroreduction current in alkaline solution presents almost no pH dependence.[48]

In this work, we emphasised on the nitrate reduction at low concentration of nitrate and nitrite. We studied the electrocatalytic activities of Rh nanoparticles on carbon substrate Rh/C, AuRh/C and Sn-modified Rh/C for nitrate reduction and nitrite reduction in sulphuric acid have been investigated. On-line electrochemical mass spectrometry (OLEMS) was employed to detect the volatile products. On-line ion chromatography (IC) was combined with voltammetry to determine the formation of soluble products, in particular the formation of NH_4^+ and NH_3OH^+ in acidic media.

5.2 Experimental

5.2.1 Materials

All experiments for nitrate and nitrite reduction were carried out at room temperature. All glassware was cleaned in an acid bath as described in chapter 3.2. Sodium nitrate ($NaNO_3$, 99.99 %) was obtained from Merck. Sodium nitrite ($NaNO_2$, 99.99 %), Germanium (IV) oxide (GeO_2, 99.99%), Tin (II) chloride dehydrate ($SnCl_2$ $2H_2O$, 99.99%), and sodium hydroxide (NaOH, 99.99%), were purchased from Sigma Aldrich. All chemicals mentioned above were stored in vacuum desiccator. Sulphuric acid (H_2SO_4, 96%) was purchased from Merck. Sodium hexachlororhodate ($Na_3RhCl_6 \cdot 12H_2O$) and indium (III) sulphate hydrate ($In_2(SO_4)_3$) was purchased from Alfa Aesar. Cetyltrimethylammonium bromide (CTAB) and L-ascorbic acid were purchased from Acros, sodium borohydride ($NaBH_4$) was obtained from Riedel-de Haën. Ultrapure water (purified with a Millipore Milli-Q: resistivity 18.2 MΩ cm, TOC ≤ 5 ppb) was used throughout.

5.2.2 Catalyst preparation

Co-reduced Au–Rh nanoparticles used in this work were prepared by the procedure described in Chapter 3.2. Bare Rh particles were prepared by chemical reduction. 0.225 mL 0.02 $Na_3RhCl_6 \cdot 12H_2O$ was added to 3 mL 0.1 M CTAB and was reduced by 1.5 mL 0.1 M $NaBH_4$ at 40 °C with 2 h sonication. The total volume was adjusted to 6.0 mL. The content of Rh particles in this work is the same as the content of Rh in co-reduced Au:Rh particles of 1:1 ratio. The sample was then kept at 25 °C for 24 h. In order to obtain Rh catalyst ink, the catalyst suspension was mixed with cleaned carbon powder (Vulcan XC-72R) under sonication for 2 h. The catalyst was then centrifuged twice at 6000 rpm for 1 h and redispersed in 1 mL of H_2O. For Au particles, bare Au particles were prepared with the same procedure stated in chapter 3.2.

The particle size and morphology of Rh nanoparticles were characterised by scanning transmission electron microscopy (STEM). The images were obtained with a Jeol 2100F STEM, fitted with a CEOS spherical aberration corrector and a high-angle annular dark field (HAADF) detector, operated at an accelerating voltage of 200 kV.

5.2.3 Electrochemical measurements

A polycrystalline Rh electrode, co-reduced Au:Rh/C particles and Rh/C particles were used in this work. The polycrystalline Rh electrode (flag shape) with 99.9% purity was flame-annealed and quenched in water saturated with argon. For Au:Rh/C and Rh/C particles, the glassy carbon electrode was polished using increasingly finer aqueous alumina powder slurries (1.0, 0.3 and 0.05 μm, Buehler), followed by sonication in ultrapure water for 5 min and potential cycling in blank solution to clean and check the electrode surface. The electrode was then removed from the electrochemical cell, rinsed with ultra pure water and dried under

an Ar stream. 4 μL of the freshly sonicated catalyst suspension was pipetted onto the surface of the glassy carbon disc (0.071 cm^2) and dried under argon atmosphere at room temperature. Afterwards, the electrode was gently rinsed with ultra pure water before be transferred to the electrochemical cell.

For all electrochemical measurements, the counter and reference electrodes were a Pt coil and a reversible hydrogen electrode (RHE). All potentials reported in this work are referred to the RHE. The Autolab Pgstat20 was employed for all electrochemical measurements except for the experiments involving on-line electrochemical mass spectrometry, which employed an Ivium A06075 potentiostat. Prior to the electrochemical measurements, both acidic (0.1 M H_2SO_4) and alkaline (0.1 M NaOH) electrolytes were saturated with argon. In order to protect the solution from oxygen ingress, argon also was purged above the electrolyte during the measurements. The working electrode was immersed in the electrochemical cell whilst applying the potential at 0.5 V (in the double layer region of the catalyst), in order to stabilise the electrode surface and to ensure reproducibility of the measurements. The working electrodes in hanging menicus were activated in blank electrolyte scanned from 0.0 V to 0.55 V with scan rate 0.05 V s^{-1} for 10 scans before starting the measurement, which employed a scan rate 0.01 V s^{-1}. Nitrate reduction and nitrite reduction experiments were carried out in the Ar-saturated electrolyte with freshly prepared 10 mM $NaNO_3$ and 0.8 mM $NaNO_2$ solution, respectively, with scan rate 0.01 V s^{-1}. The pH of the electrolyte was checked after the experiment with a Radiometer Copenhagen pH electrode. A pH change of the electrolyte was not observed.

NO adsorption and stripping were carried out by following procedure. The activated electrode was immersed in Ar-saturated 0.1 M H_2SO_4 containing 0.8 mM $NaNO_2$ and applied the potential at 0.20 V (*vs* RHE) for 2 min. The electrode was rinsed, protected with the water

droplet and transferred to another cell containing Ar-saturated blank electrolyte. The NO stripping was performed with various scan rates. The nitrite concentration of NO adsorption experiment is equal to that of stationary continuous reduction experiment.

On-line electrochemical mass spectrometry (OLEMS) measurements[29] were performed with an evolution mass spectrometer (MS) system (European Spectrometry Systems Ltd.). The system consists of a Prisma QMS200 (Pfeiffer), brought to vacuum with a TMH-071P turbo molecular pump (60 l/s, Pfeiffer) and a Duo 2.5 rotary vane pump (2.5 m^3/h, Pfeiffer). During measurement, the pressure inside the MS was below 1×10^{-6} mbar and products at the electrode interface were collected through a small inlet tip positioned close to (~10 μm) the electrode in the electrochemical cell. A video camera was used to adjust the position of the tip. The entire tip configuration was cleaned in chromic acid and rinsed with large amount of ultra pure water before use.[79] The fragmentation ratio of N_2O (*m/z* = 44) to other important volatile compounds, such as N_2 (*m/z* = 28), NO (*m/z* = 30), was considered and calibrated in order to estimate the products that really form on the electrode. In this work, the fragmentation ratios of N_2O were determined as N_2:N_2O = 0.0685, and NO:N_2O = 0.202, following Yang *et al.*[29] The OLEMS set up is shown in Figure 5.4.

Figure 5.4 OLEMS set up.

The IC experiment is set up follows explanation by Yang *et al*. The combines an ion chromatography unit (Shimadzu, Prominence) with a conductivity detector (CDD-10Ap, Shimadzu), with an automatic fraction collector (FRC-10A, Shimadzu), to collects samples by using a small Teflon tip which positioned in the solution close to the surface of hanging meniscus working electrode in the electrochemical cell. The samples were collected every 60 mV during voltammetry of 0.1 M HNO_3 with scan rate 0.001 V s^{-1}. A microtiter plate with the collected samples was placed in an autosampler (SIL-20A) holder and 20 µL of sample was injected into the column. The column used was a Shodex IC Y-521 single column for the Rh/C samples and a Shodex IC Y-521 two columns for the SnRh/C samples. Diluted 4 mM HNO_3 was used as the eluent with 1 mL min^{-1} flow rate. The temperature of the column was maintained at 40 °C for the Rh/C samples and at 30 °C for the SnRh/C samples.

5.2.4 Tin (Sn), Indium (In), and Germanium (Ge) modifications of working electrodes

The experiment studying Sn-modified working electrodes were performed in another electrochemical cell after checking the electrode surface in blank electrolyte. For spontaneous Sn deposition, the working electrode was immersed in Ar-saturated 0.1 M H_2SO_4 + 0.025 mM $SnCl_2$ at open circuit for 2 min to induce a spontaneous adsorption. For electrodeposition Sn, the electrode was immersed in Ar-saturated 0.1 M H_2SO_4 + 0.05 mM $SnCl_2$ and a potential of 0.20 V was applied for 10 min. After Sn modification, the electrode potential was controlled at 0.5 V and the electrode was caused at this potential, rinsed with ultrapure water and directly transferred to the electrochemical cell for cyclic voltammetry in 0.1 M H_2SO_4 to estimate the Sn coverage on the electrode by recording the voltammogram in hydrogen rerion. The electrode was then used to study nitrate reduction.

For In modification, 6.9 mM $In_2(SO_4)_3$ was prepared. Then 0.77 g Na_2SO_4 was mixed with 100 mL of ultra pure water. The Na_2SO_4 solution was then adjusted to pH 3 by adding 0.1 M H_2SO_4. 100 mL of Na_2SO_4 was mixed with 1 mL of 6.9 mM $In_2(SO_4)_3$ and served as electrolyte. The electrochemical cell was set up as described previously. The working electrode was immersed in the electrochemical and potential of 0.1 V was applied for 10 min.

For Ge modification, 50 mL 0.2678 mM GeO_2 were prepared in 0.5 M H_2SO_4. Then 1 mL of the obtained GeO_2 solution was mixed with 100 mL 0.1 M H_2SO_4. The Ge modification was carried out with the same procedure as for Sn modification.

5.3 Results and Discussion

The catalytic activity for nitrate reduction and nitrite reduction of Au, Rh and Au:Rh particles were compared in both acidic media and alkaline media. The electrodes were characterised using cyclic voltammetry (CV), on-line electrochemical mass spectrometry (OLEMS) and ion chromatography (IC).

5.3.1 Electrocatalyst characterisation of Au/C, Rh/C, Au:Rh/C and polycrystalline Rh electrodes.

5.3.1.1 Acid media

5.3.1.1.1 Nitrate reduction

5.3.1.1.1.1 Au/C

The cyclic voltammogram of Au/C particles is presented in Figure 5.5. The anodic and cathodic peaks at 0.6 V arise from quinodal species on the carbon substrate. The Au oxide formation and Au oxide reduction peaks are at 1.4 V in the forward scans and at 1.15 V in the negative scan, respectively. Figure 5.6 shows the cyclic voltammogram of Au/C particles in

the double layer region in blank electrolyte and in 10 mM $NaNO_3$ + 0.1 M H_2SO_4. The carbon substrate does not catalyse nitrate reduction, which is in agreement with the literature.[52] The nitrate reduction is very slow and hardly detectable on Au/C particles. Literature reports that Au is the least catalytically active of the coinage metals for nitrate reduction.[10,80] Da Cunha *et al*. reported that this may be because of the low nitrate adsorption energy of Au.[81] However, Au is a good support for the other metals for nitrate reduction. It can be modified by foreign metal atoms, such as Cd[82,83], Pb[84], Ag [84] etc.[80], to form a monolayer or multilayers to improve the catalytic activity for nitrate reduction.

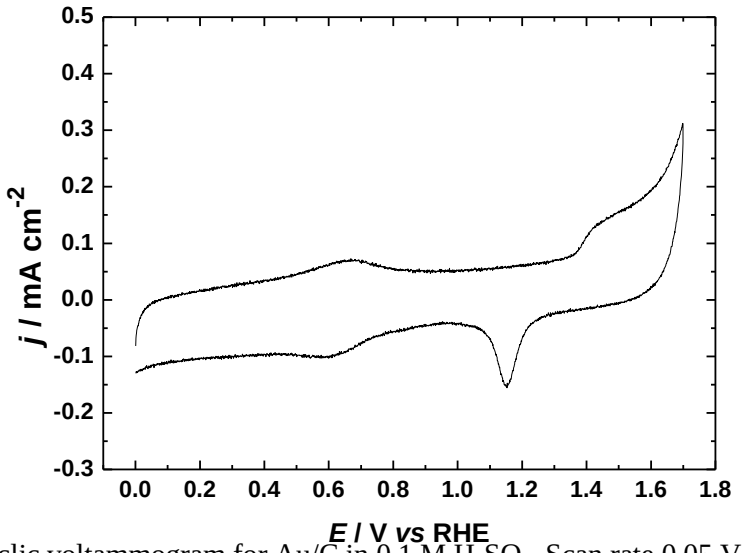

Figure 5.5 Cyclic voltammogram for Au/C in 0.1 M H_2SO_4. Scan rate 0.05 V s^{-1}.

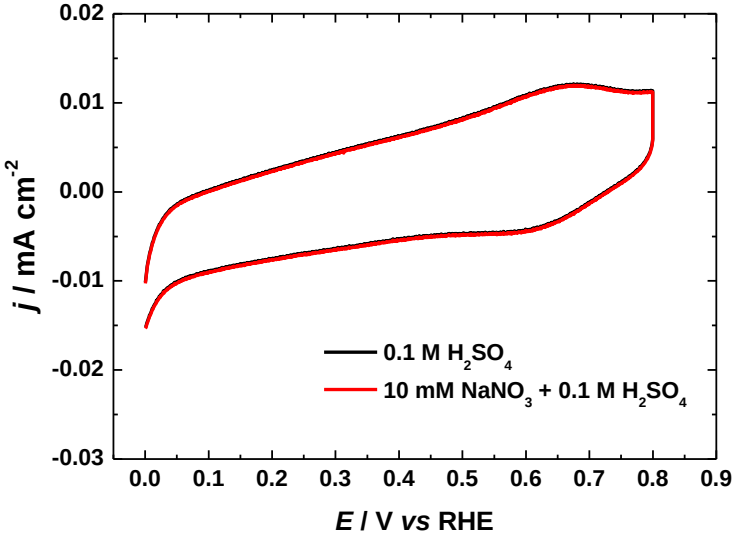

Figure 5.6 Cyclic voltammograms for Au/C in 0.1 M H_2SO_4 and in 10 mM $NaNO_3$ + 0.1 M H_2SO_4. Scan rate 0.01 V s^{-1}.

5.3.1.1.1.2 Rh/C

STEM images were kindly provided by Ruth Chantry, School of Physics and Astronomy, University of Birmingham. Figure 5.7 shows representative transmission electron microscopy (TEM) and high angle annular dark field (HAADF) images of Rh nanoparticles. The spherical-shaped particles have average size 2-5 nm.

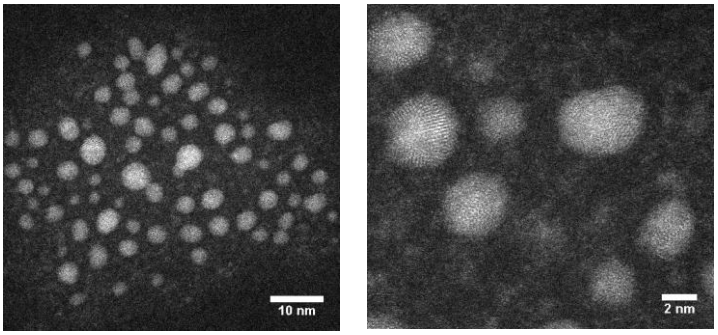

Figure 5.7 STEM-HAADF images of Rh nanoparticles.

Rh is the most promising catalyst for nitrate reduction[53] and nitrate removal[52] in acidic media. The Rh commercial catalyst for nitrate removal in groundwater is a 30% Rh coated on carbon cloth (1 μg cm^{-1}), ELAT (E-Tek Inc., Natick, MA).[52] The literature reports that most metals yield higher catalytic activity in $HClO_4$ than in H_2SO_4 as sulphate ion is strongly adsorbed on the electrode surface, hindering the adsorption of nitrate and nitrite.[10,57] Despite this H_2SO_4 was used in this present work as it is known that Rh reduces and catalyses the decomposition of ClO_4^- to Cl^- in the studied potential range[20,43] and Cl^- strongly adsorbs on both Au and Rh even more strongly. The potential range utilised covers the double-layer region and hydrogen adsorption/desorption region. Meanwhile, the upper potential limit does not exceed 0.6 V, in order to stabilise the surface during the measurement.[57]

The cyclic voltammograms of Rh/C in blank electrolyte and in 10 mM $NaNO_3$ + 0.1 M H_2SO_4 are shown in Figure 5.8. The cyclic voltammogram in the blank solution exhibits two peaks corresponding to hydrogen desorption and one peak corresponding to hydrogen

adsorption. It is known that the reduction of NO_3^- is a stepwise reduction, in which the rate-determining step is the step of nitrate reduction to nitrite. The inhibition happens because of the competitive adsorption between H_{ads}, NO_3^- and the intermediates of NO_3^- reduction.[78] The CV results suggest that H_{ads} and $NO_3^-{}_{ads}$ start to be formed at starting potential of 0.55 V. The nitrate ions are then reduced slowly to nitrite at double layer region potentials. The onset potential of nitrate reduction for Rh/C is at 0.30 V, at which the surface of the electrode is largely covered by NO, giving higher current density due to its reduction. The reduction current increases at more negative potentials until a maximum is reached at ~0.10 V. A reduction current decrease is then observed at potentials negative of 0.10 V, due to H_{ads} stronger adsorption on the electrode surface.[7,8] More electrons are needed for nitrate reduction than hydrogen adsorption so if H_{ads} prevails, less current flows. This current decrease is also found for Pt and Pd metal, although their activities significantly decrease compared with Rh because Pt and Pd have lower adsorption enthalpy of nitrate compared with hydrogen.[10] The PZC of Rh is more negative than Pt and Pd, which leads to a stronger anion adsorption at these potentials.[8]

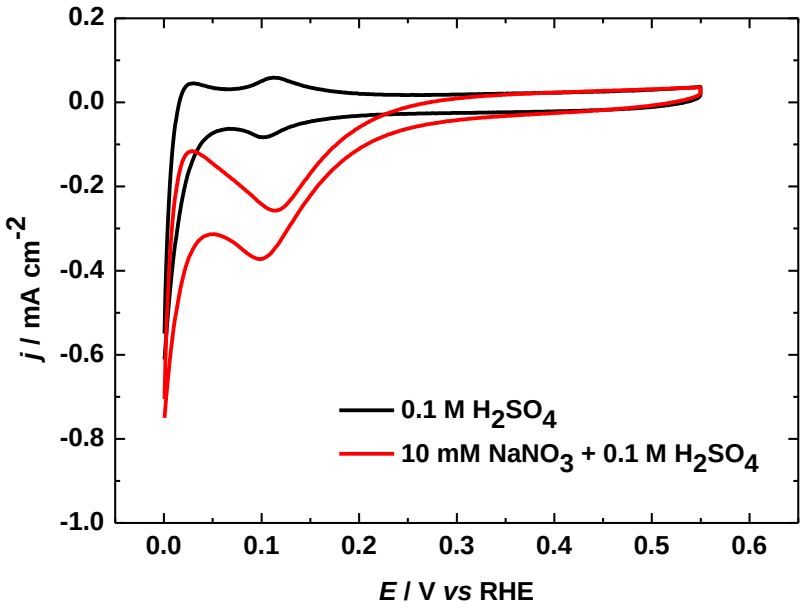

Figure 5.8 Cyclic voltammograms for Rh/C in 0.1 M H_2SO_4 and in 10 mM $NaNO_3$ + 0.1 M H_2SO_4. Scan rate 0.01 V s^{-1}.

5.3.1.1.1.3 Polycrystalline Rh electrode

Figure 5.9 presents cyclic voltammograms of a polycrystalline Rh electrode in 0.1 M H_2SO_4 and in 10 mM $NaNO_3$ + 0.1 M H_2SO_4. The blank voltammogram displays major peaks at 0.13 V in the anodic scan and at 0.10 V in the cathodic scan. There are minor shoulders at more positive potentials due to adsorption on Rh (100) facets.[37] The voltammogram of this Rh electrode is similar to that of Rh/C. The polycrystalline Rh electrode has smaller current background than Rh/C, for the larger current background arises from the carbon support. A large nitrate reduction current is observed due to the large geometric area of the electrode. The onset potential of the reaction is at 0.35 V. The reduction current reaches a maximum at 0.10 V. These results are in good agreement with Rh/C, suggesting that the carbon support has insignificant effect on the activity of Rh.

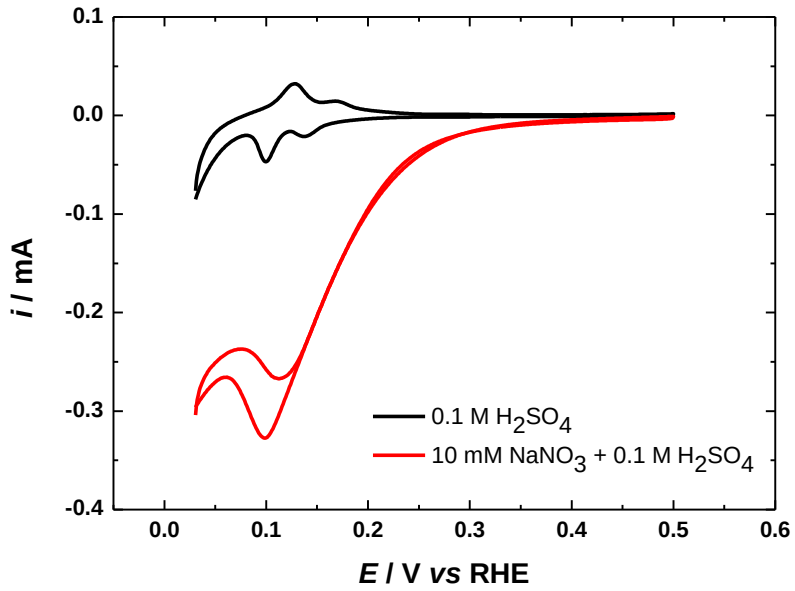

Figure 5.9 Cyclic voltammograms for polycrystalline Rh electrode in 0.1 M H_2SO_4 and in 10 mM $NaNO_3$ + 0.1 M H_2SO_4. Scan rate 0.01 V s^{-1}.

5.3.1.1.1.4 Au:Rh/C

Figure 5.10 presents the cyclic voltammograms for carbon supported AuRh nanoparticles of different ratios. Figure 5.10(a) presents the voltammograms of a 10:1 Au:Rh/C sample. The

small hydrogen desorption is noticeable in the blank voltammogram. The nitrate reduction is very small and hardly detectable for this sample, as there only small Rh content with large Au content. For the 7:3 ratio Au:Rh/C sample in Figure 5.10(b), the hydrogen adsorption and desorption increase slightly, as does the activity for nitrate reduction. The hydrogen adsorption and desorption, as well as the catalytic activity for nitrate reduction, dramatically increases for the 1:1 and 1:2 Au:Rh/C samples, as shown in Figure 5.10(c) and 5.10(d).

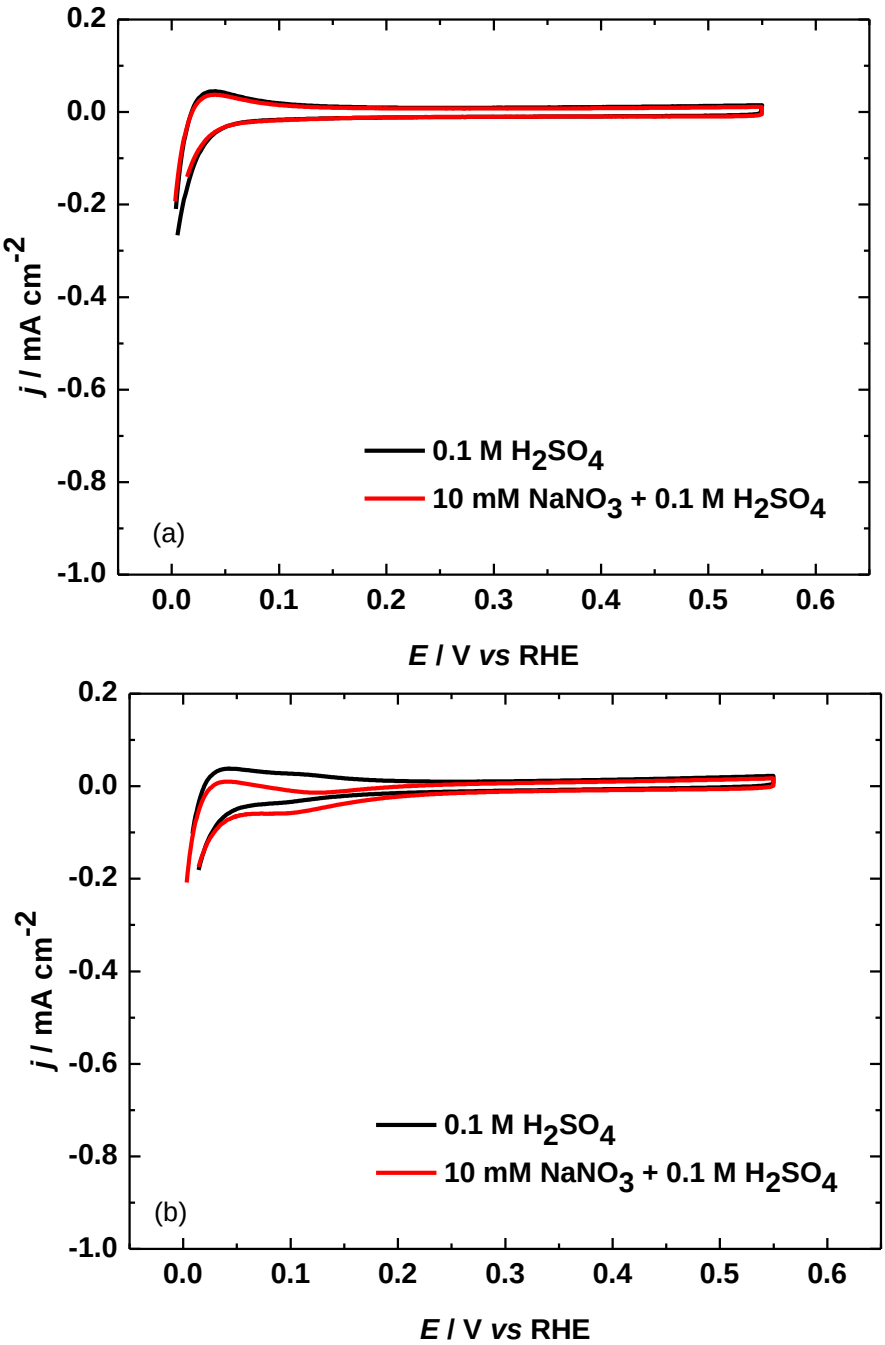

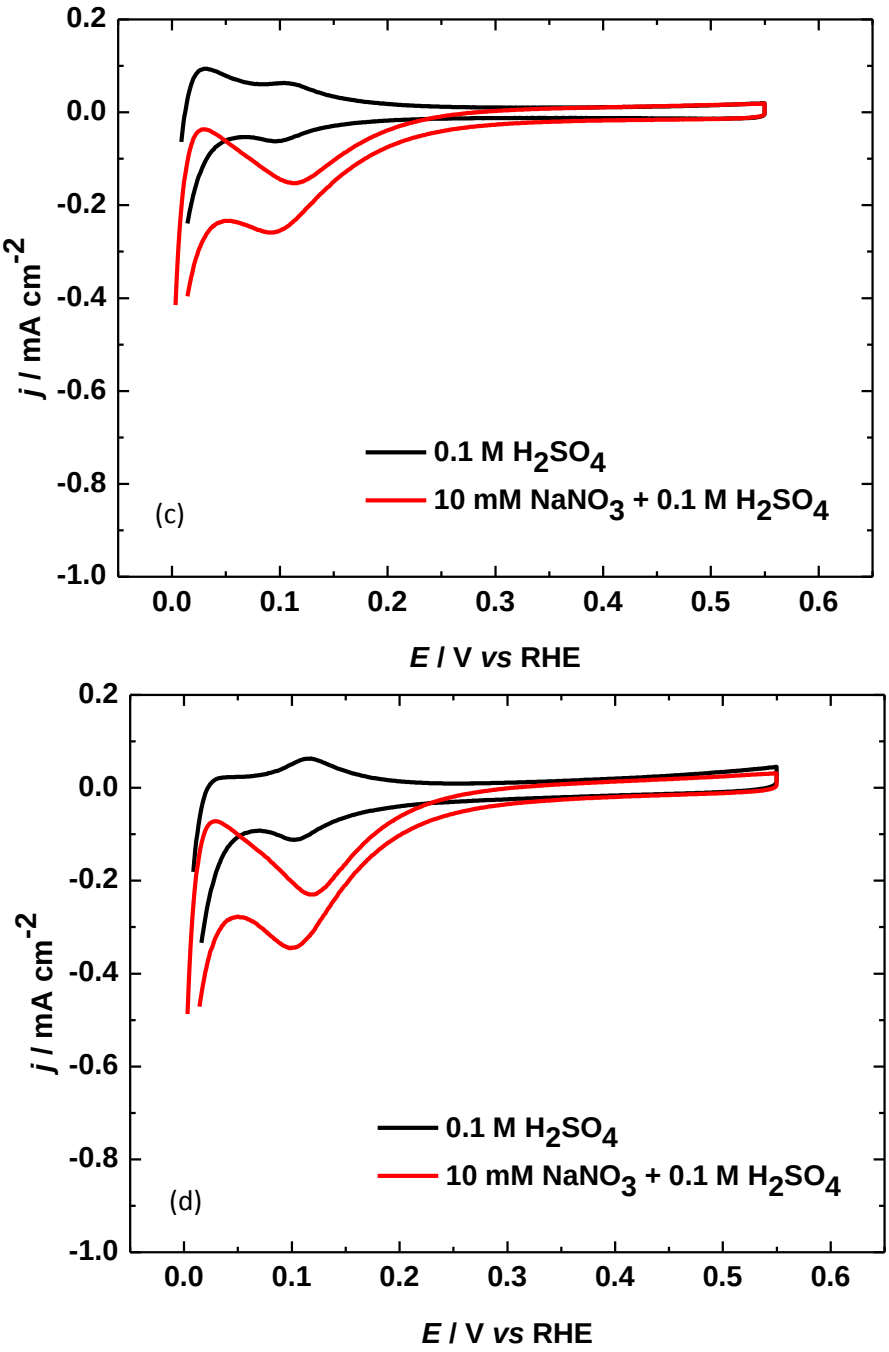

Figure 5.10 Cyclic voltammograms for Au:Rh/C (a) 10:1, (b) 7:3, (c) 1:1 and (d) 1:2 in 0.1 M H_2SO_4 and in 10 mM $NaNO_3$ + 0.1 M H_2SO_4. Scan rate 0.01 V s^{-1}.

The voltammograms of each Au:Rh/C ratio for nitrate reduction are compared together in Figure 5.11 in order to observe clearly the catalytic activity change. The onset potentials of the reaction shift to more positive potential from the lowest ratio of Rh and drastically increase at the 1:1 and 1:2 ratios.

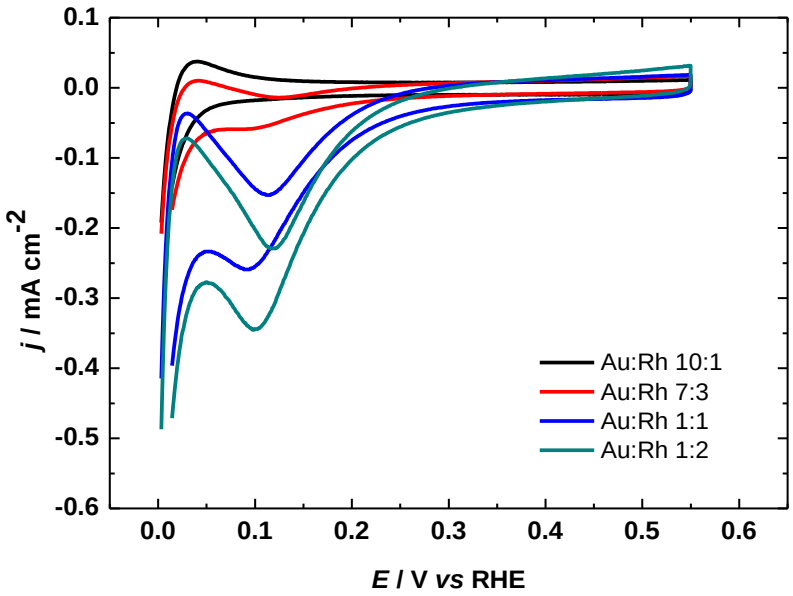

Figure 5.11 Cyclic voltammograms for Au:Rh/C in 10 mM $NaNO_3$ + 0.1 M H_2SO_4. Scan rate 0.01 V s^{-1}.

Figure 5.12 compares the cyclic voltammograms of Rh/C and 1:1 Au:Rh/C samples where both samples have the same Rh loading. The Rh/C sample shows higher reduction current and the onset potential is slightly shifted to more positive potential than for the Au:Rh/C sample.

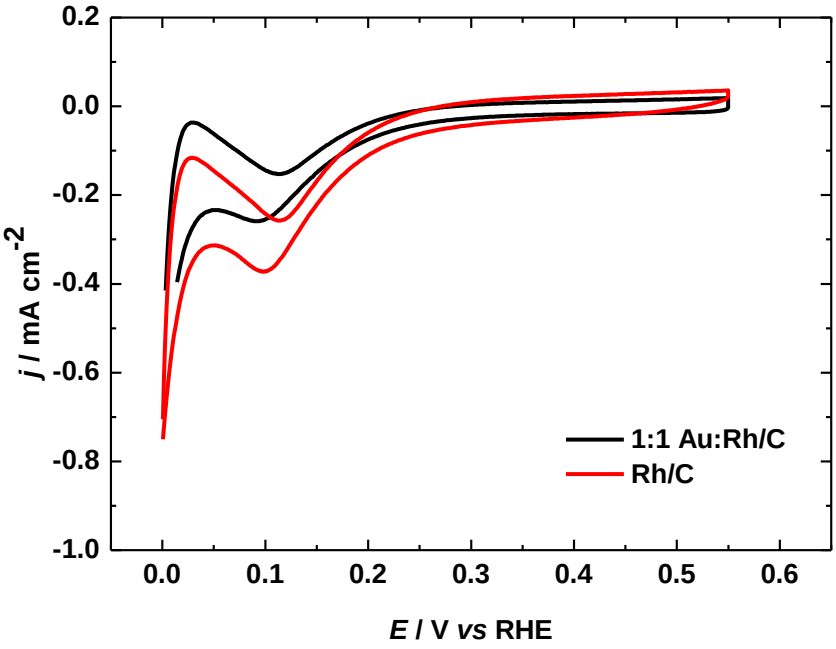

Figure 5.12 Cyclic voltammograms for Au:Rh/C and Rh/C in 10 mM $NaNO_3$ + 0.1 M H_2SO_4. Scan rate 0.01 V s^{-1}.

5.3.1.1.2 Nitrite reduction

5.3.1.1.2.1 Au/C

Figure 5.13 presents cyclic voltammograms of Au/C in 0.1 M H_2SO_4 and 0.8 mM $NaNO_2$ + 0.1 M H_2SO_4. In this work, a low concentration of $NaNO_2$ was used to minimise the chemical decomposition of nitrous acid (HNO_2).[20] Additionally, the cyclic voltammogram was measured immediately after adding $NaNO_2$. As stated previously, it is difficult to detect nitrate reduction for the Au/C sample. For nitrite reduction, the Au/C sample also shows small activity; however, more appreciable reduction current can be detected in this potential range before the potential of hydrogen evolution.

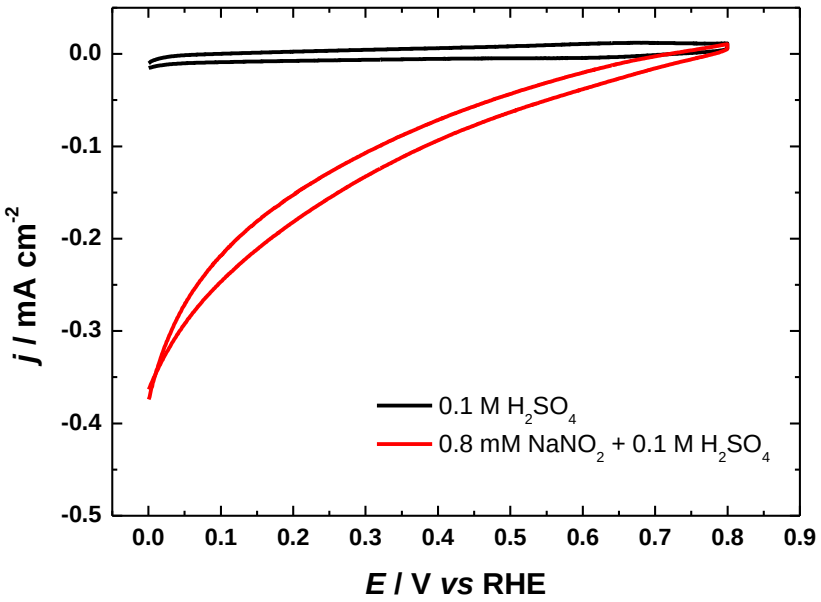

Figure 5.13 Cyclic voltammograms for Au/C in 0.1 M H_2SO_4 and in 0.8 mM $NaNO_2$ + 0.1 M H_2SO_4. Scan rate 0.01 V s^{-1}.

It is known that nitrite is more easily reduced than nitrate. A broad potential range is used for Au/C and the onset potential is at around 0.75 V. This is related to the potential of NO reduction on gold electrodes in acidic electrolytes, which have been studied previously.[14,21] It suggests that NO is at least one of the N-containing species which can be

adsorbed on gold surfaces and is reduced to ammonia. The formation of NO can be confirmed by on-line electrochemical mass spectrometry in section 5.3.2.1.

5.3.1.1.2.2 Rh/C

Figure 5.14 shows the cyclic voltammogram of Rh/C for nitrite reduction. The reduction current is small in the potential range between 0.55 V and 0.30 V but, at potentials negative of 0.30 V, the reduction current dramatically increases. The main reduction current at potential negative of 0.30 V is due to the reduction of NO_{ads} on electrode surface.[85] In mild acid, the main electroactive form of nitrite is HNO_2, which generates dissolved NO in the electrolyte. NO_{aq} reacts with NO_{ads} on the electrode surface to form N_2O. N_2O is reduced further to form N_2 or NO is reduced and hydrogenated to from NH_4^+ or NH_3OH^+.[86]

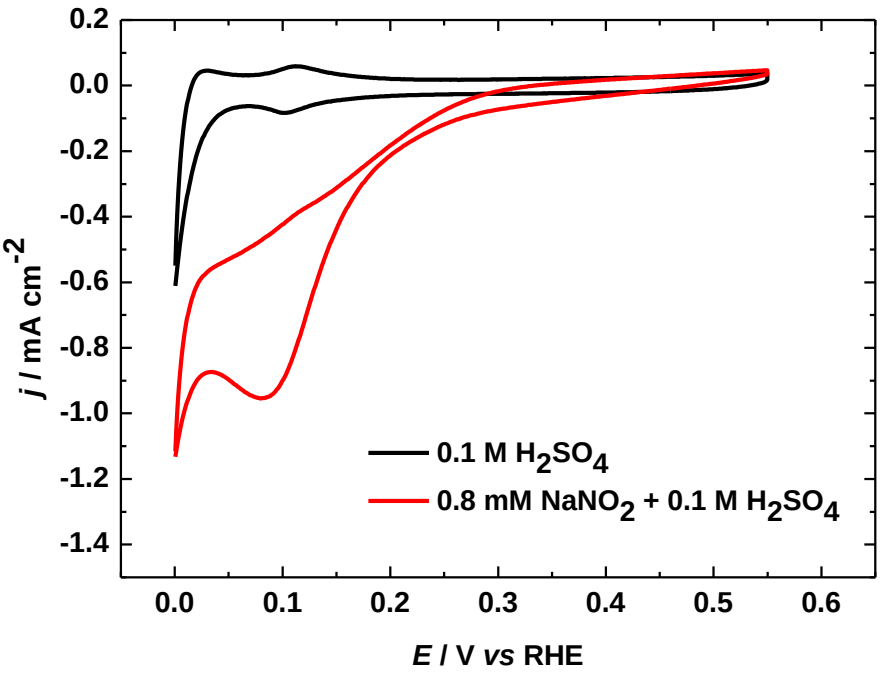

Figure 5.14 Cyclic voltammograms for Rh/C in 0.1 M H_2SO_4 and in 0.8 mM $NaNO_2$ + 0.1 M H_2SO_4. Scan rate 0.01 V s^{-1}.

NO adsorption experiment were carried out to analyse the adsorbed species during nitrite reduction by transfer of NO_{ads} to clean, NO-free electrolyte, where an adsorbate stripping experiment was performed. Figure 5.15 displays the voltammetric profiles for the

first and second scans of NO stripping. On Rh/C, a large NO reduction peak can be observed at the potentials negative of 0.3 V, followed by a small shoulder peak. The nitrite reduction peak on Rh/C is diminished at potentials negative of 0.1 V. The reduction of NO_{ads} to NH_4^+ is formed in the potential range of 0.0 - 0.20 V through a reduction and hydrogenation.[15]

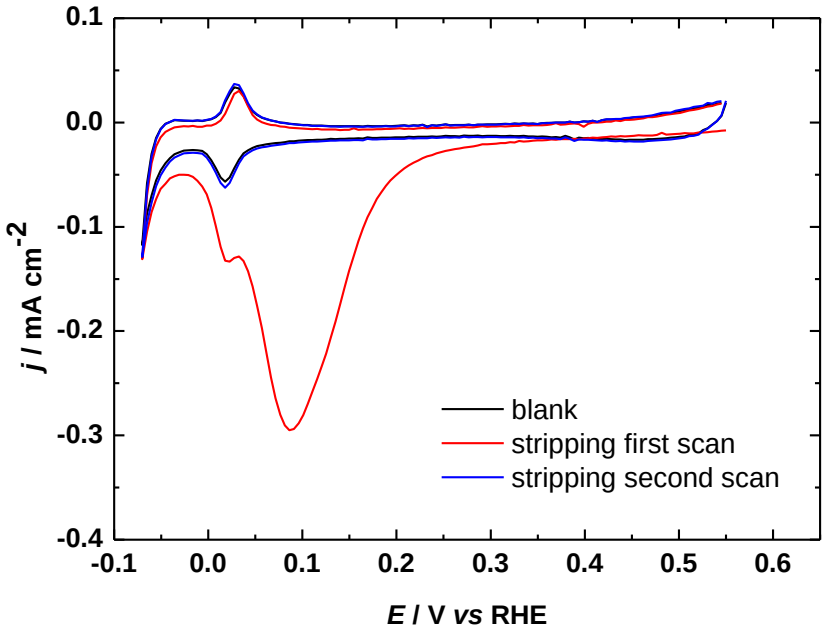

Figure 5.15 Voltammetric profiles for the first scan and second scan of adsorbate stripping on Rh/C electrode in 0.1 M H_2SO_4. Scan rate 0.01 V s^{-1}.

It is noticeable that the Rh/C electrode is not fully recovered after NO stripping, as peaks are diminished compared with the blank voltammogram. Similar behaviour has been reported in previous literature: irreversible poisoning from NO adsorption takes place on Rh (100) surfaces.[37]

The Tafel slope is usually based on the plot of E and log j, corresponding the Tafel equation in Eq. (5.14).[87]

$$E = E_r + a \pm b \log j \qquad (5.14)$$

Where E is the electrode potential, E_r is the reversible potential, j is current density, a is a parameter containing exchange current, b is Tafel slope. The value of b can be also determined using the linear dependence of the peak potential value on the logarithm of the scan rate applied in accordance with Eq. (5.15).[87]

$$E_p = E^0 + b\left[0.52 - \frac{1}{2}\log\left(\frac{a}{b}\right) - logk^0 + \frac{1}{2}logv\right] \qquad (5.15)$$

Figure 5.16 shows the plot which is equivalent to the Tafel plot of NO stripping, which refers that the stripping peak potential depends on a scan rate. The Tafel slope has been plotted with the logarithm of the stripping potential versus scan rate (ν). This plot can be used to determine the Tafel slope when the rate of the reaction is first order or second order. [14,15,88,89] The rate of the NO coverage has been reported to be first order.[15] The stripping charge[15,20] (corrected for hydrogen adsorption in NO-free 0.1 M H_2SO_4) corresponds to NO coverage of 0.87. The Tafel slope is 83 ± 4 mV dec^{-1}, which is reasonably close to the Tafel slope acquired for a Rh electrode in 0.1 M H_2SO_4 by De Vooys *et al.*[14] A value of Tafel slope of *ca* 60 mV dec^{-1} would suggest that the first electron transfer is the rate-determining step.

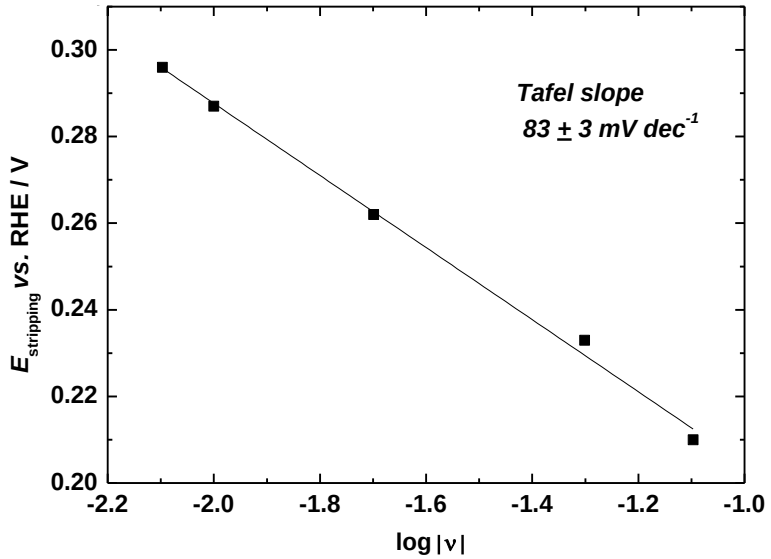

Figure 5.16 Tafel slope for adsorbate stripping in NO-free 0.1 M H_2SO_4.

5.3.1.1.2.3 Polycrystalline Rh

During nitrite reduction on polycrystalline Rh, a broad peak corresponding to NO reduction can be observed similarly to the case of the Rh/C electrode; however, there is a small shoulder peak at more negative potentials in the hydrogen adsorption/desorption region, as shown in Figure 5.17. The current for the return positive scan is greater than for negative scan at potential positive of 0.2 V, suggesting that the activity of polycrystalline Rh electrode is enhanced after scanning to more negative potential.[20]

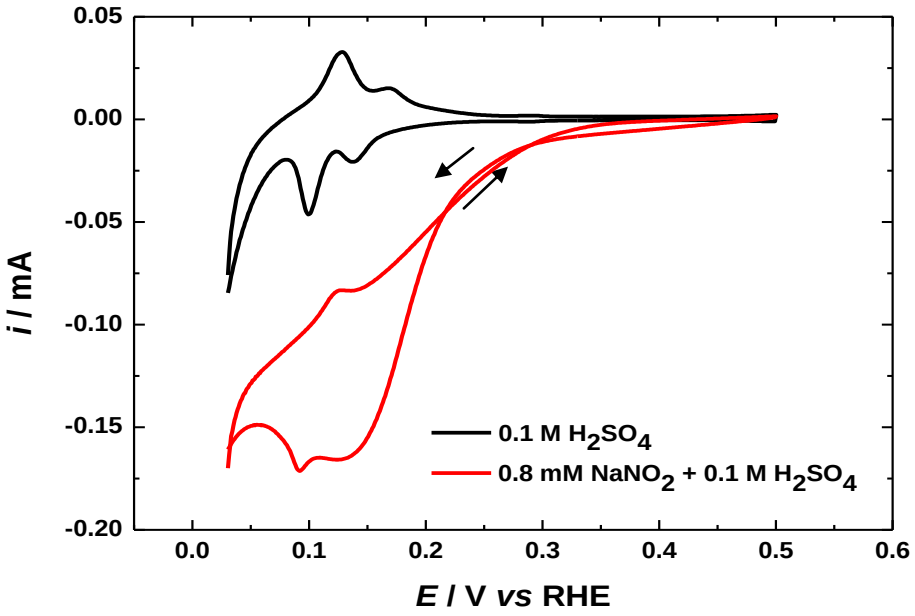

Figure 5.17 Cyclic voltammograms for polycrystalline Rh electrode in 0.1 M H_2SO_4 and in 0.8 mM $NaNO_2$ + 0.1 M H_2SO_4. Scan rate 0.01 V s^{-1}.

5.3.1.1.2.3 Au:Rh/C

Figure 5.18 presents CVs of nitrite reduction carried out on Au:Rh/C samples of different ratios. The currents relating to nitrite reduction are increased when increasing Rh content; however, these currents are all smaller than the current measured for Rh/C catalysts. This implies that Au free sites might be poisoned by NH_4^+ produced during the reaction.

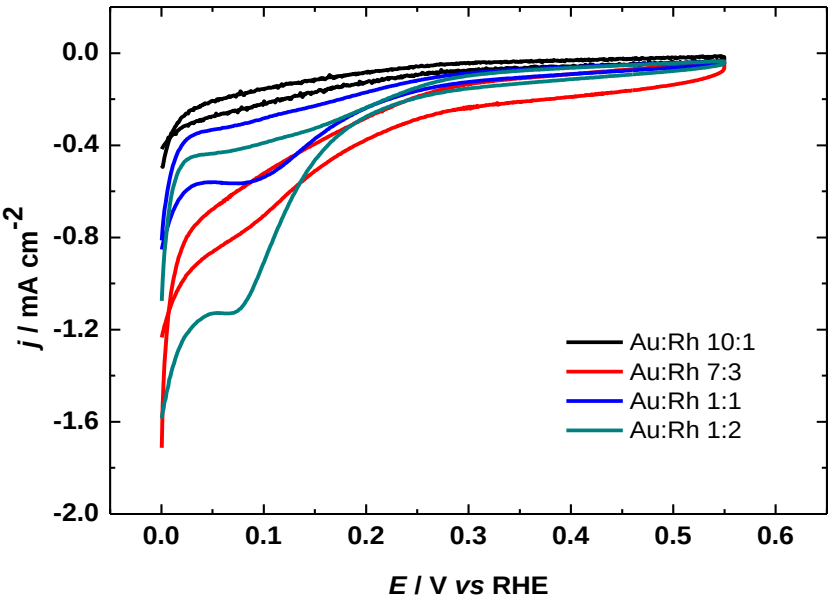

Figure 5.18 Cyclic voltammograms of different ratio Au:Rh/C in 0.1 M H_2SO_4 and in 0.8 mM $NaNO_2$ + 0.1 M H_2SO_4. Scan rate 0.01 V s^{-1}.

5.3.1.2 Alkaline media

It is known that the pH of the electrolyte is one of the factors that has an effect on the nitrate and nitrite reduction.[19] As reported previously, Rh has low selectivity to generate nitrogen oxide and high selectivity to generate NH_3 in alkaline media. Nitrate reduction reaction in alkaline media can proceed *via* the equations given below:

$$NO_3^- + H_2O + 2e^- \leftrightarrow NO_2^- + 2OH^- \qquad E^0 = 0.01 \text{ V } (vs \text{ NHE}) \qquad (5.16)$$

$$NO_2^- + H_2O + e^- \leftrightarrow NO + 2OH^- \qquad E^0 = 0.46 \text{ V } (vs \text{ NHE}) \qquad (5.17)$$

$$NO_3^- + 6H_2O + 8e^- \leftrightarrow NH_3 + 9OH^- \qquad E^0 = -0.12 \text{ V } (vs \text{ NHE}) \qquad (5.18)$$

The hydrogen evolution reaction competes with nitrate reduction in alkaline electrolytes:

$$2H_2O + 2e^- \leftrightarrow H_2 + 2OH^- \qquad E^0 = -0.83 \text{ V } (vs \text{ NHE}) \qquad (5.19)$$

Figures 5.19 and 5.20 present CVs acquired for nitrate and nitrite reduction of Rh/C and Au:Rh/C in alkaline media, respectively. The maximum currents are at 0.18 V and 0.13 V for nitrate and nitrite reduction, respectively. The Au:Rh/C samples present a similar trend to

Rh/C samples. The current density increases with increasing Rh content. The currents from both nitrate reduction and nitrite reduction in alkaline media are very small as H^+ is necessary to promote the reaction. However, the reaction still can take place using H^+ from water.

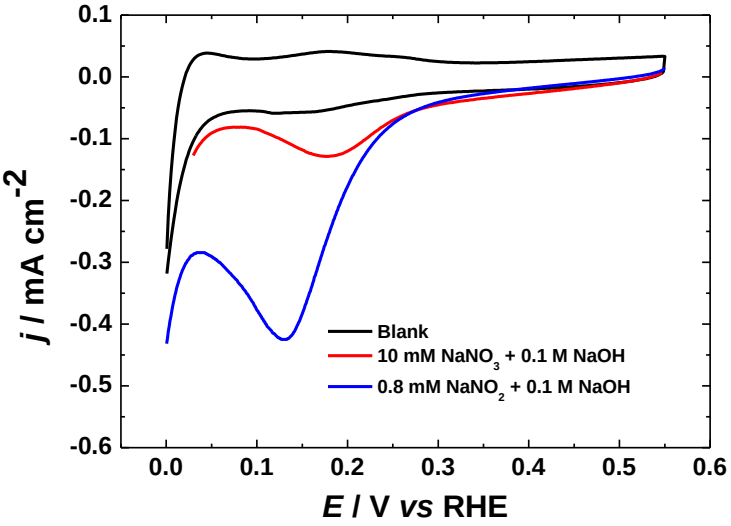

Figure 5.19 Cyclic voltammograms of Rh/C in 0.1 M NaOH, 10 mM $NaNO_3$ + 0.1 M NaOH and in 0.8 mM $NaNO_2$ + 0.1 M NaOH. Scan rate 0.01 V s^{-1}.

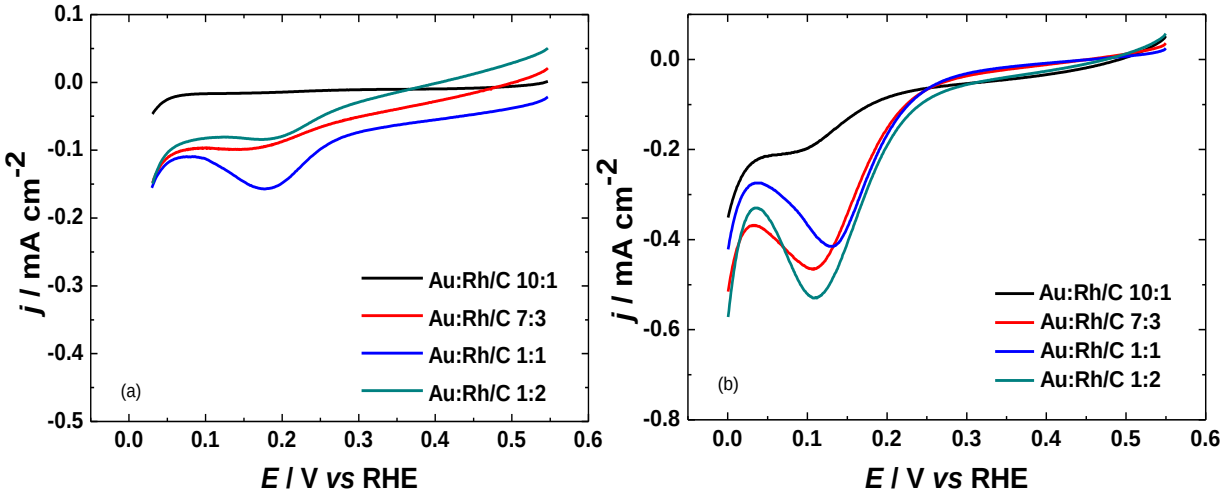

Figure 5.20 Cyclic voltammograms for Au:Rh/C (a) in 10 mM $NaNO_3$ + 0.1 M NaOH and (b) in 0.8 mM $NaNO_2$ + 0.1 M NaOH. Scan rate 0.01 V s^{-1}.

5.3.2 On-line electrochemical mass spectrometry (OLEMS)

OLEMS has been used in this study in order to detect volatile reaction products, such as H_2 (*m/z* = 2), NH (*m/z* = 15), N_2 (*m/z* = 28), NO (*m/z* = 30) and N_2O (*m/z* = 44) during nitrate reduction and nitrite reduction. During nitrate reduction, adsorbed nitrate was reduced

stepwise to nitrite. The nitrite quickly produces NO_{ads}, which strongly adsorbs on Rh and Pt. The NO_{ads} is reduced further to produce ammonium or hydroxylamine as the main products following reactions:

$$NO_3^- \leftrightarrow NO_{3,ads}^- \quad \text{(in equilibrium)} \quad (5.20)$$

$$NO_{3,ads}^- + 2H^+ + 2e^- \leftrightarrow NO_{2,ads}^- + H_2O \quad \text{(rate-determining step)} \quad (5.21)$$

$$NO_{2,ads}^- + 2H^+ + e^- \leftrightarrow NO_{ads} + H_2O \quad \text{(fast)} \quad (5.22)$$

$$NO_{ads} + 4H^+ + 3e^- \leftrightarrow NH_3OH^+ \quad \text{(fast)} \quad (5.23)$$

$$NO_{ads} + 6H^+ + 5e^- \leftrightarrow NH_4^+ + H_2O \quad \text{(fast)} \quad (5.24)$$

The volatile products cannot be detected for nitrate reduction at moderate nitrate concentration and mild acidity because N_2O formation is impossible without NO in solution.[10] For nitrite reduction, HNO_2, an active species in acidic media, decomposes and generates NO_{aq} and NO_{ads} which can form N_2O.

5.3.2.1 Nitrite reduction.

5.3.2.1.1 Au/C

The cyclic voltammograms measured during nitrite reduction on a Au/C electrode is presented in panel A in Figure 5.21. The lower panels are the signal of volatile products *m/z* 30, NO and *m/z* 44, N_2O. The products were detected in the negative-going scan from 0.8 V and the positive-going scan from 0.0 V. The signal of volatile products produced at Au/C is very small and broad, extending to near hydrogen evolution.

NO is detected as the first volatile products from the starting potential. This NO signal is obtained from the NO_{aq} in the solution at equilibrium which produced from the decomposition of HNO_2. The NO signal increases until reaching the maximum at 0.5 V, which is the onset potential of the N_2O signal. This implies that the NO_{aq} formation is larger than NO_{aq} consumption in the positive potential range. At potentials negative of 0.5 V, the

signal of NO_{aq} decreases until zero, while the signal of N_2O increases to a maximum at 0.1 V, indicating that NO_{aq} consumption to produce N_2O exceeds NO_{aq} formation. The N_2O signal starts to decrease at the potentials close to hydrogen evolution, corresponding to voltammetric profile at potential negative of 0.1 V.

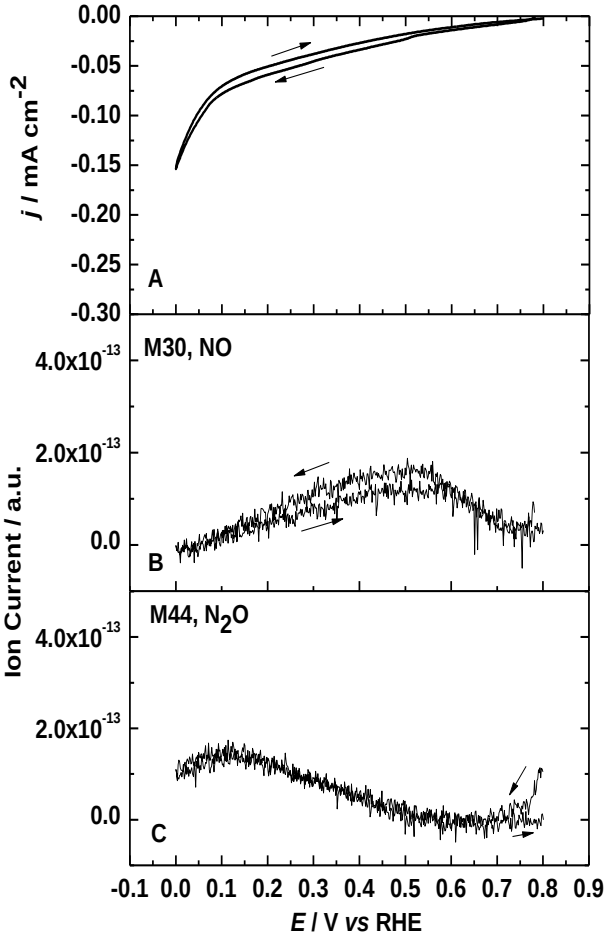

Figure 5.21 Cyclic voltammogram of Au/C in 0.8 mM $NaNO_2$ + 0.1 M H_2SO_4 and ion current profiles for *m/z* = 30 and *m/z* = 44. The arrows indicate the direction of potential sweep. Scan rate 0.001 V s^{-1}.

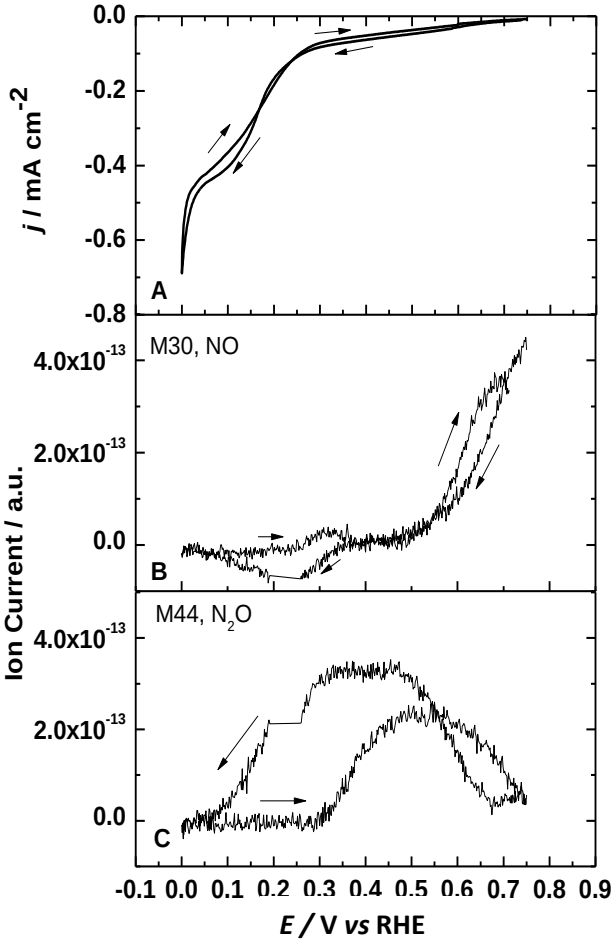

Figure 5.22 Cyclic voltammogram of Rh/C in 0.8 mM $NaNO_2$ + 0.1 M H_2SO_4 and ion current profiles for *m/z* = 30 and *m/z* = 44.Scan rate 0.001 V s^{-1}.

5.3.2.1.2 Rh/C

Figure 5.22 displays the results of nitrite reduction on Rh/C. Starting from 0.75 V, NO signal produced in the solution is detected and steeply decreased until zero at 0.45 V, where it has constant intensity, indicating that NO_{aq} is consumed during the measurement. Meanwhile, an

increase of N_2O is evident from the starting potential of 0.75 V with a maximum in the potential range of 0.5 – 0.3 V, suggesting high selectivity toward N_2O. The intensity of N_2O is then rapidly diminished until it disappears at the potential 0.0 V, indicating that the selectivity is shifted to hydrogenated species formation. On the backward scan, the shape of N_2O signal is similar to forward scan; however, the signal is smaller and shifted to higher potential. It is known that the formation of NO_{aq} is not only from the decomposition of HNO_2 but also from the fragmentation of N_2O. Here, the NO signal has been corrected by the factor mentioned in section 5.2. It thoroughly consider that a change in the slope of NO signal between 0.45 – 0.3 V, maximum intensity of N_2O, is owing to N_2O fragmentation. This profile is similar to those previously noticed on Pt and Ru.[21] Both signals of NO and N_2O on Rh/C are somewhat larger than on Au/C, presenting higher selectivity and activity to form volatile products of nitrogen oxide.

5.3.2.1.3 Au:Rh/C

The voltammetric profile and recorded mass for different ratios of Au:Rh/C samples are presented in Figure 5.23. The signals of NO and N_2O were detected for all samples.

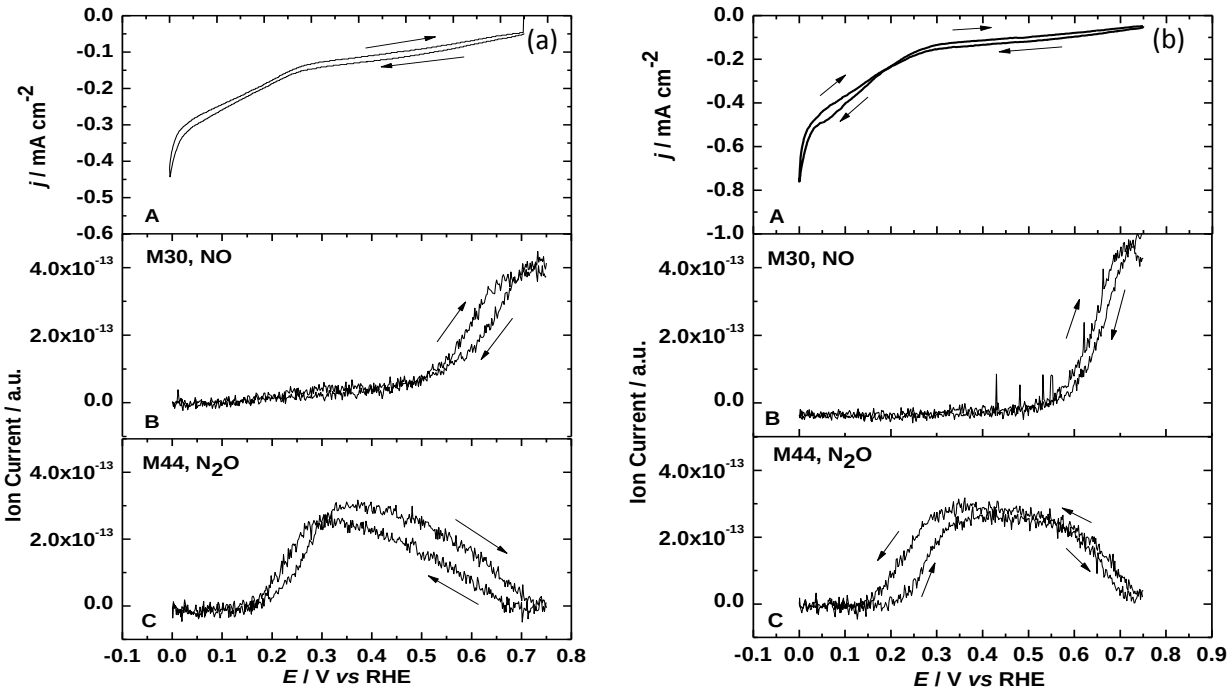

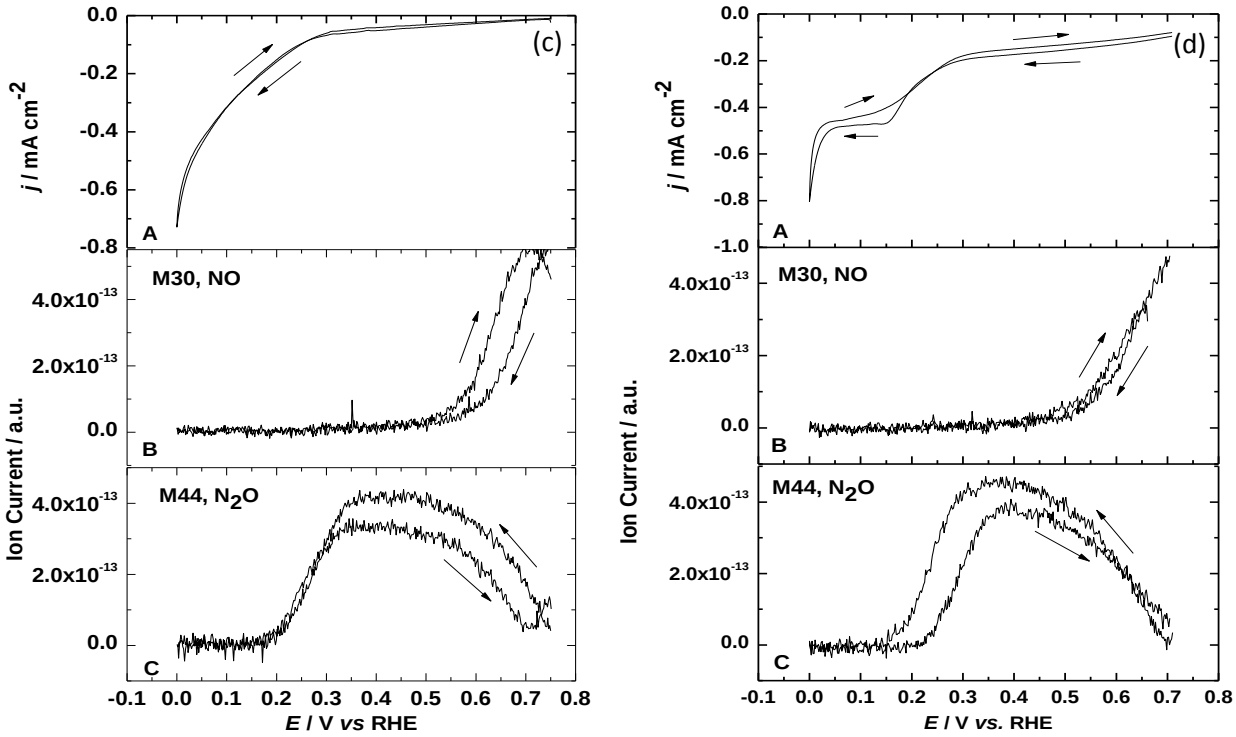

Figure 5.23 Cyclic voltammograms in 0.8 mM $NaNO_2$ + 0.1 M H_2SO_4 and ion current profiles for *m/z* = 30 and *m/z* = 44 of Au:Rh/C (a) 10:1, (b) 7:3, (c) 1:1 and (d) 1:2 ratios. Scan rate 0.001 V s^{-1}. The arrows indicate the direction of potential sweep.

The current density in the voltammetric profile increases with increasing Rh content. The 10:1 Au:Rh/C sample presents lower mass signals than other ratios. The mass signals of this sample are mixed between Au and Rh features. The NO signal decreases as a function of potential until get to zero, while the N_2O signal increases until 0.3 V. There is no current plateau of NO signal for this sample similar to Au/C. The N_2O intensity suddenly decreases at potential negative of 0.3 V, until reaching to zero at 0.1 V. This means that introducing a small amount of Rh to Au can enhance the formation of volatile products in nitrite reduction. For the other samples, the NO signals steeply decrease from the starting potential of 0.8 V and reach to zero at 0.5 V. A slope change for the NO signal (fragmentation of N_2O) is not seen, which might caused by less N_2O generation at Au:Rh/C compared with Rh/C. It may be also because presenting Au in catalyst can reduce the fragmentation of N_2O.

Comparing NO_{ads} reduction (NO adlayers, Figure 5.15) with NO continuous reduction of Rh, the latter reaction presents the reduction of NO from the starting potential with high selectivity towards N_2O. The NH_4^+ ions are then produced at the potential negative of 0.3 V. The reduction of NO_{ads} starts at 0.3 V and generates NH_4^+ as the main product without producing N_2O.[15] It seems the kinetic of the reaction is slow if only NO_{ads} is a reacting species in the reaction and the hydrogenation of NO_{ads} is preferential. It is noticeable that the continuous change from NO to NH_4^+ is happened at the same potential as the onset potential of NO_{ads} reduction at 0.3 V. It is believed that the continuous NO reduction to NH_4^+ has the same mechanism as adsorbed NO reduction, because both reduction have the same onset potential.[14]

The formation of N_2O takes place as the mechanism involving the formation of NO dimers (HN_2O_2) on the electrode surface, as shown in reactions (5.25–5.27).[14,15]

$$* + NO_{aq} \rightarrow NO_{ads} \quad (5.25)$$

$$NO_{ads} + NO_{aq} + H^+ + e^- \rightarrow HN_2O_{2,ads} \quad (5.26)$$

$$HN_2O_{2,ads} + H^+ + e^- \rightarrow N_2O + H_2O + 2* \quad (5.27)$$

where * stands for a free site at the electrode surface. The reaction of NO_{aq} and NO_{ads} begins to progress at potentials negative of 0.7 V.

De Vooys *et al.* reported that the formation of N_2O from continuous NO on Rh proceeds *via* a different mechanism on Pt, with a different Tafel slope of NO in solution. The Tafel slope for Pt is close to 120 mV/dec, indicating that the rate-determining step is the step of the first electron transfer, as shown in reaction (5.26). The Tafel slope is significantly higher than 120 mV/dec for Rh, which implies that the rate-determining step is a chemical step, as shown in reaction (5.25).[14] This behaviour correlates with the higher NO coverage and stronger NO adsorption on Rh than on Pt.[78] It is also confirmed by the DFT calculation

predicting that Rh (111) has the strongest NO adsorption energy compared to the other transition metals.[90] The existence of NO dimers on metal surfaces is confirmed by the weak adsorption on several metals in UHV conditions.[91] Due to the weak adsorption of NO dimers, most of metals illustrate similar activity to form N_2O, as shown in reaction (5.27).

OLEMS has been also employed for nitrite reduction in alkaline media. Figure 5.24, in panel B and C, shows the MS ion current of H_2 (*m/z* = 2) and NH (*m/z* = 15). Both signals are compared together to ensure that the formation of NH_3 in alkaline media is from the reduction of nitrite and hydrogenation of nitrite on rhodium. The NH signal arises from the reduction of nitrite to ammonia while the H_2 signal departs from the baseline at 0.1 V, at the onset of the hydrogen evolution.

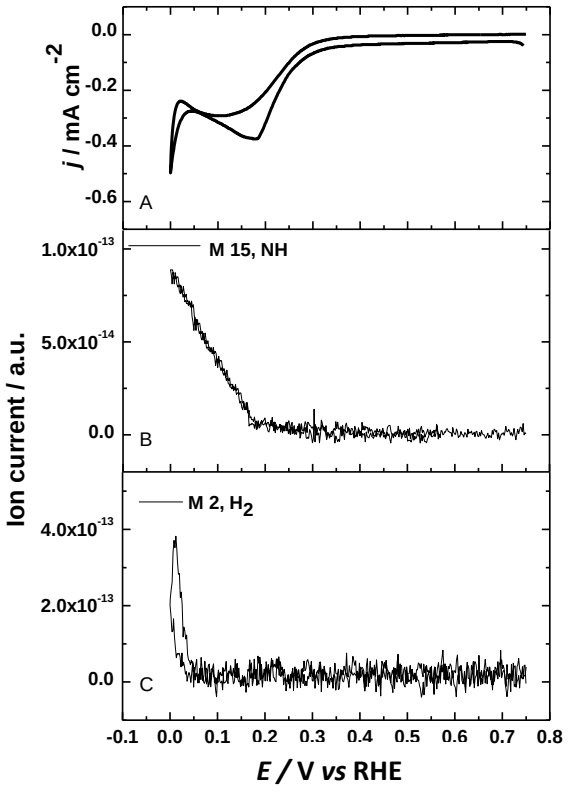

Figure 5.24 Cyclic voltammogram in 0.8 mM $NaNO_2$ + 0.1 M NaOH and ion current profiles for *m/z* = 2 and *m/z* = 15 of Rh/C. Scan rate 0.001 V s^{-1}.

During nitrate reduction in alkaline media, nitrate is reduced to nitrite and nitrite is reduced further to NO on the electrode surface. NO_{ads} is reduced to NH_3, as shown in reactions (5.16) – (5.18). It is known that nitrous acid is the active species for nitrite reduction in acidic media and its decomposition easily takes place, generating NO in the solution, whereas nitrite ion is the active species formed in alkaline media. The Rh electrode surface is covered by NO_2^- and some NO at the starting potential. The latter is produced from the reduction of NO_2^-. NO is not detectable in the solution, suggesting that NO is not desorbed from the Rh surface, owing to the preferential adsorption of NO on Rh. This means that N_2O formation cannot be detected in alkaline media. Hence, the hydroxide ion is only competitively absorbed species in the solution. Rh is able to reduce adsorbed NO species to NH_3 by breaking the N−O bond and forming N−H bonds in a hydrogenation potential range. The kinetics of the reaction is slower than in acid, suggesting a kinetically mixed control at potential negative of 0.2 V. The formation of NH_3 near the hydrogen evolution region can poison the electrode surface since at potentials negative of 0.1 V, dehydrogenation of adsorbed NH_3 can take place to generate NH_x species,[14] particularly on Rh surface. NH_x can be further dehydrogenated to N_{ads} which strongly adsorbed on Rh, as studied by Noovell-Leruth *et al.*[92] The formation of NH_x is seen with OLEMS in Figure 5.24.

5.3.3 Ion chromatography (IC)

Ion chromatography (IC) was combined with voltammetry to determine the formation of soluble products, particularly NH_4^+ and NH_3OH^+ in acidic media. Optimum conditions are required for this measurement such as, column type, voltammetric scan rate, flow rate etc. In this present work, nitrate reductions were carried out in nitric acid (HNO_3) in order to avoid interference of Na^+ from $NaNO_3$. A cationic exchange resin was used in conjunction with

HNO_3 as mobile phase. The IC results and analysis were accompanied by Youngkook Kwon and Yang Jian, University of Leiden.

Figure 5.25 shows ion chromatogram and voltammogram of nitrate reduction at different reduction potentials for Rh/C with an injection volume of 20 μL. A glassy carbon electrode with 7 mm diameter (area 0.3847 cm^2) was used as working electrode with 8 μL of the Rh/C catalyst suspension. The onset potential of NO_3^- reduction is ~0.3 V and no signal can be detected at the potentials positive of 0.3 V. Similarly no volatile products were observed with OLEMS for nitrate reduction. At potentials negative of 0.3 V, the signals of NH_4^+ can be detected at a retention time of 6 min, estimated from the retention time of standard solution of NH_4^+, and the signals increase when the potential is scanned to more negative values, as shown in Figure 5.25(a). It presents that the NO_3^- is reduced stepwise to $NO_{2\ ads}^-$, NO_{ads} and NH_4^+, corresponding to reactions (5.20) - (5.24). The increase of NH_4^+ concentration, calculated from the peak area, as a function of potential has been displayed in Figure 5.25(c). The concentration enhances drastically between 0.3 – 0.05 V and is slightly enhanced at potentials negative of 0.05 V, close to the onset of hydrogen evolution. The appearance of NH_4^+ is presented at the potential negative of 0.3 V, consistent with the idea that NO is preferentially hydrogenated to form NH_4^+ or NH_3OH^+. It is notable that NH_3OH^+ cannot be detected on Rh/C. The current of voltammogram with sample collection is slightly higher than without collection. This might cause by the removal of NH_4^+ on electrode surface, lessening surface poisoning, or by the enhancement of reactant diffusion to the electrode surface.

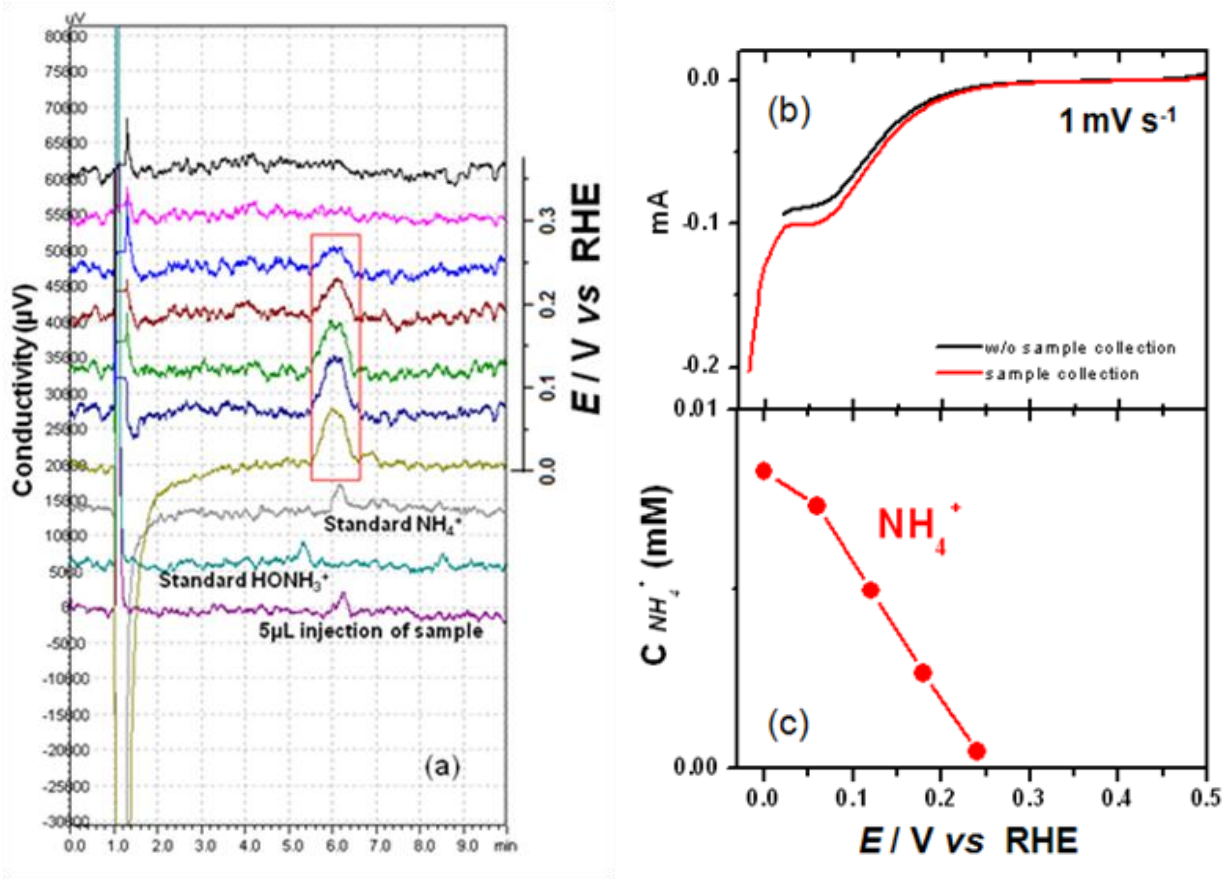

Figure 5.25 (a) Ion chromatogram for products detected from Rh/C, (b) voltammogram of Rh/C in 0.1 M HNO_3, scan rate 0.001 V s^{-1} and (c) concentration of ammonium.

Figure 5.26 presents ion chromatograms and voltammograms of nitrate reduction at different reduction potentials for a polycrystalline Rh electrode with an injection volume of 10 μL. A signal for NH_4^+ is detectable at potential negative of 0.3 V, similarly to Rh/C. Owing to the high surface area of Rh electrode, high intensities are obtained, as can be seen from the sharp peak of the signal. The concentration of NH_4^+ is quite high. Although the high surface area electrode was used, the formation of NH_3OH^+ was still not found. Thus, it is likely that detection limit of the technique is not a cause of the non-detection of NH_3OH^+.

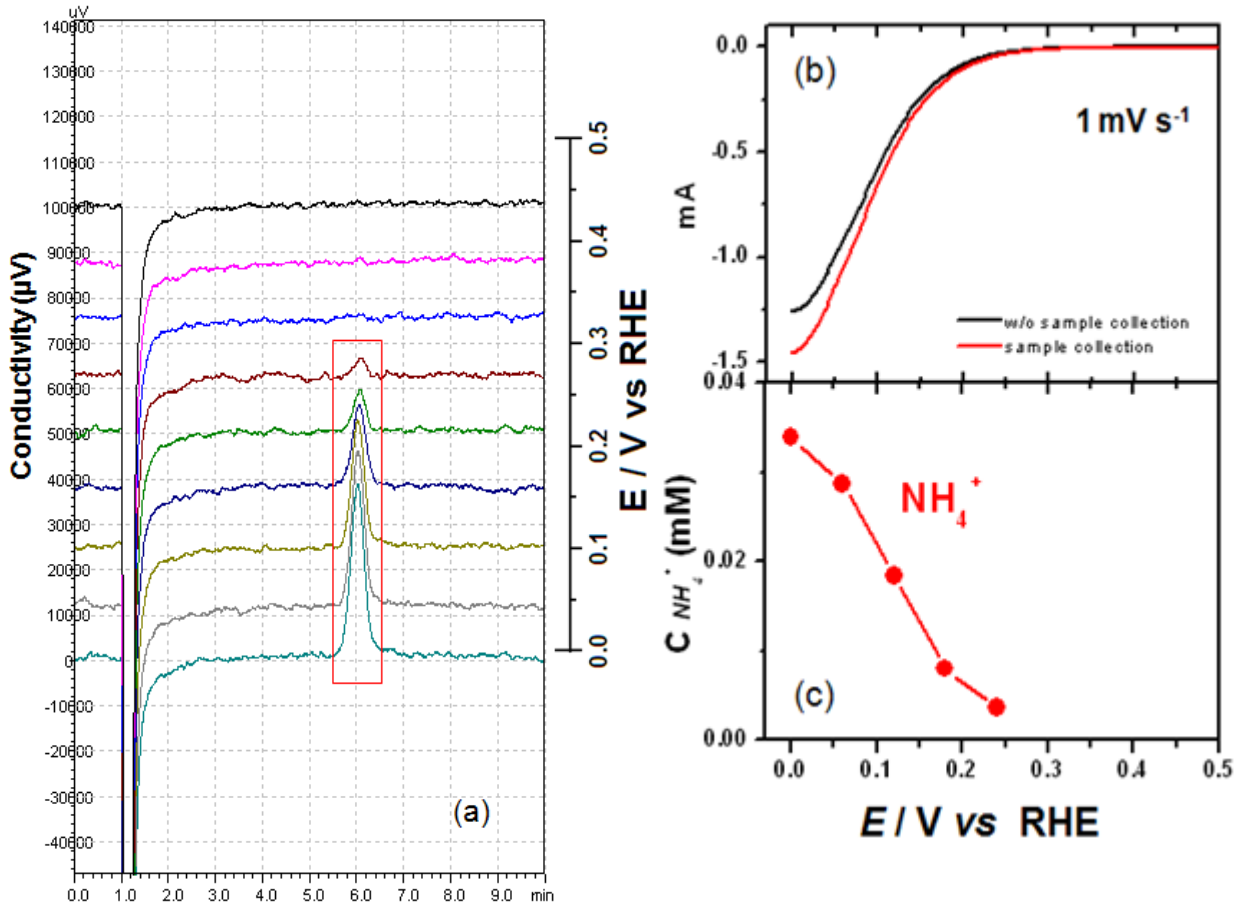

Figure 5.26 (a) Ion chromatogram for products detected from polycrystalline Rh electrode, (b) voltammogram of polycrystalline Rh electrode in 0.1 M HNO_3, scan rate 0.001 V s^{-1} and (c) concentration of ammonium.

Ion chromatograms and voltammograms of nitrate reduction at different reduction potentials for 1:1 Au:Rh/C are displayed in Figure 5.27. A signal for NH_4^+ is found at potentials negative of 0.4 V, a more positive potentials than seen for Rh/C and polycrystalline Rh. The signal increases to reach a maximum at 0.1 V and progressively diminishes when the potential is close to that where hydrogen evolution occurs. It coincides with the voltammetric profile in Figure 5.27(b) which also reaches maximum current density at 0.1 V. The presence of NH_4^+ at more positive potentials than on Rh/C and polycrystalline Rh electrode can be explained by the preference for Au to produce NH_4^+ during nitrate and nitrite reduction, as only small signals for volatile products were detected with OLEMS. Likewise, the NH_4^+

concentration decrease after 0.1 V is due to the dehydrogenation of NH_4^+ to NH_x species. The current in the voltammogram for Au:Rh/C with sample collection is remarkable higher than that obtained without collection. This could be because the sample collection removes NH_4^+ from the electrode surface, lessening the poisoning. The lower obtained for without sample collection is a result of electrode poisoning, especially on Au sites.

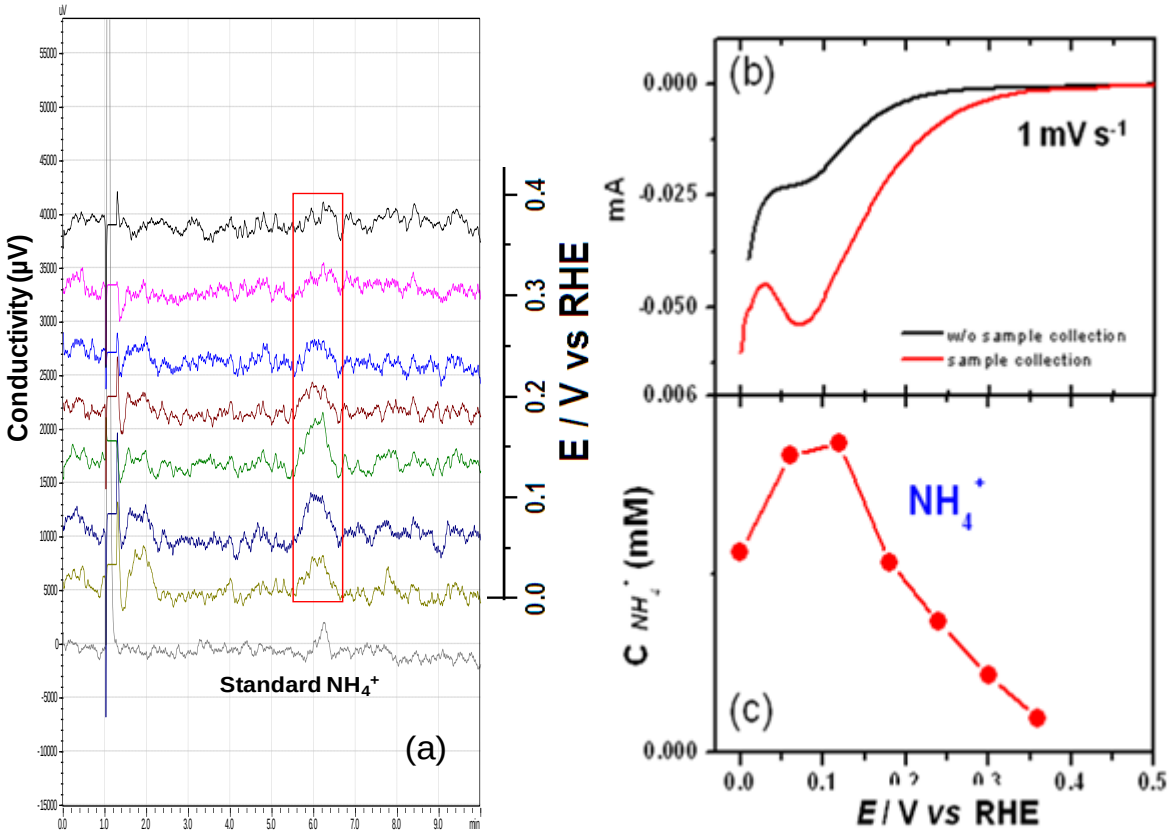

Figure 5.27 (a) Ion chromatogram for products detected from 1:1 Au:Rh/C, (b) voltammogram of 1:1 Au:Rh/C in 0.1 M HNO_3, scan rate 0.001 V s^{-1} and (c) concentration of ammonium.

Comparing Rh to Pt, IC measurements were also carried out for a polycrystalline Pt electrode. The results are presented in Figure 5.28. A signal for NH_4^+ is observed and increases until a maximum at 0.15 V, a more positive potential than observed on Rh. The signal then steeply declined. The decrease in reduction current is due to the competitive adsorption of H^+. The detected NH_4^+ signal on Pt is smaller than on Rh. An NO adlayer is strongly adsorbed on the Rh surface when immersing the electrode in nitrate-containing

solution. Rh is able to break the N−O bond. Pt has lower NO adsorption than Rh. Due to the different ability to break N−O bond of Rh and Pt, it distinguishes different activity to produce the products of both metals.[14,15,93] Rh particularly produces NH_4^+ from nitrate reduction, on the contrary, Pt can produce NH_3OH^+ along with NH_4^+.[94]

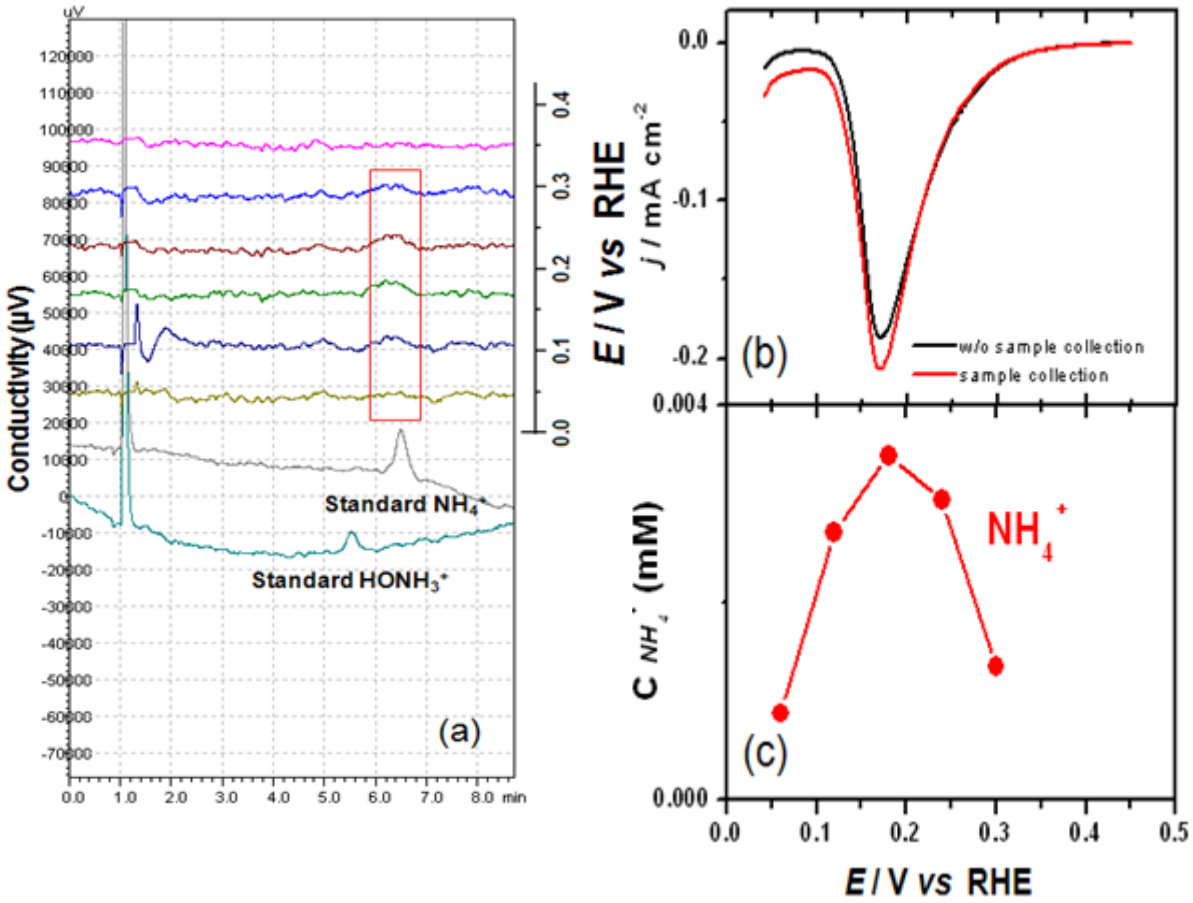

Figure 5.28 (a) Ion chromatogram for products detected from polycrystalline Pt electrode, (b) voltammogram of Pt in 0.1 M HNO_3, scan rate 0.001 V s^{-1} and (c) concentration of ammonium.

5.3.4 Tin (Sn) modification on Rh/C, Au:Rh/C and polycrystalline Rh electrodes.

It is found that, even though Rh is effective to remove nitrate, no volatile products from nitrate reduction are detected. NH_4^+ is detected as the dominant product, similarly to the other metals.[10] In order to enhance the catalytic activity of Group 8-10 metals, such as Pt, Pd, Rh or Ru, a second metal has been introduced as a modifier, such as tin,[11,27,29,30,59,95,96] bismuth,[97]

copper,[98] germanium,[17] and cadmium[83,99]. Shimazu *et al.* modified Pt and Pd with Sn. It was found that, after modification, both metals presented an enhanced electrocatalytic activity for nitrate reduction.[30,59] Shimazu *et al.* also studied Sn-modified Rh, Ru and Ir which also exhibited high activity.[11] The modified electrodes yielded N_2, a harmless product, which was detected in the collected gas after several hours of electrolysis.[11,59] A pure Sn electrode has also been employed, although studied under different conditions. Nitrogen gas was detected with high selectivity at cathodic potential and ammonium was the by-product. Recently, Yang *et al.* studied nitrate reduction on Sn-modified Pt electrodes by a combination of voltammetry and online electrochemical mass spectrometry. N_2O and NO were observed as the two main volatile products, and a small amount of N_2 is obtained from the further reduction of N_2O.[29] They also studied the nitrate reduction on a variety of p-block metal-modified Pt electrodes in sulphuric acid and in perchloric acid, and showed that Sn is the most active promoter.[100] Based on density functional theory (DFT) calculations, the active site of Sn-Pt surface for nitrate reduction consists of $Sn(OH)_x$ and Pt.

In this work, Sn modification has been applied to Rh/C, Au:Rh/C and polycrystalline Rh electrodes in order to investigate the feasibility of forming nitrogen gas during nitrate reduction in acidic media.

5.3.4.1 Comparison of nitrate reduction on Rh and Sn modification

The working electrode was prepared by spontaneous deposition and electrodeposition, as described in section 5.2.4. CVs of the Rh/C electrode before and after spontaneous Sn deposition and electrodeposition are shown in Figures 5.29 and 5.30, respectively. The hydrogen adsorption and desorption peaks of Rh decrease after the adsorption of Sn, suggesting the charge corresponding to the oxidation and reduction of hydrogen atom on the

Rh surface is less than before modification. This is caused by the surface blockage from Sn adsorption. The relative surface coverage of Sn (θ_{Sn}) on Rh/C can be calculated using the following equation:[29]

$$\theta_{Sn} = 1 - \frac{q_{Rh/Sn}}{q_{Rh}} \qquad (5.28)$$

where q_{Rh} is adsorbed in the hydrogen region on a clean Rh electrode and $q_{Rh/Sn}$ is the charge in the same potential region on the Sn-modified Rh electrode. Eq. (5.28) is able to calculate accurately the surface coverage of the foreign metal for Rh as the hydrogen adsorption and desorption region are well separated from the surface oxide region.[11] The θ_{Sn} of spontaneous Sn deposition and electrodeposition are 0.66 and 0.80, respectively. It is reported that the amount of adsorbed Sn on Rh is controlled by the immersion time in 0.25 mM $SnCl_2$, whereas, for, Ru, it is controlled by the concentration of $SnCl_2$ and for, Ir, it is controlled by immersion time along with $SnCl_2$ concentration.[11] Considering the oxidation state of adsorbed Sn on Rh, it is feasible that Sn is in its metallic state at potentials negative of 0.25 V and in the Sn (II) state for more positive potentials.[29,101]

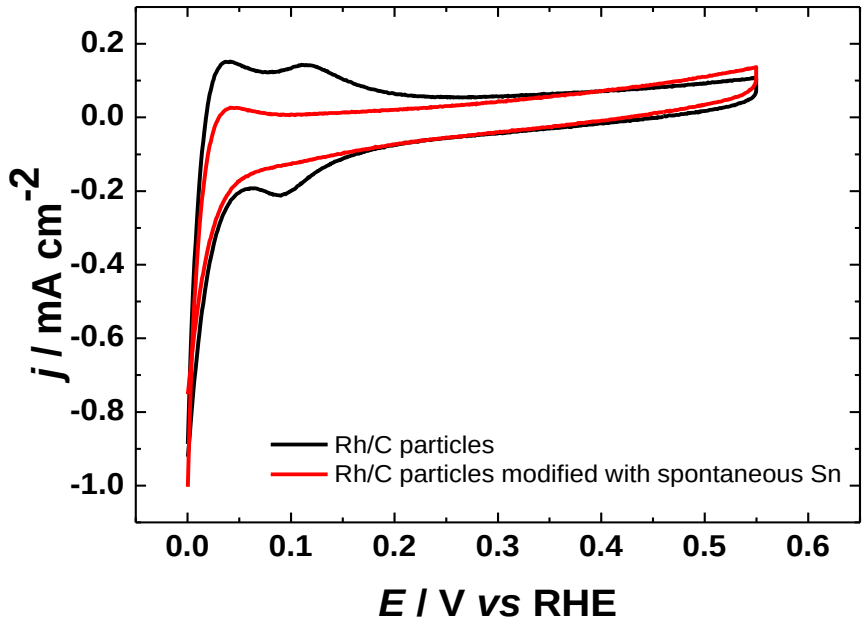

Figure 5.29 Cyclic voltammograms of Rh/C electrode before and after spontaneous Sn deposition in 0.1 M H_2SO_4. Scan rate 0.05 V s^{-1}. θ_{Sn} = 0.66.

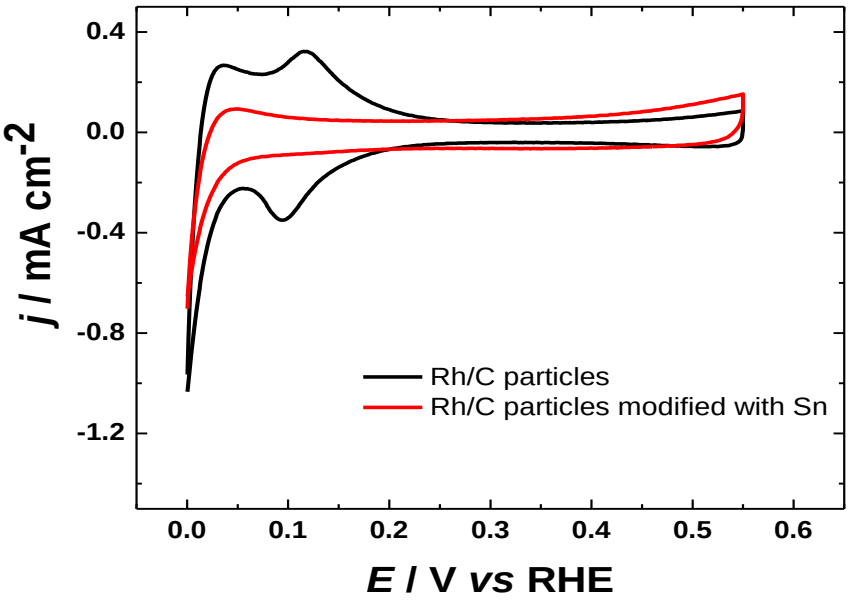

Figure 5.30 Cyclic voltammograms of Rh/C electrode before and after Sn electrodeposition in 0.1 M H_2SO_4. Scan rate 0.05 V s^{-1}. θ_{Sn} = 0.80.

Figures 5.31 and 5.32 present the cyclic voltammograms of SnRh/C electrodes prepared by spontaneous deposition and electrodeposition, compared with those acquired for Rh/C electrodes in 10 mM $NaNO_3$ + 0.1 M H_2SO_4. It is obvious that the catalytic activity of Sn-modified Rh/C is effectively enhanced as the onset potential of nitrate reaction is shifted to more positive potentials. The decrease of reduction current at potential negative of 0.1 V is observed for Rh/C electrode, while it not observed for SnRh/C electrode. This may due to the strong hydrogen adsorption on Rh/C surface. Sn is likely to block the hydrogen adsorption. The 0.80 θ_{Sn} provides slightly higher nitrate reduction current than 0.66 θ_{Sn}. These results are in accordance with the reports from Tada *et al*. that the nitrate reduction current on Sn-modified Rh increases from partial adsorption until the maximum on covered Rh (θ_{Sn} equal 0.75).[59] This behaviour is different from that of Pt, for which the catalytic activity decreases at high θ_{Sn}. This can be explained that NO_3^- is more strongly adsorbed on Rh than on Pt,[10,78] which can compete with other ions. Although Sn-modified Rh/C electrode enhances the catalytic activity of catalyst, Sn fully covered on Rh/C electrode can decrease the catalytic

activity by blocking hydrogen adsorption. It is noteworthy that H^+ is necessary for nitrate reduction.

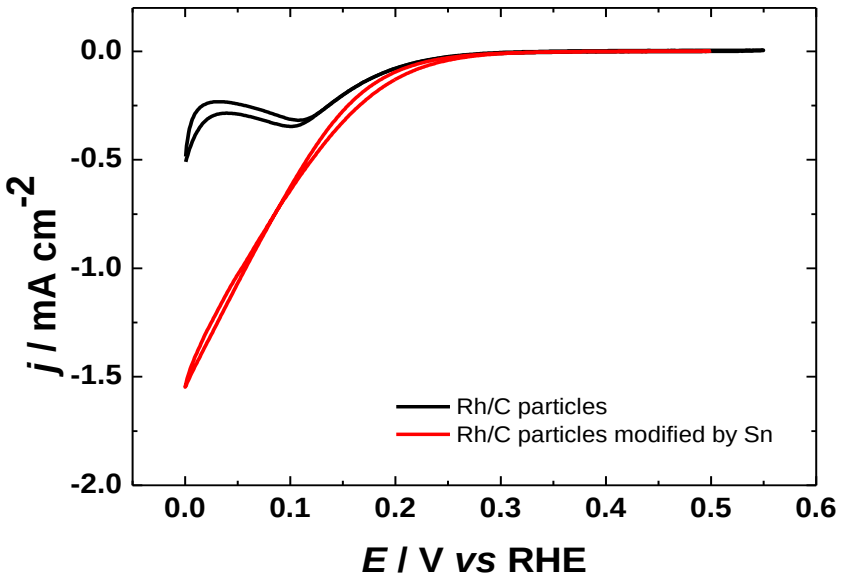

Figure 5.31 Cyclic voltammograms of Rh/C and spontaneous deposition SnRh/C in 10 mM $NaNO_3$ + 0.1 M H_2SO_4. Scan rate 0.01 V s^{-1}. θ_{Sn}= 0.66.

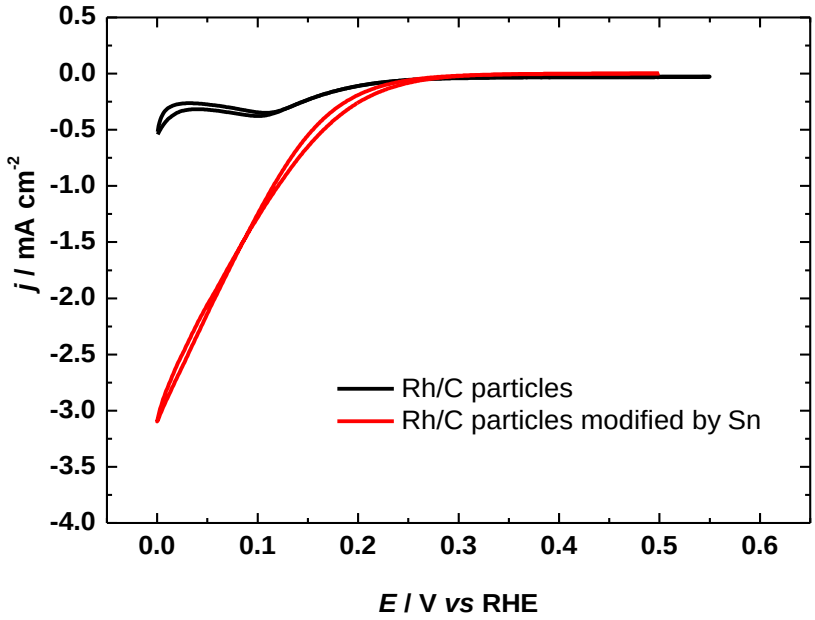

Figure 5.32 Cyclic voltammograms of Rh/C and electrodepostion SnRh/C in 10 mM $NaNO_3$ + 0.1 M H_2SO_4. Scan rate 0.01 V s^{-1}. θ_{Sn} = 0.80.

Figures 5.33 and 5.34 present the cyclic voltammogram of a Rh polycrystalline electrode and the electrodeposited SnRh polycrystalline electrode in blank electrolyte and in

nitrate-containing electrolyte. The θ_{Sn} is 0.76 for this electrode. The onset potential of Sn/Rh polycrystalline electrode is at 0.30 V, the same potential as for SnRh/C. Also, the current density is significantly increased. It can be concluded that the carbon support has no effect on Sn modification.

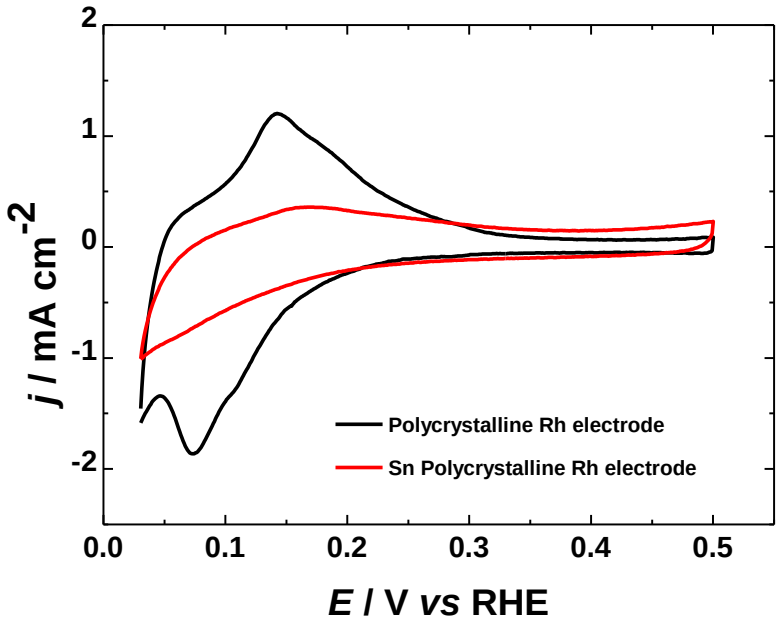

Figure 5.33 Cyclic voltammograms of polycrystalline Rh electrode before and after Sn electrodeposition in 0.1 M H_2SO_4. Scan rate 0.05 V s^{-1}.

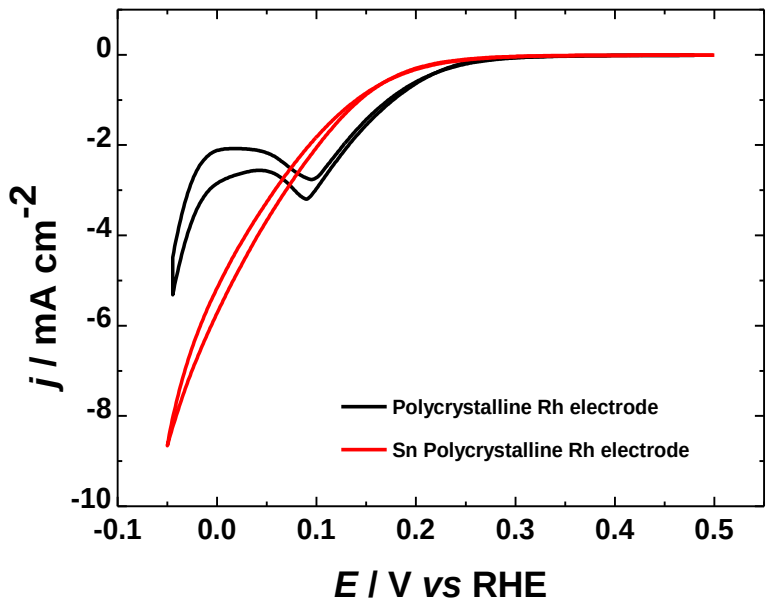

Figure 5.34 Cyclic voltammograms of polycrystalline Rh electrode and Sn polycrystalline Rh electrode in 10 mM $NaNO_3$ + 0.1 M H_2SO_4. Scan rate 0.01 V s^{-1}.

The same experiment was carried out for 1:1 Au:Rh/C (because this sample has the same amount of Rh as Rh/C) so that the effect of Au on Sn modification of Rh can be investigated. The cyclic voltammograms are presented in Figure 5.35. The θ_{Sn} is ~0.80, similar to that of the SnRh/C electrode investigated in Figure 5.32. The catalytic activity of this electrode, as shown in Figure 5.36, is similar to that of SnRh/C and SnRh polycrystalline electrodes, suggesting that Au has little effect on Sn modification. However, the products produced during the reaction are necessary to be considered.

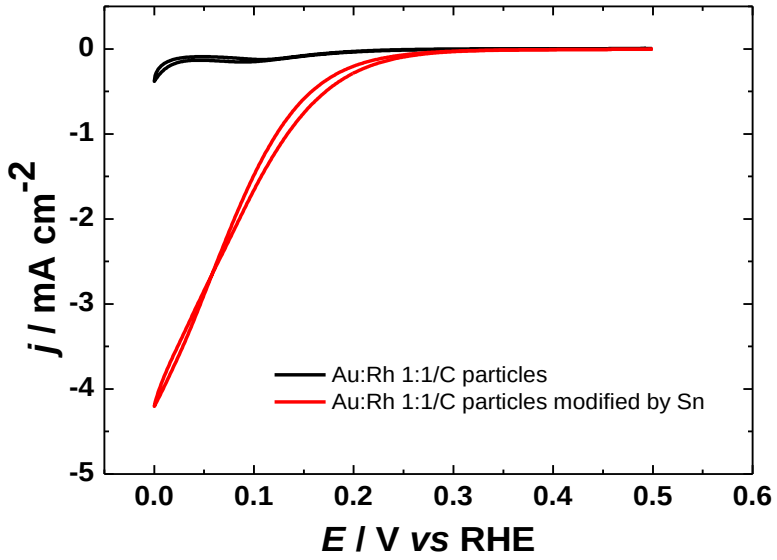

Figure 5.35 Cyclic voltammograms of 1:1 Au:Rh/C before and after Sn electrodeposition in 0.1 M H_2SO_4. Scan rate 0.05 V s^{-1}.

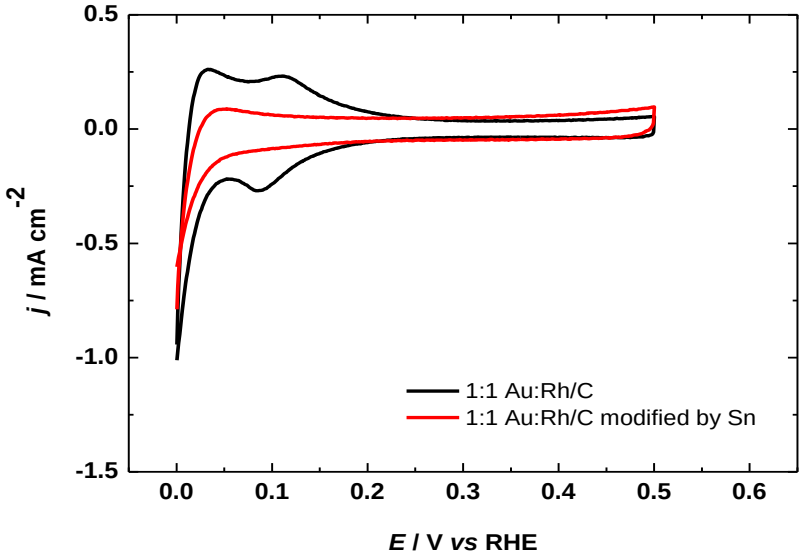

Figure 5.36 Cyclic voltammograms of 1:1 Au:Rh and Sn 1:1 Au:Rh in 10 mM $NaNO_3$ + 0.1 M H_2SO_4. Scan rate 0.01 V s^{-1}.

5.3.4.2 On-line electrochemical mass spectrometry for nitrate reduction on Sn-modified Rh

OLEMS was used to determine the volatile products produced at Sn-modified Rh electrodes. Interestingly, the volatile products of NO, N_2O and N_2 are detected after Sn modification. It seems that Sn modification not only enhances the activity of Rh but also enhances the selectivity of Rh. Figures 5.37 and 5.38 present the voltammograms and recorded mass of volatile products for spontaneously deposited (θ_{Sn}= 66) and electrodeposited (θ_{Sn}= 80) SnRh/C electrodes. Signals for NO, N_2O and N_2 are detected for both electrodes and N_2O is the dominant product. This result is in good agreement with those of Piao *et al.*[11] The intensity of the N_2O signal increases from the starting potential until a maximum at 0.25 V and then decreases to background levels at potentials close to the onset of hydrogen evolution. The signal of NO is very weak after correcting for the fragmentation ratio (explained in the experimental section). It is clear that the detected NO signal is from the electrode reaction rather than from fragmentation of HNO_2. If NO is produced from the fragmentation of HNO_2, the signal of NO will display the opposite trend to the signal of N_2O, since NO is consumed while N_2O is produced. In the case of highly covered Sn on Pt electrodes, NO is the main product, since the NO intermediate weakly binds on Sn-covered Pt surfaces.[29] However, the NO signal is very small for the SnRh/C catalyst, owing to strong adsorption of NO_{ads} on Rh.

The electrodeposited SnRh/C electrode exhibits N_2 signal. The N_2 signal increases at potentials negative of 0.40 V, which corresponds to a potential of maximum N_2O current. It shows that N_2 is produced from further reduction of N_2O. Some Sn may electrodeposit on the surface of the carbon support; however, the activity of the carbon support is very low for this reaction so this effect on the reaction is negligible. These results have shown that Sn is an effective modifier to promote both activity and selectivity of Rh towards nitrate reduction,

particularly at the rate-determining step in which nitrate is reduced to nitrite, as shown in reaction (5.19).

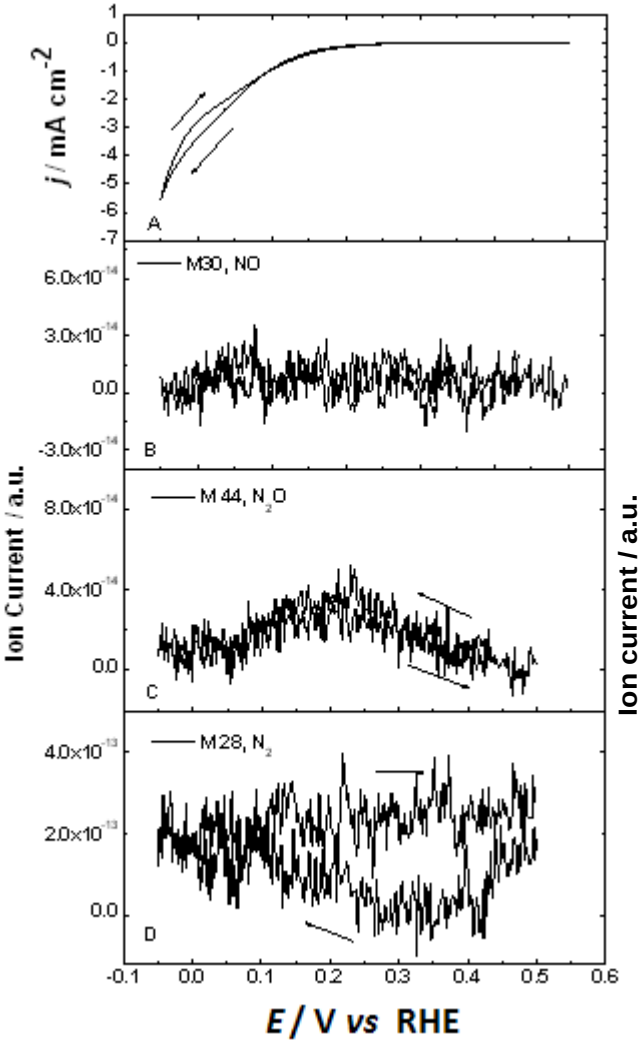

Figure 5.37 Cyclic voltammogram in 10 mM $NaNO_3$ + 0.1 M H_2SO_4 and ion current profiles for *m/z* = 30, *m/z* = 44 and *m/z* = 28 of spontaneous deposition SnRh/C. Scan rate 0.001 V s^{-1}. The arrows indicate the direction of potential sweep.

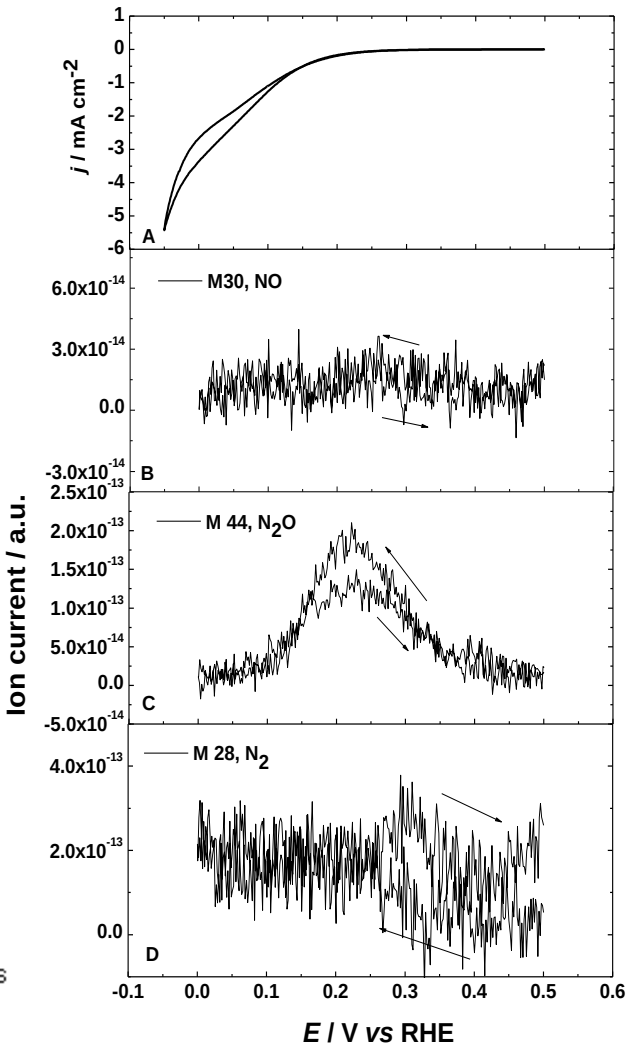

Figure 5.38 Cyclic voltammogram in 10 mM $NaNO_3$ + 0.1 M H_2SO_4 and ion current profiles for *m/z* = 30, *m/z* = 44 and *m/z* = 28 of electrodeposition SnRh/C. Scan rate 0.001 V s^{-1}. The arrows indicate the direction of potential sweep.

The formation of N_2O may proceed *via* nitrite/nitrous acid reduction on SnRh sites, as shown in reaction (5.29). This reaction is believed to proceed through NO_{ads} intermediate.[19,24]

The consecutive reduction of N_2O to N_2 may simultaneously take place on bare Rh sites *via* reaction (5.30).[19,29]

$$2NO_2^- + 6H^+ + 4e^- \rightarrow N_2O + 3H_2O \quad (5.29)$$

$$N_2O + 2H^+ + 2e^- \rightarrow N_2 + H_2O \quad (5.30)$$

The mechanism of nitrate reduction on Sn-modified Rh is still unclear. Sn modification on Rh drastically enhances the reaction at high coverage, indicating that only atomically dispersed Sn is not enough to enhance the electrocatalytic activity. Instead, numbers of Sn are needed to form active sites.[11] Tada *et al.* suggested that Sn can activate the adsorption of nitrate on the electrode surface, while reducing hydrogen adsorption capacity.[102] This may explain why during nitrate reduction on SnRh nitrate prefers to be adsorbed on both Rh and Sn sites. Sn is believed to supply highly oxophilic sites where one oxygen atom of nitrate can be adsorbed and Sn facilitates the breaking of the N−O bond during nitrate conversion to nitrite, as shown in Figure 5.39.

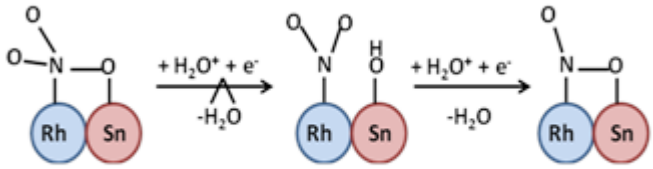

Figure 5.39 Model of the rate-determining step reaction along with the next step on SnRh/C.[29,59]

The reduction of nitrate to nitrite can be achieved by electron transfer from a bimetallic ensemble to adsorbed nitrate,[63] as shown in reaction (5.31). The following step is the reduction of OH_{ads} on Sn to generate free Sn sites as in reaction (5.32). Reactions (5.31) and (5.32) are combined together to give the overall reaction in equation (5.33). The rate of reaction of (5.32) is very small compared with the rate-determining step in reaction (5.31) so

it is negligible in reaction (5.33).[59] An oxygen atom of adsorbed nitrite will be adsorbed on a free Sn site and NO_2^- is further reduced.

$$NO_{3,ads}^- + H_3O^+ + e^- \rightarrow NO_{2,ads}^- + OH_{ads} + H_2O \quad (5.31)$$

$$OH_{ads} + H_3O^+ + e^- \rightarrow 2H_2O \quad (5.32)$$

$$NO_{3,ads}^- + 2H_3O^+ + e^- \rightarrow NO_{2,ads}^- + 2H_2O \quad (5.33)$$

Recently, Yang *et al.* suggested that Sn modification improves the nitrate reduction by enhancing the nitrate adsorption on active sites which comprise Pt with $Sn(OH)_x$ species. It is interesting that the active sites are composed of $Sn(OH)_x$ instead of Sn species. The coordination of nitrate to Pt and metallic Sn, which seems to be the general model accepted for promotion, leads to a rather insignificant enhancement of the nitrate binding. The mechanism of Sn for promoting nitrate reduction on Rh is still unclear.

Figures 5.40 and 5.41 present the CVs and recorded masses of volatile products for the SnRh polycrystalline electrode and the Sn-modified 1:1 Au:Rh/C electrode. For the SnRh polycrystalline electrode, the signals for NO, N_2O and N_2 can be detected. The features of NO and N_2O are similar. The intensities detected on the SnRh polycrystalline electrode depart from the background at 0.3 V, in contrast to the signals in SnRh/C, where the signal increases from the starting potential. A small signal of N_2 has been detected, suggesting that it arises from further reduction of N_2O. It seems that the reaction rate and the selectivity for this electrode are lower than those of SnRh/C. This may be caused by Sn dispersion on the Rh polycrystalline electrode. The Rh polycrystalline electrode used in this study is a high surface area electrode. Hence, Sn atoms may prefer atomic dispersion rather than multiple atom dispersion. As discussed above, multiple atoms of Sn are needed to catalyse the reaction. The Sn-modified 1:1 Au:Rh/C electrode on Figure 5.41 presents lower current density and

significantly lower mass signals of NO, N_2O and N_2 compared with SnRh/C, that has the same amount of Rh. However, the features of mass signals for both electrodes are similar. It is likely that Sn-modified Rh on Au:Rh/C is effective to produce some volatile products but NH_3 is preferentially produced on Au, suppressing the selectivity to produce volatile products.

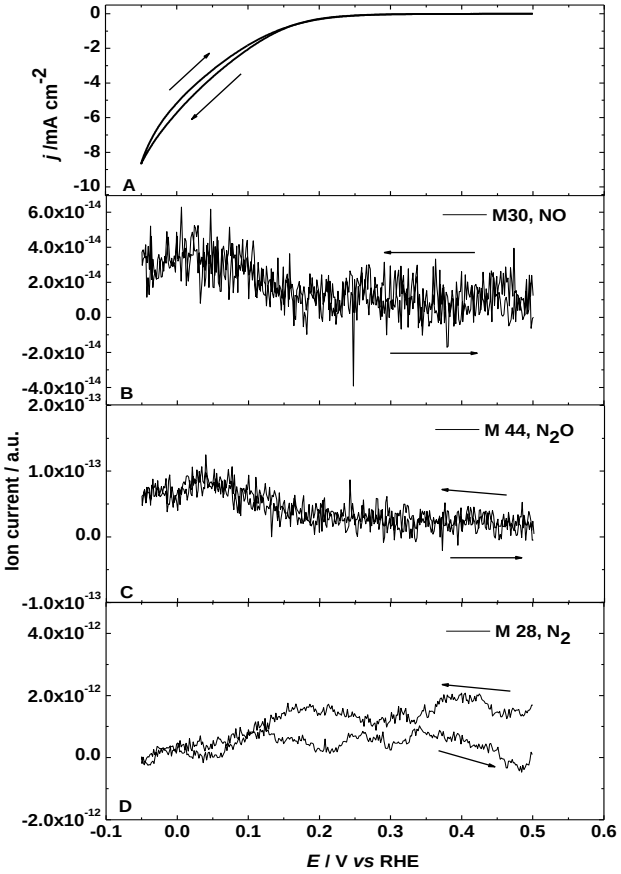

Figure 5.40 Cyclic voltammograms in 10 mM $NaNO_3$ + 0.1 M H_2SO_4 and ion current profiles for *m/z* = 30, *m/z* = 44 and *m/z* = 28 of Sn polycrystalline Rh electrode. Scan rate 0.001 V s^{-1}. The arrows indicate the direction of potential sweep.

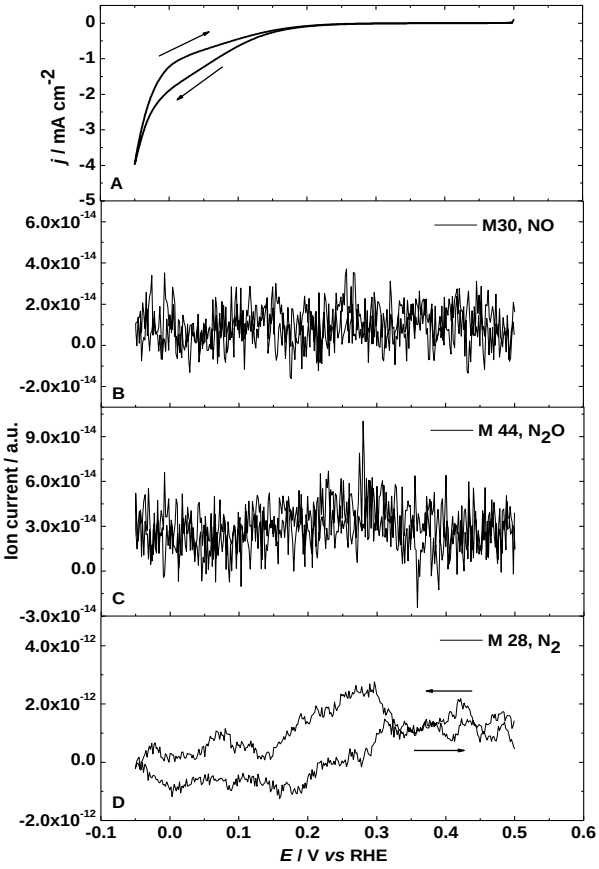

Figure 5.41 Cyclic voltammograms in 10 mM $NaNO_3$ + 0.1 M H_2SO_4 and ion current profiles for *m/z* = 30, *m/z* = 44 and *m/z* = 28 of Sn 1:1 Au:Rh/C. Scan rate 0.001 V s^{-1}. The arrows indicate the direction of potential sweep.

Figure 5.42 presents the ion chromatogram and voltammogram of nitrate reduction at different reduction potentials for SnRh/C with an injection volume of 20 µL. In Figure 5.42(a) the signal of NH_4^+ can be detected at the negative potential of 0.25 V and the signal steeply

increases at more negative potentials. The signal of NH_3OH^+ can be also detected at 0.25 V and the signal increases at more negative potentials, although a moderate Sn surface coverage is used. The concentration of NH_3OH^+ is significantly lower than that of NH_4^+, as shown in Figure 5.42(c). Figure 5.42(b) shows the cyclic voltammogram of Rh/C and SnRh/C in 0.1 M HNO_3. The onset potential of nitrate reduction of SnRh/C electrode takes place at 0.25 V, where the NH_4^+ signal can be detected. The current density dramatically increases at more negative potentials, corresponding to the increases of NH_4^+ and NH_3OH^+ concentrations. Comparing with the Rh/C electrode, the NH_4^+ signal of SnRh/C is observed at more negative potentials. The NH_3OH^+ signals present for the SnRh/C electrode, suggesting that Sn modification reduces the hydrogen adsorption and the cleavage of the last N−O bond. This result shows that Sn modification only promotes the step of nitrate reduced to nitrite at the onset potential and the promotion decreases at potentials near hydrogen evolution.

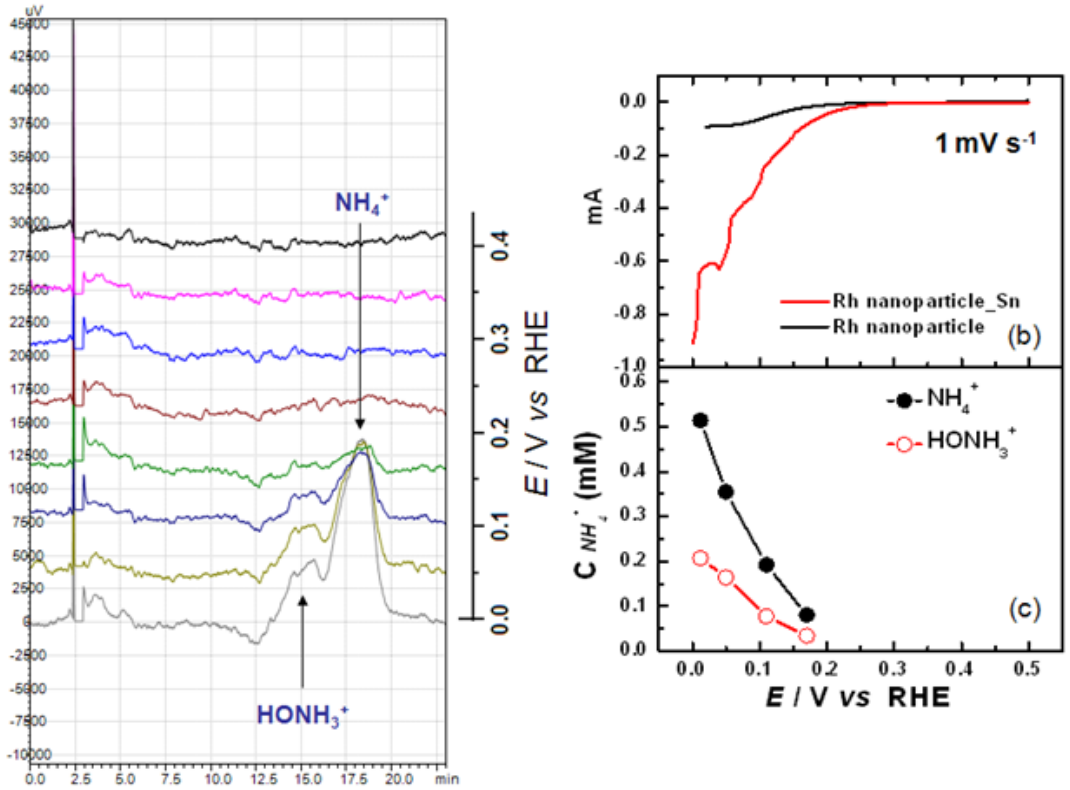

Figure 5.42 (a) Ion chromatogram for products detected from SnRh/C, (b) voltammogram of Rh/C and SnRh/C in 0.1 M HNO_3, scan rate 0.001 V s^{-1} and (c) concentration of ammonium and hydroxylamine.

The production of N_2 is observed for all Sn-modified Rh electrodes. Piao *et al.* evaluated the activity and selectivity of electrodes for nitrate reduction and found that these depend on the ability of electrodes to cleave N−O bonds, to form N−N bonds and to form N−H bonds. For N−O bond cleavage, N−O bond breaking can be activated by Sn modification on noble metal electrodes, increasing the kinetics of the rate-determining step. N−N and N−H formations depend on electrode materials.[11,27] It is known that Rh has promising ability to form N−N bonds as we can see that high amounts of N_2O, the intermediate to form N_2, have been detected. The formation of N−H bonds also needs to be considered. In order to obtain high selectivity for volatile products, it is necessary to reduce the hydrogenation capability. SnRh has low capability to form N−H bonds since the ability to form N−H bonds is opposite to the ability to form N−H bonds. Both N−N and N−H formations will happen after N−O bond cleavage nitrate reduction.[11] Sn modification can enhance the first N−O bond cleavage, reduce N−H bond formation and reduce the last N−O bond cleavage, corresponding to the selectivity of nitrate reduction towards N_2, N_2O, NH_3OH^+ and NH_4^+ of SnRh/C electrode.

5.3.5 Germanium (Ge) modification on Rh/C electrode

Apart from Sn, Ge and In were used to modify Rh/C electrode and to evaluate their activity towards nitrate reduction in sulphuric acid. Figure 5.43 presents CVs of Ge-modified Rh/C and Rh/C, where Ge was deposited following the procedure in section 5.2. The upper potential limit is maintained negative of 0.6 V so that the electrode surface remains in stable.[103] Introducing Ge on Rh suppresses hydrogen adsorption and desorption.[17] The $\theta_{\mathrm{Ge}}$was calculated from hydrogen desorption in the same manner as for θ_{Sn}. The θ_{Ge} on Rh/C is 0.22,

close to 0.25 ML, equal to the maximum coverage of Ge on polycrystalline Pt electrode,[104] low-index single crystal Pt electrodes[103] and Pd electrodes[61]. Figure 5.44 displays CVs acquired for Rh/C and GeRh/C in 10 mM $NaNO_3$ + 0.1 M H_2SO_4. The GeRh electrode exhibits slightly more reduction current than the Rh/C electrode. With the same onset potential, GeRh/C displays a maximum in current at 0.1 V, which is at more negative potential than for Rh/C, suggesting that Ge suppresses hydrogen adsorption. It is likely that Ge does not significantly enhance the catalytic activity of Rh for nitrate reduction. This behaviour is different from that of Pt[12,17] and Pd[61], whose activities are improved by Ge modification. The inactivity for nitrate reduction of Ge on Rh may explain by the stronger adsorption of nitrate ions on Rh than on Pd and Pt. In the case of Pt and Pd, Ge acts as an inhibitor for anion and hydrogen adsorption instead of as a promoter for nitrate reduction, as described by Dima.[17] Ge is likely to have a clear catalytic effect on Pt and Pd, particularly in sulphuric acid. In this present work, Rh is affected less than by other anions since nitrate can compete with sulphate to adsorb on Rh surface. This means that Ge is not as highly effective on Rh as Sn, which mainly acts as the promoter for nitrate reduction. Volatile products cannot be detected for GeRh/C, while GePt and GePd give a signal for NO.[17]

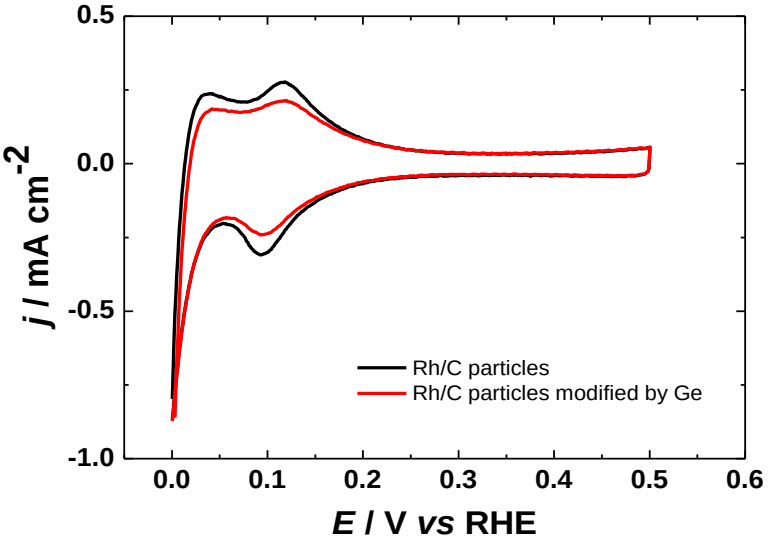

Figure 5.43 Cyclic voltammograms of Rh/C electrode before and after Ge modification in 0.1 M H_2SO_4. Scan rate 0.05 V s^{-1}.

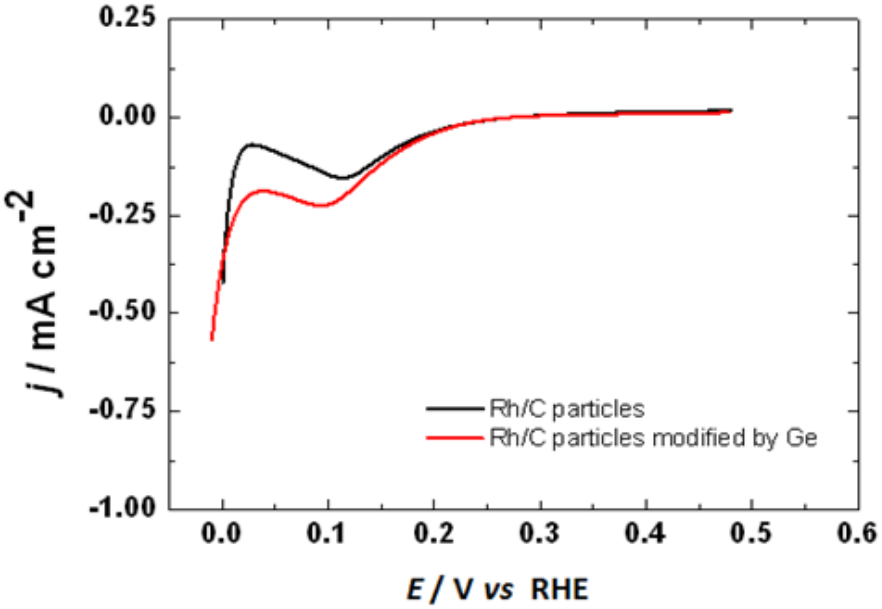

Figure 5.44 Voltammograms of Rh/C and GeRh/C in 10 mM $NaNO_3$ + 0.1 M H_2SO_4. Scan rate 0.01 V s^{-1}.

5.3.6 Indium (In) modification on Rh/C electrode

Indium was chosen to modify Rh/C in this work since PtIn and PdIn catalysts are good candidates for nitrate reduction and nitrate removal with high selectivity to N_2.[62-69,105] In was electrodeposited on Rh/C, as explained in section 5.2. Figure 5.45 presents CVs of Rh/C and In-modified Rh/C. A small amount of In was deposited on Rh/C with an In surface coverage (θ_{In}) equal to 0.20. The ratio of Pt or Pd to In, that is widely used for bimetallic catalyst to give high nitrate conversion, is 4:1 Pt:In or Pd:In ratio.[62] Indium suppresses hydrogen adsorption and desorption on Rh/C. Figure 5.46 displays CVs acquired for Rh/C and InRh/C in 10 mM $NaNO_3$ + 0.1 M H_2SO_4. The reduction current of InRh/C is around double that of Rh/C. The maximum reduction current of InRh/C is at 0.085 V, which is at more negative potential than Rh/C and GeRh/C. This confirms that In suppresses hydrogen adsorption and weakly promotes nitrate reduction, as can be seen from the current increase; however, In has less ability to promote nitrate reduction than Sn.[63] Krawczyk *et al.* reported that the final products of nitrate reduction from InPd catalysts are ammonium and dinitrogen. From

OLEMS results of InRh/C, the signals of NO and N_2O are hardly detectable, which might be caused by sulphate blocking the surface of Rh. The anion effect on nitrate reduction for Rh/C and Sn-modified Rh/C will be discussed in the next section.

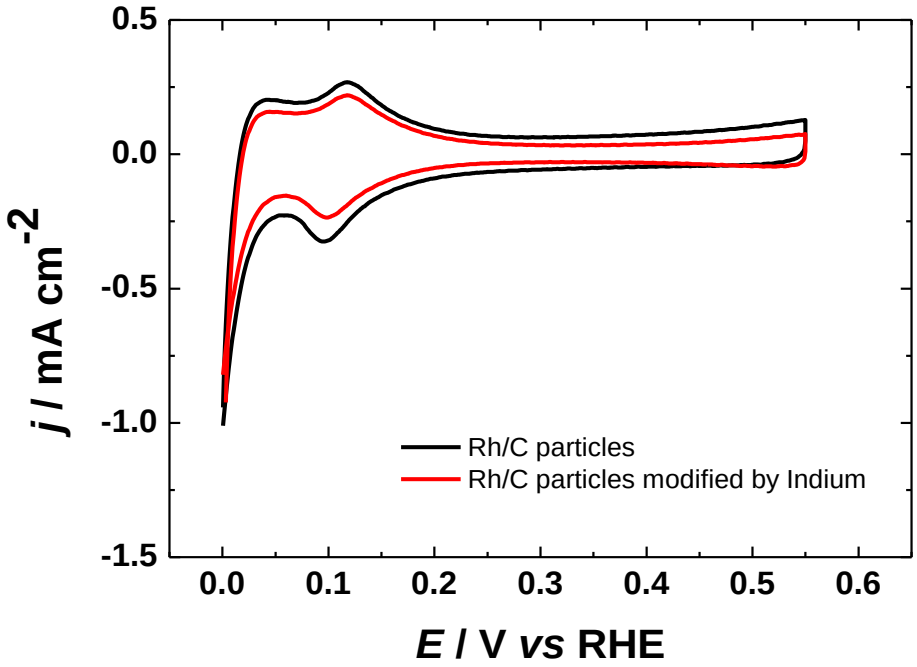

Figure 5.45 Cyclic voltammograms of Rh/C electrode before and after In modification in 0.1 M H_2SO_4. Scan rate 0.05 V s^{-1}.

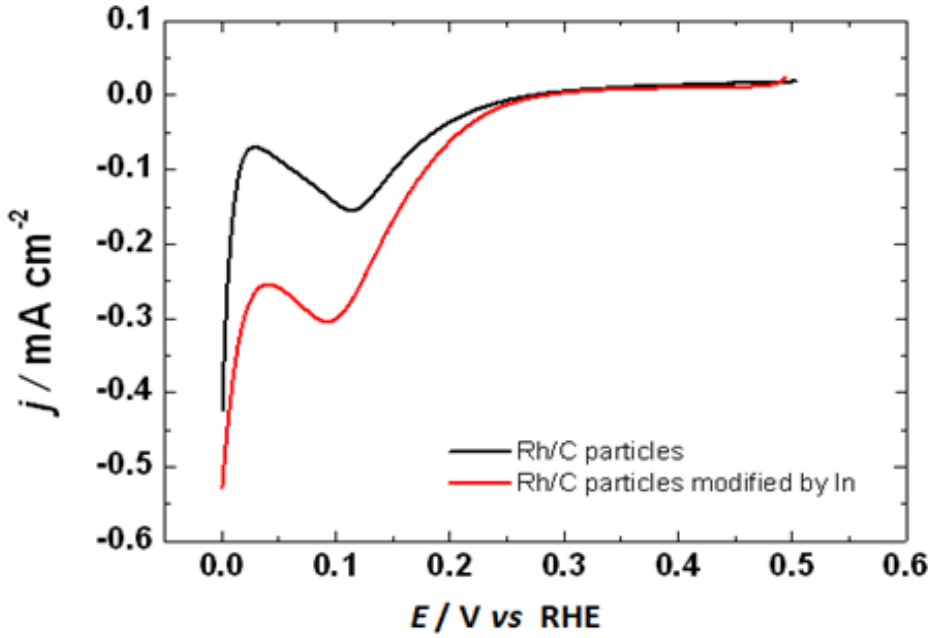

Figure 5.46 Voltammograms of Rh/C and In-modified Rh/C in 10 mM $NaNO_3$ + 0.1 M H_2SO_4. Scan rate 0.01 V s^{-1}.

5.3.7 Anion effect

Apart from the ability of a catalyst to reduce nitrate, its tolerance to competing adsorbates must be considered. The adsorption extent of both nitrate ion and nitric acid are not far from that of the numeral acids and their corresponding anions, indicating the competitive adsorption of these species. Rh and SnRh exhibit high catalytic activity for nitrate reduction, particularly SnRh, which has high selectivity to produce volatile products. It is necessary to study the effect of electrolyte anions on catalytic activity and selectivity of electrode material of interest.

In the present work, experiments were also carried out in nitric acid in order to compare with nitrate reduction in sulphuric acid. It is known that NO_3^- adsorption can be hindered by the adsorption of sulphate.[10] Figure 5.47 displays cyclic voltammograms of Rh/C in 10 mM $NaNO_3$ + 0.1 M H_2SO_4, 10 mM HNO_3 and 0.1 M HNO_3. Comparing the same concentration of nitrate, the reduction current of Rh/C in 10 mM HNO_3 is lower than in 10 mM $NaNO_3$ + 0.1 M H_2SO_4 acid, since the pH in 10 mM HNO_3 in lower than in 0.1 M H_2SO_4. Also, the pKa value of H_2SO_4 is higher than in HNO_3. When the concentration of HNO_3 is increased to 0.1 M, the reduction current is increased higher than in 10 mM $NaNO_3$ + 0.1 M H_2SO_4. The increase of reduction current is due to the increase of nitrate concentration. Interestingly, the maximum reduction current of Rh/C in high concentration of nitrate is shifted to near hydrogen evolution, suggesting that nitrate is fully adsorbed on the surface. On the other hand, the maximum reduction current in lower concentration of nitrate in sulphuric acid is at ~0.1 V, suggesting that competition between sulphate and nitrate. These data agree well with the literature in that the shape of polarisation curve is changed when the concentration of nitric acid is increased.[50] It is noticeable that the onset potentials of nitrate reduction for Rh/C in the three different electrolytes are at similar potentials and the reduction

currents are not dramatically different. These results suggest that the influence of anions on nitrate reduction on Rh is not as large as that seen for Pt from the literatures.[10,50,59,78] Nitrate reduction on Pt is heavily hindered by sulphate, as well as by the adsorption from other anions.[50,51] These phenomena can be explained by the strong adsorption of nitrate on Rh compared with Pt. Rh has higher adsorption enthalpy of nitrate and larger anion affinity to anion adsorption than Pt. The PZC for Rh is more negative than for Pt, suggesting strong anion adsorption on Rh.[8,10] Figure 5.48 presents the cyclic voltammogram of 1:1 Au:Rh/C in 10 mM $NaNO_3$ + 0.1 M H_2SO_4 and in 0.1 M HNO_3. The reduction current for both electrolytes are similar. However, the reduction currents of 1:1 Au:Rh/C in both electrolytes are lower than those of Rh/C. This observation may arise from sulphate blocking or surface poisoning of Au on the surface. It is noticeable that the influence of the anion is still less for Rh with and without the presence of Au.

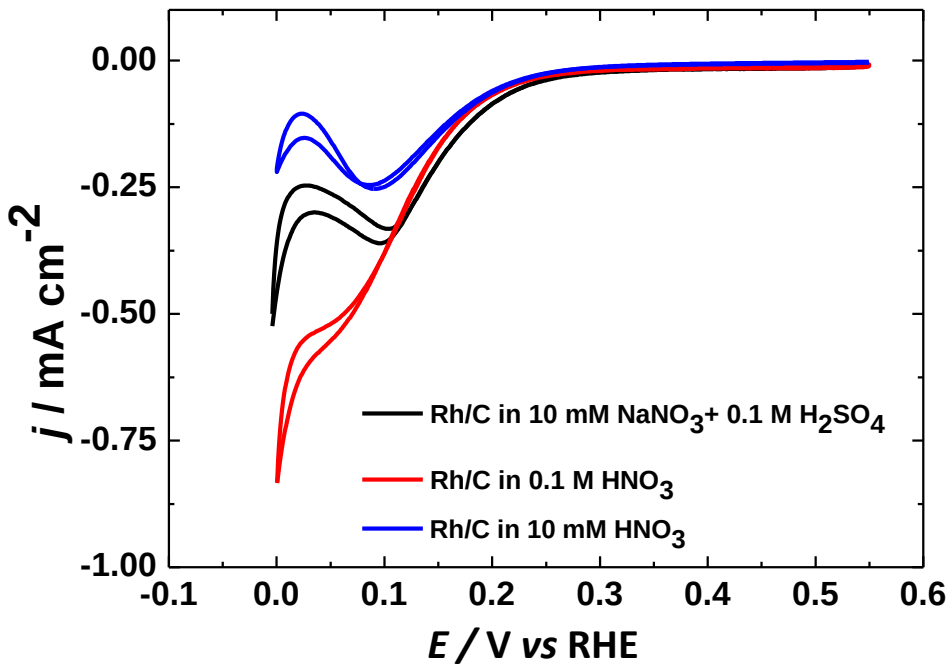

Figure 5.47 Cyclic voltammograms of Rh/C in 10 mM $NaNO_3$ + 0.1 M H_2SO_4, 10 mM HNO_3 and 0.1 M HNO_3, scan rate 0.001 V s^{-1}.

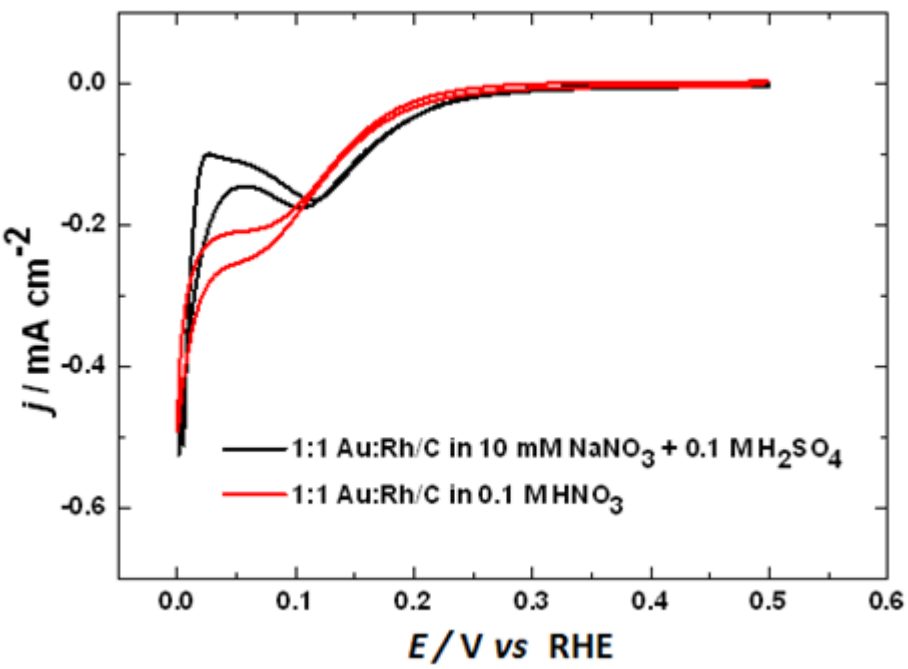

Figure 5.48 Cyclic voltammograms of 1:1 Au:Rh/C in 10 mM $NaNO_3$ + 0.1 M H_2SO_4 and 0.1 M HNO_3, scan rate 0.001 V s^{-1}.

Figure 5.49 presents CVs of SnRh/C in 0.1 M HNO_3 and in 10 mM $NaNO_3$ + 0.1 M H_2SO_4. The shapes of the polarisation curves for SnRh/C in both electrolytes are similar and have the same onset potential. The reduction current of SnRh/C at 0 V in nitric acid is *ca* 3 mA cm^{-2}, which is the same value as that of nitrate reduction in sulphuric acid, indicating there is significantly less hindrance by sulphate on SnRh/C than on Rh/C and Au:Rh/C. Perhaps Sn does not only facilitate nitrate reduction but also acts as an inhibitor for the other anions and hydrogen. Figure 5.50 presents cyclic voltammograms of Sn 1:1 Au:Rh/C in 0.1 M HNO_3 and in 10 mM $NaNO_3$ + 0.1 M H_2SO_4. The onset potential in the latter electrolyte is at more negative potential than the first electrolyte. This may imply that Sn is preferentially deposited on Rh than Au and that activity on Au sites is hindered by strong sulphate adsorption.

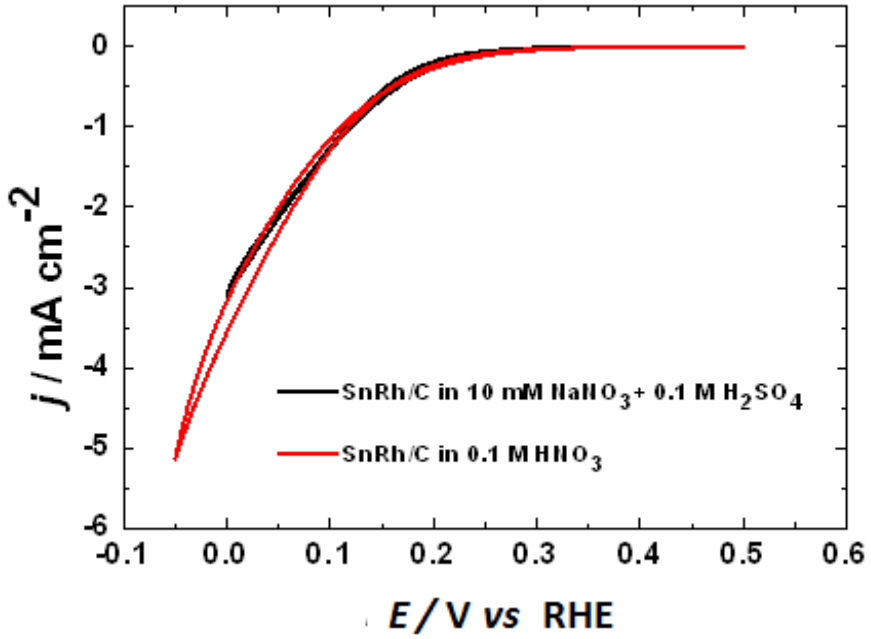

Figure 5.49 Cyclic voltammograms of SnRh/C in 10 mM $NaNO_3$ + 0.1 M H_2SO_4 and 0.1 M HNO_3, scan rate 0.001 V s^{-1}.

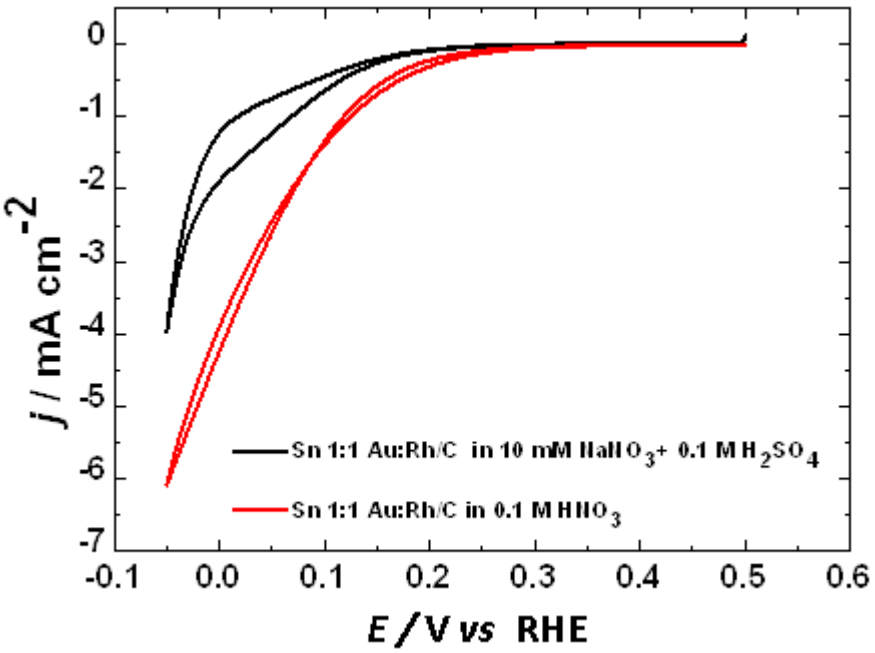

Figure 5.50 Cyclic voltammograms of Sn 1:1 Au:Rh/C in 10 mM $NaNO_3$ + 0.1 M H_2SO_4 and 0.1 M HNO_3, scan rate 0.001 V s^{-1}.

Apart from Sn modification, the anion effect was also studied on Ge- and In-modified Rh/C. Figures 5.51 and 5.52 show the cyclic voltammograms of GeRh/C and InRh/C, respectively, in nitric acid and nitrate reduction in sulphuric acid. In both GeRh/C and InRh/C

cases, the reduction currents in nitric acid are slightly higher than nitrate reduction in sulphuric acid. It has been reported that Ge mainly acts an inhibitor for acid anions,[17] hence, the reduction current of GeRh is not significantly enhanced even there is no effect from sulphate. The InRh/C electrode has the similar feature with GeRh/C, that the reduction current is slightly enhanced in the absence of sulphate. However, the mechanism of nitrate reduction on In-modified Rh is still unclear. From our results, it can be assumed that there is low anion effect on Rh, even if it has been modified by a second metal, such as Sn, Ge or In. However, further investigation of the anion effect on selectivity was investigated with OLEMS is discussed in the next section.

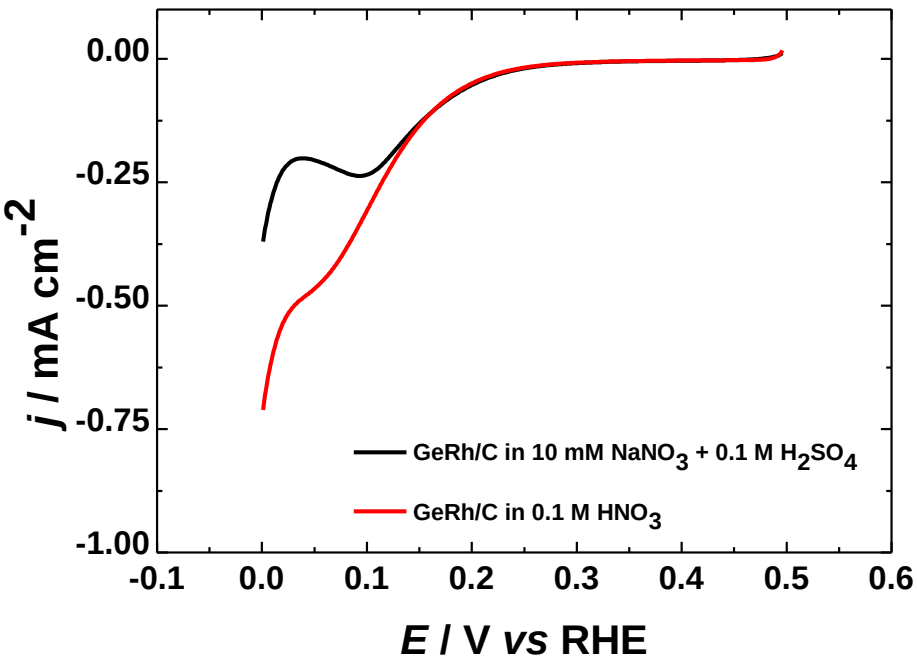

Figure 5.51 Cyclic voltammograms of GeRh/C in 10 mM $NaNO_3$ + 0.1 M H_2SO_4 and 0.1 M HNO_3, scan rate 0.001 V s^{-1}.

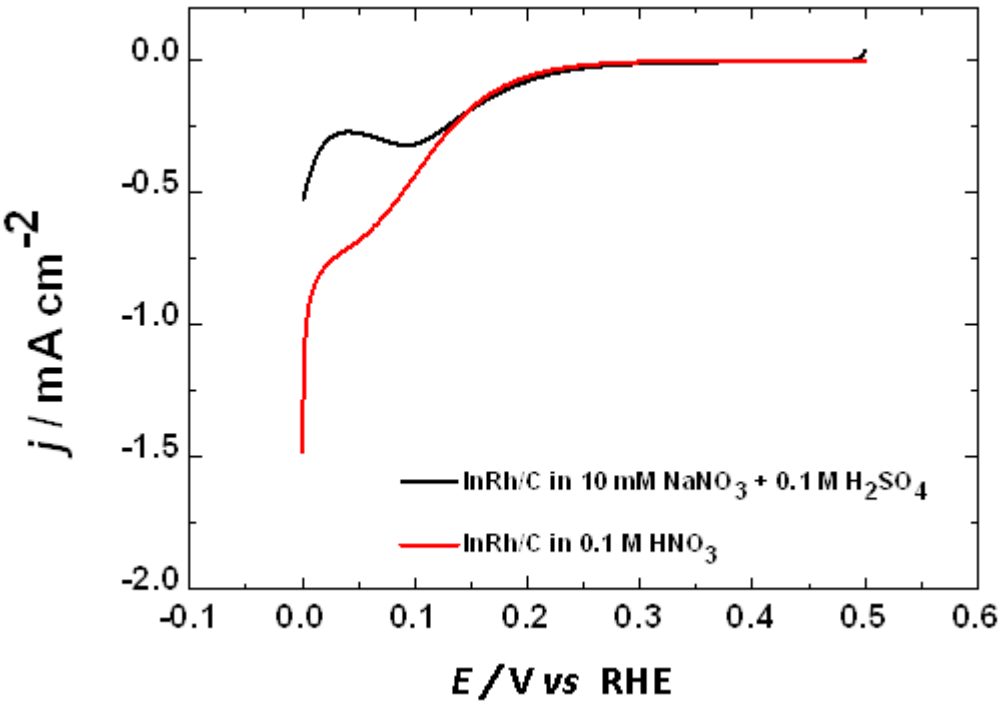

Figure 5.52 Cyclic voltammograms of InRh/C in 10 mM $NaNO_3$ + 0.1 M H_2SO_4 and 0.1 M HNO_3, scan rate 0.001 V s^{-1}.

In order to study the anion effect on the selectivity of Rh, OLEMS was carried out in 0.1 M HNO_3 so that the results are discussed and compared with nitrate reduction in sulphuric acid. Although Rh is known to be a promising catalyst for nitrate reduction, no volatile products can be detected from Rh electrodes either in nitric acid or nitrate reduction with supporting electrolyte. However, it is feasible to detect the signal of volatile products after modification of electrode by a second metal. Figure 5.53 displays cyclic voltammogram and mass signal for SnRh/C in 0.1 M HNO_3. The signals of NO, N_2O and N_2 are detectable, similarly to nitrate reduction of SnRh/C in sulphuric acid; however, the features of the signals in nitric acid are markedly dissimilar from of those in sulphuric acid. The signal of NO is significantly small. The signal of N_2O in nitric acid departs from the background at 0.4 V and reaches a maximum at 0.05 V. The signal of N_2O decreases at potentials near hydrogen evolution, suggesting that ammonium is produced.

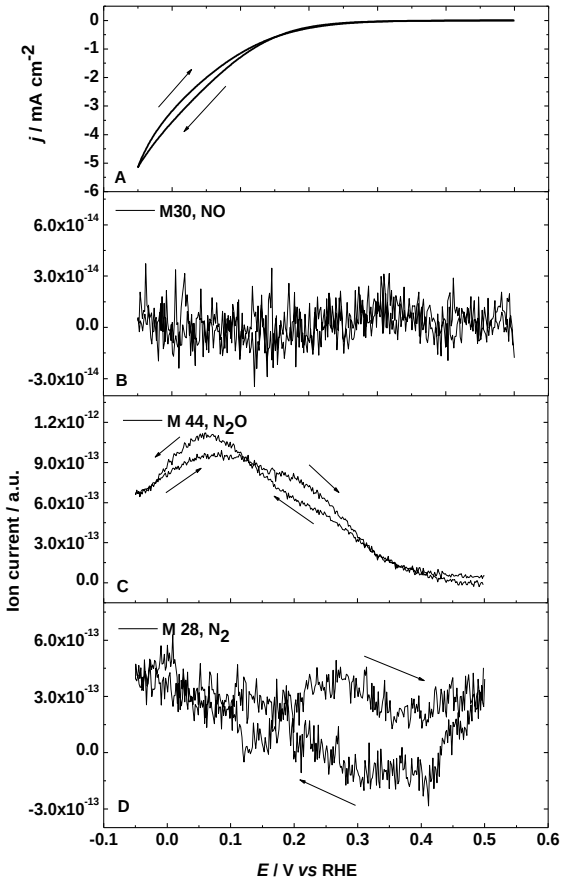

Figure 5.53 Cyclic voltammograms in 0.1 M HNO_3 and Ion current profiles for *m/z* = 30, *m/z* = 44 and *m/z* = 28 of SnRh/C electrode. Scan rate 0.001 V s^{-1}. The arrows indicate the direction of potential sweep.

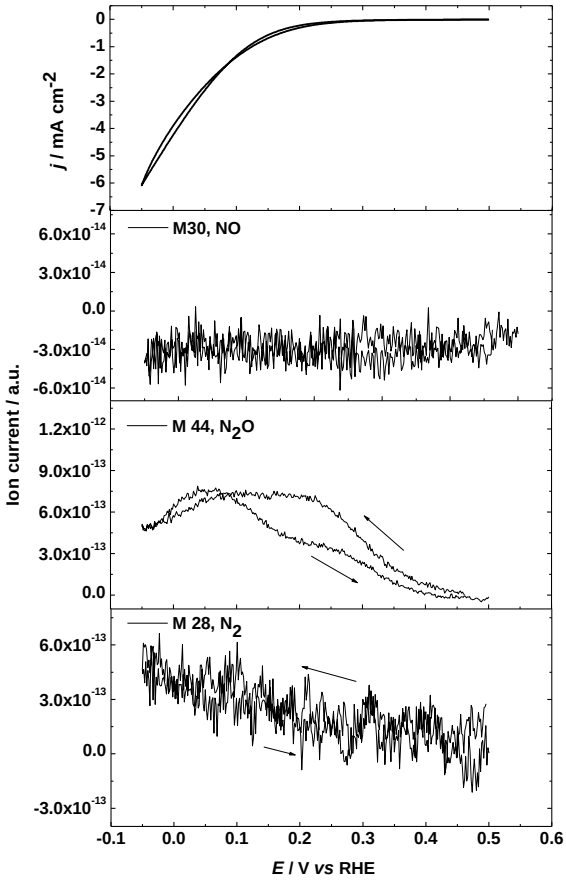

Figure 5.54 Cyclic voltammograms in 0.1 M HNO_3 and Ion current profiles for *m/z* = 30, *m/z* = 44 and *m/z* = 28 of Sn 1:1 Au:Rh/C electrode. Scan rate 0.001 V s^{-1}. The arrows indicate the direction of potential sweep.

The N_2 signal begins from 0.4 V (the potential N_2O produced) and increases until the switching potential. The formation of N_2O is likely to be greater than the consumption of N_2O to produce N_2. Comparing the reaction in nitric acid with that in sulphuric acid, the signal of N_2O in the former electrolyte begins from 0.5 V and reaches the maximum at 0.05 V whilst the signal in the latter electrolyte begins at the starting potential and reaches a maximum at 0.25 V. The signal of N_2 in both nitric acid and sulphuric acid are similar. These results suggest that in nitric acid NO intermediate is strongly adsorbed and is reduced to N_2O with larger potential region than in sulphuric acid.

Nevertheless, the further reduction of N_2O to N_2 in nitric acid occurs at more positive potentials than in sulphuric acid, indicating that the rate of this step in nitric acid is faster than in sulphuric acid.

Figure 5.54 displays the voltammogram and the mass signal of Sn 1:1 Au:Rh/C in 0.1 M HNO_3. The NO, N_2O and N_2 signals of Sn 1:1 Au:Rh/C are detected with similar features as for SnRh/C. The N_2O signal of Sn 1:1 Au:Rh/C is slightly lower than for SnRh/C, suggesting that SnRh/C has higher selectivity toward N_2O. Comparing with sulphuric acid, the N_2O signals in nitric acid are appreciable higher than in sulphuric acid containing nitrate. It can be assumed that the influence of the anion is greater for Sn 1:1 Au:Rh/C than for SnRh/C.

In this work, Au also has been modified by Sn and its activity towards nitrate reduction investigated in nitric acid in order to study the anion effect on Au. Interestingly, Sn-modified Au/C, as shown in Figure 5.55, yields small signals of NO which cannot be observed in sulphuric acid, suggesting that sulphate blocks the surface of SnAu/C. This may imply that the nitrate reduction current of SnAu/C is accompanied by the formation of NO in the solution, which appears since NO desorbs from the SnAu/C surface. Because of this reason, NO cannot be reduced further.[10] This behavior of SnAu/C is different from that of SnRh/C, which NO_{ads} can be reduced further to form other products. It has been reported that Au electrode can be modified by a second metal to enhance the catalytic activity towards nitrate reduction, for example Cd-modified Au electrodes produce nitrite as the product of the reaction.[83,99]

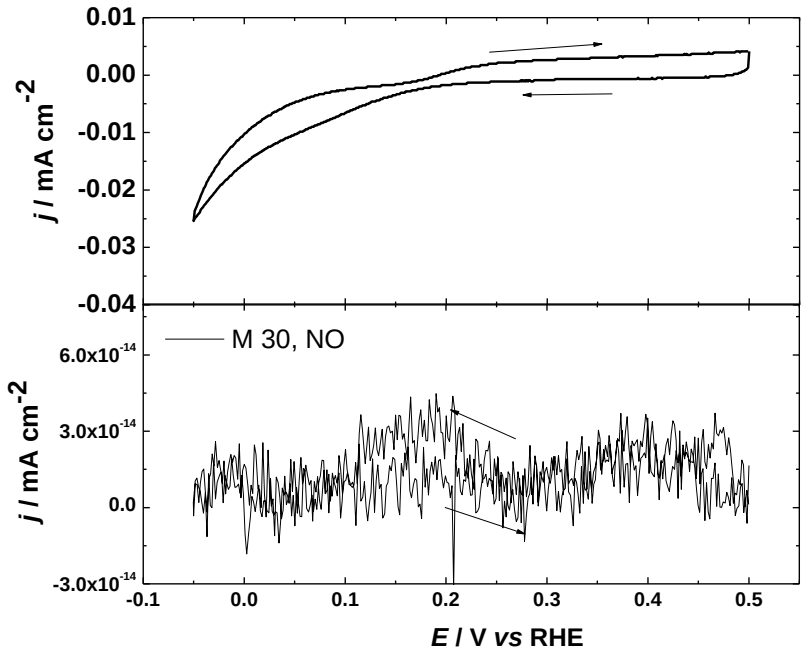

Figure 5.55 Ion current profiles for *m/z* = 30 of SnAu/C electrode in 0.1 M HNO_3 and. Scan rate 0.001 V s^{-1}.

5.4 Conclusions

The nitrate reduction and nitrite reduction have been studied on Rh/C, Au:Rh/C nanoparticles, polycrystalline Rh and second metal-modified Rh electrodes in acidic and alkaline media. The main approach for this work is to determine volatile products. In acidic media, Au does not show catalytic activity for nitrate reduction and presents relatively low activity for nitrite reduction, which yields a small signal of NO in OLEMS. Volatile products cannot be detected for nitrate reduction at the Rh/C electrode but NO and N_2O signals are detected on nitrite reduction. The formation of N_2O takes place from a reaction between NO_{ads} and NO_{aq} the potential range studied. Au:Rh/C nanoparticles exhibit lower activity for both nitrate reduction and nitrite reduction than pure Rh/C as a result of surface poisoning by NH_3 on the Au surface. NH_3 is produced at potentials near hydrogen evolution for all electrodes, as shown in IC data. It is likely that there is a competition between NO and H_{upd} at negative potentials. The Sn-modified Rh/C electrode produces mainly NH_3OH^+, suggesting that Sn modification

only promotes the rate of the determining step and reduces the hydrogen adsorption and the cleavage of the last N−O bond.

The catalytic activities of the electrodes towards nitrate reduction and nitrite reduction in alkaline media are smaller than in acidic media, suggesting pH dependent activity and selectivity. NO is the main intermediate in acidic media, while HNO_2 is the main intermediate in alkaline media. The catalytic activity and selectivity of Rh towards nitrate reduction are enhanced by Sn modification and N_2O and N_2 signals are detected. NH_4^+ and NH_3OH^+ are detected for nitrate reduction on the SnRh/C electrode. These arise because of the enhancement of the first electron transfer in the rate-determining step. Ge modification does not significantly enhance the activity of Rh/C electrode towards nitrate reduction. In modification weakly increases the catalytic activity of Rh; however, its activity is still much lower than that of Sn-modified Rh. The mechanism of nitrate reduction at In-modified Rh/C is still unclear. The influences of anions on nitrate reduction at Rh/C and SnRh/C electrodes are smaller than those previously observed for Pt electrodes.

5.5 References

(1) Powlson, D. S.; Addisott, T. M.; Benjamin, N.; Cassman, K. G.; de Kok, T. M.; van Grinsven, H.; L'Hirondel, J. L.; Avery, A. A.; van Kessel, C. *Journal of Environmental Quality* **2008**, *37*, 291.

(2) Ward, M. H.; deKok, T. M.; Levallois, P.; Brender, J.; Gulis, G.; Nolan, B. T.; VanDerslice, J. *Environmental Health Perspectives* **2005**, *113*, 1607.

(3) Manassaram, D. M.; Backer, L. C.; Moll, D. M. *Environmental Health Perspectives* **2006**, *114*, 320.

(4) Gu, B. H.; Ku, Y. K.; Jardine, P. M. *Environmental Science & Technology* **2004**, *38*, 3184.

(5) Molinari, R.; Argurio, P.; Romeo, L. *Desalination* **2001**, *138*, 271.

(6) Elmidaoui, A.; Elhannouni, F.; Sahli, M. A. M.; Chay, L.; Elabbassi, H.; Hafsi, M.; Largeteau, D. *Desalination* **2001**, *136*, 325.

(7) Brylev, O.; Sarrazin, M.; Belanger, D.; Roue, L. *Applied Catalysis B-Environmental* **2006**, *64*, 243.

(8) Brylev, O.; Sarrazin, M.; Roue, L.; Belanger, D. *Electrochimica Acta* **2007**, *52*, 6237.

(9) da Cunha, M.; De Souza, J. P. I.; Nart, F. C. *Langmuir* **2000**, *16*, 771.

(10) Dima, G. E.; de Vooys, A. C. A.; Koper, M. T. M. *J. Electroanal. Chem.* **2003**, *554*, 15.

(11) Piao, S.; Kayama, Y.; Nakano, Y.; Nakata, K.; Yoshinaga, Y.; Shimazu, K. *J. Electroanal. Chem.* **2009**, *629*, 110.

(12) Gootzen, J. F. E.; Peeters, P.; Dukers, J. M. B.; Lefferts, L.; Visscher, W.; vanVeen, J. A. R. *J. Electroanal. Chem.* **1997**, *434*, 171.

(13) de Groot, M. T.; Koper, M. T. M. *J. Electroanal. Chem.* **2004**, *562*, 81.

(14) de Vooys, A. C. A.; Koper, M. T. M.; van Santen, R. A.; van Veen, J. A. R. *Journal of Catalysis* **2001**, *202*, 387.

(15) de Vooys, A. C. A.; Koper, M. T. M.; van Santen, R. A.; van Veen, J. A. R. *Electrochimica Acta* **2001**, *46*, 923.

(16) Dima, G. E.; Beltramo, G. L.; Koper, M. T. M. *Electrochimica Acta* **2005**, *50*, 4318.

(17) Dima, G. E.; Rosca, V.; Koper, M. T. M. *J. Electroanal. Chem.* **2007**, *599*, 167.

(18) Duca, M.; Figueiredo, M. C.; Climent, V.; Rodriguez, P.; Feliu, J. M.; Koper, M. T. M. *Journal of the American Chemical Society* **2011**, *133*, 10928.

(19) Duca, M.; Kavvadia, V.; Rodriguez, P.; Lai, S. C. S.; Hoogenboom, T.; Koper, M. T. M. *J. Electroanal. Chem.* **2010**, *649*, 59.

(20) Duca, M.; van der Klugt, B.; Hasnat, M. A.; Machida, M.; Koper, M. T. M. *Journal of Catalysis* **2010**, *275*, 61.

(21) Duca, M.; van der Klugt, B.; Koper, M. T. M. *Electrochimica Acta* **2012**, *68*, 32.

(22) Maloy, J. T. *In Standard Potentials in Aqueous Solutions;* ; Marcel Dekker: New York, 1985.

(23) Plieth, W. J. *In Encyclopedia of the Electrochemistry of the Elements;*; Marcel Dekker, 1978; Vol. Vol. 8.

(24) Rosca, V.; Duca, M.; de Groot, M. T.; Koper, M. T. M. *Chemical Reviews* **2009**, *109*, 2209.

(25) Bothe, H., Ferguson, S., Newton, W. E., *The Biology of the Nitrogen Cycle*; Elsevier: Amsterdam, 2006.

(26) Jetten, M. S. M. *EnVironmental Microbiology* **2008**, *10*.

(27) Nakata, K.; Doi, Y.; Kubota, S.; Shimazu, K. *J. Electroanal. Chem.* **2010**, *647*, 187.

(28) Duca, M.; Khamseh, S.; Lai, S. C. S.; Koper, M. T. M. *Langmuir* **2010**, *26*, 12418.

(29) Yang, J.; Duca, M.; Schouten, K. J. P.; Koper, M. T. M. *J. Electroanal. Chem.* **2011**, *662*, 87.

(30) Shimazu, K.; Goto, R.; Tada, K. *Chemistry Letters* **2002**, 204.

(31) Witonska, I.; Karski, S.; Rogowski, J.; Krawczyk, N. *Journal of Molecular Catalysis a-Chemical* **2008**, *287*, 87.

(32) Ahmadi, A.; Bracey, E.; Evans, R. W.; Attard, G. *J. Electroanal. Chem.* **1993**, *350*, 297.

(33) Haq, S.; Hodgson, A. *Surface Science* **2000**, *463*, 1.

(34) Rosca, V.; Beltramo, G. L.; Koper, M. T. M. *Langmuir* **2005**, *21*, 1448.

(35) Rosca, V.; Koper, M. T. M. *Journal of Physical Chemistry B* **2005**, *109*, 16750.

(36) Rosca, V.; Koper, M. T. M. *Surface Science* **2005**, *584*, 258.

(37) Rodes, A.; Gomez, R.; Perez, J. M.; Feliu, J. M.; Aldaz, A. *Electrochimica Acta* **1996**, *41*, 729.

(38) Yan, Y. G.; Huang, B. B.; Wang, J. Y.; Wang, H. F.; Cai, W. B. *Journal of Catalysis* **2007**, *249*, 311.

(39) Alvarez, B.; Rodes, A.; Perez, J. M.; Feliu, J. M.; Rodriguez, J. L.; Pastor, E. *Langmuir* **2000**, *16*, 4695.

(40) Ye, S.; Hattori, H.; Kita, H. *Berichte Der Bunsen-Gesellschaft-Physical Chemistry Chemical Physics* **1992**, *96*, 1884.

(41) Duca, M.; Cucarella, M. O.; Rodriguez, P.; Koper, M. T. M. *Journal of the American Chemical Society* **2010**, *132*, 18042.

(42) Wasberg, M.; Horanyi, G. *J. Electroanal. Chem.* **1995**, *386*, 213.

(43) Wasberg, M.; Horanyi, G. *Electrochimica Acta* **1995**, *40*, 615.

(44) Pletcher, D.; Poorabedi, Z. *Electrochimica Acta* **1979**, *24*, 1253.

(45) Yang, G. C. C.; Lee, H. L. *Water Research* **2005**, *39*, 884.

(46) Vijh, A. K. *Journal of Catalysis* **1974**, *32*, 230.

(47) Khomutov, N. E. a. S., U. S. *Elektrokhimiya* **1971**, *7*, 332.

(48) Horanyi, G.; Wasberg, M. *Electrochimica Acta* **1997**, *42*, 261.

(49) Santos, A. L.; Deiner, L. J.; Varela, H. *Catalysis Communications* **2008**, *9*, 269.

(50) Horanyi, G.; Rizmayer, E. M. *J. Electroanal. Chem.* **1982**, *140*, 347.

(51) Horanyi, G.; Rizmayer, E. M. *J. Electroanal. Chem.* **1985**, *188*, 273.

(52) Peel, J. W.; Reddy, K. J.; Sullivan, B. P.; Bowen, J. M. *Water Research* **2003**, *37*, 2512.

(53) Reddy, K. J.; Lin, J. P. *Water Research* **2000**, *34*, 995.

(54) Witonska, I.; Karski, S.; Goluchowska, J. *Kinetics and Catalysis* **2007**, *48*, 823.

(55) Warna, J.; Turunen, I.; Salmi, T.; Maunula, T. *Chemical Engineering Science* **1994**, *49*, 5763.

(56) Epron, F.; Gauthard, F.; Pineda, C.; Barbier, J. *Journal of Catalysis* **2001**, *198*, 309.

(57) Pronkin, S. N.; Simonov, P. A.; Zaikovskii, V. I.; Savinova, E. R. *Journal of Molecular Catalysis a-Chemical* **2007**, *265*, 141.

(58) Tada, K.; Kawaguchi, T.; Shimazu, K. *J. Electroanal. Chem.* **2004**, *572*, 93.

(59) Tada, K.; Shimazu, K. *J. Electroanal. Chem.* **2005**, *577*, 303.

(60) Shimazu, K.; Goto, R.; Piao, S. Y.; Kayama, R.; Nakata, K.; Yoshinaga, Y. *J. Electroanal. Chem.* **2007**, *601*, 161.

(61) Gootzen, J. F. E.; Lefferts, L.; van Veen, J. A. R. *Applied Catalysis a-General* **1999**, *188*, 127.

(62) Prusse, U.; Hahnlein, M.; Daum, J.; Vorlop, K. D. *Catalysis Today* **2000**, *55*, 79.

(63) Prusse, U.; Vorlop, K. D. *Journal of Molecular Catalysis a-Chemical* **2001**, *173*, 313.

(64) Prusse, U.; Horold, S.; Vorlop, K. D. *Chemie Ingenieur Technik* **1997**, *69*, 93.

(65) Mendow, G.; Marchesini, F. A.; Miro, E. E.; Querini, C. A. *Industrial & Engineering Chemistry Research* **2011**, *50*, 1911.

(66) Marchesini, F. A.; Querini, C. A.; Miro, E. E.; Requejo, F. G.; Ramallo-Lopez, J. M. *Catalysis Communications* **2008**, *10*, 355.

(67) Marchesini, F. A.; Picard, N.; Miro, E. E. *Catalysis Communications* **2012**, *21*, 9.

(68) Marchesini, F. A.; Irusta, S.; Querini, C.; Miro, E. *Applied Catalysis a-General* **2008**, *348*, 60.

(69) Marchesini, F. A.; Gutierrez, L. B.; Querini, C. A.; Miro, E. E. *Chemical Engineering Journal* **2010**, *159*, 203.

(70) Krawczyk, N.; Karski, S.; Witonska, I. *Reaction Kinetics Mechanisms and Catalysis* **2011**, *103*, 311.

(71) Ghafari S., H. M., Aroua M. K. *Bioresource Technology* **2008**, *99*, 3965.

(72) Waite M. , T. P. M. a. H. B. E.; Ltd., I., Ed. United Kingdom, 2000; Vol. Patent GB 2 365 023 B

(73) Waite, M.; Ltd., I., Ed. United Kingdom, 1998; Vol. Patent GB 2348209.

(74) Katsounaros I., D. M., Kyriacou G. *Journal of Hazardous Materials* **2009**, *171* 323.

(75) Katsounaros, I.; Kyriacou, G. *Electrochimica Acta* **2008**, *53*, 5477.

(76) Katsounaros I., K. G. *Electrochimica Acta* **2007** *52*, 6412.

(77) Safonova, T. Y.; Petrii, O. A. *J. Electroanal. Chem.* **1998**, *448*, 211.

(78) Petrii, O. A.; Safonova, T. Y. *J. Electroanal. Chem.* **1992**, *331*, 897.

(79) Wonders, A. H.; Housmans, T. H. M.; Rosca, V.; Koper, M. T. M. *Journal of Applied Electrochemistry* **2006**, *36*, 1215.

(80) El-Deab, M. S. *Electrochimica Acta* **2004**, *49*, 1639.

(81) daCunha, M.; Weber, M.; Nart, F. C. *J. Electroanal. Chem.* **1996**, *414*, 163.

(82) Hsieh, S. J.; Gewirth, A. A. *Langmuir* **2000**, *16*, 9501.

(83) Xing, X. K.; Scherson, D. A.; Mak, C. *Journal of the Electrochemical Society* **1990**, *137*, 2166.

(84) Hwang, S.; Lee, J.; Kwak, J. *J. Electroanal. Chem.* **2005**, *579*, 143.

(85) Gadde, R. R.; Bruckens.S *J. Electroanal. Chem.* **1974**, *50*, 163.

(86) Nishimura, K.; Machida, K.; Enyo, M. *Electrochimica Acta* **1991**, *36*, 877.

(87) Iotov P., K. S. *Journal of Chemical Technology and Metallurgy* **2013**, *48,1*, 80.

(88) Koper, M. T. M.; Jansen, A. P. J.; van Santen, R. A.; Lukkien, J. J.; Hilbers, P. A. J. *Journal of Chemical Physics* **1998**, *109*, 6051.

(89) Christensen P.A. , H. A. *Techniques and Mechanisms in Electrochemistry* Blackie, Glasgow, 1994.

(90) Zeng, Z. H.; Da Silva, J. L. F.; Li, W. X. *Physical Chemistry Chemical Physics* **2010**, *12*, 2459.

(91) Paseka, I.; Vonkova, J. *Electrochimica Acta* **1980**, *25*, 1251.

(92) Novell-Leruth, G.; Valcarcel, A.; Perez-Ramirez, J.; Ricart, J. M. *Journal of Physical Chemistry C* **2007**, *111*, 860.

(93) Brown, W. A.; King, D. A. *Journal of Physical Chemistry B* **2000**, *104*, 2578.

(94) Rosca, V.; Beltramo, G. L.; Koper, M. T. M. *J. Electroanal. Chem.* **2004**, *566*, 53.

(95) Wang, Y.; Qu, J. H.; Wu, R. C.; Lei, P. J. *Water Research* **2006**, *40*, 1224.

(96) Janssen, M. M. P.; Moolhuysen, J. *Electrochimica Acta* **1976**, *21*, 861.

(97) Figueiredo, M. C.; Souza-Garcia, J.; Climent, V.; Feliu, J. M. *Electrochemistry Communications* **2009**, *11*, 1760.

(98) Soares, O.; Orfao, J. J. M.; Pereira, M. F. R. *Applied Catalysis B-Environmental* **2009**, *91*, 441.

(99) Xing, X. K.; Scherson, D. A. *J. Electroanal. Chem.* **1986**, *199*, 485.

(100) Yang, J.; Calle-Vallejo, F.; Duca, M.; Koper, M. T. M. *ChemCatChem* **2013**.

(101) Lamypitara, E.; Elouazzanibenhima, L.; Barbier, J.; Cahoreau, M.; Caisso, J. *J. Electroanal. Chem.* **1994**, *372*, 233.

(102) Chamam, M.; Lazar, K.; Pirault-Roy, L.; Boghian, I.; Paal, Z.; Wootsch, A. *Applied Catalysis a-General* **2007**, *332*, 27.

(103) Gomez, R.; Llorca, M. J.; Feliu, J. M.; Aldaz, A. *J. Electroanal. Chem.* **1992**, *340*, 349.

(104) Furuya, N.; Motoo, S. *J. Electroanal. Chem.* **1979**, *99*, 19.

(105) Neyertz, C.; Marchesini, F. A.; Boix, A.; Miro, E.; Querini, C. A. *Applied Catalysis a-General* **2010**, *372*, 40.

CHAPTER 6

CONCLUSIONS AND FUTURE WORK

6.1 Conclusions

This thesis focuses on metal nanoparticles for electrocatalysis of oxygen reduction and nitrate reduction. The objectives of this work are: to study the feasibility of Rh coated on Au NRs and Au NPs as an electrocatalyst for the ORR, to investigate the formation of active sites of the Co/TETA/C catalyst along with heat treatment and to investigate the selectivity of and the kinetics of the ORR, to investigate the electrocatalytic activity and selectivity of Rh/C and Sn-modified Rh/C for nitrate reduction and nitrite reduction. Electrochemical techniques are promising techniques in providing a comprehensive understanding of the mechanism, kinetics and on selectivity of the electrochemical oxygen reduction reaction and nitrate reduction reactions. The mechanism and selectivity of the ORR in this thesis has been elucidated by cyclic voltammetry (CV), rotating disc electrode (RDE) and rotating ring-disc electrode (RRDE) in order to determine the products and intermediates of the ORR. Due to the complexity of nitrate reduction, the electrochemical technique was combined with on-line electrochemical mass spectrometry (OLEMS) so that a more comprehensive analysis could be obtained. OLEMS can detect the volatile reaction products during the electrochemical nitrate reaction. In particular, the chromatography technique enables us to detect the soluble products, particularly NH_4^+ and NH_3OH^+. In addition, non-electrochemical, supplementary techniques have been applied to confirm the structure of the catalyst, such as scanning transmission electron microscopy (STEM) with an added high angle annular dark field (HAADF) and energy-dispersive X-ray spectrometry (EDS), X-ray photoelectron

spectroscopy (XPS), X-ray diffraction (XRD), thermo gravimetric analysis (TGA) and differential thermal analysis (DTA).

Chapter 3 of this thesis provides better understanding of the structure of Au NRs, the growth of Rh on Au NRs and Au NPs and their electrocatalytic activity on the ORR. The body of Au NRs obtained by the seed mediated method consists of alternate {100} and {110} facets. The ends of Au NRs comprise {110} and {111} facets, resulting in a more-rounded end and a less-rounded end on Au NRs. The formation of Au NRs is influenced by several factors. The strong adsorption of CTAB at the {100} facet at the side of Au NRs suggests that it forms a CTAB bilayer soft template which induces the rod-shape in particles. The presence of CTAB has an effect on Rh deposition. CTAB removal enhances the Rh deposition onto Au NRs because Rh^{3+} forms micelles with CTAB, which slows down the collision frequency. The Ag^{+} ions at the rod end result in the preferential growth of Rh on the ends of Au NRs. At a low Rh content, Au NRs are not completely coated by Rh and Au−Rh alloy formations are present. The overgrowth of Rh is noticeable at the rod end. At a high Rh content, Au NRs are completely coated and a Rh-rich phase is formed. The co-reduced Au and Rh nanoparticles present separated Au and Rh nanoparticles except for the Au:Rh of 1:2 ratio, which contains particles of partial Au-Rh form. The sequentially reduced Au and Rh nanoparticles show the Au−Rh alloy formation from the Au:Rh of 7:3 ratio and above and the particle size increases when the Rh content is increased.

The electrocatalytic activity of Rh coated on Au NRs for the ORR slightly increases for the Au NRs:Rh ratios of 10:1 and 7:3 and dramatically increases for that of 1:1 and 1:2 ratios. The electrocatalytic activity of co-reduced Au:Rh nanoparticles dramatically increases when Rh nanoparticles are introduced into the catalysts. The electrocatalytic activity of sequentially reduced Au:Rh nanoparticles slightly increases for the Au:Rh of 10:1 ratio and

largely increases from the 7:3 ratio due to the alloy formation at low Au:Rh ratio and the formation of a Rh-rich phase at high ratio. The *n* values acquired for Au NRs:Rh and sequentially reduced Au:Rh nanoparticles increase when increasing Rh, with the exception for the 10:1 ratio which has *n* values lower than that of Au NRs and Au NPs. These results suggest that the composition of the Rh on the Au surface enables control over the selectivity of the reaction. Interestingly, diluted Rh atoms on Au surfaces yield a high H_2O_2 selectivity which is similar to pure Au, thus indicating that the formation of Au−Rh alloys suppresses the further reduction of H_2O_2 to H_2O. The Rh-rich phase on Au surfaces yields a high H_2O selectivity.

Chapter 4 of this thesis presents a detailed investigation of the ORR on non-precious metal catalysts, which aimed to address the second main objective of this research. Co/TETA/C was chosen to produce H_2O_2. Although this non-precious catalyst is not as active as Rh, Co/TETA/C is very interesting because its electrocatalytic activity and selectivity on the ORR is appreciable and tunable *via* heat treatment. The voltammetric profile of Co/TETA/C does not show the oxidation or reduction peak of Co in this potential range. The double layer capacitive current of carbon substrate decreases when TETA is introduced and decreases even further when Co is introduced onto the carbon surface. The onset potential of Co/TETA/C shifts to more positive potential with increasing heat-treatment temperature. The current density also increases in response to heat treatment; however, a current plateau is not obtained. Metallic Co particles are only present on the catalysts heat-treated at 700 °C and higher temperatures. The Co/TETA/C heated at 700 °C yields the highest H_2O selectivity probably, as a result of the presence of Co metallic particles; however, the H_2O selectivity decreases for the Co/TETA/C heat-treated at 1000 °C.

A greater understanding of the selectivity and kinetics of the ORR on Co/TETA/C were obtained by analysing the rate constant for the ORR. The low k_1/k_2 ratio and k_3 values were obtained for the samples that were heated at temperatures lower than 500 °C. It can be concluded that the Co (II) complex tends to produce hydrogen peroxide with a low hydrogen peroxide reduction current. The greatest k_1/k_2 ratio and k_3 value obtained from the Co/TETA/C 700 °C sample indicates that the presence of co-existing Co(II) complex and Co crystallite enhances the reduction of oxygen to water and the reduction of hydrogen peroxide. The k_1/k_2 ratio and k_3 values acquired for the reaction at Co/TETA/C 1000 ºC are lower than those of 700 ºC. This is probably a result of lower metallic Co surface area; the TEM showed larger particles on this sample.

The nitrate and nitrite reduction reactions on Au/C nanoparticles, Au:Rh/C nanoparticles, Rh/C nanoparticles and Sn-modified Rh/C nanoparticles are reported in detail in chapter 5. Au/C does not show any activity for nitrate reduction and presents very small activity for nitrite reduction, suggesting that NH_3 is a main product. Rh/C has promising catalytic activity for nitrate reduction in acidic media; however, only a selectivity towards NH_4^+ is obtained. The nitrate reduction takes place stepwise with NO as the key intermediate. The rate-determining step is the step in which nitrate is reduced to nitrite. The NO_{ads} on Rh/C surface is then reduced to NH_4^+ when the potential is lowered to potentials near that of hydrogen evolution, as NH_4+ was detected by IC at these potentials. Rh/C for nitrite reduction presents promising catalytic activity with the detection of volatile products of NO and N_2O. The formation of N_2O is from the reaction between NO_{ads} on Rh/C surface and NO_{aq} in the solution. NO_{aq} is present from the decomposition of HNO_2. The Tafel slope acquired from the NO_{ads} experiment of Rh/C is 83 ± 4 mV dec^{-1}, indicating that the first electron transfer is the

rate-determining step. Au:Rh/C nanoparticles present lower catalytic activity than Rh/C because the strong NH_4^+ adsorption on the Au surface poisons the electrode surface.

The results of Sn modification demonstrate that there is plenty of room left to enhance the catalytic activity of Rh/C. The catalytic activity of Sn-modified Rh/C is dramatically enhanced and the selectivity towards N_2 is also enhanced. The volatile products NO and N_2O can be detected. The further reduction of N_2O gives rise to the formation of N_2. Sn modification enhances the rate of the rate-determining step. IC data show that the NO_{ads} on the SnRh/C surface is reduced further not only to NH_4^+ but also NH_3OH^+ at potentials near that of hydrogen evolution. The NH_3OH^+ is formed because Sn modification decreases the amount of hydrogen adsorption and also decreases the cleavage of the last N−O bond. The improvement of nitrate reduction on SnRh/C relates to the enhancement of nitrate adsorption on the active sites which comprise Rh and $Sn(OH)_x$ species. Ge modification weakly promote the catalytic activity of Rh/C for nitrate reduction in sulphuric acid. In modification promotes the catalytic activity of Rh/C; however, its activity is still lower than that of the Sn-modified Rh/C electrode. The catalytic activity in HNO_3 is similar to in $NaNO_3$+H_2SO_4, suggesting that the anion effect has a lower impact on Rh surfaces than on Pt surfaces. This is because of the stronger adsorption of nitrate on Rh surfaces, which can compete with hydrogen adsorption.

6.2 Future work

This thesis paves the way for several future researches. Nevertheless, several modifications and drawbacks need to be addressed in order to better improve future studies:

In chapter 3, the details of Rh deposition on Au NRs and Au NPs by chemical reduction are given. There are great possibilities to study the deposition of Rh on Au NRs and Au NPs by electrochemical deposition and to control the deposition of Rh on Au NRs by CO

adsorption.[1] Jirkovsky *et al.* studied the single atom of Pd on Au substrate towards the ORR.[2] The ORR of a single Rh atom on Au substrate is also interesting to study in order to elucidate the mechanism of H_2O_2 production at low Rh content. This experiment should be carried out in parallel with DFT calculations in order to provide more theoretical evidence. More information on surface structure in situ of Au:Rh catalysts will be studied and obtained with the on-going Extended X-Ray Absorption Fine Structure **(**EXAFS).

In chapter 4, the selectivity and kinetics of the ORR on Co/TETA/C heat-treated at different temperatures are revealed. The future research of non-precious metal for the ORR would focus on the factors influencing the catalysts' performance and stability. The active site density of non-precious metal is an ongoing challenge. The development of smaller non-precious metal nanoparticles with controlled properties and surface morphology could provide higher active site density. It would also be interesting to explore high surface area carbon supports or the alternative supports with tunable pore size to improve the catalyst structures.

In chapter 5, the N_2 formation from nitrate reduction can be obtained with Sn-modified Rh/C; however, it is derived from the further reduction of N_2O. The direct pathway to from N_2 is more important. It would be useful if we could design an electrocatalyst which is capable of stabilising NH_2 and NO simultaneously in order to achieve N_2 formation pathways. The Sn-modified Rh/C yields NO, N_2O, N_2, NH_4^+ and NH_3OH^+. There is a possibility that the specific model of Sn-modified Rh (100) might yield direct N_2 formation; however, the single atom of Sn should be initially studied. The Sn deposition Rh (100) should be then varied.

6.3 References

(1) Fennell, J.; He, D.; Tanyi, A. M.; Logsdail, A. L.; Johnston, R. L.; Li, Z. Y.; L., H. S. *J. Am. Chem. Soc.* **2013**, *135*, 6554.

(2) Jirkovsky, J. S.; Panas, I.; Ahlberg, E.; Halasa, M.; Romani, S.; Schiffrin, D. J. *Journal of the American Chemical Society* **2011**, *133*, 19432.